UNIVERSITY OF CALIFORNIA,
IRVINE

Electrical Aspects of Impinging Flames

DISSERTATION

submitted in partial fulfillment of the requirement for the degree of

DOCTOR OF PHILOSOPHY

in Mechanical and Aerospace Engineering

by

Yu-Chien Chien

Dissertation Committee:
Professor Derek Dunn-Rankin
Professor Yun Wang
Professor Jack Brouwer

2014

UMI Number: 3682710

![UMI Dissertation Publishing logo]

UMI 3682710

![ProQuest logo]

DEDICATION

To my respected father, Dr. Chien.
To my lovely and loving mother.
To my sweet sister.
To my grandfather in heaven.

TABLE OF CONTENTS

LIST OF FIGURES

ACKNOWLEDGEMENTS

CURRICULUM VITAE

Yu-Chien (Alice) Chien

Dec, 2014

Office:
Department of Mechanical and Aerospace Engineering
University of California,
Irvine, CA 92697-3975
949-824-8330
chieny@uci.edu

EDUCATION

University of California, Irvine
Studying Doctor of Philosophy in Mechanical Engineering   2009- 2014
Thermal Science (Combustion)

National Cheng Kung University (NCKU), Tainan, Taiwan
Department of Aeronautics and Astronautics (DAA)   2007
Master of Science in Aeronautics and Astronautics

TamKang University (TKU), Taipei, Taiwan
Department of Aerospace Engineering   2005
Bachelor of Science in Aerospace Engineering
With high honors

RESEARCH EXPERIENCE

Graduate Student Researcher

University of California, Irvine, Mechanical and Aerospace Engineering Department.
Lasers, Flames & Aerosols Group
> Electric field effect flames, in-situ optical measurements, carbon monoxide generation from impinging flames;
> Fall 2010 – Now.

> Tomography reconstruction by using Hitran database; Winter 2009 – Summer 2010.

National Cheng Kung University, Department of Aeronautics and Astronautics,
Combustion Laboratory,
> Optical chemiluminescence diagnoses measurement by using optical telescopes; 2006-2007.

> Improvement on the design of the burner of water heater for shower with lean and high efficiency combustion;
> July 2005-2006.

Undergraduate Project

Tamkang University, Aerospace Engineering,
Thermal Fluids Laboratory; 2004-2005
> Looking for potential of the simulation software, Fire Dynamics Simulator, and to see whether if it is appropriate
> for the use of the goal on predicting phenomenon in fire.

Unmanned Aerial Vehicle Laboratory; 2002-2003
> Research and report training/practice, produce and build up a self-designed UAV, assist teaching to make water
> rocket and hand launch glider, National college UAV design competition, Taiwan Aerospace & Defense
> Technology Exhibition.

OTHER EXPERIENCES

Library administrative assistant, National Cheng Kung University, Department of Aeronautics and Astronautics; Academic year 2006

Education equipment assistant, Tamkang University, Education Technology Division. Resolve the issues occur on computer system in classrooms, the job also includes resolving software issue, IP management, remote control system building, ghost, maintenance periodically etc.; 2004

Assistant of Community Service Education Class, Tamkang University;Academic year 2003.

Volunteer of Dietary Commission, Tamkang University; Academic year 2002-2004.

AWARDS

Fellowships, Mechanical and Aerospace Engineering, University of California, Irvine, 2009-Now; Fellowships, Department of Aeronautics and Astronautics, National Cheng Kung University, Academic year 2005, 2006; Certificate of citation of dietary commission, Tamkang University, Academic year 2002-2004; Finest report award, National College Unmanned Arial Vehicle (UAV) Design Competition, Dec, 2002; Third Champion, National College Unmanned Arial Vehicle (UAV) Design Competition, Dec, 2002; School of Excellent of Academic Performance, Tamkang University, Academic year 2001; Da-Yu Scholarship of Engineering Department, Engineering Department, Tamkang University, Academic year 2001, 2003

TEACHING EXPERIMENCE

Graduate program

Manufacturing process in engineering for Women doctoral researchers, University of California, Irvine, Mechanical and Aerospace Engineering. Instructor; Summer 2013.

Manufacturing process in engineering for Women doctoral researchers, University of California, Irvine, Mechanical and Aerospace Engineering. Teaching Assistant; Summer 2012.

Undergraduate class

The list of teaching assistant jobs at UCI:
Fluid Thermal Science Laboratory; 2010, 2014
Thermal dynamics; 2011
Mechanical Engineering Design (2 quarters); 2012, 2013

The list of teaching assistant jobs in NCKU:
Thermodynamics; 2005
Avionics; 2005

Pre-College program

California State Summer School for Mathematics and Science (COSMOS), Teaching Assistant; 2011-2012.

SPECIAL PROGRAMS

"Sounding Rocket-5 launching", National Space Organization. Visitor ;Jan 2006.
"MAE Graduate Student Pizza Party(GSPP)", University of California, Irvine, Mechanical and Aerospace Engineering. Event organizer; 2011 – Now.

WORKSHOP PARTICIPANT

Combustion Energy Frontier Research Center Combustion Summer School, Princeton, June, 2013, 2014.
"Pacific Rim Workshop on Deep Ocean Power Science", University of California, Irvine, February 23-26 2014.

CONFERENCE PARTICIPANT

Annual Meeting of the American Society for Gravitational and Space Research, Pasadena, CA, Oct 22-26, 2014
Western States Section of the Combustion Institute, Pasadena, CA, March 23-25, 2014.
The 24th International Colloquium on the Dynamics of Explosions and Reactive Systems, Taiwan, July 28-August 02, 2013.
The 8th US National Combustion Meeting, Utah, May 19-22, 2013.
The 23rd International Combustion Symposium, Warsaw, Poland, July 30-August 3, 2012.
Western States Section of the Combustion Institute, Riverside, CA, October 17-18, 2011.

International Colloquium on the Dynamics of Explosions and Reactive Systems, Irvine, University of California, Irvine, July 24-July 29, 2011.
The 18th Energy and Combustion Meeting, Yunlin, Taiwan, March, 2008.
The 16th Energy and Combustion Meeting, Keelung, Taiwan, March, 2006.
Aeronautical and Astronautical Society of the Republic of China Conference, Kaohsiung, 2005.

PUBLICATIONS

Conference papers (full papers, acceptance based on abstract)
Chen, C.P., Chao, Y.C., Wu, C.Y. Lien, Y.S., Chien, Y.C., and Cheng, T.S. (2006), "Structure and Stabilization Mechanism of a Microjet Methane Diffusion Flame Near Extinction," The 16th Energy and Combustion Meeting, Keelung, Taiwan, March.

Cheng, T.S., Chien, Y.C., Chao, Y.C., Li, Y.H., Wu, C.Y., and Cheng, Y.Y. (2008), "Development of Chemiluminescence Sensor for Combustion Measurements," The 18th Energy and Combustion Meeting, Yunlin, Taiwan, March.

Chien, Y.C., Garman, J., and Dunn-Rankin, D. (2011), "Tomographic Analysis of Quantum Cascade Laser Absorption by Carbon Monoxide," Paper 11F-41, Fall Technical Meeting of the Western States Section/The Combustion Institute, Riverside, CA, October 17-18.

Yamashita, K., Chien, Y.C., Karnani, S., Dunn-Rankin, D. (2013), "The influence of Electric Field Power Systems on flame behavior," 8th US National Combustion Meeting, Utah, May 19-22.

Chien, Y.C., and Dunn-Rankin, D. (2013), "Electric Field Effects on Carbon Monoxide Release from Impinging Flames," 8th US National Combustion Meeting, Utah, May 19-22.

Chien, Y.C., Yamashita, K., and Dunn-Rankin, D. (2013), "Electric Aspects of Impinging Flames," International Colloquium on the Dynamics of Explosions and Reactive Systems, Taipei, Taiwan, July 28- August 02.

Chien, Y.C., and Dunn-Rankin, D. (2014), "Temperature measurement over a quenching plate with electric field flames," Paper 87LF-0060, Spring Meeting of the Western States Section/The Combustion Institute, Pasadena, CA, March 23-25.

Escofet-Martin D., Chien, Y.C., and Dunn-Rankin, D. (2014), "OH PLIF of an impinging flame," Paper 87DI-0032, Spring Meeting of the Western States Section/The Combustion Institute, Pasadena, CA, March 23-25.

Conference Papers (only abstract required)
Chien, Y.C., Jaquez-Nunez, M., Francis, M., Jacobs, J., Karnani, S., and Dunn-Rankin, D. (2012),"Recent Progress in Studying Emissions from Electric Field Effects on Flames," W5P040- Work-in-Progress Poster, International Combustion Symposium, Warsaw, Poland, July 30-August 3.

Chien, Y.C., and Dunn-Rankin, D. (2014),"Electric Field Controlled Diffusion Flames," Poster session, Pacific Rim Workshop on Deep Ocean Power Science, Honolulu, Hawaii, February 23-26.

Other Publications
Chien, Y.C., "Development of a Chemiluminescence Diagnose system for Combustion Measurements" Thesis of Master degree of Department Aeronautics and Astronautics, National Cheng Kung University.

ABSTRACT OF THE DISSERTATION

Electric Aspects of Impinging Flames

By

Yu-Chien Chien

Doctor of Philosophy in Mechanical and Aerospace Engineering

University of California, Irvine 2014

Professor Derek Dunn-Rankin

This dissertation examines the use of electric fields as one mechanism for controlling combustion as flames are partially extinguished when impinging on nearby surfaces. Electrical aspects of flames, specifically, the production of chemi-ions in hydrocarbon flames and the use of convective flows driven by these ions, have been investigated in a wide range of applications in prior work but despite this fairly comprehensive effort to study electrical aspects of combustion, relatively little research has focused on electrical phenomena near flame extinguishment, nor for flames near impingement surfaces. Electrical impinging flames have complex properties under global influences of ion-driven winds and flow field disturbances from the impingement surface. Challenges of measurements when an electric field is applied in the system have limited an understanding of changes to the flame behavior and species concentrations caused by the field. This research initially characterizes the ability of high voltage power supplies to respond on sufficiently short time scales to permit real time electrical flame actuation. The study then characterizes the influence of an electric field on the impinging flame shape, ion current and flow field of the thermal plume associated with the flame. The more significant further examinations can be separated into two parts: 1) the potential for using electric fields to control the release of carbon monoxide (CO) from surface-impinging flames, and 2) an investigation of controlling electrically the heat transfer to a plate on which the flame impinges. Carbon monoxide (CO) results from the incomplete oxidation of hydrocarbon fuels and, while CO can be desirable in some syngas processes,

it is usually a dangerous emission from forest fires, gas heaters, gas stoves, or furnaces where insufficient oxygen in the core reaction does not fully oxidize the fuel to carbon dioxide and water. Determining how carbon monoxide is released and how heat transfer from the flame to the plate can be controlled using the electric field are the two main goals of this research. Multiple diagnostic techniques are employed such as OH chemiluminescence to identify the reaction zone, OH PLIF to characterize the location of this radical species, CO released from the flame, IR imaging and OH PLIF thermometry to understand the surface and gas temperature distribution, respectively. The principal finding is that carbon monoxide release from an impinging diffusion flame results from the escape of carbon monoxide created on the fuel side of the flame along the boundary layer near the surface where it avoids oxidation by OH, which sits to the air side of the reaction sheet interface. In addition, the plate proximity to the flame has a stronger influence on the emission of toxic carbon monoxide than does the electric field strength. There is, however, a narrow region of burner to surface distance where the electric field is most effective. The results also show that heat transfer can be spatially concentrated effectively using an electric field driven ion wind, particularly at some burner to surface distances.

Chapter 1

Introduction

This research is motivated by the potential use of electric fields as a mechanism for controlling combustion. In particular, it studies the use of the electrical properties of the flame to determine the combustion behavior and the use of the electric field driven ion wind to improve the burning in real time. This dissertation focuses on the specific configuration of a non-premixed diffusion flame impinging on a plate as a model geometry that represents flames interacting with surfaces more generally. The study explores the use of electric fields in this configuration for affecting heat flux to the surface and for reducing the emission of carbon monoxide.

1.1 Ultimate goal of combustion research

Combustion is among the most ancient of processes used by humankind; it is generally considered to involve the conversion of stored chemical energy into heat, with the concomitant conversion of fuel and oxidizer into products. While the exact technologies can vary, combustion research is basically to accomplish this conversion

efficiently and with minimal formation of adverse products. In the recent past decades, and with the depletion of energy resources and the increase of global warming, more precise control of combustion process for reduced pollutant emissions, enhanced efficiency, and optimized combustor operation and monitoring is of great importance to industries and the population of the world. In combustion, the extensive and often inefficient use of fossil fuel has damaged the environment. In addition, it has caused rapid depletion of high-value and convenient fuels around the globe. Therefore, advanced precise combustion technologies with high efficiency and near-zero pollution emissions have attracted extensive attention in the combustion research community[1].

While there is not complete agreement on all of the sources and impacts of climate change, dramatic events renew the debates and demands for information on the rising temperature[2] over the planet during the 20th century. Understanding opportunities to control anthropogenic upsets in order to protect our environment is an essential concern[3]. Combustion remains one of the major sources of environmental impact because it represents a transformation of stored chemical energy into useful work or heat. Hence, as demands for products and living comfort grow, the demands to burn fuels also grow. It is critical, therefore, that all efforts be made to improve our utilization of these fuels, and fundamental research in controlling combustion, which includes reducing emission release into the atmosphere and improving combustion heat transfer, is an important, if not essential, component of a sustainable energy future. This dissertation describes a detailed study of one piece of the hydrocarbon combustion landscape that can possibly be exploited for control.

1.2 Motivation

This research examines the use of electric fields as one approach for controlling combustion. In particular, it studies the use of the electrical properties of a diffusion flame to determine its combustion behavior and it then explores the use of the electric field driven ion wind to improve combustion performance. Diffusion flames are the flame type in most practical combustion devices[4]. Several studies on electrical properties of diffusion flames have been carried out in a microgravity environment to remove the effects of buoyancy, and further, some studies have simulated microgravity by the electric conductive nature inside a flame[5]. These prior studies of the electric field effects on flames helped provide some fundamental knowledge about flame reaction properties[6] and how they can also be used as an actuator to control the flame. So far, however, there have been no studies examining how electrical effects might be useful during the quenching of flames near surfaces. There is evidence that this quenching is responsible for dangerous releases of toxic carbon monoxide, making the electrical properties during quenching an attractive topic of research to examine for effective combustion control.

1.2.1 Exhaust near quenching - Carbon monoxide

There is a classic trade-off in combustion between the emission of the primary pollutants (in particular, carbon monoxide versus the oxides of nitrogen, NOx). Low temperature combustion is known as a method to reduce NOx emissions and soot generation compared to high-temperature combustion. But at the same time, low temperature combustion can generate excess carbon monoxide from incomplete reaction.

Carbon monoxide is toxic and potentially lethal for any air-breathing animal. Moreover, incomplete reaction, which is caused from insufficient oxidizer, mostly occurs near relatively cool walls during intermittent or incipient extinguishment of the flame.

A home wood fire is capable of creating an exhaust plume containing up to 5000ppm CO[7]; this concentration, if inhaled by human beings will lead to headache and dizziness within a few minutes, and then cause death within 30 minutes. Smoke inhalation, including carbon monoxide poisoning, is more often the cause of death in building fires than burns[8]. Because CO is colorless and odorless, people need non-bio based detectors to monitor the amount of CO in the surroundings as an alert to its dangerous presence. As mentioned earlier, CO poisoning is mostly seen in incomplete combustion situations, such as forest fires, building fires, gas stoves, or gas heaters, etc., where there is insufficient oxygen available in the core reaction zone to fully oxidize the products to carbon dioxide and water[9]. As a result CO widely occurs when a non-premixed or fuel rich premixed flame source burns near a relatively cool surface, which can create conditions near extinction (quenching) of the fire[10].

Concentration	Symptoms
35 ppm (0.0035%)	Headache and dizziness within six to eight hours of constant exposure
100 ppm (0.01%)	Slight headache in two to three hours
200 ppm (0.02%)	Slight headache within two to three hours; loss of judgment
400 ppm (0.04%)	Frontal headache within one to two hours
800 ppm (0.08%)	Dizziness, nausea, and convulsions within 45 min; insensible within 2 hours
1,600 ppm (0.16%)	Headache, tachycardia, dizziness, and nausea within 20 min; death in less than 2 hours
3,200 ppm (0.32%)	Headache, dizziness and nausea in five to ten minutes. Death within 30 minutes.
6,400 ppm (0.64%)	Headache and dizziness in one to two minutes. Convulsions, respiratory arrest, and death in less than 20 minutes.
12,800 ppm (1.28%)	Unconsciousness after 2–3 breaths. Death in less than three minutes.

Fig. 1-1 The acute effects produced by CO in relation to ambient concentration[11].

One goal of this study is to determine if there is any correlation between the electrical properties of flames and the release of carbon monoxide from them. A brief review of the general electrical properties of flames follows.

1.2.2 Ions in flames

The story of the electrical properties of flames starts from 1600, when William Gilbert noted that the electrical nature of flames could be measured and manipulated[12]. Volta in 1801 demonstrated a similar discovery that a flame from burning charcoal produced a signal when brought in contact with a gold leaf electrometer[13]. A compilation of development and study on this subject was established in the 20th century, including the electrical nature of incandescent solids and flames[14]. Lawton and Weinberg integrated and published a treatise on the electrical aspects of combustion[12], and UCI recent work included the electrical aspects of gaseous fuel flames for microgravity combustion[5] and continued work on electric field-driven dynamics[6].

1.2.2.1 Mechanisms leading to ion generation

The fundamentals of chemi-ion production and the transport of these ions is well-documented in the references already cited so a complete repeat of this topic is not necessary [12]. A few of the most salient aspects of the process are briefly noted in the following. Several physical mechanisms could possibly lead to or involve ionization. These comprise molecule collision; electron transfer between molecules; excitation energy transfer; chemi-ionization when molecular bonds are breaking and reforming; thermal ionization for electron ejection; photoionization when energetic photons are

involved; three-body attachment during high pressure reaction; dissociative attachment when electron attachment occurs in the products of dissociation[5]. Not all of these are relevant during combustion but they can complicate the analysis when systems operate near thresholds of these different processes. Under the combustion conditions relevant to this dissertation research the chemi-ionization process, where energetic reactions lead to charged species, is the dominant mechanism of ion production.

1.2.2.2 Ions in flames

Two primary ionization steps indicate that initiating chemi-ions arise through radical-radical reactions:

$$CH + O \rightarrow CHO^+ + e^-$$

$$CH^* + O \rightarrow CHO^+ + e^-$$
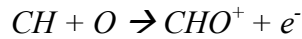
The dominant ion in the flame zone and one that survives into the interelectrode space when a field is applied, H_3O^+, is found experimentally and numerically to arise from the reaction:

$$CHO^+ + H_2O \rightarrow H_3O^+ + CO$$
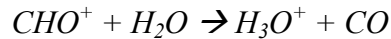
In hydrocarbon flames, H_3O^+ is therefore the most important ion for near stoichiometric mixture combustion, having a much higher concentration than other ions such as $C_2H_3O^+$, $C_3H_3^+$ and HCO^+ (Figure 1-2), and it is also the most likely ion to leave the reaction zone under the influence of an external electric field. Prager, et al. examined and found H_3O^+ dominant in lean flames. In all cases, the weak plasma naturally

occurring inside flames is not essential for heat release reactions[4,15] so changes in ion concentrations and reactions do not affect the essential burning behavior in flames. It is interesting to note that H_3O^+ is associated directly with carbon monoxide formation, suggesting a link between CO emission and ion currents in flames but it is important to remember that ion concentrations are exceedingly small (ppb levels are typical) so any associated carbon monoxide will be insignificant relative to the major species reactions.
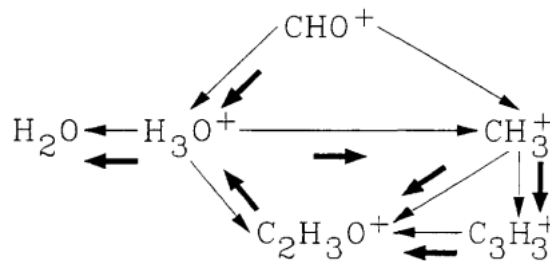
Fig. 1-2 Positive ion pathway in a stoichiometric methane flame. Black arrows denote primary pathways.

1.2.3 Electrical properties near quenching

Electrical aspects in flames have been studied for many years and during that time several different experimental methods on how to measure the ions generated in flames have been developed[12]. Despite this fairly comprehensive effort to study electrical aspects of combustion, however, the only study on electrical phenomenon near flame extinguishment was presented at the 2012 international symposium on combustion by Weinberg et al.[16]. The paper included measurements of carbon monoxide concentration with respect to each location of a diffusion flame to evaluate the possibility of developing a sensor for surface proximity by detecting electrical currents in the flame. The research focused on sensing and so supplied a partially premixed flame with low DC voltage from

7

batteries (37 and 56 volts) and probed with an electrode around the flame to observe the first ion current appearance. The experiment was also conducted with different electrode materials (Figure 1-3).

The results showed that aluminum is chemically and catalytically active, with the generation of CO near quenching, while brass, copper or steel are catalytically inactive materials. The electrical structure of quenching flames was also studied under small (<10V/mm) electric fields, and the current detection area was compared with the quenching regime where CO release was maximum (Figure 1-4).
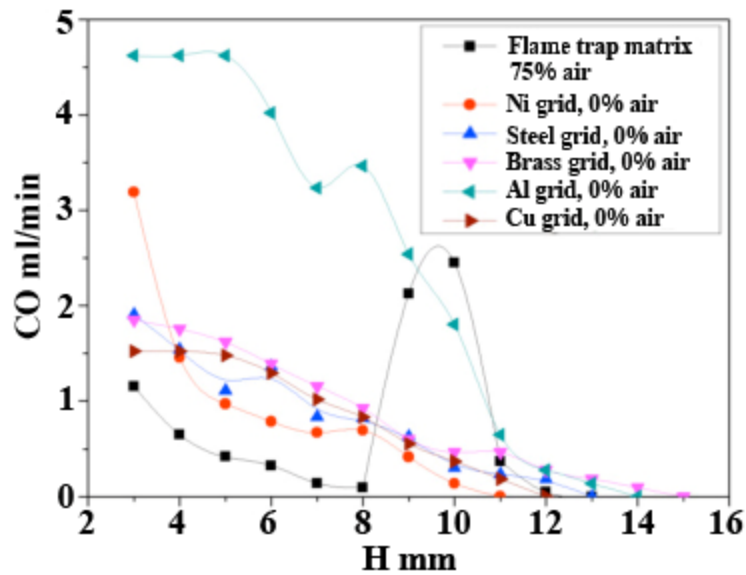
Fig. 1-3 CO detected with different electrode materials
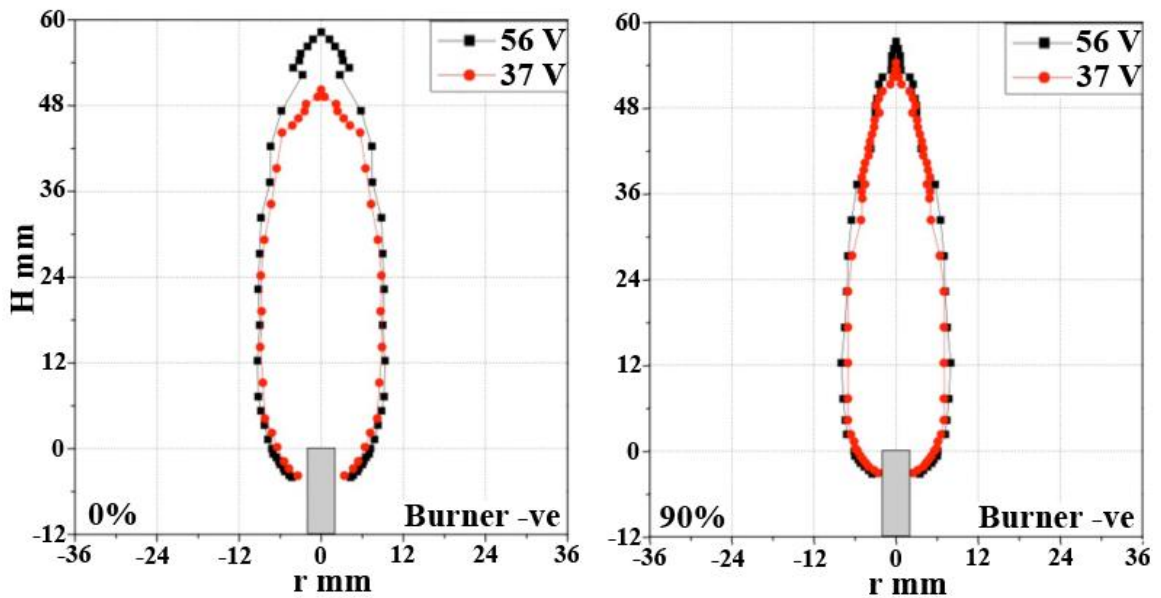
Fig. 1-4 Spatial contours of initial current detection by positive probe at $<10^{-8}$ A

threshold

The catalytic effects are significant since they can lead to erroneous interpretations of the carbon monoxide formed by the flame directly as compared to that produced during interaction with the quenching surface. Nevertheless, this prior research revealed the possibility of using a low voltage source with different probe materials as a CO detecting sensor, and also opened another field to investigate – electric field control of CO release. To begin exploring the effects associated with impinging flames interacting with an electric field as an active control mechanism, this dissertation includes an investigation of high voltage electric field effects on CO release near a quenching surface.

1-3 Objectives

The basic objective of this study is to understand the fundamental electrical aspects of flame behavior near quenching. The study involves determining the relationship between carbon monoxide production and the electrical signal generated by the flame under different conditions near surfaces. In addition, the research involves exploring the possibility of detecting and changing the flame behavior electrically. The ultimate goal is to control the emission of carbon monoxide from flames near surfaces. The research comprises detailed experimental measurements of electric field flame properties, carbon monoxide emission, and heat flux near an impingement surface.

Chapter 2

Scientific Background

This chapter explains some of the relevant scientific background of electric field actuated flames and impinging flames, as well as providing an overview of the related measurement methods involved in their study.

2.1 Electric field effects on flames

Inside a hydrocarbon flame, positive ions and negative charge carriers (generally electrons) appear in the reaction zone. The electrons have far higher mobility and move much faster through the field than do positive ions. Therefore, fewer electrons are needed to provide an electric current balance, which leads to a higher concentration of positive ions in the electrode gap region. When an anode, which is charged positively, is moving toward a flame, the electrons in the reaction zone are highly attracted, drawing them downstream from the burner. The burner itself is taken as a negative electrode, and the electric field lines are directed toward the burner from the downstream electrode plate. At the same time, the positive ions collide with neutral molecules in the surrounding gas which creates an ion wind[4,5,12].

The ion wind (also called Chattock wind[17]) is a phenomenon where chemi-ions are accelerated by an external electric field, and following a short acceleration they collide with the closely packed neutral gas molecules. When the collisions happen quickly and frequently, the momentum from these mean free path collisions is imparted to the neutral gas molecules. The kinetic energy thereby transfers to the bulk flow.

For the case shown in Figure 2-1, the positive ions move towards the burner as an anode (with positive charge) comes close to the flame and negative ions move downstream and are attracted by the positive electrode. Figure 2-1 [4–6] shows a schematic of ion and electron flow in an idealized case of a flat flame and flat electrodes. A more realistic configuration uses a small burner with a large mesh electrode downstream. Several experiments have been conducted to understand the flame shape and behavior in relation to the overall ion current in this jet flame to plane electrode configuration[6].
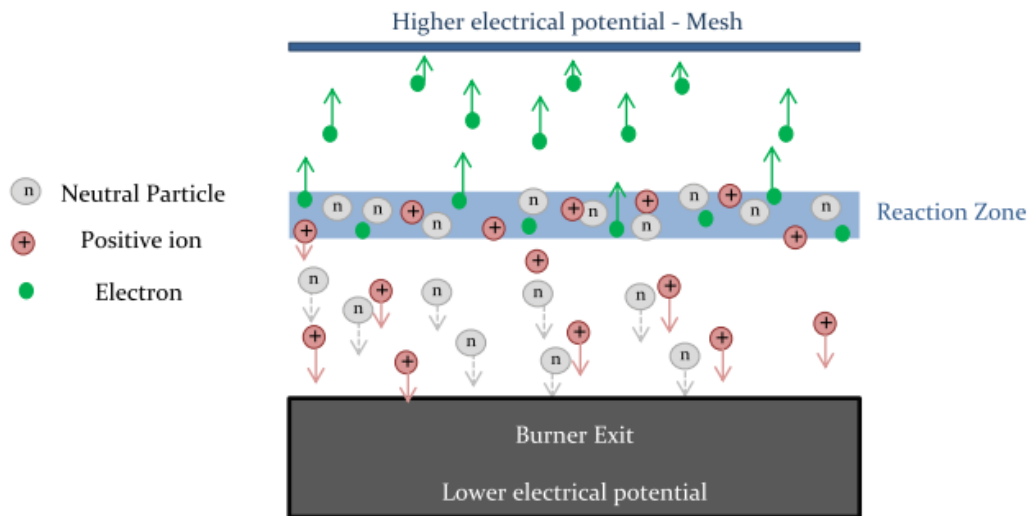
Fig. 2-1 Schematic representation of ion wind[18]

2.1.1 Electric field flame studies

Proper application of electric fields can act on the charge carriers in flames and modify combustion behavior. As mentioned earlier, The use of electrical aspects of flames has been explored for many years, with continuing investigations in microgravity and zero gravity combustion [19–21]. Recent work also demonstrated a direct current electric field effect on the thermoacoustic behavior of flat premixed flames, where the ion-driven wind has been used to suppress thermo-acoustic oscillations [22]. Emissions such as carbon monoxide and NOx can be minimized with electric fields, even when they are weakly applied [23,24], and these effects are also seen in turbulent premixed flames at high pressure [25]. Optically based experiments, such as particle image velocimetry (PIV) and planar laser induced fluorescence (PLIF), have been used to study how the shape of premixed fuel/air flames responds to high electric fields [26–28]. These past studies have helped demonstrate several different experimental methods for measuring the ions generated in flames and their influence [12] but they have not been used in the context of flames near surfaces. Surprisingly, many of these studies do not include measurement of the ion current from the flame, and it is this ion current that is most indicative of effects through the production of ion driven winds.

2.1.2 Ion detection

The mystery of the ion current in relation to the ion-driven wind, flame shape, and flame characteristics, including extinction or oscillations in heat release, has been tested using microgravity experiments and optical measurements[5,6]. In all of these prior studies, the ion current response change with electric fields in methane diffusion flames shows three distinct regions: sub-saturation, saturation and enhanced saturation (Figure 2-2).
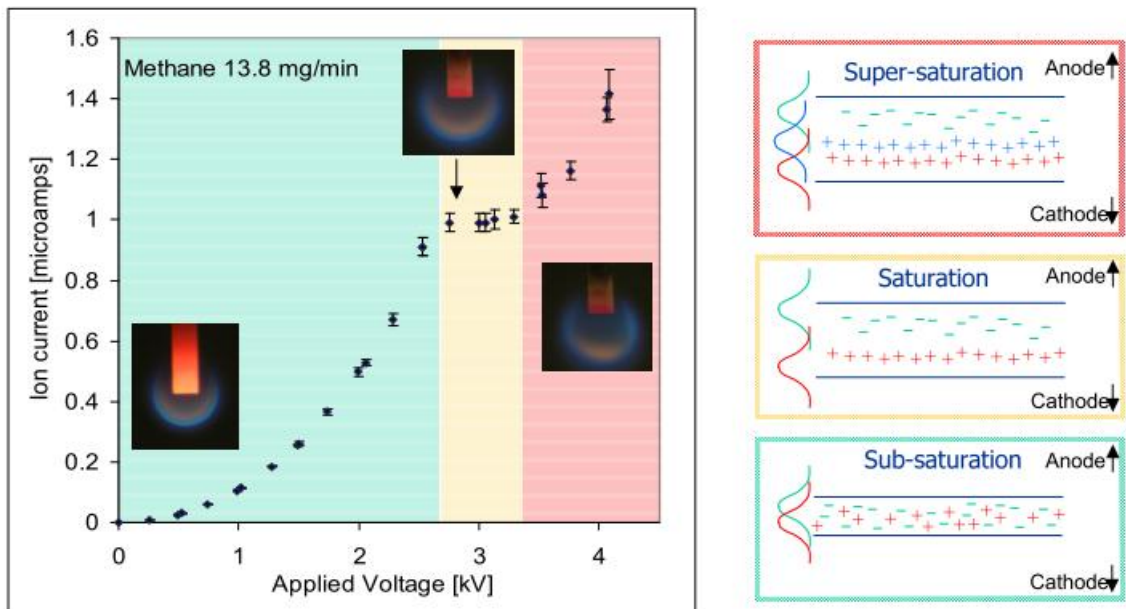
Fig. 2-2 Ion current response illustration in charge separation regions of a methane flame[5].

The sub-saturation region starts from zero nominal field and the curve responds parabolically with increasing the applied field strength. The mobility of the charge carrying species is related to the slope of the curve. In the saturation region, ion current has a minor change with the applied voltage. This is because the ions are removed from

the flame zone as quickly as they are generated. Hence, only at saturation can the ion current be considered fundamentally representative of the combustion of the mixture. In the enhanced saturation region, the field strength is increased beyond the saturation level. Different explanations are possible according to numerical simulations and experimental tests, including additional production of ions due to air drawn into system producing a flame that burns at partially premixed conditions other than stoichiometric[29]; or mild thermionic emission from hot surfaces combined with collision-induced ionization[6].

2.2 Impinging flames

Past studies of impingement from a jet are mostly research on stagnation flow in the turbulent regime[30–34]. Viskanta has listed and compared detailed jet impinging flame studies including jet geometry, equivalence ratio, jet speed, etc.[35]. Four typical impinging flow reacting patterns with turbulent flames have also been studied and identified[31]. Zuckerman et al. has a detailed comparison between turbulent models of heat transfer coefficients and their correlations[34] in the impinging jet regime.

Within the laminar flow region, the early completed research related to impinging hot jets is a study with a circular cylinder over a hot impinging jet for a variety of flow field properties, separation locations, and heat transfer coefficients; it does not include studies near a flat surface plate[36]. Relatively fewer studies focus on impinging laminar flames [35,37–42] but such a configuration would be useful to consider because of its steady flow property and straightforward opportunity for modeling[34]. The following

paragraph covers some of the key aspects of laminar impinging jet flames, including the important scientific background.

2.2.1 Impingement jet geometry and property

For an axisymmetric laminar flame jet impinging on a flat surface, the flow structure can be characterized as comprising four distinguished regions: the flame jet region, the free jet region, the stagnation region and the viscous boundary layer region (Figure 2-3)[35,41,43].

Wall jet region

Impingement surface

Viscous boundary layer

Stagnation region

Free jet region

Flame jet region

x, u

r, v
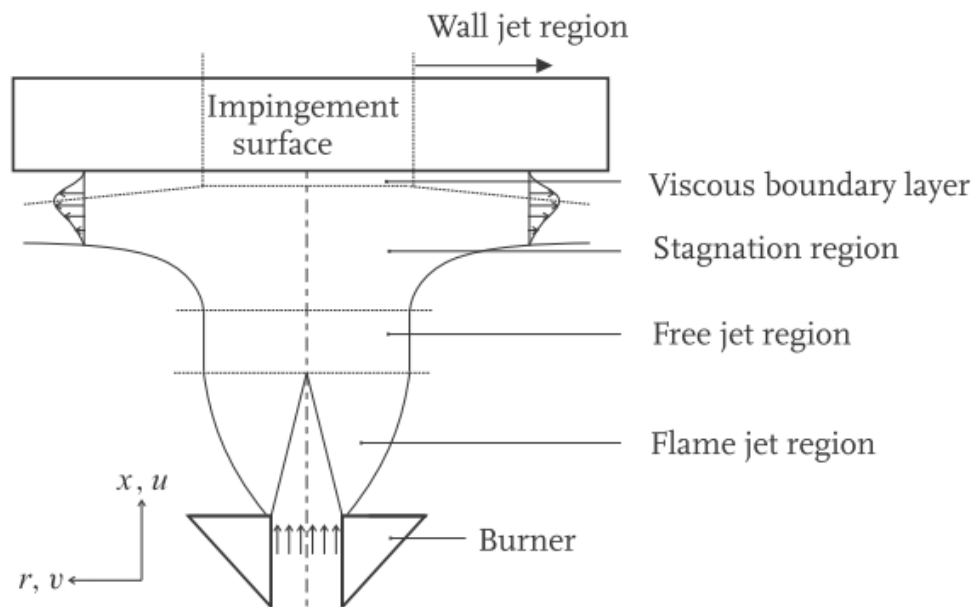
Burner

Fig. 2-3 Flow region of a stagnation flame impinging on a surface[43].

When unburnt gas or a gas-air mixture leaves the burner exit, the flow encounters a sudden expansion in the flame jet region because of the ignition and reactions at the flame front. The surrounding air interacts with the shear flow jet resulting in mass, momentum, and energy entrainment in the flame jet region. The hot burnt mixture then

develops and travels through the free jet region. The impinging region includes two characterized zones: stagnation region and the turning of the jet outward along the plate called the wall jet region. As the flow moves toward the flat surface, the hot gas mixture enters the stagnation region with reducing speed from the interference of the surface and the changing flow direction. A viscous boundary layer will develop with an approximately constant thickness along the surface[44]. Detailed fundamental aerodynamics of stagnation flow can be found in fluid mechanics or fluid dynamics textbooks[45].

To a large extent, impinging flame jets can be treated as impinging isothermal gas jets according to their similar aerodynamic properties[35]. Particularly in their developing geometry, isothermal jets have very similar flow zones to impinging flames. Also the radial velocity gradient at the stagnation point are very similar in impinging flames and isothermal stagnating jets[41]. Impinging jet flames have been, therefore, analyzed as hot inert jets in heat transfer[40], and the only difference is the presence of the reaction zone in the stagnation region and the viscous boundary layer which can contain free radicals at high temperature. With recombination chemical reactions near the cold boundary layer, impinging jet flames release extra heat, resulting in large temperature gradients (and changes in heat transfer coefficient) in the stagnation and wall jet regions[46].

2.2.2 Close distance impingement

When the impinging surface is close to the flame, a decoupling effect appears between the stagnation region and the flame front because the flame jet region is interacting with the stagnation zone[37]. Hence, study over a range of flame jet tip-to-plate distance and the effect of the jet speed with small impinging spacing is important. The jet velocity starts to change when the free jet width is approximately equal to or larger than the flame tip-to-plate distance[40]. Further exploration of convection heat flux (q) at the impinging surface with analytical prediction, shown in Figure 2-4, characterizes a close relationship between the flame jet tip-to-plate distance (H), the free jet width (2R), and the convection heat flux[42]. The result predicts that the heat flux depends on an increasing impinging distance when the flame jet tip-to-plate distance (H) is smaller than 5/3 the radius of the jet (5R/3). This relation has been validated with optical experiments using a photomultiplier tube (PMT) detecting emission at 355 nm from a quartz plate coated with a thermal phosphor in a CH_4-O_2 flame.
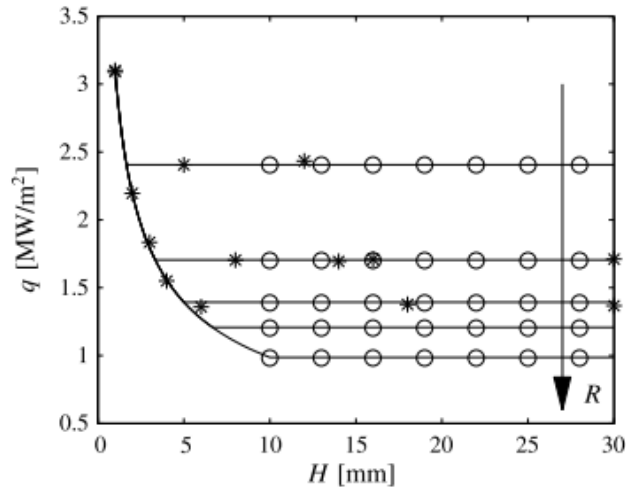
Fig. 2-4 Convective heat flux as a function of the flame tip-to-plate distance (H) for burnt

gas flow tube radii of R=1, 2, 3, 4 and 6mm.

Besides the study of convective heat transfer to a quartz plate, it is rare to find

studies directly on the temperature changes over a stagnation plate with a laminar

diffusion flame impinging on it. One related study of a quenching plate and laminar jet

flame is conducting with a butane premixed flame at stoichiometric conditions[39]. The

experiment compares heat flux between a brass and a stainless steel plate at Reynolds

numbers from 500-1800 with different plate distances. The local heat flux is measured by

ceramic heat flux transducer. The result shows lower heat flux with stainless steel at the

stagnation region compared to the brass plate. This research developed into other further

studies but switched to an inverse jet diffusion flame, which had an air tube in the center

and 12 evenly distributed fuel ports outside the air tube, similar to a typical home kitchen

gas stove. The experiment is operating in the turbulent regime (Reynolds number various

between 2000 and 8000) at different impinging heights using a butane and propane

mixture simulating LPG gas. The results show that the inverse diffusion flame produces

higher heat transfer rate in comparison to a premixed flame jet with the augmented turbulence level of strong mixing of fuel and air[38].

In addition to the interest in turbulent jet flame heat transfer analysis/experiments, among the impinging flame jet research, there is only one paper from Mishra showing interest in sensing emission released from the stagnation region[30]. Mishra measured the flame temperature, CO, CO_2 and NO from premixed LPG turbulent flames at equivalence ratio in the range from 1-4 but at high burner-to-plate distance 10-14 (H/d, where H is impinging plate height above the burner exit and d is the burner jet diameter) and Reynolds number 2500 to 7000. The results show that the local flame temperature drops sharply along the radial direction at a particular distance from the center, and this distance depends on the burner-to-plate spacing. The CO level also increases with the burner-to-plate distance for all flow speeds within the tested turbulent region because of the air entrainment near the flat surface.

There is a distinct lack of research on laminar impinging flames and their carbon monoxide emission, and there is also no heat flux study over an impingment plate with laminar diffusion flames of natural gas or methane below. In addition, while the potential of using electric field effects on laminar flames near impingment surfaces is visible and promising (mentioned in Chapter 1-2-3), none of the past studies relate to electric field flames near surfaces. How an electric field controlled flame can change the emission and temperature distribution over a quenching plate is the central theme of the research described in this dissertation.

2.3 Combustion research methods

The important research tools and their implementation are described in the experimental chapter of this dissertation, but it is also useful to provide an overview of the broad range of techniques that were considered or that were used with only limited success because of the special circumstances of combining high electric fields with flames. In general, combustion studies involve measurements of temperature as a determination of combustion energy and chemical species as a measure of flame structure and pollutant formation. Methods can be intrusive, such as thermocouples for measuring flame temperature, and also nonintrusive. Nonintrusive optical diagnostic techniques offer the advantage of high frequency response and they are able to gather data from hostile conditions like those in the combustion reaction zone over a wide range of conditions. Compared with sample-based sensors, optical diagnostic techniques can reduce the time lag and avoid delays of controller response. While some optical methods involve complex and sophisticated instruments, several optical methods are convenient techniques for monitoring combustion processes. These include absorption, scattering, fluorescence, and chemiluminescence. The methods offer information about the reaction process. These techniques have developed and been studied for years but the information they provide has rarely been used to actively control the flame when it misbehaves. The appropriate combustion research measurement methods that can be used in this research will be covered in this section.

2.3.1 Concentration measurements

Concentration measurement methods include intrusive and non-intrusive approaches. Intrusive methods are usually some form of sampling probe with off-line chemical analysis. Laser-based techniques provide the combustion field with the capability for remote, nonintrusive, in-situ, spatially and temporally precise measurements of important chemical parameters[47]. Non-intrusive methods mostly rely on optical measurements such as Raman scattering, Coherent Anti-Stokes Raman Scattering (CARS), Laser Induced Fluorescence (LIF), planar LIF (PLIF), and chemiluminescence, and absorption. All of these techniques were considered but PLIF and chemiluminescense were the ones implemented. The following sections describe the topic interests related to this research.

2.3.1.1 Chemiluminescence

Chemiluminescence is light, luminescence, emitted from chemically excited species. During combustion reactions, various molecules are created for very short times and excited to a higher energy state before reacting into subsequent products. Some of these radical molecules are formed in electronically excited states and they release photons as they decay back to a lower equilibrium state. Different excited molecules will emit different wavelengths (or wavelength bands) of light. The main emitters of light from hydrocarbon flames are electronically excited CH*(432nm), OH*(308nm), C_2*(436-563nm) and CO_2* molecules. Due to production of these at the original location of high intensity reaction, they can often be used as markers for the flame front[1].
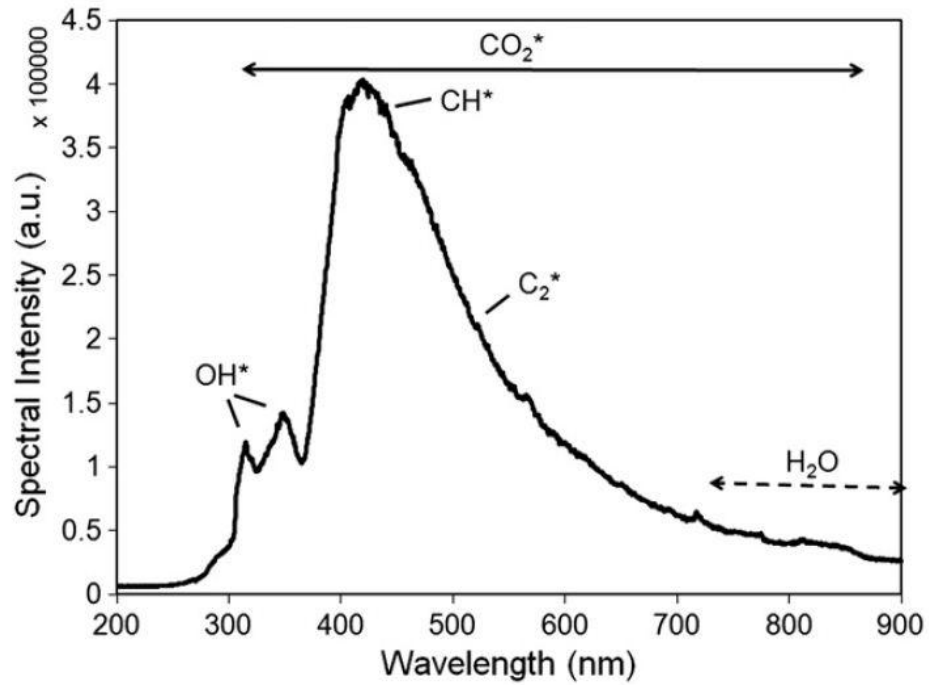
Fig. 2-5 Emitted spectrum from a natural gas turbine combustor – experiment[48].

In hydrocarbon flames, CH* and OH* are reacted and excited from the following reactions[1,4,49]:

$$O + H + M \rightarrow M + OH^*$$

$$HCO + O \rightarrow CO + OH^*$$

$$CH + O_2 \rightarrow CO + OH^*$$

$$OH + C_2 \rightarrow CO + CH^*$$

$$C_2H + O \rightarrow CO + CH^*$$

23
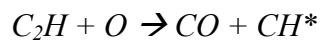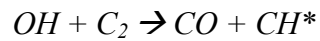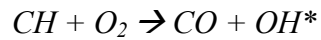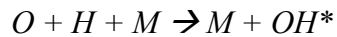
2.3.1.2 OH PLIF

The use of laser induced fluorescence to measure combustion species started in the 1970's. Initially researchers were looking for a species of interest with the approximate wavelength which corresponds to the first excited electronic energy level (Figure 2-6) because the complexity of rotational-vibrational structure in molecules in the ground state cannot be measured by visible or ultraviolet fluorescence[50]. Soon after this first fluorescence study, research obtaining OH number density profiles by using a single shot pulsed lasers with fluorescence detected around 309 nm gave an OH concentration profile mapped along the burner radius(Figure 2-7)[51].

OH planar laser induced fluorescence (PLIF) started in 1982 diagnosing in combustion hot gas as a quantitative measurement by Kychakoff et al[52]. The method was motivated by single-pulse laser-induced OH florescence research which detected the excited OH Q1(6) line at 282.9 nm in a CH_4/air flame[53]. The result, shown in Figure 2-8, has an intense signal acquired from OH fluorescence and elastic Rayleigh scattering around 282 nm. OH was detected because it is a strong fluorescence response and it has relatively high concentration in methane/air flames, as it is an important oxidant within flame reactions. The OH PLIF method contributes to combustion research a convenient technique in understanding the qualitative species concentration/location.

Species	Approximate wavelength
Na	5890
K	7676
OH	3060
O_2	12,629
C_2	5180
CH	4320
NO_2	6660
S_2O	3222
SO_2	3881

Fig. 2-6 List of primary fluorescing wavelengths (angstroms) of suitable species of importance in combustion system[50].
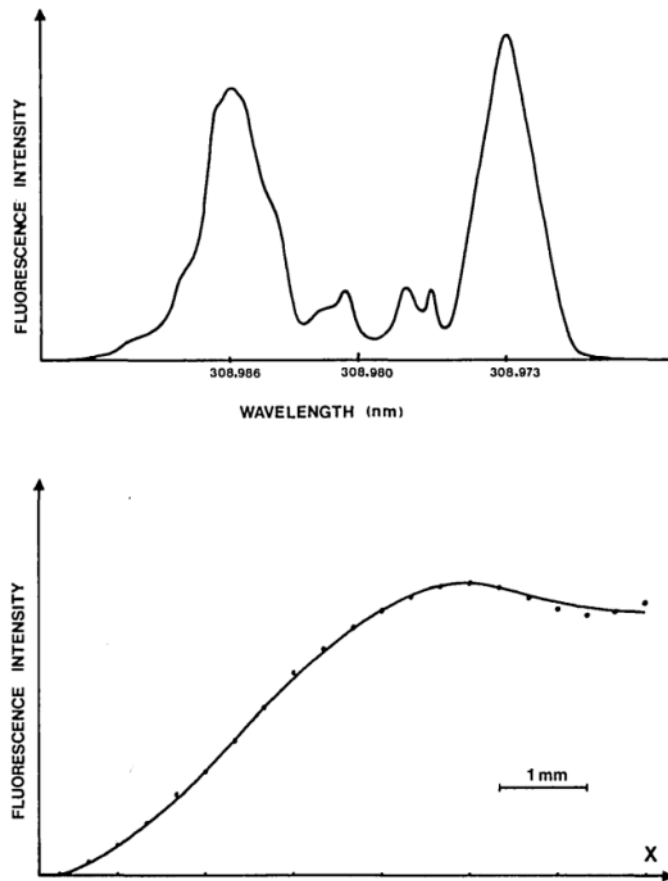
Fig. 2-7 OH furorescence intensity with wavelength and intensity detected along the

burner radius[51].
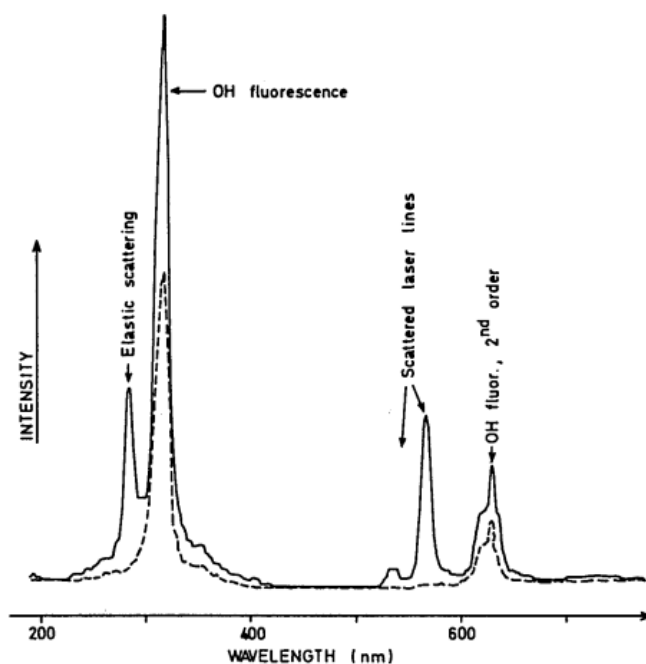
Fig. 2-8 Spectral distribution of the laser induced light[53].

2.3.1.3 Absorption

Laser absorption spectroscopy, in particular, has high signal strength, species specificity, and relative simplicity of equipment and data interpretation characteristics, so it is especially outstanding among the laser-based techniques[54,55]. Laser absorption spectroscopy allows the study of internal structure or distributions such as temperature and concentrations of a variety of molecules by path-integrated measurement if effective tomographic reconstructions are available. It is often worth the additional effort of tomography because absorption spectroscopy measurements are well suited for application to environments that are hostile since absorption signals can be robust if the laser wavelength matches a strong molecular-absorption line. The tomographic techniques require reconstruction along the line-of-sight to retrieve the spatial

distributions of interest from the measured data[56]. There are some popular approaches for this retrieval, including Abel, onion-peeling, and the backprojection methods[57]. For the particular use in hostile combustion exhaust, there are commercial instruments using similar techniques which act as a combustion monitor with the goal of burning coal in power plants more efficiently[58]. The method uses quantum cascade lasers (QCL) and a special tomographic method. Quantum cascade lasers can operate at high power in the mid-infrared region, λ=4 to 20μm, and represent a good light source for detecting gas species and temperature because they provide access to the fundamental rotational-vibrational transitions of many molecules of interest[59–61]. By using the mid-IR, the sensitivity can be improved by several orders of magnitude compared to near-IR laser approaches that rely on overtone detection. In effect, the mid-IR provides much stronger absorption lines for many more molecules important in combustion. Quantum cascade lasers have been used to detect gas species such as CO, CO_2, NO, NO_2, NH_3, CH_4 and N_2O [62]. A preliminary study (analysis and gas cell experiment; see the conference paper attached in the appendix) was accomplished to evaluate the feasibility of QCL detection of CO with tomographic extraction of its spatial distribution but ultimately the needed equipment was unavailable and so this option was not adopted.

2.3.2 Temperature measurements

Although some optical spectroscopic techniques can be used for both temperature and species concentrations, temperature measurement is a separate section outside of concentration measurement because there are several methods to acquire temperature without lasers. Common probing using thermocouples has been used widely in both industry and research but with electric fields present they are not an available option for the gas temperature (they are used in the current work for plate temperature and calibration). Thin filament pyrometry can be accomplished by calibrating the intensity color ratio of a heated filament to predict local temperature but the fiber interacts with the electric field, even to the extent of emitting electrons so this method, like thermocouples, is limited to non-field conditions. Temperature thermometry using optical techniques such as sodium line reversal, CARS, LIF, or absorption and emission spectroscopy are also popular in combustion research. LIF thermometry should be convenient to employ if fluorescence is being conducted for concentration measurement[47]. Figure 2-9 shows the basic approach of two-line fluorescence thermometry. The concept is to measure the relative populations of two states and calculate the temperature via Boltzmann expressions. The method involves an excitation scan within the linear fluorescence region. This approach can be used for steady state flame applications since it requires the long duration scan of the fluorescence. The other limitation is that the method provides the temperature only in the region where the fluorescing species exists, and for typical radical species like CH and OH, this region is mostly at high temperature near the primary reaction zone. For more complete temperature information a seed molecule is

sometimes introduced. This dissertation research employs PLIF thermometry to a limited extent to describe the thermal field near the flame.
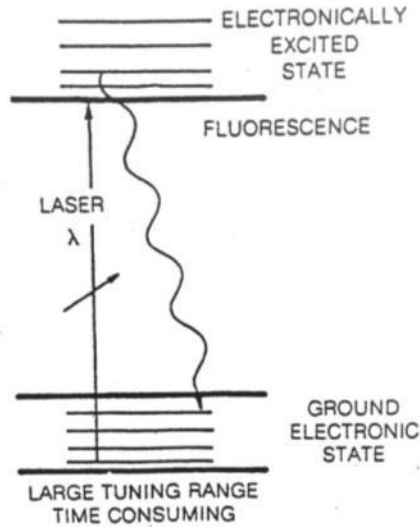
Fig. 2-9 General approachs on excitation scans to LIF thermometry[47].

2.3.3 Numerical and analytical methods for electric field flames

Numerical simulation is not a significant part of this dissertation, but elements of simulation were used at various times to understand some of the potential chemical and flow effects involved. There is an ongoing effort to combine chemical kinetics and CFD for predicting the behavior of flames under the influence of electric fields but for the time being the coupling of the reacting flow computations with electric field forcing are rare. There are numerous computational methods and commercial software packages available in the combustion field, including for example FLUENT, Chemkin, OpenFOAM, or similar CFD tools. The details of these software tools can be found in online resources and are not included in this section. Instead, a general description of numerical research

on electric field interactions with flames, including chemi-ionization in flames will be presented.

Simulating electric field effects on flames requires mechanisms and reactions involving charged species. Chemi-ionization and the ion species in hydrocarbon flames have been studied and various authors list the related reaction mechanisms used in simulations[63,64]. These studies also led to further study, including electric field effects on flames[15,29,65−67]. A numerical and experiment validation study of CH, CH* and OH* in a laminar methane nitrogen coflow flame has successfully predicted CH concentration but CH* and OH* needs further research because there remains a mismatch of prediction with experiment[64]. A list of reactions of the charged species for lean stoichiometric methane-oxy flames includes positive and negative ions, and neutral species. The use of these reactions shows that the ionic reaction mechanism is still incomplete[67]. A reduced reaction mechanism has been used in predicting the charged species concentrations in coflow flames[65] with limited success. There are not yet any simulations that effectively capture the coupling between the reaction and the ion driven wind changes to the transport and mixing in flames, and there are no numerical simulations of flames impinging on a plate with an electric field applied. The experimental findings from this dissertation can be used as validation and verification of such models when they are finally developed.

Chapter 3

Experimental Background

All of the experiments are conducted using a coflow burner and a diffusion flame as it impinges on a metal plate progressively lowered toward the burner surface so that it gradually quenches the flame.

3.1 UCI coflow burner

The system setup is shown in Figure 3-1. The stainless steel coflow burner is 13 cm tall and has a 4 cm outer diameter. The burner has a 2 mm inner diameter center tube carrying fuel, and air is provided separately through a concentric outer ring. The annulus is designed to have a uniform air flow distribution at the exit after it passes through a bed of beads and a honeycomb mesh close to the exit. Inside the burner, the length of the fuel tube is sufficient to ensure fully developed flow at the exit for the range of desired Reynolds numbers. The Yale Laser Diagnostic Center provided construction plans for this burner because it is part of the same NASA microgravity combustion project that supports the current work. The burner is comprised of two plenums threaded together. The fuel is injected into the bottom plenum while the air is injected into the top plenum

(Figure 3-1a, [6]). Electronic thermal mass flow meters and a calibrated rotameter are used to monitor the fuel and air flow (Figure 3-2). The burner sits on a self designed square Teflon block mounted onto moving slides in order to prevent current from conducting through the base connection (Figure 3-3). The detailed engineering drawing is attached in the appendix. The diffusion flame used for this work has flow rates equivalent to a constant nominal speed of 20 cm/s for methane (which translates to fuel flow rate of 37.7 ml/min ± 0.6ml/min) and air at the burner exit, as laminar flow.

The configuration of all tests is with the burner and the plate upright and the plate directly above the burner. The vertical upright configuration is used for symmetry. The downward burning direction is not ideal because buoyancy can drive the flame onto the burner surface when the ion-driven wind is not active[21]. Past work has shown that a downward directed flame creates unwanted soot fouling of the burner surface without providing additional insight[5][19]. Venting on top of the burner is provided by an opening in the surrounding enclosure.
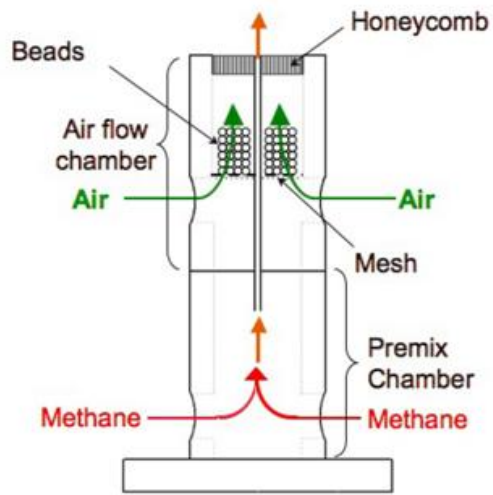
(a)   (b)

Fig. 3-1 (a) Side view of coflow burner and the gas flow schematic[6]. (b) A photograph

of coflow burne

Fig. 3-2 Flowmeters
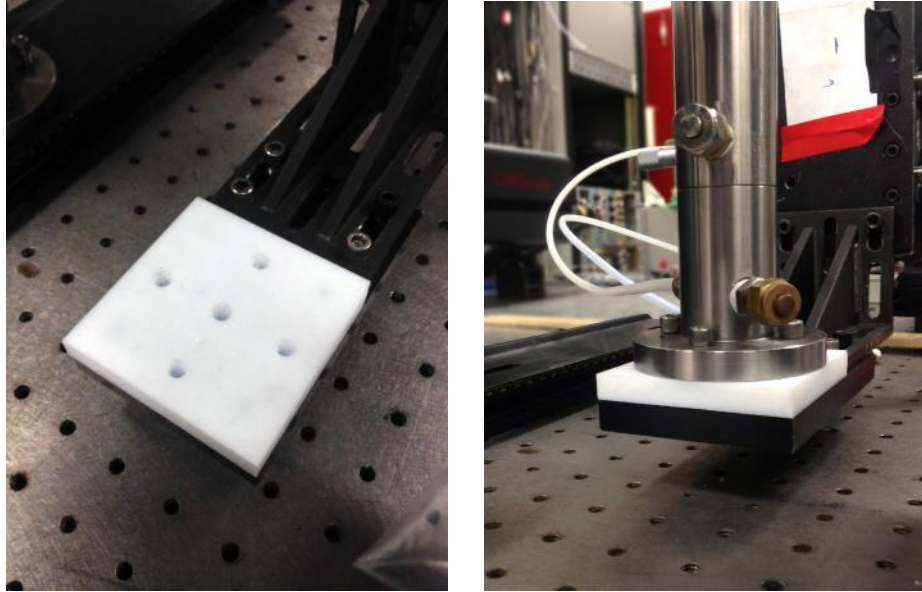
<div style="text-align:center">(a)   (b)</div>

Fig. 3-3 A self-designed and manufactured square Teflon insulation base and a photograph of it connected between the burner and the moving optical mounts.

3.2 Impinging plate

The impinging plate is 4 inches by 4 inches square thin stainless steel with 2mm thickness (Figure 3-4). In order to acquire steady measurements and results with electric field affected flames, the choice of material of the impinging plate is important because the impinging plate is used as one electrode while the burner is the other. In addition, stainless steel has been tested and proven to be chemically and catalytically inactive with carbon monoxide[16]. The impinging plate is indirectly connected onto a vertically-axis translation stage through two cylindrical ceramic threaded posts for electrical insulation.
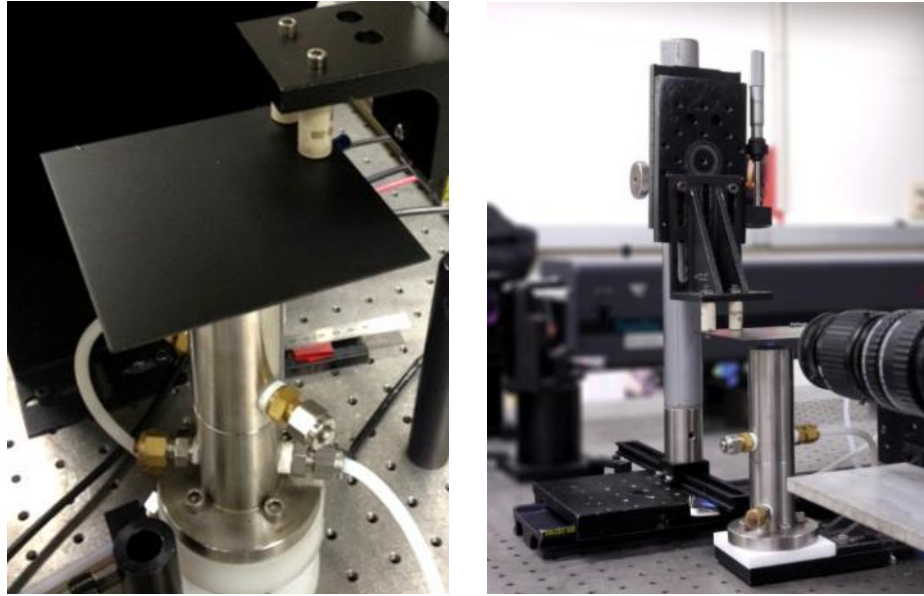
(a)   (b)

Fig. 3-4 (a) The impinging plate and (b) the vertical-axis translation stage with optical

moving slides

3.3 High voltage power supply (HVPS) and apparatus schematic diagram

A high voltage power supply (HVPS or TREK Model 609A-3) is connected onto

the quenching plate and controlled by a computer using MATLAB with a data acquisition

board. The power supply can produce from -10,000 volts to +10,000 volts with a

response time below 10 ms. The power supply response examination will be described in

chapter 4 and a report on characterizing the response time is attached in the appendix[68].

Figure 3-6 is the schematic diagram of the electric field flame experimental setup. The

high voltage electric potential is connected onto the impinging plate while the burner is

grounded as another electrode from the shunt current measurement system (details will be

shown in chapter 4 in the section describing the ion current measurement). The computer

programs an output request to the high voltage power supply to generate the desired high

voltage. The detailed program is attached in the appendix.

Fig. 3-5 TREK high voltage power supply.
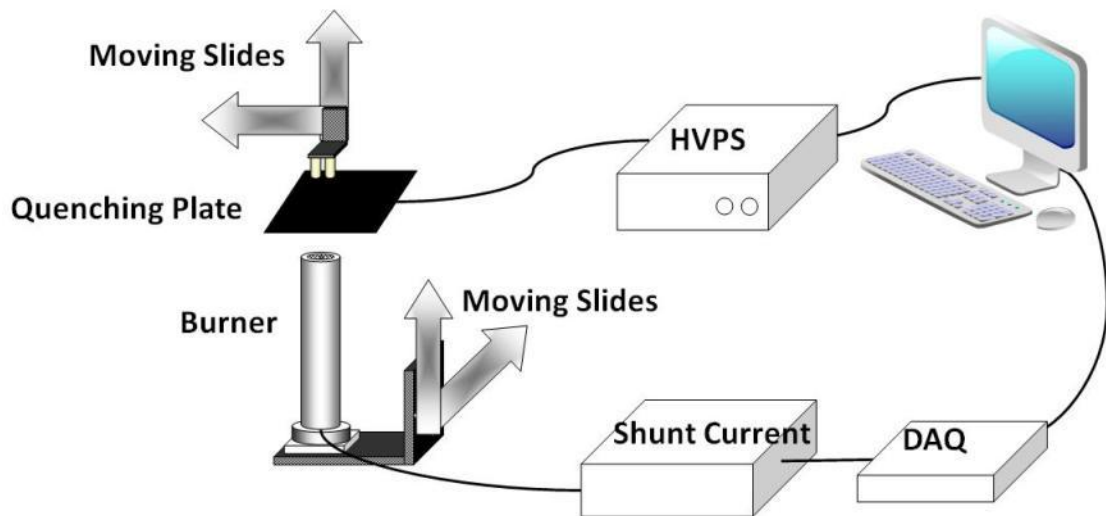
Fig. 3-6 Experimental schematic diagram: a coflow burner and a quenching plate are

separately connected with a shunt current system and high voltage power supply into a

computer.

3.4 ELECTRIC FIELD FLAMES

3.4.1 Electric field effects on flame shape

The flame shape visualization is taken when the plate is 11 mm above the burner (**Fig.** 3-7 a). While there are some effects on flame shape and appearance at all plate locations, at this position the change is very clear as the plate is very close to the flame but has not touched the outer dim luminous region. The flame is pushed down gradually as the positive charge on the plate grows. With a negative charge to the plate the electric field supplies more current and ion wind so that the flame is pulled up and the top of the flame narrows. The luminous zone at the flame front is brighter, presumably because the ion drift wind (or Chattock wind [17]) has entrained more oxidizer and shifted the reaction zone. When a very high electric field is applied (-7kV) from the plate to the flame, the flame quenches. In the positive 7 kV case, an arc generates between the plate and jet which then quenches the flame. Similar phenomena can be seen when the plate is located at 9 mm where it touches the outer dim luminous region of the flame but does not reach the brightest tip of the flame front (**Fig.** 3-7b). Also, images of the combustion as the plate actually disturbs the flame, and of the flame attaching to the plate through an arc mediated by the flame at 5kV/ 7 mm are visible in the pictures (**Fig.** 3-7c). The flame opens wider with positive polarity at the plate, with the bottom rim of the flame close to the burner exit. This opening behavior results from downward directed positive ions producing a downward blowing wind when the burner is negatively charged. The downward ion wind spreads the flame and opens it. Similar phenomena can be seen when the plate is located at 5 mm, **Fig.** 3-7d, except that the flame is already opened by the

stagnating flow at the plate with zero field. Nevertheless, the flame opens wider with increasing field strength over the plate.
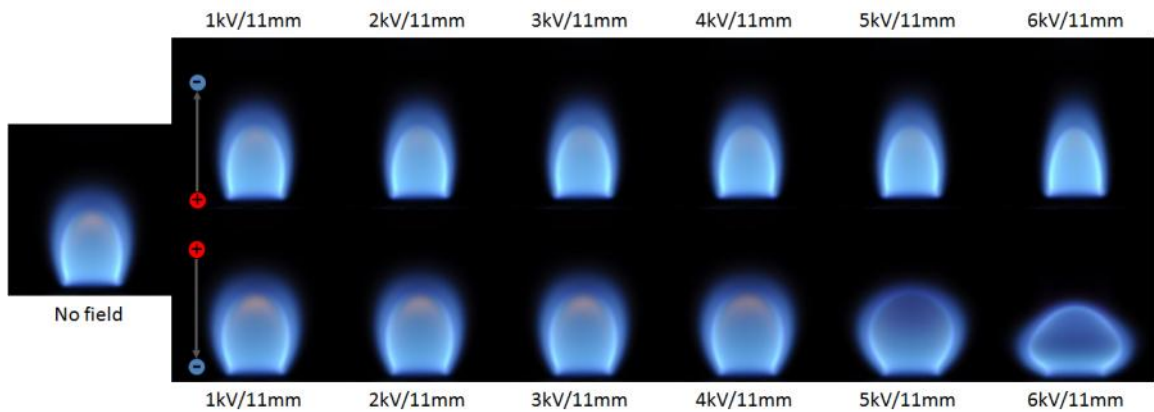
(a) At 11mm
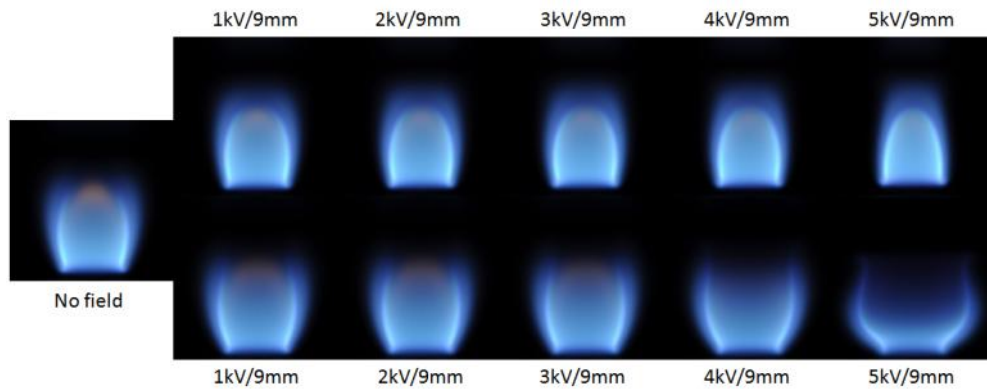
(b) At 9mm
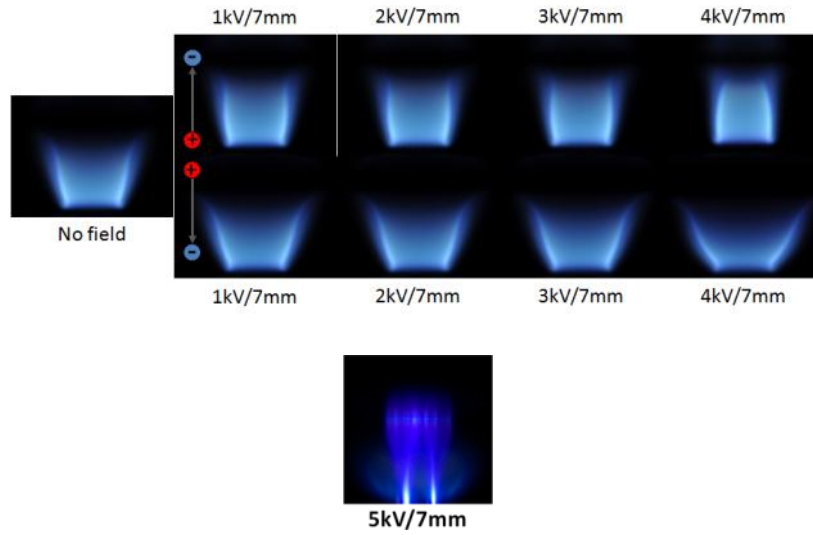
(c) At 7mm
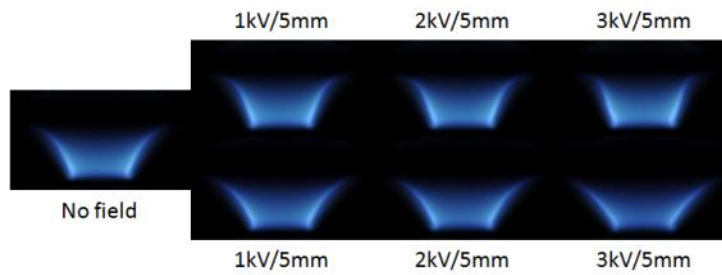
(d) At 5mm
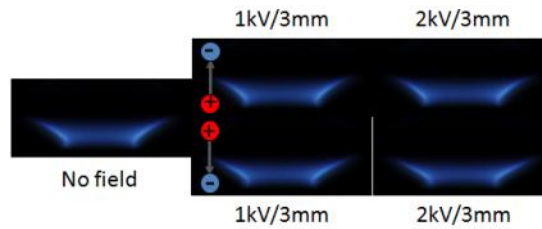
(e) At 3mm

Fig. 3-7 Electric effect on flame near quenching with different height of the plate

position: (a) 11mm(b) 9mm(c) 7mm (d) 5mm (e) 3mm

3.4.2 Burner-to-plate spacing and field direction definition

An overall integrated electric fields with flames image at various burner-to-plate spacings is shown in Figure 3-8; H/D denotes the plate height to the diameter of the center fuel tube. Before doing further exploration of electric field effects on quenching flames it is important to clarify the direction of the field interacting with the combustion zone. There are several definitions/terms for the direction of the field in the electric-field/flame literature. With the terms anode and cathode, the definition can be altered with the electrode that loses or gains electrons; that is, the active electrode and ground can have a different field direction with the electrode charged positively or negatively. These varied uses of potential, electric field, voltage, and polarity in the literature can confuse some of the features of electrical interactions in combustion.

To avoid confusion, the field direction in the current work is based on the electric potential of the burner relative to that of the downstream plate electrode according to how the electric field direction between potentials is defined. It is the consistent view that the direction of the field is as defined in the physics interpretation, from high-to-low potential (where the potential is a relative value in the context of its use). This definition has the advantage that it coincides with the direction of the ion driven wind for the more commonly seen positive ion dominated flows (i.e., positive ions flow from high toward low potential). In Figure 3-8, therefore, the right-hand side represents the positive field in which the electric field drives positive ions and the ion wind toward the plate so that the flame is pulled up and the top of the flame narrows. In this way, the upward electric field direction represents positive field strength while the downward arrow indicates a negative field, which at the same time refers to the direction that the ion wind blows. The flame

quenches when a field is applied above the maximum limit in both field directions. It is clearer to represent the field strength, ion wind direction, and flame behavior/shape all at once by solely field direction. With this qualitative understanding of how the flame shape changes under the influence of the plate and the electric field it is now possible to examine linkages to the possible release of carbon monoxide. The next chapter gives details of the measurement methods.
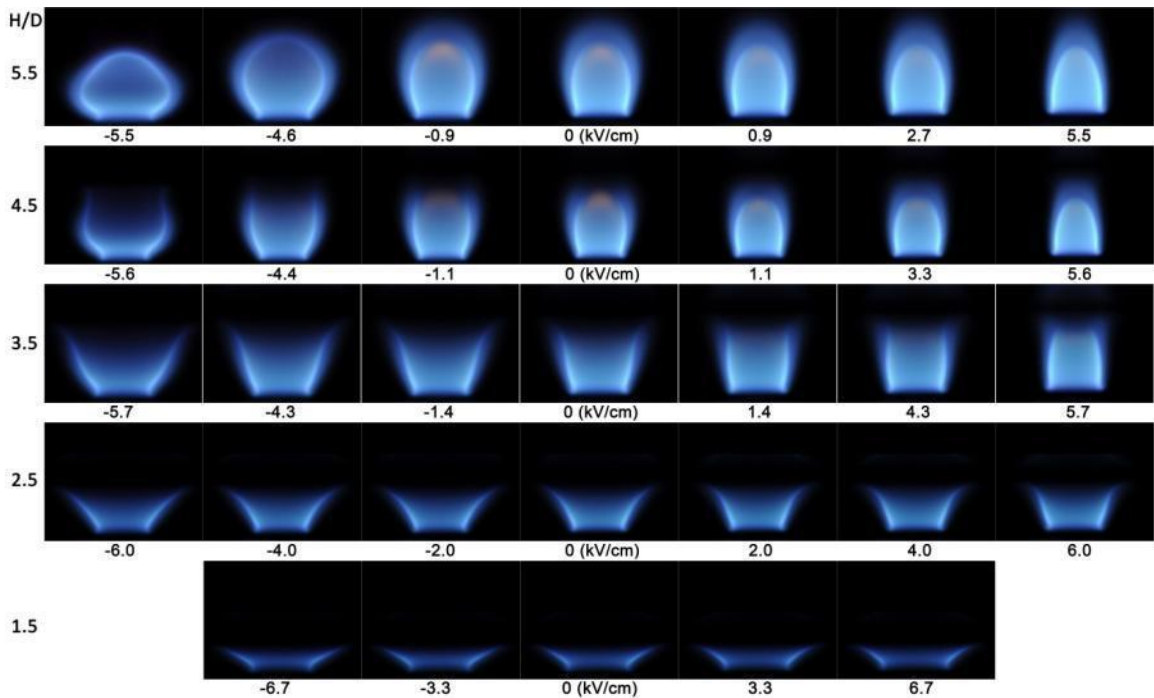
Fig. 3-8 Overall electric field flames with a plate impinging at different burner-to-plate spacing H/D.
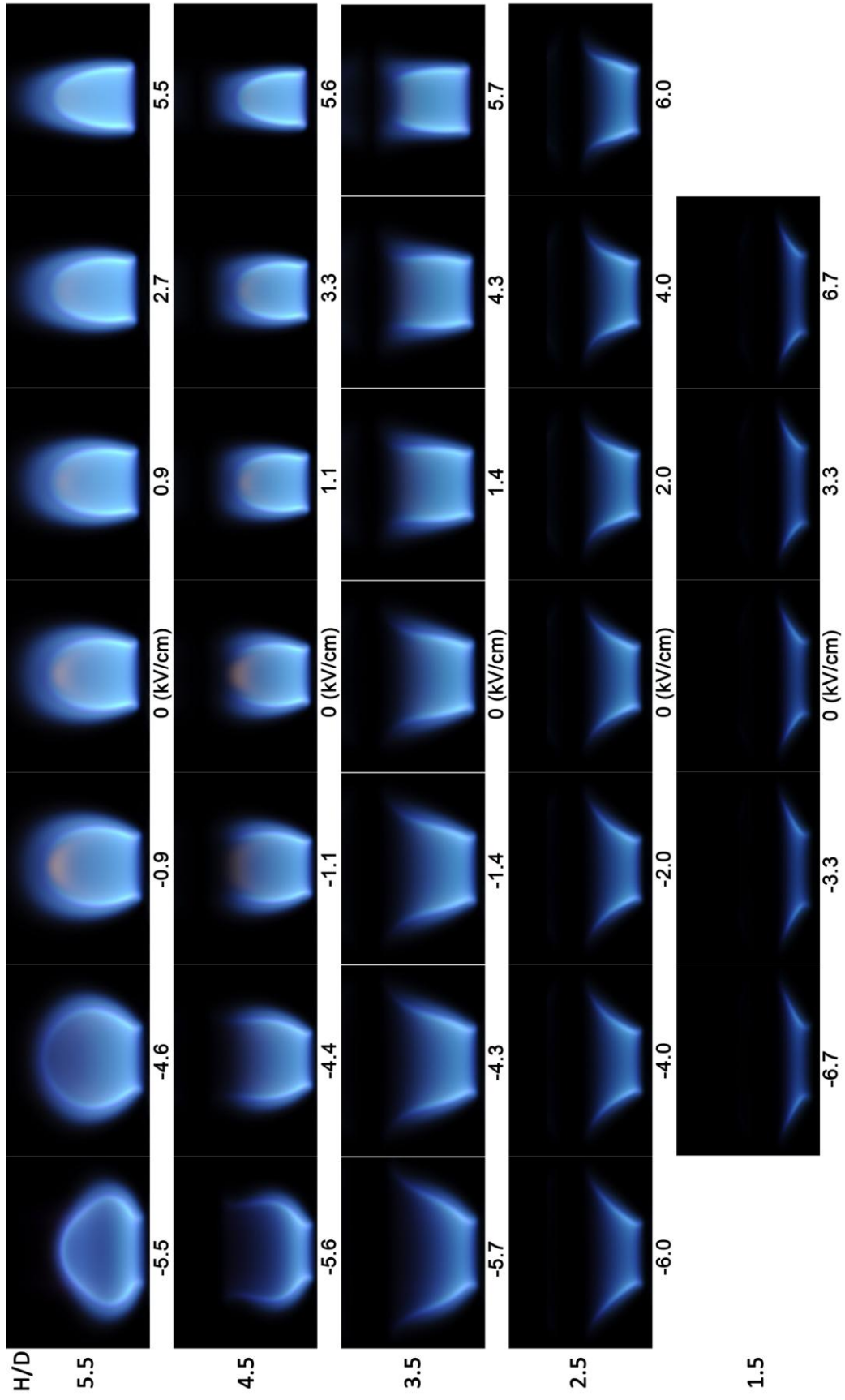
Chapter 4

Diagnostics/Research Principle,

Methods and Setup

All of the experiments are conducted using a diffusion flame from a coflow burner as it impinges on a metal plate progressively lowered toward the burner surface so that it gradually quenches the flame [68,69].

4.1 Power supply response

One of the important aspects of research examining the influence of electric fields on flames is the separation of the dynamic response of the electronics from the dynamic response of the flame. There is a non-trivial coupling between these two systems that needs to be understood in order to accurately isolate the flame forcing behavior of a time varying electric field. The project had access to two different power supplies – one a laboratory instrument (TREK 609A-3) which is mentioned in chapter 3 and the other is an UltraVolt HVPS high voltage power supply pair (20A12-P4-F-M-C-AS), which has the same maximum capability as TREK from -10 kilovolts to +10 kilovolts.

The performance of the high voltage power supplies with respect to flame response is tested with various voltage requests (input) controlled by a MATLAB program while monitoring any difference between the electrode voltage obtained and the request voltage desired. A stainless steel mesh electrode sits 2.5 cm above the burner and receives electric potential from the power supply. The burner is grounded and acts as the other electrode (Figure 4-1). A high voltage probe directly measures the electric potential between the stainless steel mesh and the burner. A MATLAB program collects data of the high voltage probe via a data acquisition card (NI-DAQ, SCB-68).
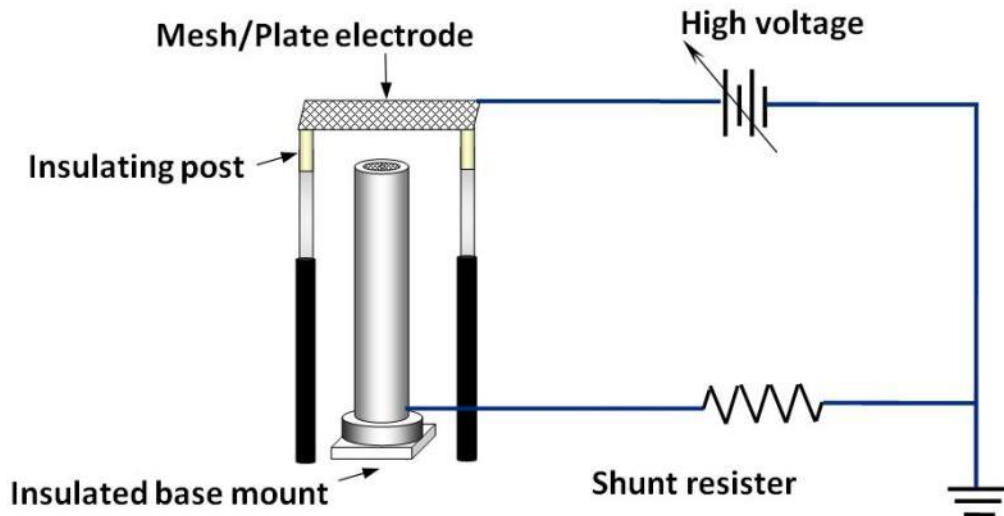
Fig. 4-1 High voltage power supply connection schematic with shunt current measurement.

4.2 Ion current measurement system
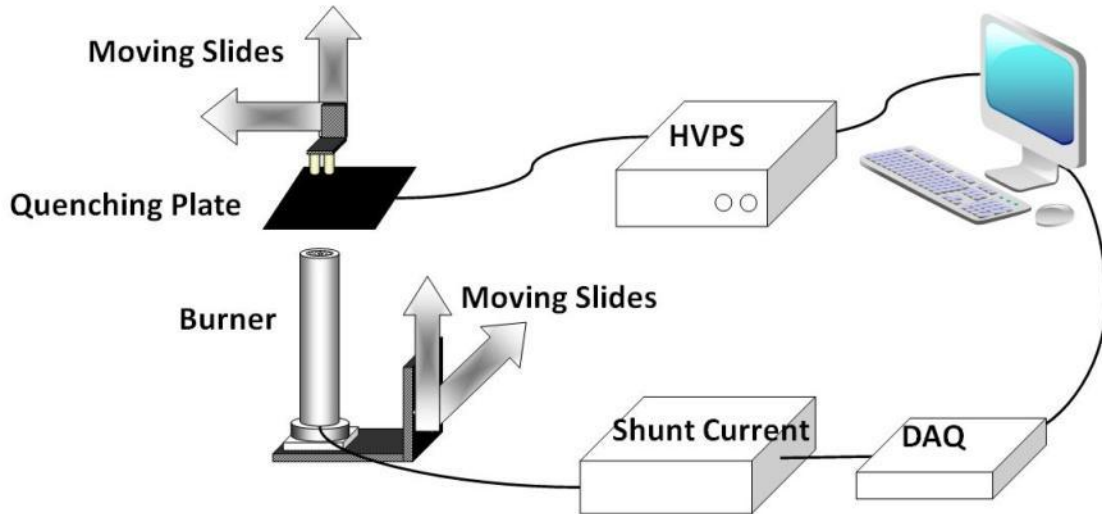
Fig. 4-2 Schematic diagram of ion current measurement system with HVPS.

The ion current is the most significant measurement for flames under the influence of electric fields because it is a characteristic of the chemical processes and is directly related to the strength of the ion-driven wind force driving convection in the surroundings. The ion current of the flame flows between the two electrodes, the plate or mesh and the burner. Therefore, the inter-electrode space, including the flame itself, can be interpreted as a nonlinear electrical resistance. The ion current of the flame is measured by a shunt current system which leads ion current to pass around a lower resistance path. A detailed electrical circuit of the shunt current system is shown in Figure 4-1. A 4.6 kΩ resister is used in the system. This resistor provides a good balance between detection sensitivity and time response. The circuitry of the shunt current system is protected with diodes and also includes a slow discharge circuit to prevent

electric shock. A National Instruments data acquisition card (SCB-68) connects the shunt current system and computer together.

The data acquisition from the DAQ card into the computer is programmed with the MATLAB computational package and Data Acquisition toolbox. Ohm's law is used in the MATLAB program for computing the ion current from the potential drop across the shunt resistance. Figure 4-2 is the schematic diagram of the whole system.

4.3 Schlieren measurement system
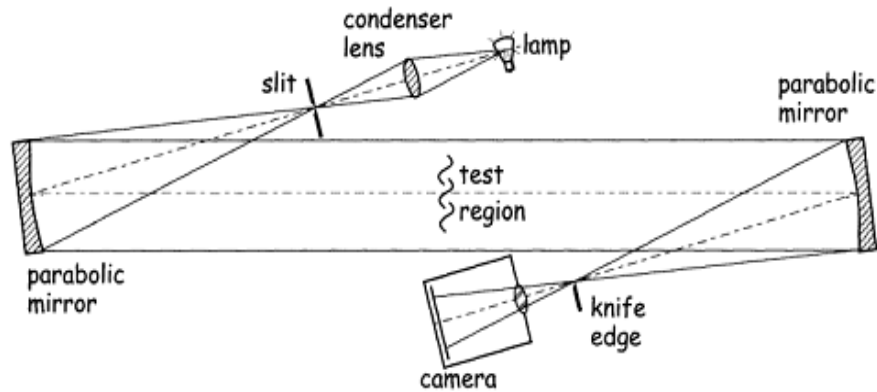
Fig. 4-3 An example of the Z-type Schlieren setup schematic, from Settles[70].

Schlieren is an imaging technique to observe the flow field by imaging density change (and thereby refractive index change), and there are different types of setups with advantages and disadvantages. We are using the so-called "Z-type" Schlieren (Figure 4-3) with two 6 inch diameter parabolic mirrors, which reduced spherical aberration as compared to equal sized lenses. An arc lamp provides white light as a bright but not tightly constrained source, and this light is then focused by a convex lens. An optical

fiber collects the focused light and acts as a point light source at the focal point of the the first parabolic mirror. The reflected light from the mirror travels parallel and across the test zone to the second mirror situated at its focal distance of 45 inches. A knife edge is placed at the refocused light from the second mirror to partially block the light that has been deviated by the refractive index gradients in the test section. The generated Schlieren image is then projected onto a glass screen by an achromatic lens. Figure 4-4a shows the point light source from the exit of the optical fiber (left), the flame (yellow) and the inverted projected Schlieren image on the glass screen. Figure 4-5b shows the detailed setup from another angle.
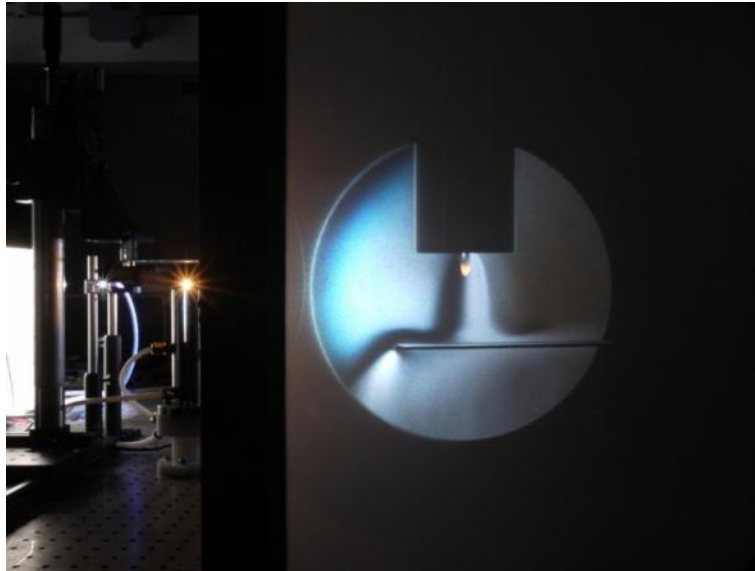
(a)
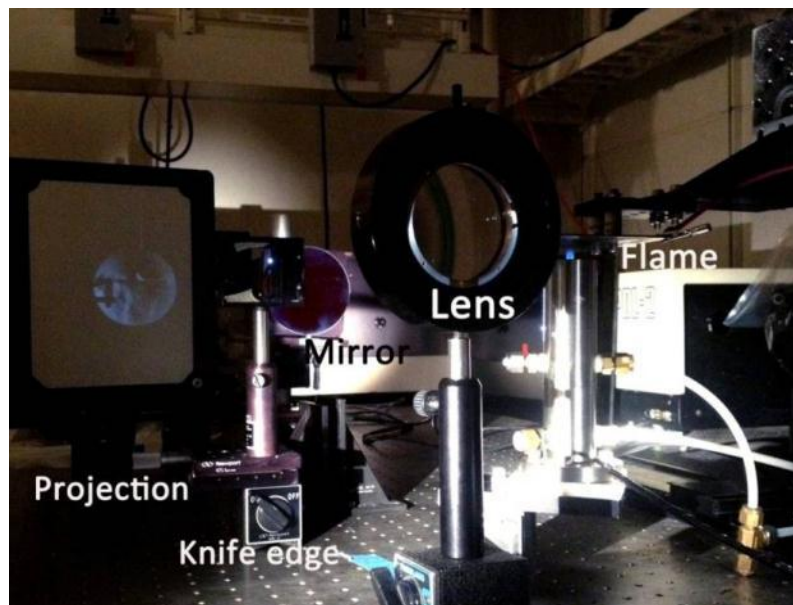
(b)

Fig.4-4 Photograph of the Z-type Schlieren experimental setup on an optical table; the

second mirror is not shown as it is out of the image towards the viewer.

4.4 Mid-IR emission detection

Global measurement of infrared emission can provide some information regarding combustion completion. Ideally, the detector would be sensitive only to the emission of light from carbon monoxide (CO) as a key indicator of incomplete combustion. Unfortunately, narrow band detection is extremely difficult (which is one reason that the narrow band absorption spectroscopy of quantum cascade lasers was investigated) so for this study the mid-IR emission was used to provide a global combustion behavior measurement. Infrared emission is measured with a mid-infrared lead selenide photoconductive detector (Hamamatsu P3207-07, Figure 4-5a) that is sensitive to light at wavelengths of 4–5 micron (Figure 4-5b). The list of emission lines in this range has been identified from the HITRAN database[71]. The major relevant emitting species in this wavelength range are carbon monoxide, carbon dioxide, and methane based on the predicted emission from the HITRAN database. A BNC housing connected to the optical mounts is built for the detector (Figure 4-6a) and an electrical circuit for the lead selenide photoconductive detector with signal amplification is shown in Figure 4-6b. Figure 4-7 is a picture of the system setup for the detecting measurement.

(a)   (b)
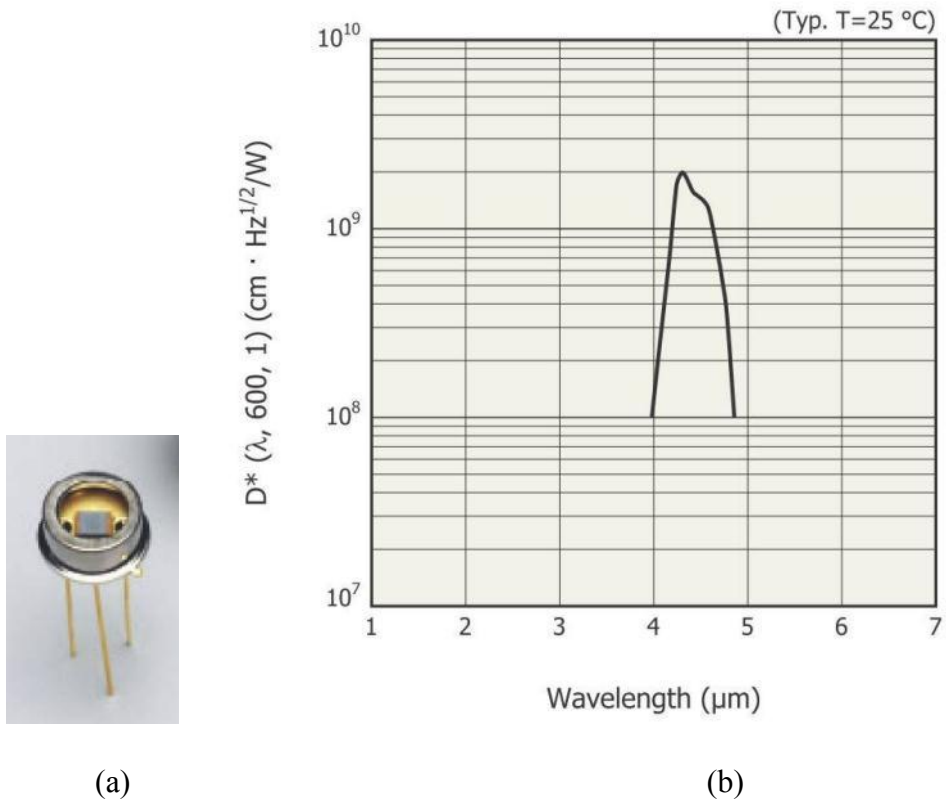
Type No.	Measurement condition Element temperature T (°C)	Peak sensitivity wavelength λp (μm)	Cut-off wavelength λc (μm)	Photo sensitivity S *3 λ=λp Vs=15 V		D* (λp, 600, 1) (cm · Hz$^{1/2}$/W)	Rise time tr 0 to 63 % Max. (μs)	Dark resistance Rd (MΩ)
				Min. (V/W)	Typ. (V/W)			
P3207-07 *2	25	4.3	4.8	1.4×10^3	1.8×10^3	2×10^9	10	0.1 to 3

*2: Half width 400 nm

(c)

Fig. 4-5 PbSe detector: (a) detector image (b) detecting wavelength range (c) detailed

electrical and optical characteristics.

(a)   (b)
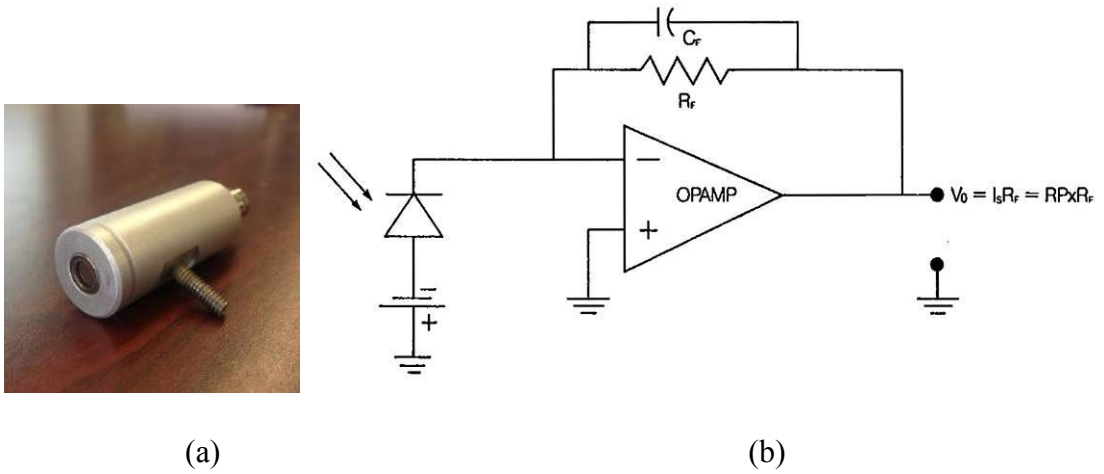
Fig. 4-6 (a) A housing built for the detector connected with a BNC and one optical screw

(b) an amplified circuitry connect with the detector(courtesy form UNITED

DETECTOR).
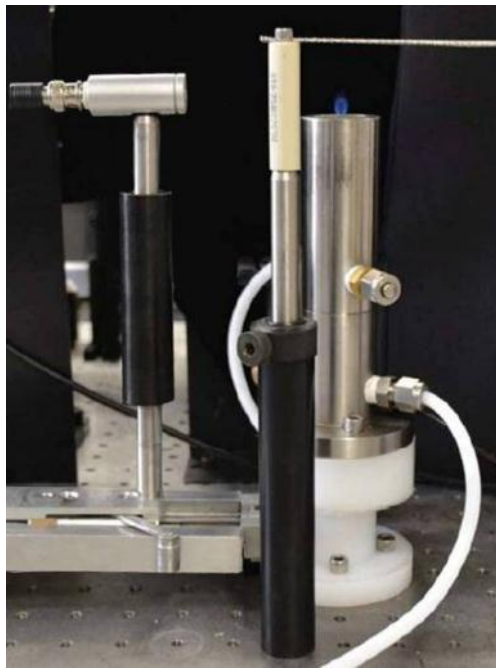
Fig. 4-7 The mid-infrared measurement system[72].

The initial experimental results after directly sensing signals from a flame show a steady IR signal at high positive and high negative electric field, with the emission showing a significant decrease as the electric field changes from zero toward the highly negative values. In order to distinguish the signal of carbon dioxide from that of carbon monoxide in the region, two sapphire band pass filters located at 4.26 (carbon dioxide) and 4.7 (carbon monoxide) microns with FWHM tolerance at ± 40 nanometers are used. The results show that the signal detected without a filter and with a carbon dioxide filter is the same. No signal is detected when using the carbon monoxide filter.

Based on the intensity predicted from HITRAN database, carbon dioxide has the strongest integrated emission while carbon monoxide has an order of magnitude less, and methane is the weakest among them, which shows agreement with the test results (Figure 4-8). The carbon monoxide emission lines in an ethylene flame are not strong enough for detection (Figure 4-9).

Therefore, this detector dominantly senses hot carbon. Because the carbon dioxide emission does not vary substantially with electric field, this mid-infrared detector alone is not an ideal sensor for flame response to electric fields. The work could be done by using a better absorption source, such as a quantum cascade laser, to focus the response on narrow separated spectral lines easily assigned to the targer molecule. This broadband carbon detection work was part of a visiting student project but its lack of sensitivity makes it unsuitable for determining changes in carbon monoxide production in the small diffusion flames of the current study; the details are available in reference[72].
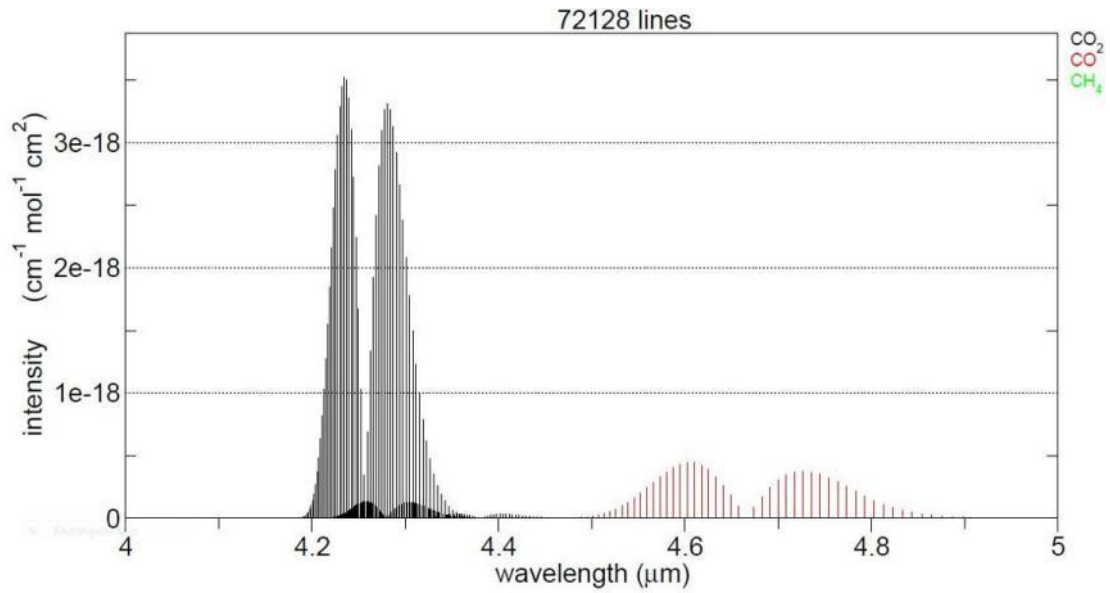
Fig. 4-8 The predicted absorption lines from HITRAN database.
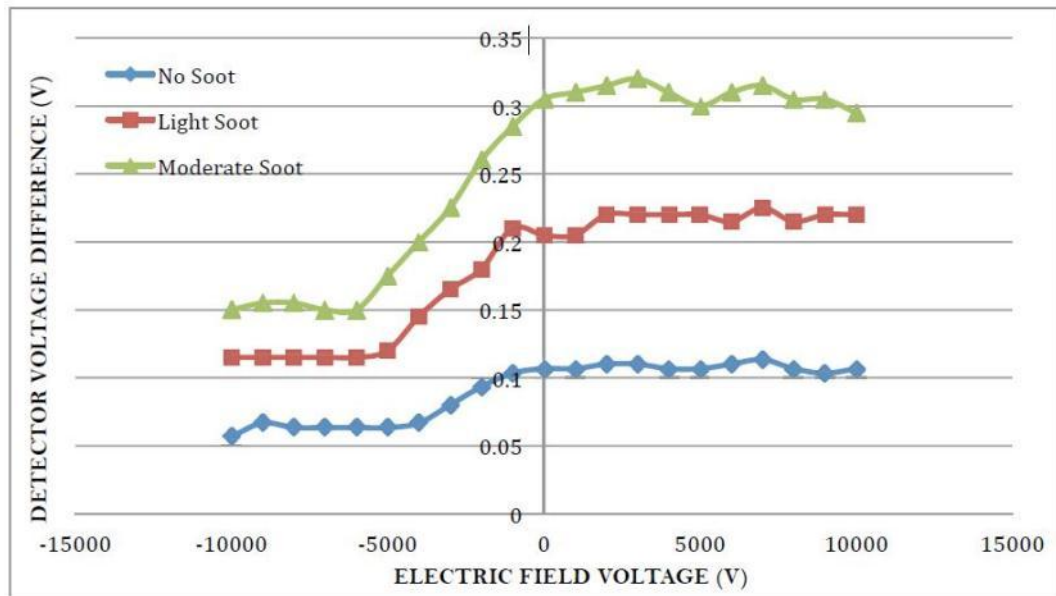
Fig. 4-9 IR detection with ethylene flame at different mesh voltage applied[72].

4.5 Carbon monoxide measurement

The mid-IR measurement of CO can give the dynamic carbon monoxide and carbon dioxide behavior but because it is a global measurement looking at the entire flame zone it cannot identify how much of this CO is released from the flame. For this measurement, a sampling system is needed. Measurement of CO released from the flame with a plate onto which the flame impinges at different heights between the burner and the plate provides an indication of the potential for CO emission control of quenching flames using an electric field. That is, applying an electric field between the plate and the burner can affect the combustion process and thereby the CO emission. The steady state carbon monoxide emission behavior of different flames is measured with a portable combustion analyzer (TSI CA-CALC 6200, Figure 4-10a) that aspirates the exhaust gas inside an acrylic chamber (Figure 4-10b) at a slow and fixed flow rate. The generated CO from the flame fills the chamber and mixes with the existing air to yield a gradually increasing natural release from the chamber. Once this product concentration stabilizes, based on the reading of the concentration, effective steady-state is confirmed. The acrylic chamber was designed to create a steady environment for the experiment and to diminish the external influence of air currents on the small flame. For each case of carbon monoxide emission measurement, the chamber is first flushed with air. The decay rate of carbon monoxide release from the chamber as well as the generation rate has been considered and is analyzed[73]. The flame is then operated for two minutes before the CO measurement is taken. Detailed analysis and tests are presented in the following chapter.
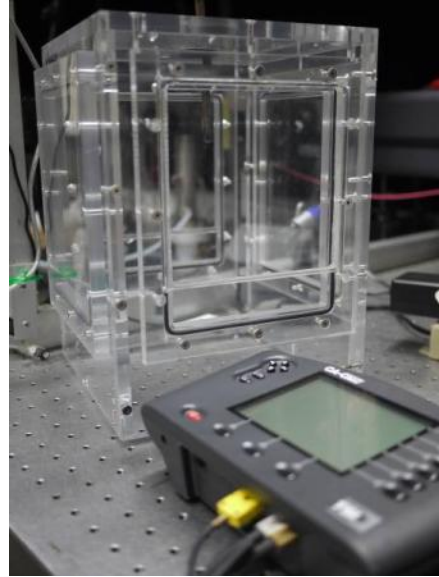
(a)   (b)

Fig. 4-10 Portable combustion analyzer and the emission probe with the acrylic chamber.

4.6 PLIF

4.6.1 OH and CO

To better understand the gross and subtle relationships among plate proximity, electric field effects, and CO emission, we explore changes in flame structure associated with these influences. Detailed experimental results in the literature for steady coflow methane/air diffusion flames show that the high CO concentration area is located on the fuel side of the high temperature reaction region [74]. In an unperturbed flame, this CO is oxidized to CO_2 and does not escape to the environment. For the case of the electrically actuated impinging flame, heat is lost to the plate, which affects the chemistry, and the flame and flow field change shape, which affects the transport. One question can be which of these has the greatest impact on CO release.

Research has shown that the gradient in OH fluorescence can be employed as a marker for the reaction zone [75–77], and it has been shown that the predominant influences on CO in hydrocarbon flames at similar velocities and compositions to ours are the reactions[78] [79]:

$$H + O_2 \rightarrow OH + O \ (1)$$

$$CO + OH \rightarrow CO_2 + H \ (2)$$

$$CH_4 + OH \rightarrow CH_3 + H_2O \ (3)$$

$$CH_3 + O_2 \rightarrow H_2CO + OH \ (4)$$
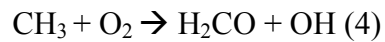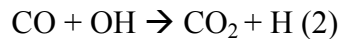
Carbon monoxide oxidation depends heavily on hydroxyl radicals to form carbon dioxide. Reaction (3) in the high-temperature oxidation of methane/air flames consumes hydroxyl faster than does the carbon monoxide oxidation reaction (2). This competition for OH leads to a CO accumulation [79]. Significant emission occurs if this accumulated CO is not oxidized in another region of the flame. It is also important to recognize that the formation of OH requires oxygen in reactions (1) and (4) so it is created in the outer layers of the reaction zone. Smyth et al. measured the distribution of carbon monoxide and marked the OH boundary of a diffusion flame in a Wolfhard-Parker slot burner during their soot research [80]. They showed that the location of the peak carbon monoxide emissions is inside the OH boundary and the overall carbon monoxide is inward but attached to the OH region. These results suggest that the distribution of OH and OH* can provide insight into the CO oxidation effects with quenching distance and

electric field. In other words, observing hydroxyl, both as OH and OH*, can be used to infer regions of effective carbon monoxide oxidation.

4.6.2 PLIF Setup
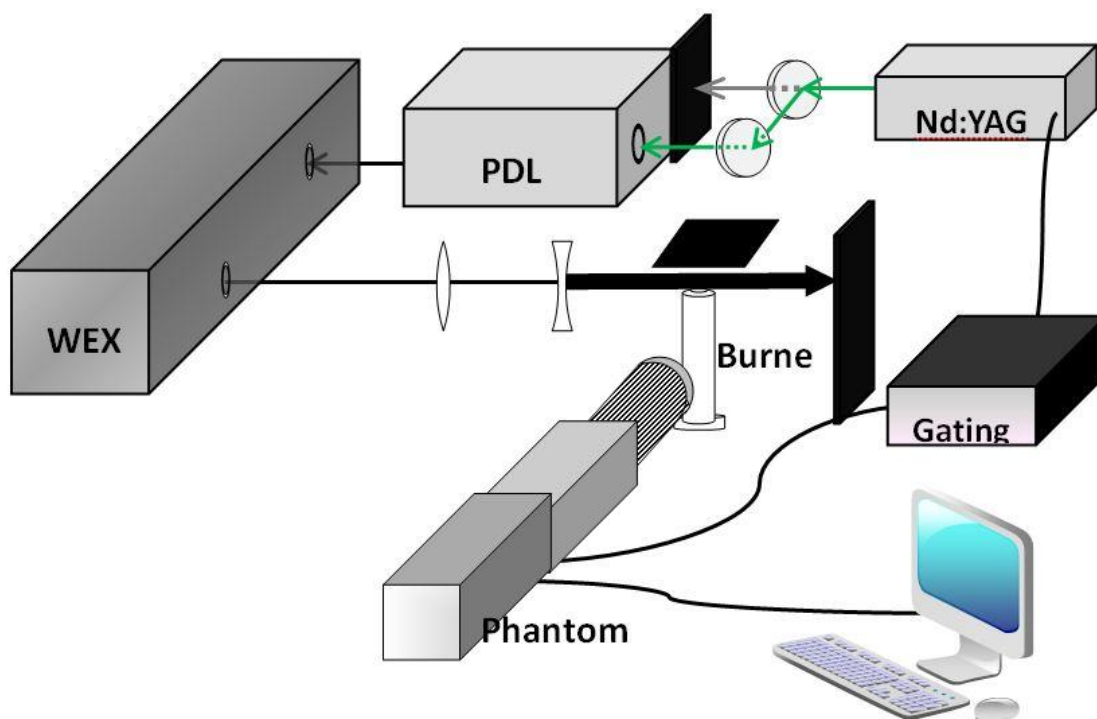
Fig. 4-11 PLIF experimental setup, including Nd:YAG pump laser, pulsed dye laser (PDL), wavelength extender (WEX), one convex UV lens, one concave UV lens, high speed camera with intensifier, gating system and control computer.

The OH PLIF technique has provided valuable information from flames for many years [75,81]. Our PLIF measurements follow generally recommended practice [75,82] except that they are conducted by pumping OH at 282.0 nm in the A-X(1,0) band and detecting fluorescence in the A-X(0,0), (1,1) band. The system is composed of a Nd:YAG laser (YAG) and a pulsed dye laser (PDL) with a wavelength extender (WEX), shown in

Figure 4-11. The Nd:YAG laser generates 1064nm light that then is frequency-doubled to 532 nm and passed through dichroic mirrors to reflect only 532 nm into the PDL. The PDL dye (Rhodamine 590 dye in methanol) fluoresces at around 564 nm. The laser light then travels into the WEX where doubling crystals generate 282 nm light. A prism guides the residual light to a beam block. The pump beam is directed through UV sheet forming optics coated from 270 nm to 350nm to focus on the flame. Being a legacy laser system, it is not automated and the experiment requires manual tweaking of the crystals to find and maintain good performance. The requirement for continuous adjustment makes precise quantification difficult but, as shown by the results, the manual effort produces very clear evidence of OH distributions in the impinging diffusion flames (recent measurements from a colleague using a new PLIF system have confirmed the quality of the images presented in this dissertation[83]). The sheet forming optics are a spherical lens plus a cylindrical lens, forming a sheet with a height of 8 mm; both lenses have long focal length to accomplish a thinner and more homogeneous sheet in the flame. The pulse energy was kept below 1 mJ to stay in the linear regime of the fluorescence. A high speed Phantom camera (v4.3) and a HiCaTT intensifier equipped with a P24 phosphor collected the images. A band pass filter centered at 320 nm was used (Semrock FF01-320/40-25) which offers 70% transmissivity to collect the light from the A-X(0,0) transition. The camera plus intensifier setup is not optimal for 10 Hz PLIF because of the loss of resolution inherent in a system that has the capability of achieving imaging up to 10 kHz. Nevertheless, the performance was adequate at 10 Hz. The images were taken using a gate of 100-150 ns to suppress background light from the flame. Detection at A-X(0,0) was selected to avoid Rayleigh scattering interferences.

4.6.3 Line selection

As mentioned above, accurate scans were difficult due to required manual adjustment of the doubling crystal for each output wavelength from the dye laser. To evaluate the system, we simulated an excitation LIF scan with LIFBASE [84] from 281.7 nm to 283.0 nm. This range of wavelengths corresponds to the A-X(1,0) band; the linewidth of the exciting pulse was estimated from similar PLIF set ups at 0.8 cm^{-1}[85]. The main peaks that are found and suitable for PLIF imaging are the stronger ones that start at 282.0 with the Q1(1) transition followed by the Q1(2), Q1(3). Most other PLIF work has been done around Q1(8) because the rotational population associated with that transition varies less than 10% for typical reaction zone temperatures between 1400-2200 K. For our particular experimental configuration we found, however, that the transition with the strongest signal was Q1(1) due to the combination of the laser power profile, the LIF cross-section, and the fact that the Q21(1) and the R2(3) lines are very close by and can contribute to the signal. A better characterization of this wavelength was therefore needed.

4.6.4 Temperature sensitivity

One concern with the pair of lines selected was a potential sensitivity to temperature (often the lines chosen in the literature are intended to minimize effects of temperature). Figure 4-12 shows the dependence of this set of lines on temperature, assuming that the laser intensity hits the three lines with the same power, that vibrational and rotational relaxation effects are negligible, and that the steady state solution is proportional to the total integrated signal. Also it has been assumed that quenching is

increasing with the mean molecular speed as $\sqrt{T}$ [86]. The emission and absorption coefficients were obtained from the LIFBAS[84] dataset. In this case, the variation is also approximately 10% in the range from 1400K to 1700K. Though it is more sensitive to temperature changes than the most commonly used transition Q1(8), the combination of lines can make a very good choice for 2D temperature PLIF measurements if used in combination with other very sensitive temperature transitions. In addition, this transition range allowed less intensifying in the camera, leading to a better signal to noise ratio, and for the purposes of the current study, the 10% variation with temperature is not significant relative to the natural variations that occur in the electrically-driven quenching flames being measured.
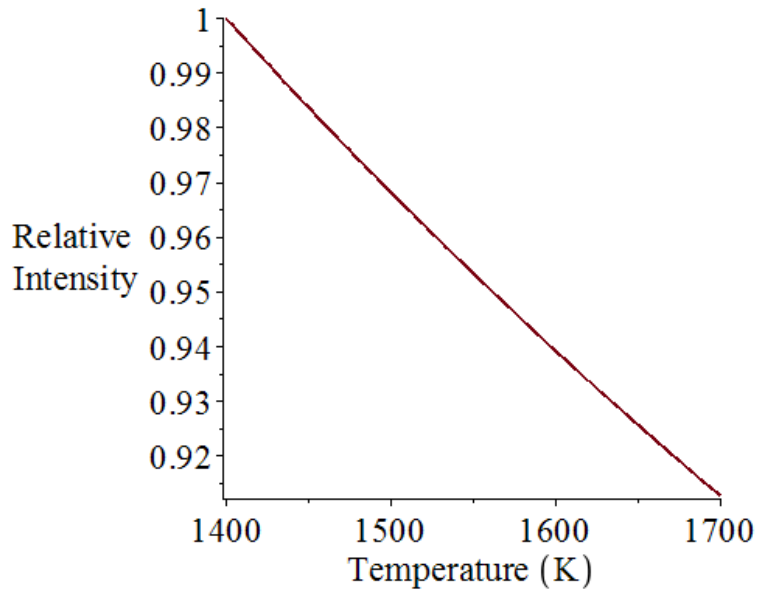
Fig. 4-12 Strength of combined Q1(1) R2(3) and Q21(1) as a function of temperature.

4.6.5 OH* chemiluminescence and tomography

OH* chemiluminescence represents the hot region of the flame or the reaction zone. It is important to identify and locate where the reaction takes place within the flame. The chemiluminescence images in the band from 300 nm to 340 nm (using the same filter as for PLIF) are recorded with a gate of 10 microseconds on the camera. Because the image is taken from the side of the flame, the OH* distribution is integrated along the line of sight. In order to retrieve the actual OH* situated at the burner center, therefore, the images are processed through an Abel transform to reveal tomographically reconstructed local distributions [57], as shown in Figure 4-13a and 4-13b. The reconstructed image is after averaging 200 pictures taken at a rate of 100Hz and after filtering with its background. The transformed image shows a clear region of hot zone.

(a)   (b)
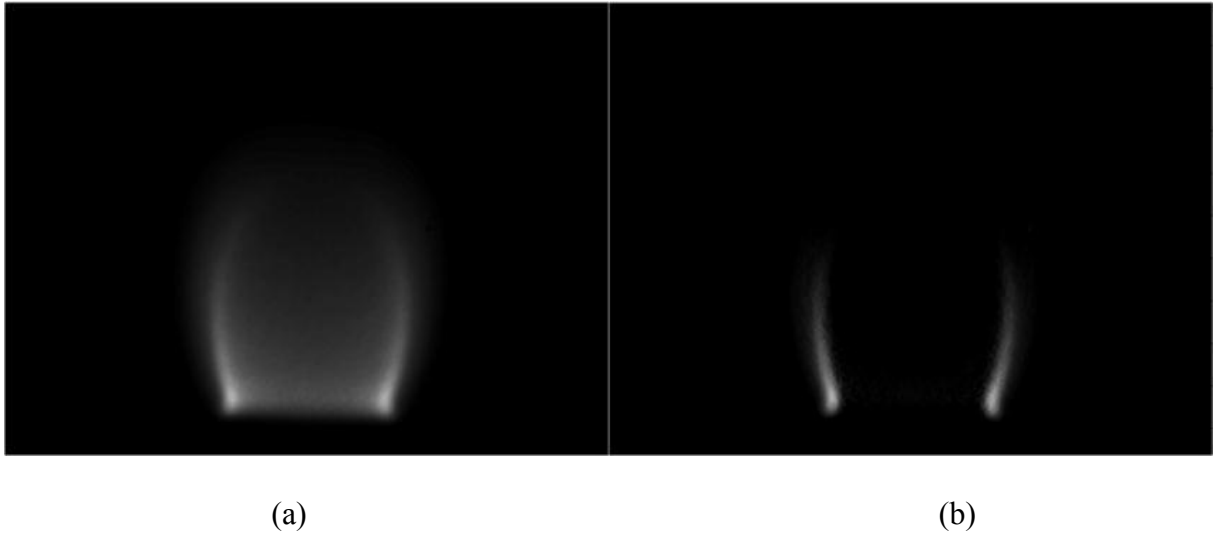
Fig. 4-13 OH Chemiluminescence images before (left) and after (right) tomographic

reconstruction.

Tomographic reconstruction is implemented, discussed, and studied related to this

work, but it is not sufficiently critical to the core findings of the research to include all of

the details here; tomographic methods are well-known and the paper describing how this

method is applied in the current flame configuration is attached as an appendix to this

document. The tomographic reconstruction approach described can be applied to all other

optical measurements along a line-of-sight.

4.7 Gas chromatography

A global carbon monoxide releasing trend is measured by the TSI emission meter, and then the OH PLIF technique helps understand the location and geometry of the reaction zone and the cloud of oxidizing species OH. The ultimate ideal is to acquire in addition, how much carbon monoxide exists at different locations of the flame. Two photon fluorescence has been used to measure carbon monoxide in flames but therew was not such a system available to the project so a sampling probe approach followed by gas chromotography was developed. Gas chromatography is a commonly used technique in chemistry to separate compounds and analyze them without decomposition. Specifically, after being sampled from the experiment, the produced gas mixture can be extracted by adsorption or solubility, which depends on the type of column used. Figure 4-14a shows a gas chromatography machine, 4-14b and 4-14c are the injection syringe (50 μl) required for injecting the sample into the GC, and the sampling bag that contains the sample gas.
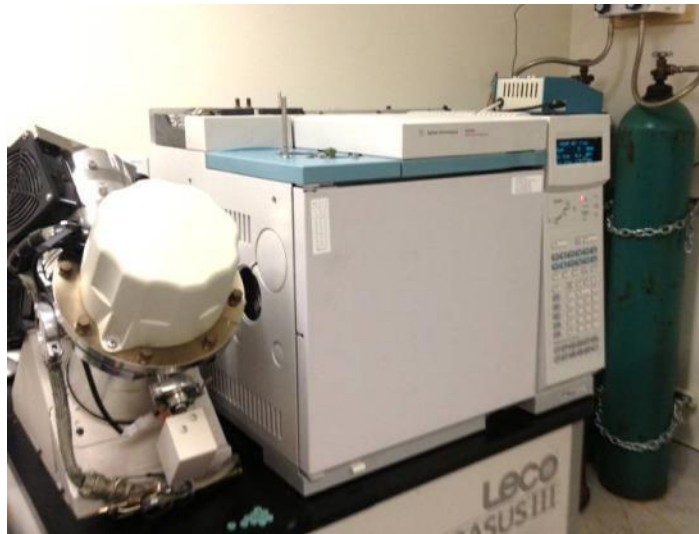
(a)

(b) 50 μl syringe   (c) sampling bag

Fig. 4-14 A Gas Chromatography machine and required equipment.

An initial calibration of standard sample gas (CH_4) with nitrogen as a carrier was conducted using a flame ionization detector (FID) and methanizer at different injection volumes. During the test, each concentration (same volume) was injected twice for a detailed reference. Figure 4-15 is a gas chromagraphic injection time line, which shows on the screen during the test; the detected gas sample signals are measured as a voltage signal in the plot. Each voltage spike represents one injection. Figure 4-16 is a calibration curve calculated from Figure 4-15 with different concentrations of methane; the result shows that the injection for the same concentration is not very consistent as a precise aspiration is required every time into the syringe.
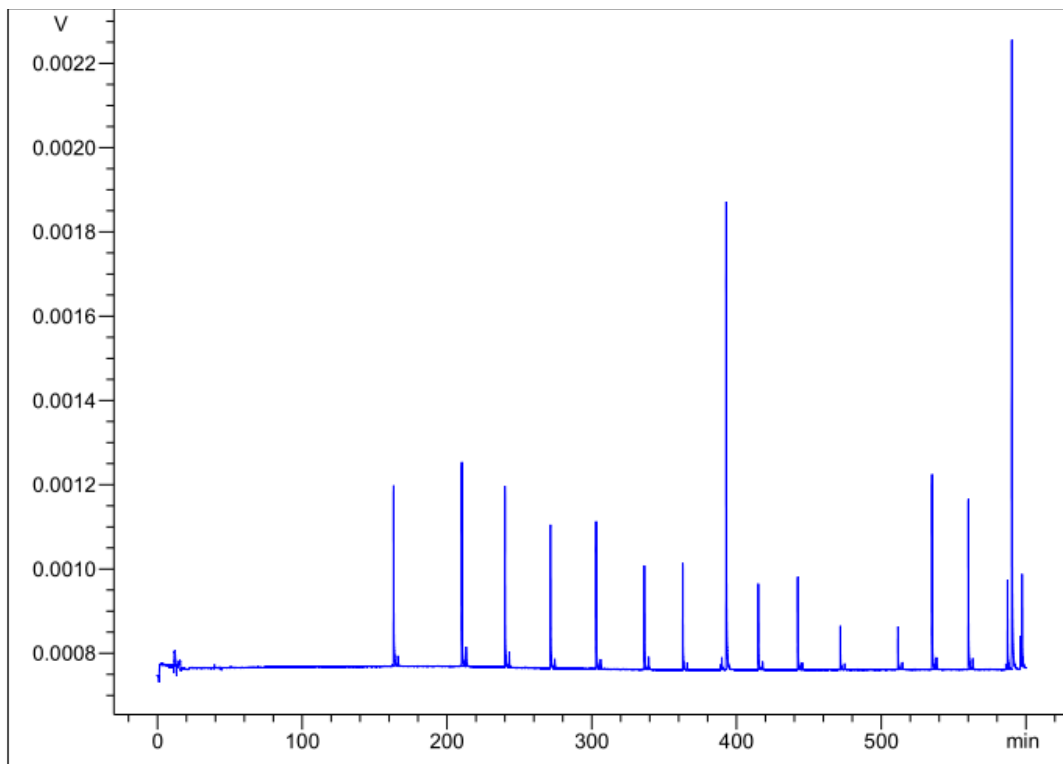
Fig. 4-15 Gas chromatographic time line with different injections which is detected as voltage signal.
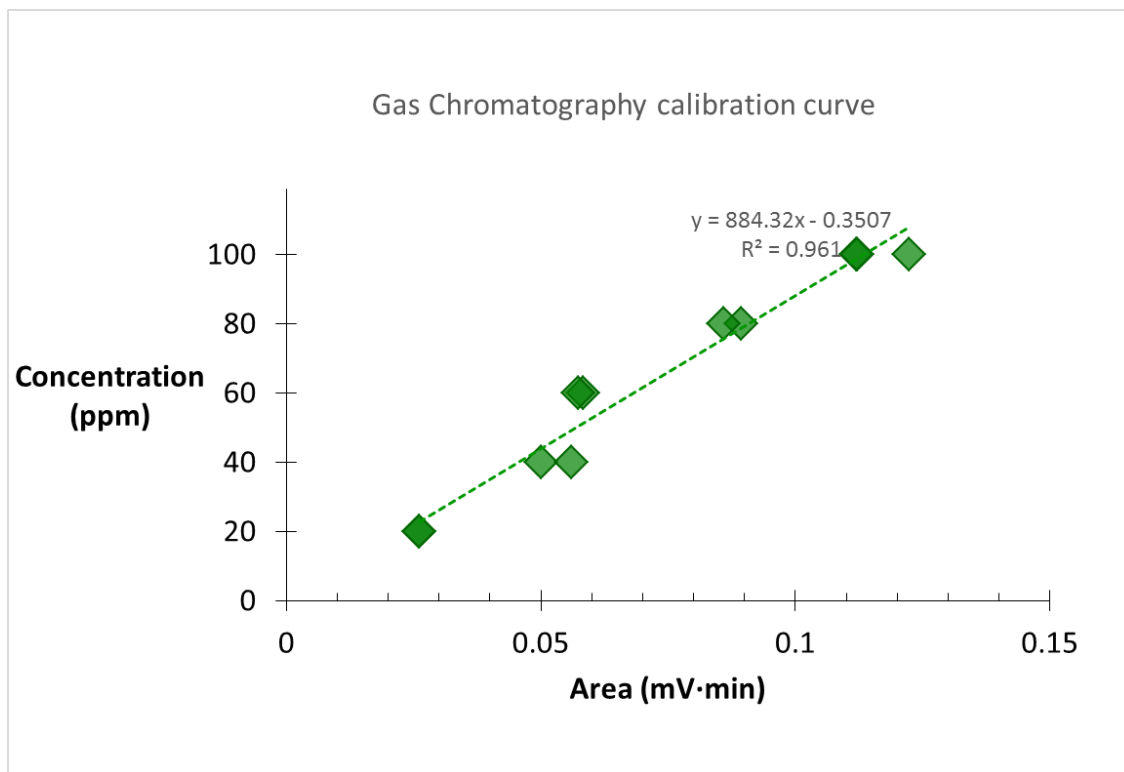
Fig. 4-16 GC calibration curve with methane.

A reproducible aspiration syringe head, therefore, is surveyed and remodeled Figure 4-17a). An aspiration syringe pump, Figure 4-17c, is designed to be placed vertically on top of the impinging plate in order to aspirate with a 0.5 liter gas tight syringe (Figure 4-17b left). The gas tight syringe is installed with a stopper lock between the syringe and the needle, and the needle can be adjusted as a speta head, as shown in Figure 4-17b middle and right. The experiment is designed to have the needle probing through the plate and sampling the exhaust gas at the desired location. This probe/GC sampling system was constructed but its implementation is reserved for future work as a direct comparison with CO two-photon fluorescence that is being developed by a colleague.
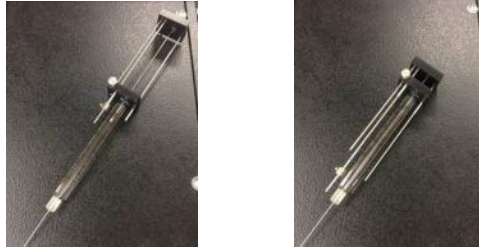
(a)

(b)
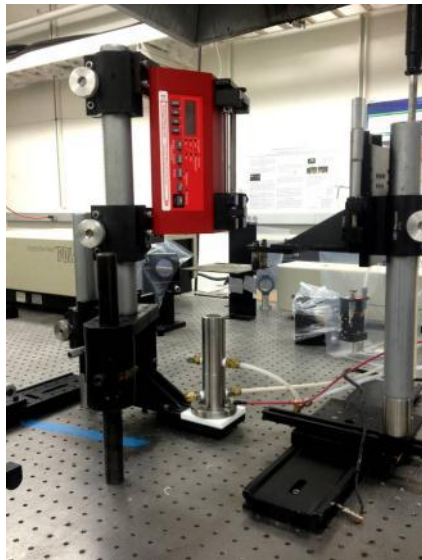
(c)

Fig. 4-17 Gas chromatography experimental design and setups (a) reproducible head with an injection syringe (b) gas tight syringe with different connecting configurations (c) aspiration syringe pump standing above the impinging plate.

4.8 Thermocouple temperature measurement

To acquire a basic knowledge about flame temperature, thermocouples are common but since thermocouples are intrusive, the flame temperature experiment cannot be conducted with electric field applied. A K type thermocouple is used and a photograph of locating the thermocouple in the flame is shown in Figure 4-18. The thermocouple is connected onto a two axis optical mount, which is able to adjust in increments of 0.5 mm in both radial and vertical directions. The impinging plate is situated 10 mm above the burner in this example measurement.
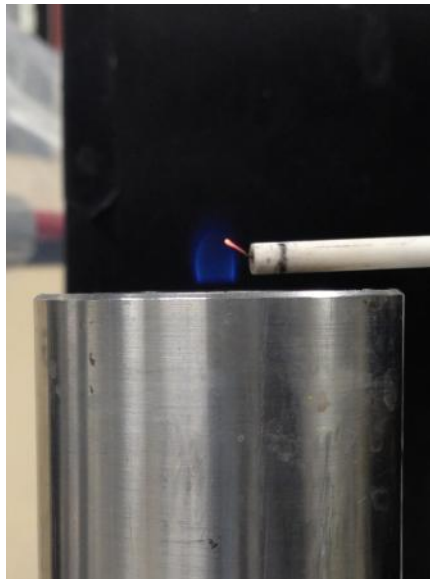
Fig. 4-18 Thermocouple measurement over the flame.

4.9 OH PLIF Thermometry

Non-intrusive optical measurement in combustion has the advantage of keeping the flow field unperturbed. PLIF temperature measurement is capable of acquiring high resolution (which relies on the camera) two-dimensional thermal maps. There is no need to have extra seeding into the flow field to trace the signal when using OH PLIF thermometry since OH molecules already exist from combustion reactions. Research has shown that OH LIF signal strength within the linear regime can be described by the following equation[87−90]:

$$S = \alpha I N_i G \Phi(T, J') = \left[\eta \frac{\Omega}{4\pi} \right] I \left[N_{total} (2J'' + 1) e^{-\frac{\varepsilon}{kT}} \right] B G \Phi(T, J')$$

where S is the LIF emission signal intensity, α can be denoted as $\left[\eta \frac{\Omega}{4\pi} \right]$ which is the optical sensitivity characteristic of the experimental setup: η is the optical detection efficiency (from the camera optics and detector), Ω is the collection solid angle. I is the incident laser energy (W/cm^2). N_i can be denoted as $\left[N_{total} (2J'' + 1) e^{-\frac{\varepsilon}{kT}} \right]$ which is the ground-state population: N_{total} represent the OH total number density, J'' is the rotational quantum number in the ground electronic state, ε is the energy with respect to the ground-state level, kT is the characteristic energy, with k the Boltzmann constant and the temperature T; B is the stimulated absorption coefficient, G is the overlap integral between the laser and molecular absorption profiles, Φ is the quantum fluorescence yield.

When collecting fluorescence signals from two electronic transitions, say one transition is having absorption from ground-state i to 1, another line from j to 2, the ratio of the two transitions of the signal is R,

$$R = \frac{S_1}{S_2}$$

where α, the optical sensitivity from the setup is the same for both transitions. Therefore the ratio is,

$$R = \frac{I_{i1} N_{total} \left(2J_i^{"} + 1\right) e^{-\frac{\varepsilon_i}{kT}} B_{i1} G_{i1} \Phi_1(T, J_1')}{I_{j2} N_{total} \left(2J_j^{"} + 1\right) e^{-\frac{\varepsilon_j}{kT}} B_{j2} G_{j2} \Phi_2(T, J_2')}$$

The N_{total} number density is the same, G_{i1}/G_{j2} approaches one with common pressure, Φ_1/Φ_2 approaches one, which is assuming both transitions are sharing a similar upper state. Including these approximations, the ratio becomes,

$$R = \frac{I_{i1} \left(2J_i^{"} + 1\right) e^{-\frac{\varepsilon_i}{kT}} B_{i1}}{I_{j2} \left(2J_j^{"} + 1\right) e^{-\frac{\varepsilon_j}{kT}} B_{j2}}$$

The temperature, therefore, can be computed from the equation above with a known ratio of two lines of laser intensity from the PLIF signal.

Two-line thermometry measurement is conducted with a similar setup to that used for the PLIF. The experiment is steady so that the probing of the two lines can be done sequentially rather than simultaneously. In order to increase the measurement sensitivity, the difference of ground-state energy between two transitions is selected taking into

account a large energy difference in the ground state and the smallest contribution from neighboring transitions[87]. Based on the LIFBASE dataset[84], $R_1(3)$ and $R_1(10)$ are the two transitions captured with the PI-MAX4 ICCD camera in the experiment. For each measurement, the camera is calibrated with its background internally. The laser intensity variation is corrected.

4.10 Heat propagation measurement
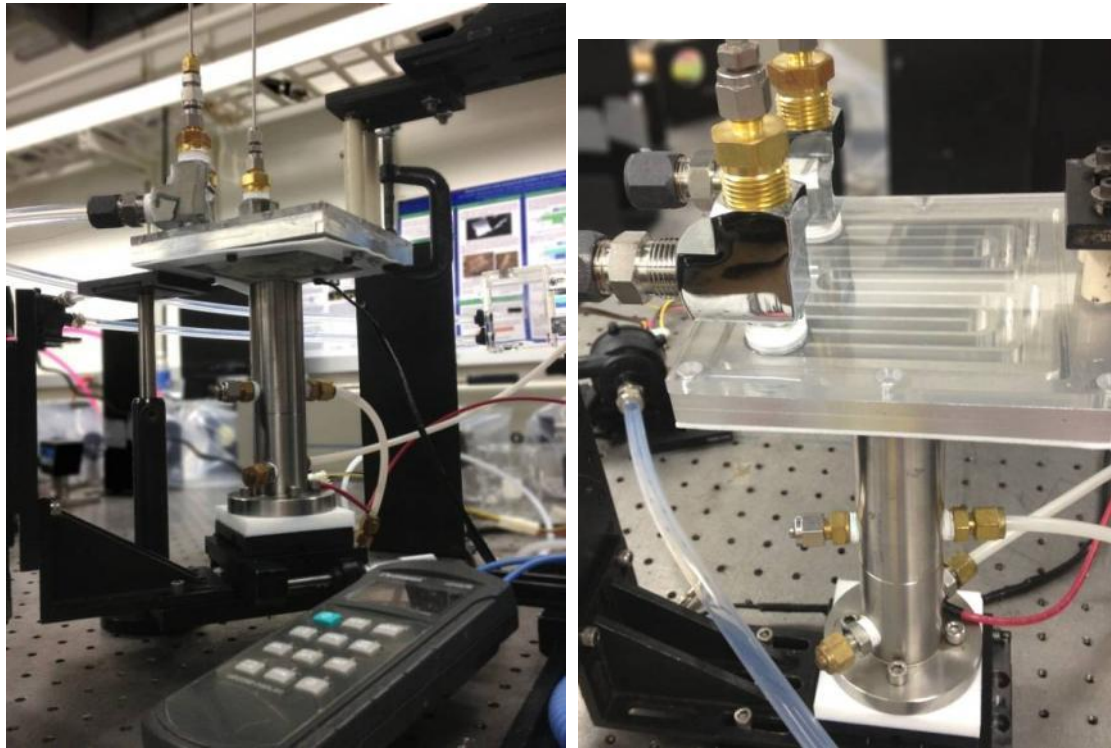
(a)   (b)

Fig. 4-19 Heat propagation measurement system.

In order to acquire the temperature change through the plate induced by changes to the flame with the electric field, an in situ heat transfer measurement system is designed to determine the level of heat transferred to the plate from the flame.

The apparatus is designed using liquid flowing in and out through channels adjacent to the plate surface; the impingement plate is attached at the bottom side of the system by a PTFE frame which insulates the system electrically and at the same time holds the plate in place. The channel is built up using aluminum which has higher thermal conductivity then the stainless steel impingement plate. The detailed design and engineering drawings are attached as an appendix. There are two T-type thermocouples measuring the liquid temperature at the inlet and outlet of the system. Water is used as the cooling liquid since the plate electrode is grounded in this measurement. The whole system is shown in Figure 4-19a and a top view of the channels are shown in Figure 4-19b.

When the plate is continuously receiving heat from the flame, the liquid flows into the channels and the water temperature is measured. The initial test showed no temperature difference between inlet and outlet because the actual heating region is very small compared to the whole quenching plate, hence, the amount of heat transfer into the channels is spreading to the whole area of the aluminum channel system. The heat transfer measurement was modified therefore to measure the time required to raise the water temperature in the channels a specific amount.

The procedure begins with filling the channels with water, and the water stays at room temperature inside the channels without flow. There are two thermocouples situated

2.25 inches from the center of the heating zone probing the water temperature right above the bottom surface in the channel. The experiment measures the amount of time in seconds required for the water temperature to increase by one Celsius degree.

4.11 Infrared measurement

Heat propagation measurements using thermocouples suggested an interesting behavior in the thermal profile of the impingement plate directly above the location where the flame interacts with it. Temperature and species concentration measurements in flames that have an electric field applied have been a challenge for exploring local property distributions because probes of any kind disrupt the electric field significantly. Non-intrusive measurement therefore is the only choice, and in this work, an infrared camera is used to understand how the temperature distributes across the impingement plate as a function of the electric field applied to the flame. The camera (FLIR SC620) measures radiative emission in the range from 7.5 to 13 microns. It has a minimum focus distance of 0.7 feet and a focal length of 0.7 inches. The temperature detector is set ranging from 0 to 500 Celsius degree (but the camera has a high temperature option that allows surface thermometry beyond 2000 K). Similar cameras are widely used in airports to detect if people show thermal signs of illness (i.e., if they have a fever). The infrared camera is controlled through a firewire (IEEE 1394) by software (ExaminIR) designed for the camera and installed in an imaging computer. The measured data and captured images are acquired from the software.

The infrared camera is situated directly above the quenching plate at normal incidence to avoid complications associated with Lambert's cosine law (or cosine emission law), where the emission rate decreases with observing angle ([91], p710). The camera is controlled by its native commercial software (ExaminIR). The plate is spray painted with a layer of flat black, heat resistant paint and is considered as a blackbody object. This assumption has been confirmed as reasonable using thermocouple temperature comparisons at a few spot locations.
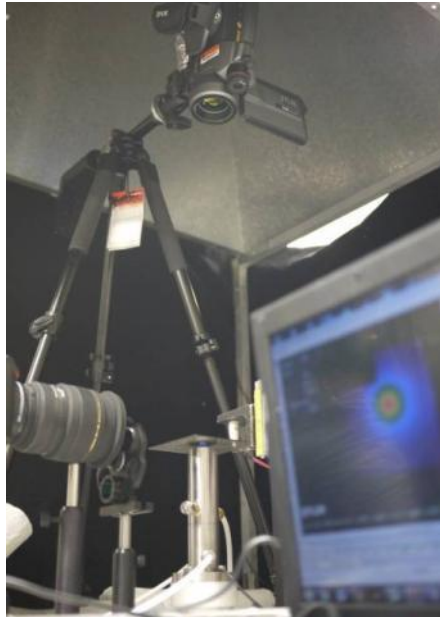
Fig. 4-21 Infrared camera connected with the software (ExaminIR) and observing the quenching plate over the burner.

The RGB image taken at thermal equilibrium shows a well-distributed temperature variation on the plate. The IR camera is measuring the thin layer of heat resistant spray paint to avoid emissivity variation in the raw metal. A validation measurement with a K-type thermocouple was conducted over the plate at the same spots

comparing temperatures with painted and non-painted surface with an absolute error of less than 3.6%. Therefore, the temperature shown in the image can be interpreted accurately as the local temperature of the plate. The measurement was recorded 60 seconds after changing the electric field, by which time the temperature is steady. The pressure drop during the experiment can affect the flow rate as a result of the small jet impinging on the plate, and the different flow rate affects slightly the temperature measured from the infrared camera, showing that about 1 ml/min difference changes the maximum plate temperature 2°C [73].

4.12 Solidworks – thermal map

In order to translate the thermal maps measured from the IR camera to thermal loading changes induced by the electric field applied to the flame, a thermal model of the heat flow within the plate was desirable. SolidWorks is a well-known and widely used computer-aided design (CAD) software package. Besides solid modeling with FEA (Finite Element Analysis) of 2D or 3D drawings, SolidWorks has the capability to simulate stress, thermal transport, fatigue, and buckling.

Under the conditions where the thermal energy of the impingement plate is influenced by electric fields acting on flames, investigating the thermodynamics and heat transfer over the plate with simulation helps interpret the key phenomena. Figure 4-21 shows a screen shot from the thermal study, and it indicates how the Solidworks package provides sufficient control variables for manipulating the desired environment. The specification of the plate is described in Chapter 3. All six faces of the plate are all

applied with natural convection while the heat transfer coefficient is set at 25 W/m^2. Both the top and bottom side of the plate permit radiative loss, with the top side assumed as a black body while the bottom side is set up at emissivity 0.28 as untreated and somewhat scratched aluminum ([92], p306). A detailed Solidworks simulation with a thermal study of the IR thermal mapping is described in the report attached as another appendix. This work was discussed and presented as a master's project, and its findings provided helpful motivation for the thermal aspect of the current work.
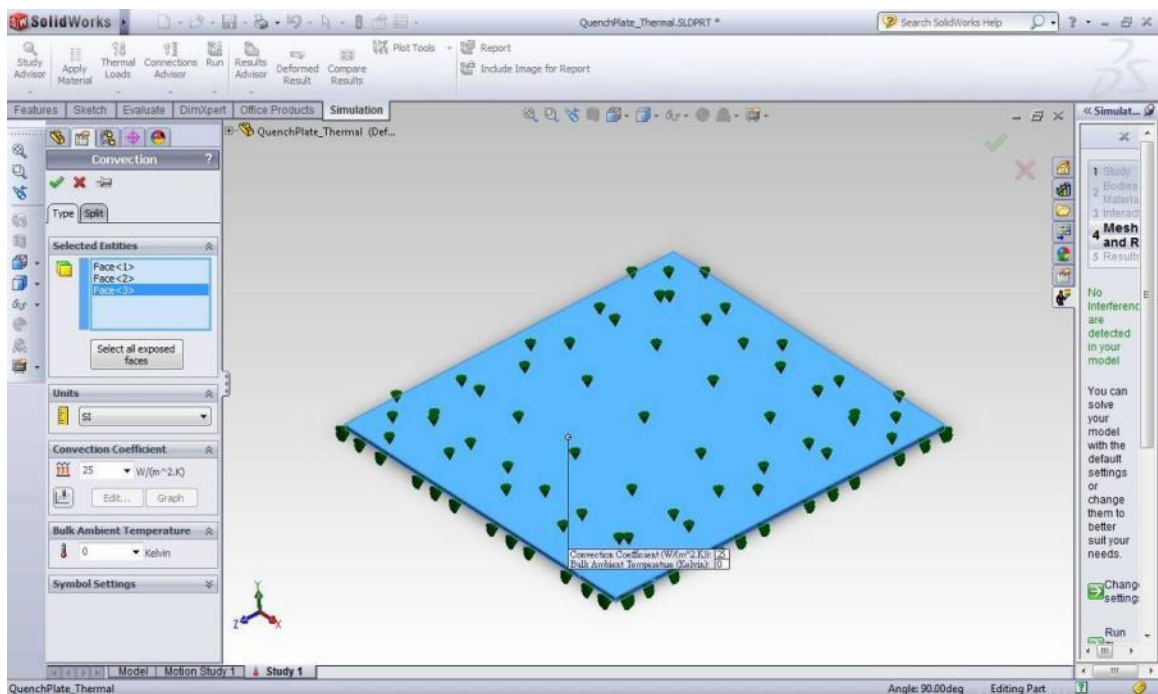
Fig. 4-21 SolidWorks Simulation – Thermal Study.

4.13 Chemkin – reaction estimation

Identifying the reaction and species locations can help explain acquired experimental observations, especially in understanding where the CO is generated and how the OH hot zone appears between the fuel and coflow air reaction layer. CHEMKIN PRO, a commercial version of CHEMKIN by Reaction Design is used for computational work to solve complex chemical kinetics such as occur in combustion, plasma, microelectronics, or chemical processing. The software requires three input files covering each of chemistry/thermochemistry, kinetics, and transport. The software provides several basic and common design models of reactor geometry for users to select and link together.

An opposed flow flame is chosen because it is simulates best the reaction zone between the center fuel and the coflow air (Figure 4-22). Therefore, one jet is set as methane while the other is air flowing out with an inlet velocity of 25 cm/s. The CH4 inlet temperature is set at 1000K and air is 600K. The ending axial position which is the distance between the two jets is set at 4 cm, estimated center position is 2 cm and estimated zone width is set at 1 cm to approximate the size of the coflow flame. Partial OH chemiluminescence and ions are included into the simulation[64]. The detailed kinetic, thermo, and transport files with ions and chemiluminescence are attached in the appendix.
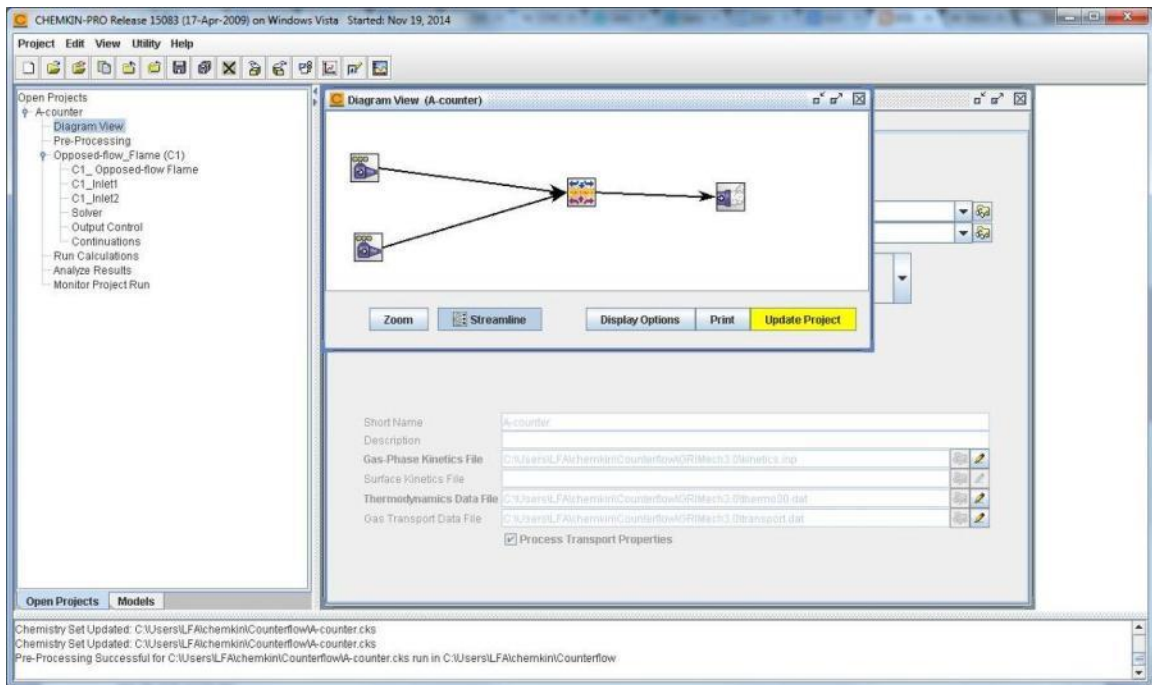
Fig. 4-22 CHEMKIN PRO interface with opposed flow.

4.14 Inverse jet visualization
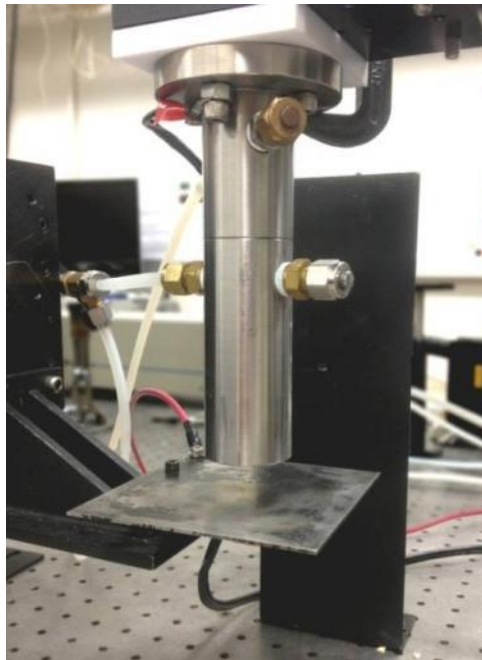
Fig. 4-23 Inverse jet measurement setup.

Prior work has shown that the body force induced by the ion driven wind in hydrocarbon combustion is comparable to that of buoyancy for small flames[5,19,66]. It is interesting, therefore, to try and isolate the direct effects of electric fields on flame ions and their ion-driven wind from possible indirect effects where changes to the flame shape might modify the buoyant forces involved. To examine this aspect, an inverted flame jet experiment is included, where the coflow burner is turned upside-down, with the plate below the burner exit (Figure 4-23). In this case, the plate is connected to the high voltage power supply while the burner is grounded. The center tube of the fuel exit is 5 mm above the coflow surface in order to have a better observation of the flame with buoyancy effect. Figure 4-24 shows an inverted jet flame under electric field forcing with the impingement plate in place. These experiments show that for cases where the flame and plate interact, the effects of buoyancy are not significant as the flame shape and its ion current response are within experimental uncertainty when compared with results from the upright flame geometry.
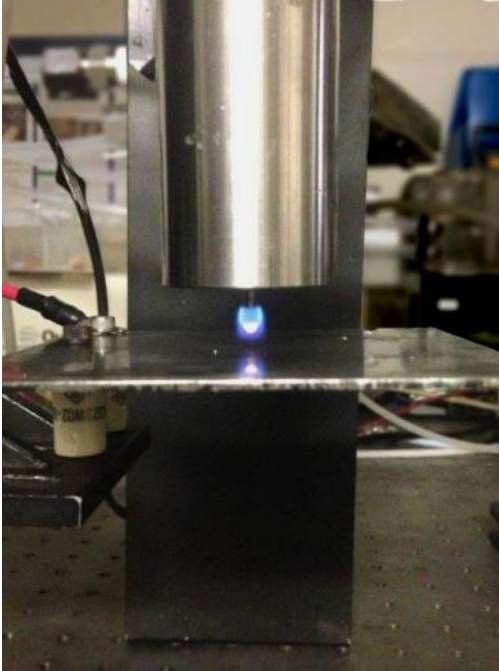
Fig. 4-24 An inverted jet flame.

This chapter provided a summary of all of the experimental methods employed. The next chapters are devoted to the results and their interpretation.

Chapter 5

Results and Discussion

This chapter describes a series of targeted investigations associated with electrical properties and control of flames both in preparation for microgravity combustion activities and for ground-based implementation of sensing and control of non-premixed flames near surfaces. Although the research in this dissertation is entirely ground-based, it is part of a broader effort supported by NASA in electrical aspects of flames that encompasses microgravity conditions as well. It was important, therefore, to examine some of the planned spaceflight hardware in the context of electrically actuated flame experiments.

5.1 ACME hardware examination

There are several NASA Engineering Models built for a planned flight launch to conduct experiments using the Combustion Integrated Rack (CIR) of the NASA Glenn Research Center's Fluids and Combustion Facility (FCF) on the International Space Station (ISS). Advanced Combustion via Microgravity Experiments (ACME) is one of the FCF investigations aimed at advanced combustion technology via fundamental

microgravity research of non-premixed flames. The E-FIELD Flames experiment, as part of ACME, is to gain an improved understanding of chemi-ionization in flames and to utilize electrical effects on these ions to control combustion. In preparation for operating the E-FIELD Flames experiment in the International Space Station, this hardware examination explores the similarities and differences between flame behavior when actuated by a typical laboratory high-voltage power supply (TREK) and a lightweight compact power supply (UltraVolt) that is suitable for use in the spaceflight experiments. The association between temporal response of the power supply and the flame behavior is a potential source of confounding effects if the power supply time response is not substantially faster than that of the flame and its interaction with the surroundings. . Micro- or zero-gravity experiments are needed for absolute certainty on this subject, and this research, therefore, begins to explore this relationship in the 1g laboratory environment. The experiment compares the response of two power systems and the effects of that response on the coflow flame with a downstream mesh electrode. The comparison includes measurements of voltage response at the electrodes and the flame response in terms of ion current.

5.1.1 Power supply response

The power supply response experiment sends a voltage request (to the power supply) from the data acquisition program (modeled after the program that will be used to actuate the flame on the ISS) and records the time response and the voltage generated between the electrodes (burner and mesh in this research). There are three different type of tests conducted (Figure 5-1).
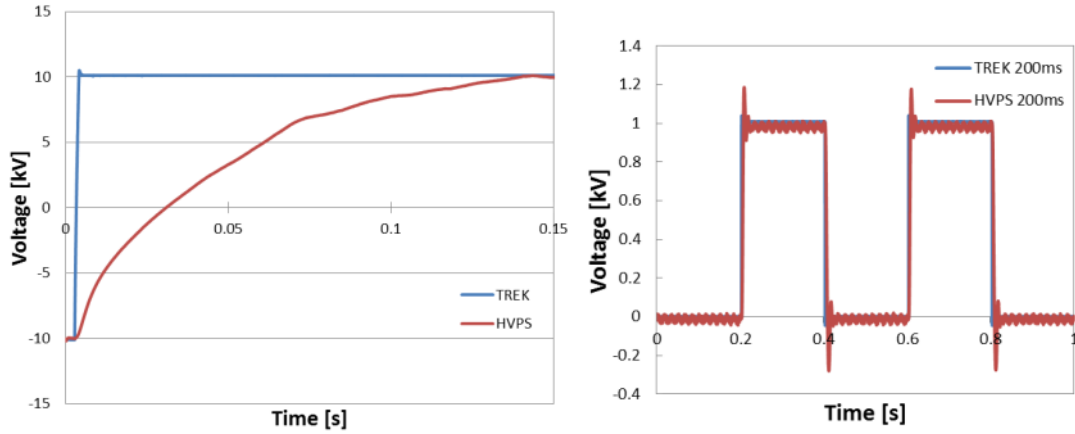
(a)

(b)
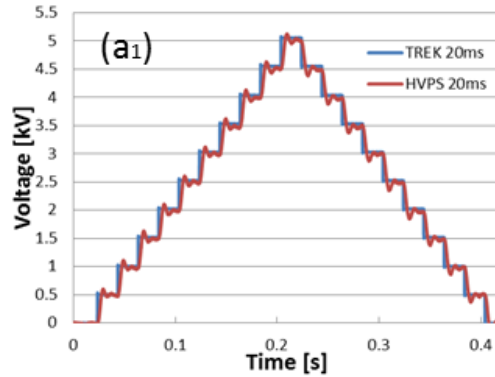
(c)

Fig. 5-1 Three different tests of the power supply response: (a) step response (b) square wave (c) step up and down response.[68]

The first test involves requesting large, from -10 kilovolts to +10 kilovolts, and small, 0 to 100 volts, voltage steps. The results show that the TREK response is on the order of milliseconds with almost vertical transition in output voltage on the scale shown while the UltraVolt takes approximately 100 milliseconds to respond with a large ripple accompanying the small step request.

The second test comprises requesting a 1 kilovolt square wave at various cycle time scales of 200, 100 and 50 milliseconds. The TREK is capable of operating stably at most conditions with a little bit of overshoot (approximately 10 volts) before settling to the 1 kilovolt request, while UltraVolt has about 200 volts of overshoot and a noticeable phase delay for the cycle time of 50 milliseconds.

The third test is to request steps up and down (a large triangle), 0 to 5 kilovolts and back to 0 kV with 500 volts as the increment step. Again, different cycle time scales are used, including 20, 10 and 7.5 milliseconds. The TREK is able to achieve the request voltage while the UltraVolt barely keeps the requested square voltage shape for the 10 milliseconds cycle time.

These results show that the TREK is superior to the UltraVolt for dynamic adjustments of the electric field. It is next useful to determine if the flame response also shows a difference between the two power supply designs.

5.1.2 Flame response

The flame response is tested with a step input from zero to 5 kilovolts while measuring voltage response and the ion current between mesh and burner. The experiments are running within a steady saturation region where the ion current does not rise with electric field strength (this will be explained further in the following section). The ion current curve of the TREK test is observed as an initial spike associated with the capacitance of the burner/mesh electrode system and then the current decays to a steady value after 30-40 milliseconds as the ions flow through the flame/electrode gas space

(Figure 5-2). The rising ion current after the initial spike is extensively characterized in [93], and it is likely due to the flame finding a new accommodation with the associated ion driven wind. The UltraVolt shows a far less pronounced spike because its slower response time does not fully capture the system's capacitance. The settling time that the ion current requires to reach steady state, and the ion current value, are consistent with the results obtained from the TREK.
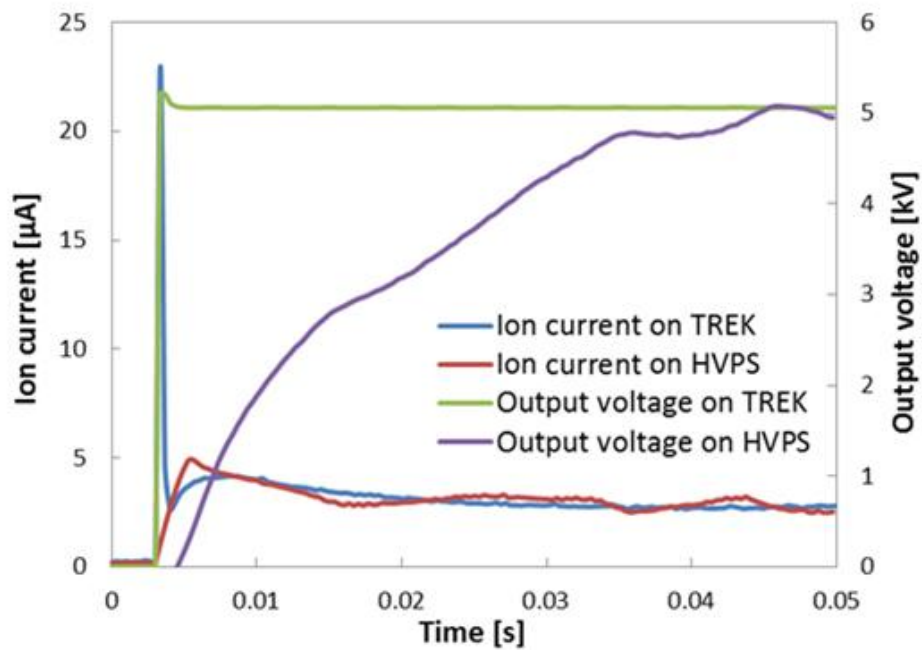
Fig. 5-2 Ion current response comparison asking for 5kV step input on two supplies[68].

These results show that although the time response of the UltraVolt power supply is significantly slower than that of the TREK, the impact on steady electrical properties of the flame, and even on moderately rapid changes due to the electric field forcing, are not substantial. Particularly when operating with step changes between ion current saturated regions more rapid response to changes in the electric field are possible because the ion current is limited by the flame chemi-ionization capability rather than by the voltage

request. This is a fortuitous condition that provides an important opportunity to maximize the understanding of flame behavior even when using a slow responding power supply. Most of the work described in this dissertation involves the higher performing TREK power supply because we have the luxury of ground-based operation but the results of the HVPS performance in comparison will be relevant to the ISS experiments.

This power supply comparison work included the research participation of a visiting student from Japan. Further details of the study are documented in a conference paper [68] that is attached as an appendix.

5.2 Impinging flame electrical properties

Most of the prior electrical properties of flames research focuses on free flame properties, including the saturation ion current. Recently, the electrical properties of flames near surfaces has been examined with the potential goals of sensing flame location and combustion performance, and changing flame behavior using the electric field as an actuator [16]. The following measurements are to more completely detail the situation of a flame under the influence of an electric field when the flame is interacting with a nearby solid boundary.

5.2.1 Ion Current

The ion current characterization experiment (or the development of the VI curve) is conducted with plate heights from 25 millimeters to 3 millimeters with different field strength limits. Figure 5-3(a) shows how the ion current changes with different electric

fields. In Figure 5-3(a), the ion current response to the electric field shows the standard three distinct regions: sub-saturation, saturation and enhanced saturation (also referred to as secondary ionization or super saturation) [19].

The ion current curve at each height shows good agreement with past studies and shows that the field strength at saturation is nearly constant but that the voltage associated with the onset of enhanced ionization varies. As the plate moves closer to the burner, the saturation ion current limit becomes smaller. The ion current response in the enhanced saturation region shows approximately parabolic behavior until an electric discharge arc appears as the field strength increases beyond breakdown.

Figure 5-3(b) shows a closer view of the transition from the sub-saturation to the saturation region. The capability to generate ions decreases as the distance between the plate and burner decreases. In the far field flow cases (i.e., from 25 to 12 mm plate distance) the plate has not reached the visible flame zone so the saturation ion current changes only a small amount (perhaps due to a slight temperature reduction effect from the plate). As the plate moves down into the visible flame from 11 mm, the saturation ion current drops consistently. The decrease appears to result from the wider opening flame tip, which decreases the flame temperature, combustion completion, and reaction volume thereby decreasing the ion production. More detailed study is needed to confirm this explanation, however, and this topic will be discussed further in later sections.

It is interesting to see that the ion current saturates faster (in electric field strength terms) on the positive side than on the negative side according to the contributions of the ion driven wind. The sub-saturation region increases as the plate gets closer in the

positive field domain while the saturation region decreases as the plate moves closer to the burner. Therefore, the quenching plate plays an important role in ion current response by affecting the flame shape, flow direction, reaction conditions, and the ion distribution with respect to the electric field.

Parabolic current/voltage curves occur in the enhanced saturation region. One hypothesis for enhanced ionization is that a small corona discharge occurs between the plate and burner at high field strengths; however, another measurement with a hydrogen diffusion flame has shown negligible ion current, which suggests that the effect is instead due to collision induced secondary ionization after thermal emission, as has been indicated by others[5,6].
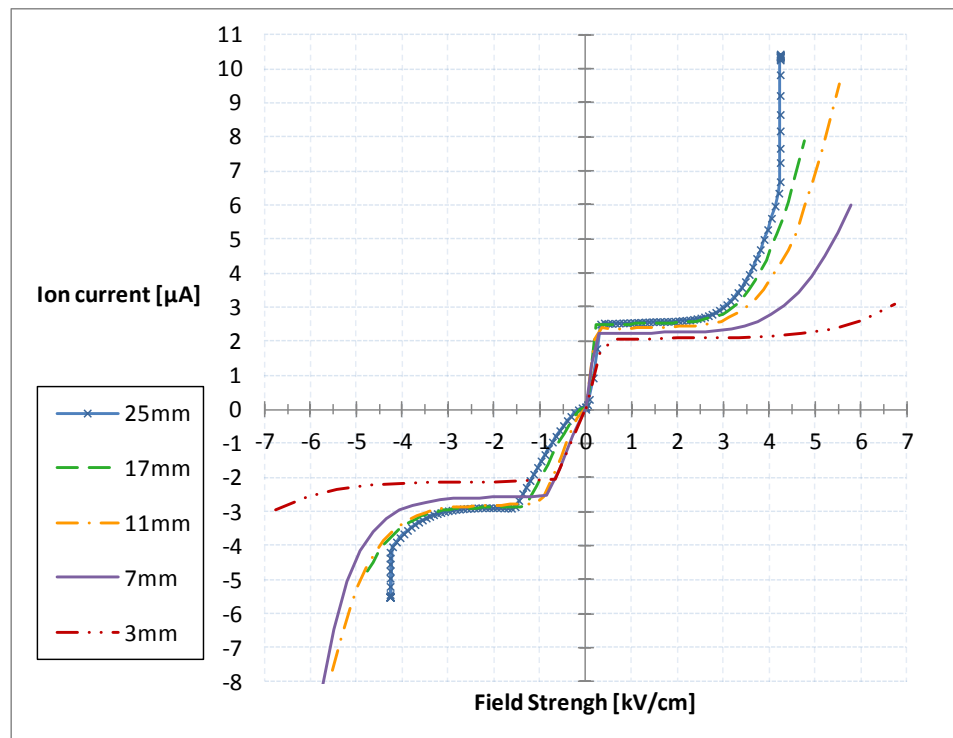
(a)
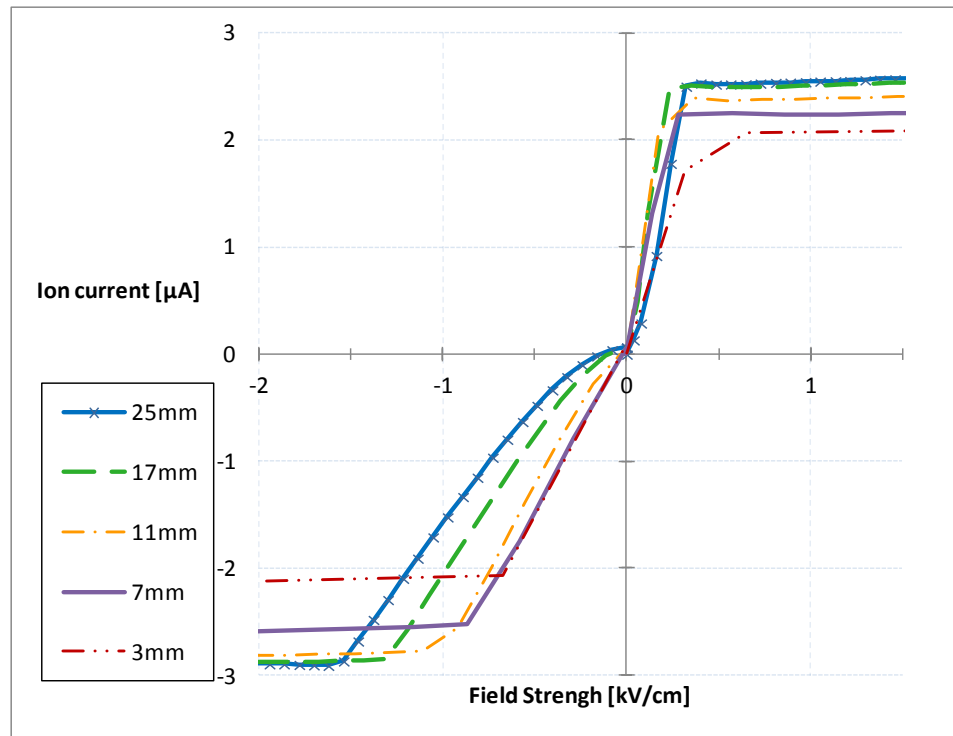
(b)

Fig. 5-3 Ion current changing with field strength applied at different heights of the plate above the burner: (a) whole region (b) detailed.

As an electric field is applied to the flame at different plate heights, the ion current increases with the field until it reaches a steady saturation region. The saturation ion current is nearly constant at each height [19,68,94]. As will be described further in a later section, it is interesting to note, for negative fields in particular, that the normalized magnitude of the saturation ion current can be used to track the influence of the plate on the CO release, as is shown in Figure 5-4. The saturation ion current decreases with relative plate-to-burner distance, H/D, reflecting in part the incomplete combustion mechanism that leads to carbon monoxide release.
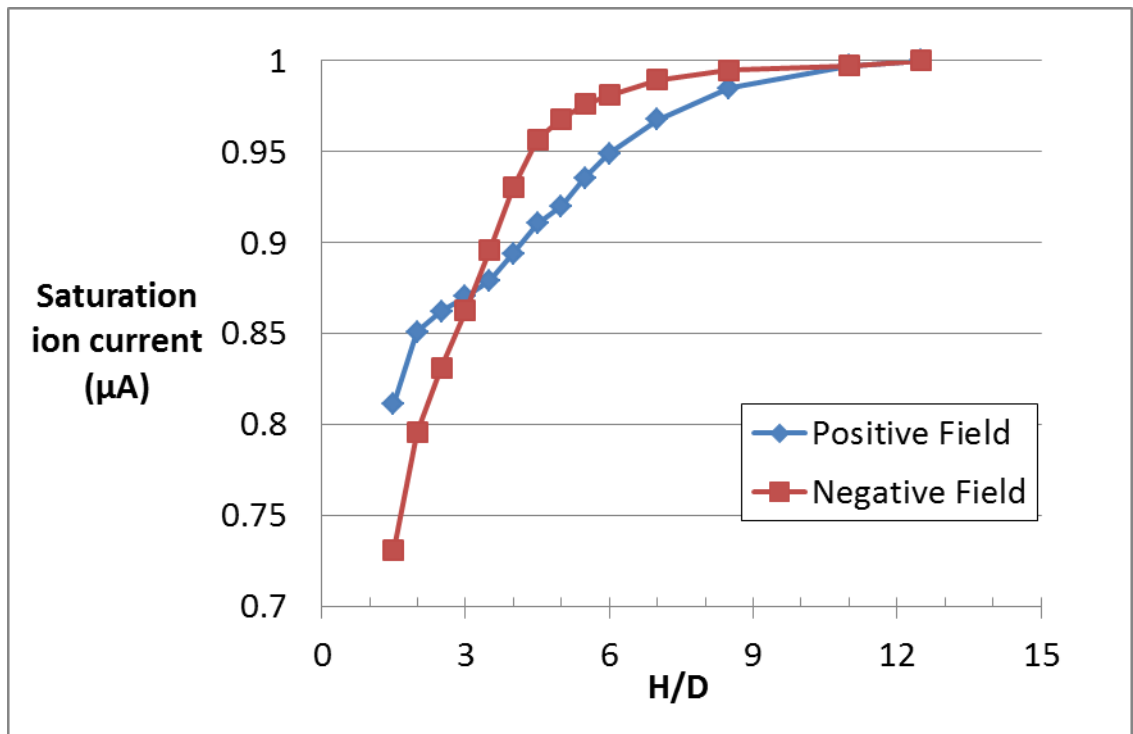
Fig. 5-4 Saturation ion current increases with H/D

5.2.2 Schlieren

There is a clear influence of the downstream plate on the flame shape and ion current. It is interesting, therefore, to examine the influence that the plate has on the thermal plume coming from the flame. This plume is seen easily using Schlieren visualization. A close view of the Schlieren image in Figure 5-5 shows that the thermal plume is created at the hot flame region and then spread along the quenching plate downstream. The small flame jet region indicates where the jet flame front is. For reference, the luminous zone of the flame under this condition extends approximately halfway across the 9 mm electrode gap.
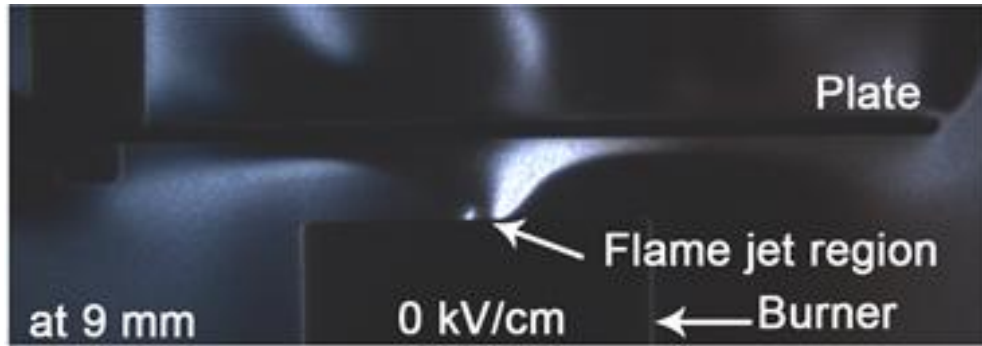
Fig. 5-5 A Schlieren image showing the flame jet, plate and the burner without electric field applied

Schlieren images with and without an electric field applied to the flame show steady laminar flow fields, as in Figure 5-6, with a typical stagnation point flow boundary layer shape extending radially outward on the plate to its edge. The -5.6kV/cm case shows a slightly broader zone as the positive ion-driven wind in this case is directed downward. At the plate edge, the hot gases rise from buoyancy. The 5.6 kV/cm case with the positive ion-driven wind directed upward has a narrower thermal zone.

Figure 5-7 shows the overall flow field change with burner-to-plate distance, the result indicates that the electric control of flames has a clear effect on the thermal plume when H/D values are larger than 4.5 while the cases at lower distances may encounter complex flow regions where the momentum of the gas jet can play a more dominant role.
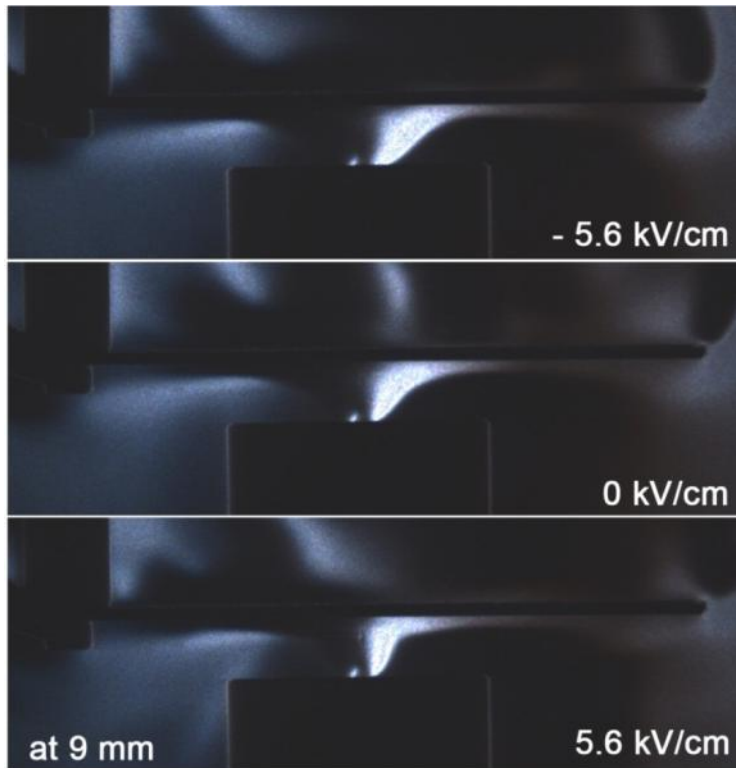
Fig. 5-6 Schlieren images with electric field applied at plate height 9 mm
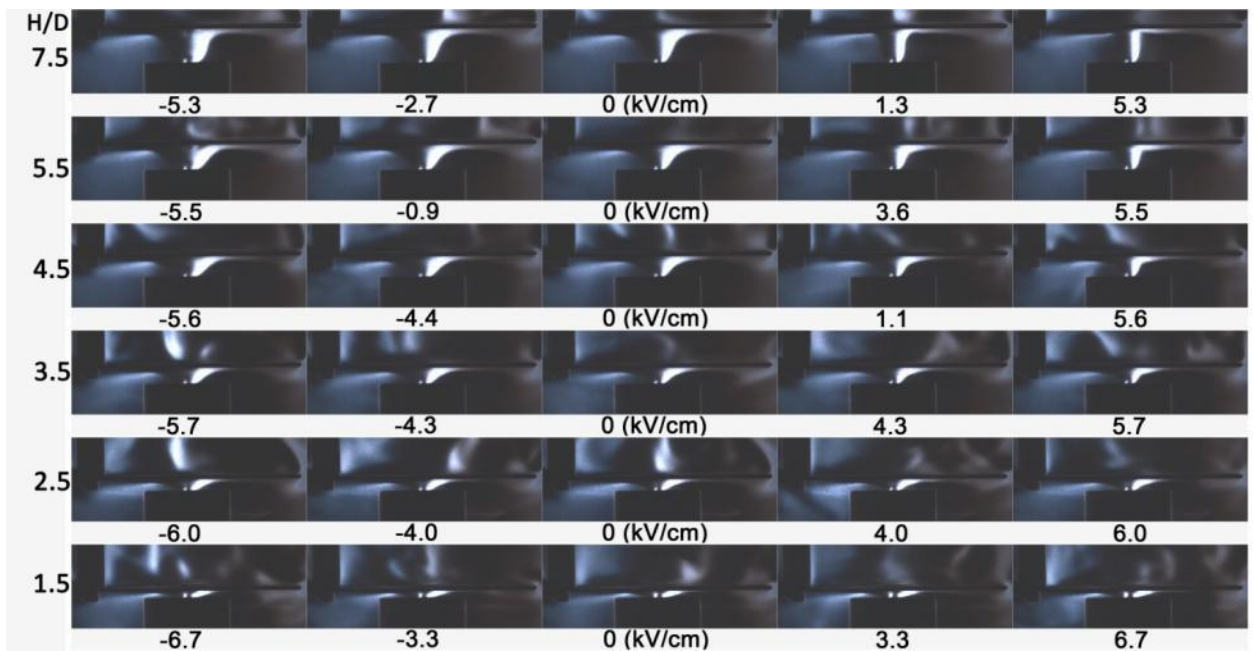
Fig. 5-7 Overall Schlieren images with different electric field and impingment plate

height

H/D				
7.5	-5.3	-2.7	0 (kV/cm)	1.3	5.3
5.5	-5.5	-0.9	0 (kV/cm)	3.6	5.5
4.5	-5.6	-4.4	0 (kV/cm)	1.1	5.6
3.5	-5.7	-4.3	0 (kV/cm)	4.3	5.7
2.5	-6.0	-4.0	0 (kV/cm)	4.0	6.0
1.5	-6.7	-3.3	0 (kV/cm)	3.3	6.7
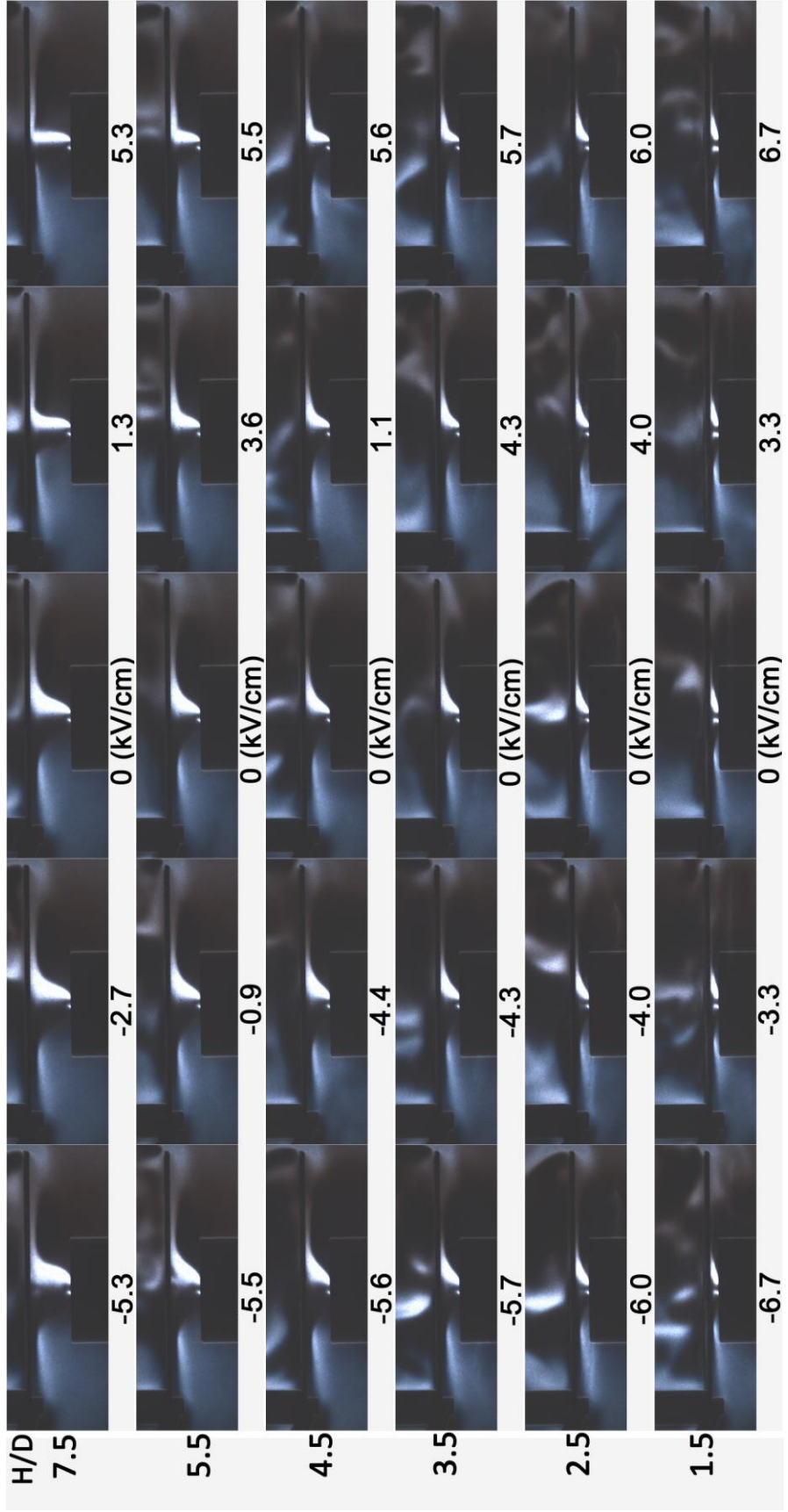
5.3 Emission study

The results of the emission tests using the mid-IR detector sensing the flame show that there is a large change in the quantity of carbon between the two different electric field directions. The mid-IR system was unable to distinguish, however, if that carbon was in the form of CO or CO_2, and it is the former species that is of the greatest interest. The following describes the series of tests used to determine the amount of CO released from flames interacting with a downstream impingement surface and what changes to an electric field on such flames might have on that release.

5.3.1 CO emission

5.3.2.1 Before applying electric fields - fundamentals

It is important to have an overview and understanding between the quenching distance and the amount of the carbon monoxide released from the non-premixed methane/air coflow burner. Figure 5-8 shows characteristic photos of flame shape changes as the plate progressively moves toward the burner exit; where 3 mm is the limit distance that still allows a stable flame. For plate to burner spacing between 7 and 3 mm, and as shown in the Schlieren images, the flow begins to strongly stagnate at the plate, with a clear transverse flow toward the outside edge.
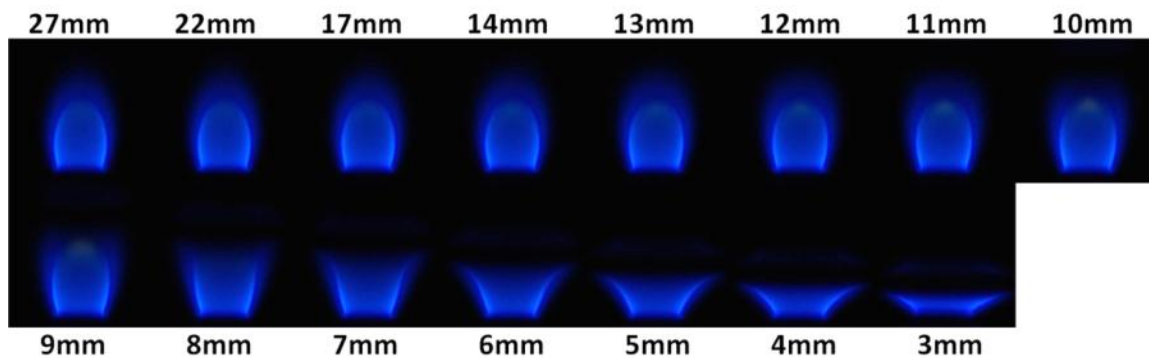
Fig. 5-8 A small diffusion flame changes with a plate progressively approaching it. As a size reference, the flame base is approximately 3 mm in diameter.

The amount of carbon monoxide is measured at the heights listed in Figure 5-8. Figure 5-9 shows that when the plate progressively moves toward the burner, carbon monoxide release increases. Because of quenching, the CO concentration grows as the distance drops. Two sets of data are presented in Figure 5-9; the first set is measured at two minutes after the plate moves to its new position and the other set is after the CO concentration reading becomes fully steady (the time required for the reading to reach an unchanging state can be more than five minutes). The time required for the reading to reach an unchanging level differs for each case. Therefore, having a well-defined time scale for recording carbon monoxide concentration at different plate heights is useful to ensure the reproducibility of the measurement

The difference between the concentration measurement at 2 minutes and fully steady is from 10 to 76 parts per million (ppm) when the plate varies from 8 to 3 millimeters. These values are generally less than 10% in all cases. When the plate distance is more than 8 mm the difference is much less than 10 parts per million. These

results show that while two minutes may not be long enough to reach steady state when there is substantial interaction between the flame and quenching plate, under most conditions it is sufficient, and it is not practical to wait until fully steady state since that time varies. Hence, as shown in an earlier transient evaluation, two minutes is generally sufficient to reach within 90% of the steady condition [69].
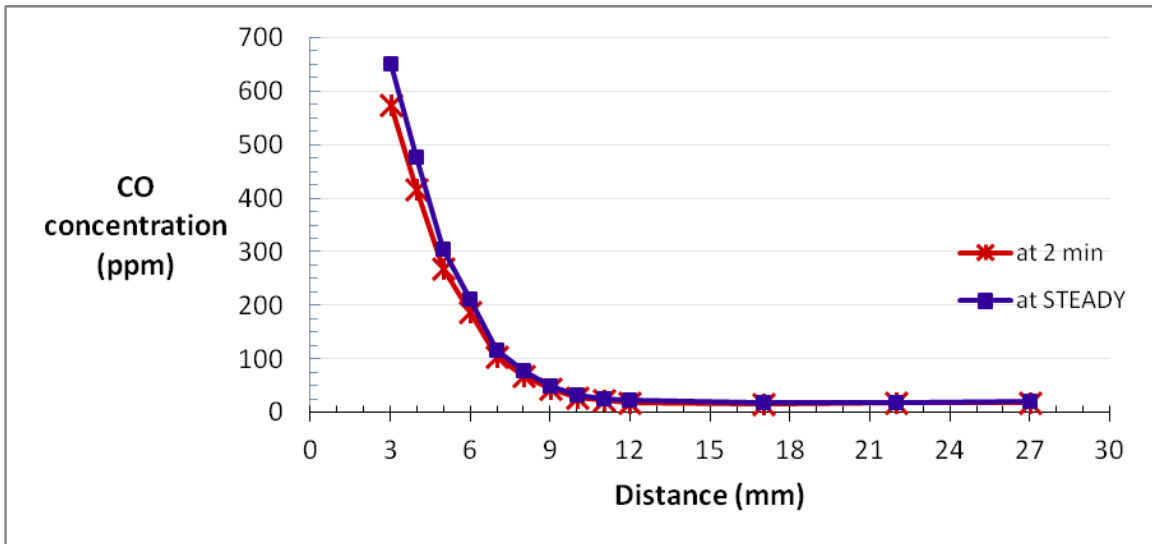
Fig. 5-9 CO concentration changing with the height of plate

Figure 5-10 shows the relative values from Figure 5-9. The CO concentration is given in scaled units relative to the unimpeded conditions that prevail beyond plate distances of 27 mm (H/D 13.5, the absolute value of CO concentration at this baseline condition is around 17.5 ppm). It is interesting to notice that carbon monoxide release increases steadily once the plate approaches the visible flame tip. Because of flame quenching, the CO concentration grows rapidly as the normalized distance drops below 4.5 and exceeds/over one hundred parts per million at 3.5 (and lower H/D values).
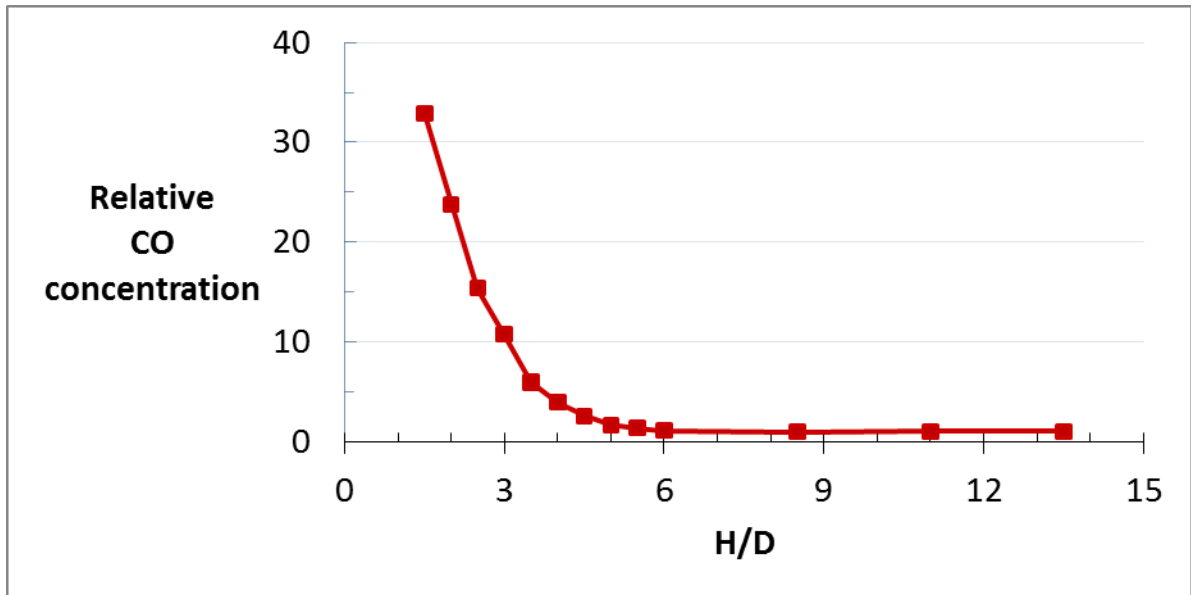
Fig. 5-10 CO emission changes with plate to burner distance.

5.3.1.2 Decay test

To further confirm the validity of the 2 minute test condition, the carbon monoxide decay trend is estimated based on a mixing plenum model to ensure that the concentration measured occurs at an approximately steady condition.

For such models,

$$\frac{dN}{dt} = -\lambda N$$

Where N is sample population, t is time, λ is a time decay constant. To acquire an accurate value of CO release from the flame, the concentration inside the chamber was measured as it filled with CO until it was steady, matching its release from the chamber to the outside.

At the first four minutes, carbon monoxide is recorded about every ten seconds. The data has the expected exponential trend with time, and the decay rate can be derived from a curve fit with concentration as shown in Figure 5-11. From the third minute to the fourth minute, the carbon monoxide concentration drops less than ten parts per million and the decay becomes slower and essentially flat compared with the results for the first three minutes. Therefore starting from the 4th minute the decay trend is steady, and the time constant derived from this condition is assumed for the CO measurements at all times.

Figure 5-11 shows an example trend as CO filled the chamber with the quenching plate 7 mm from the burner. Two values make the decay calculation straightforward; CO concentration is 126 ppm at 15 seconds and 20 ppm at 130 seconds. The time for the concentration to approach steady state in the chamber is governed by the exchange rate of fresh air and the chamber volume. Hence, the decay of CO concentration from the steady-state condition offers the same characteristic time. The exponential fit to the trend shows that, consistent with the earlier qualitative observations, over 90% of the steady CO concentration is reached within the first two minutes.
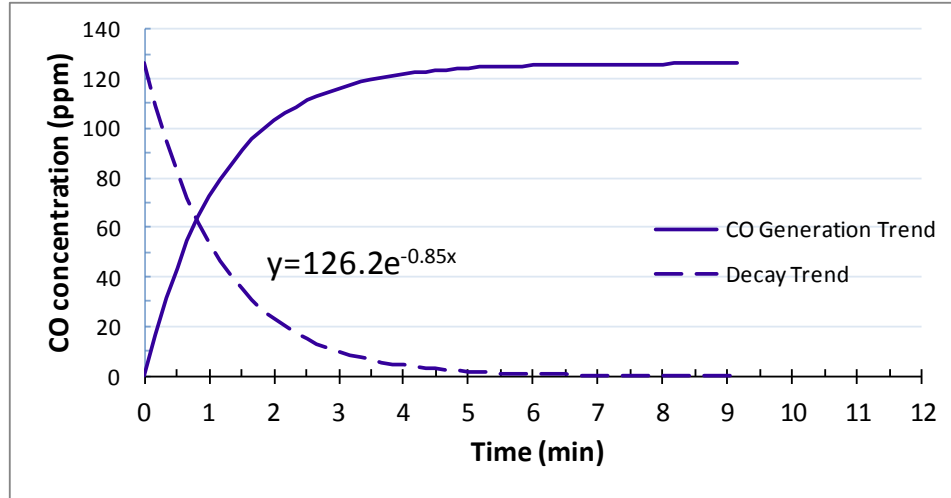
Fig. 5-11 Estimated CO concentration trend as a function of time when the quenching

plate is 7 mm downstream of the burner

5.3.1.3 Electric field impinging flames

We are next interested in the electric field interference with the flow field and whether CO release is affected. Figure 5-12 measures carbon monoxide emissions at different voltage conditions with the plate spacing from H/D=3.5 to 1.5, which are the heights where we have CO release over 100 ppm with no electric field applied. There is not much electric field influence to be expected when the CO release is not affected by the presence of the plate. As in Figure 5-11, the carbon monoxide concentrations in Figure 5-12 are normalized to the steady concentration at unaffected conditions (i.e., burner-to-plate distances beyond H/D = 13.5). Figure 5-12a demonstrates that, independent of the electric field, CO concentration is affected significantly by the plate to burner distance. With no electric field applied, as the plate moves from H/D = 3 to 2.5, the CO emission increase is almost twice that as occurs when the plate moves from 3.5 to 3. This increase continues when the plate moves down from H/D = 2.5 to 2, and from 2 to

1.5. Interestingly, although CO concentration also varies with electric field, it is difficult to distinguish a clear trend in Figure 5-12a. Figure 5-12b provides a normalized and thereby enhanced picture of the electric field effect at each height, with each value divided by the appropriate zero-field CO concentration. The normalized picture generally shows that as the negative field grows, the CO level rises. On the positive field side, CO does not show a consistent nor significant change but the concentration still grows slightly just before falling near the breakdown or extinguishment limit.

The normalized results (Figure 5-12b) indicate that both positive and negative fields can adversely affect CO release from impinging diffusion flames. The adverse effect on the negative side is reasonable in that the downward directed ion driven wind can be seen to affect the flow field similarly to moving the quenching plate slightly closer the burner (i.e. pushing the flame open to release more unreacted CO). The effect on the positive side is more complicated. It may relate to unsteady fluctuations in the combustion process driven by the electric field. This phenomenon has been observed by using a high speed phantom camera with the Schlieren imaging, and the results show that the flame begins to fluctuate within the saturation region with positive field and it continues to strengthen through the super saturation region[95]. It may be that drawing the flame upward brings the reaction zone closer to the plate, increasing the heat loss.
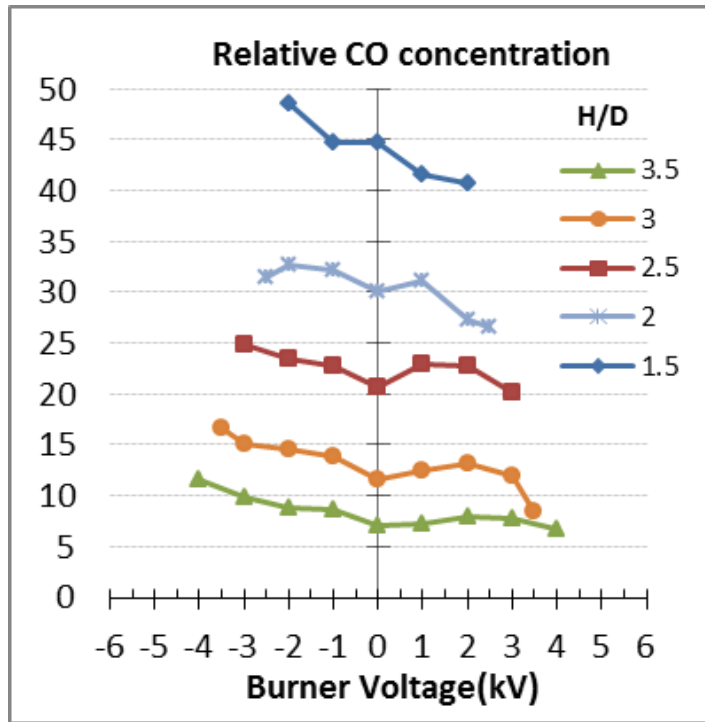
(a)
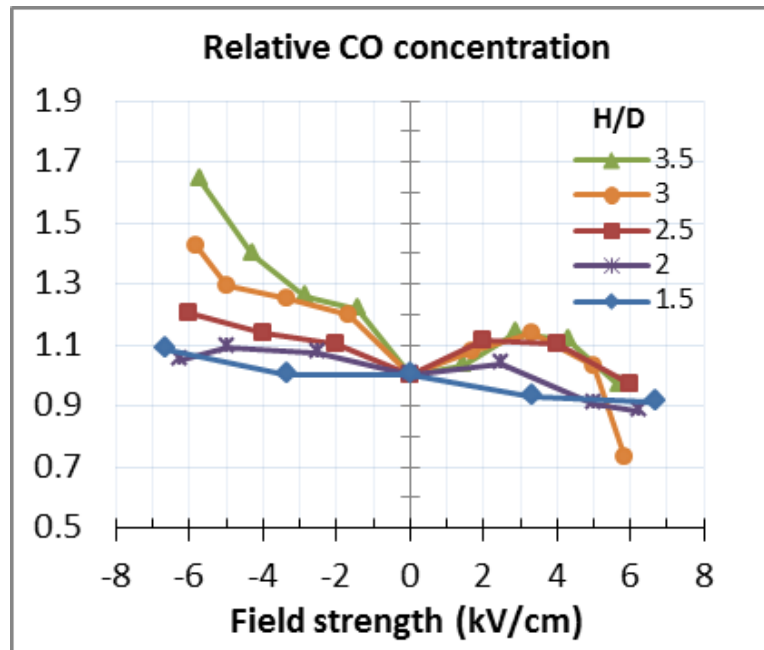
(b)

Fig. 5-12 CO concentration at different plate heights with electric fields applied.

5.3.2 Reaction zone - Chemkin

In order to help understand better how the opening up of the flame reaction zone as it stagnates against the quenching plate might affect the important chemical reactions responsible for carbon monoxide release, the chemical kinetics solver is used for a typical non-premixed flame sheet. The simulated reaction zone between the center fuel and the coflow air is shown in Figure 5-13. The fuel methane is on the left while the air is on the right. During the reaction, carbon provided from methane reacts with oxidizer to form CO toward the fuel side, and then CO_2 sits more toward the outer oxidizer region. In between CH_4 and O_2, OH represents the region where high levels of chemical reaction and energy release within the reaction zone occurs. The gradient of OH can represent the hot zone of the flame. Figure 5-13b shows that the chemiluminscent species OH*, OH, and the temperature profile peak around the same location within the temperature profile. More specifically OH* peaks within the maximum temperature region and OH peaks near the OH* edge toward the air side of the flame. The peak temperature in this simulation is approximately the adiabatic temperature. OH* can be correlated with hottest spot of the reaction layer while CH* sits right next to it in the inner blue layer of reaction zone[96–98]. Note that OH* and OH start together at the same location and the less reactive OH distributes into a larger region then OH*. This basic reaction profile confirms that, as indicated in the OH PLIF findings in the next section that to form CO_2 requires CO reacting with OH [equation (2)].

$$CO + OH \rightarrow CO_2 + H \text{ (2)}$$
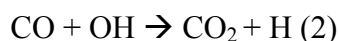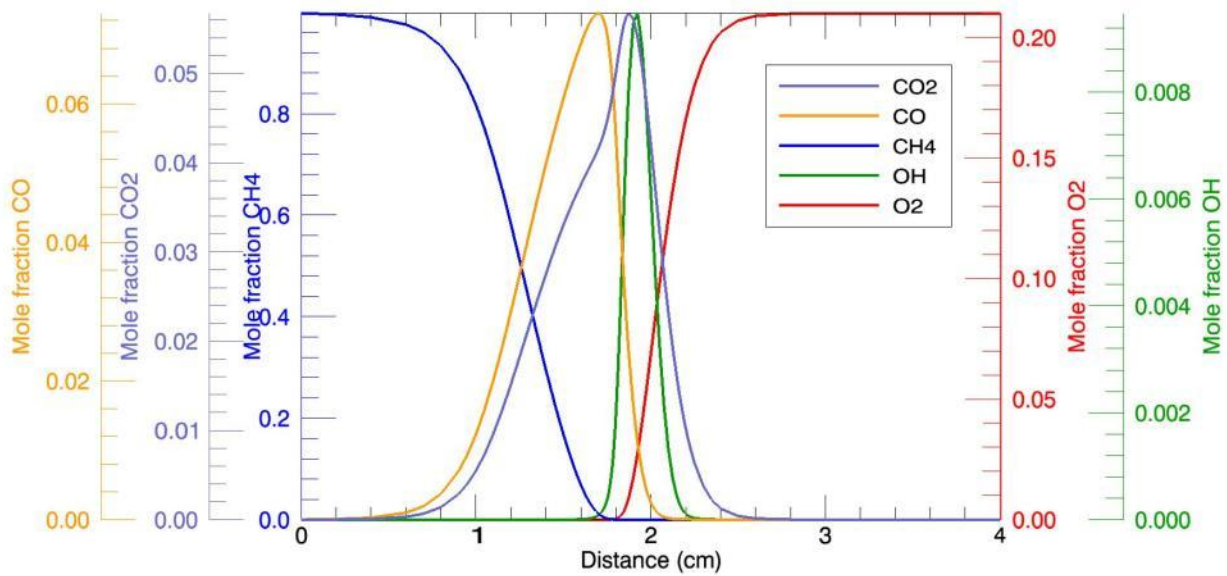
(a)
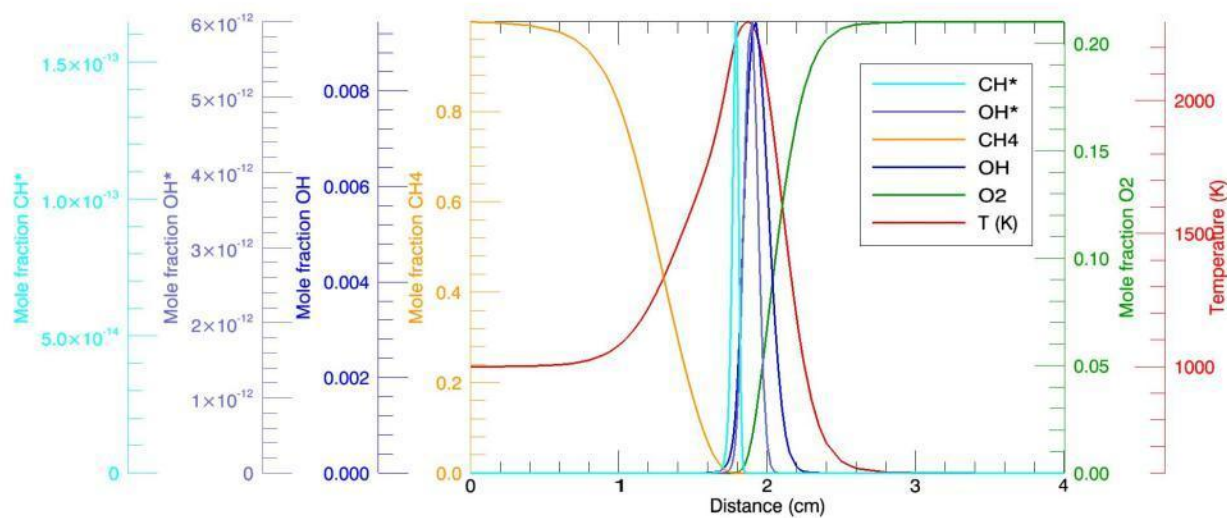
(b)

Fig. 5-13 Reaction location of different chemical species predicted by Chemkin with

opposed flow flame

5.3.3 OH PLIF

The OH PLIF measurements are meant to confirm changes to the location of this reactive species as indirect evidence of how the quenching plate can allow the release of carbon monoxide and how the electric field affects that release. The basic notion is that OH oxidizes CO, and so the location of the OH region relative to the flow path of the CO formed on the inner edge of the reaction zone has a substantial effect on CO release. Figure 5-14 is a comprehensive data record of this work. It shows separate images of OH PLIF and tomographically reconstructed OH* chemiluminescence (as a marker of the peak reaction zone and the edge of the CO formation region) in Figure 5-14(a) and combined images in Figure 5-14(b) to allow location comparisons. The plate height H/D is changed from 5 to 2.5 and the electric field is adjusted from maximum negative to maximum positive at each height. The OH fluorescence is averaged with over 900 images at a 100 Hz recording rate. When no electric field is applied and H/D = 5, or approximately the height of the visible flame, the strong OH fluorescence is mostly gathering around the flame tip, and it groups near the two reaction sheet wings. As the plate moves to H/D = 4.5 and smaller, the OH region is being opened gradually as the flow is at the same time being directed along the plate. The amount of OH fluorescence is decreasing as the flame reaction sheet changes direction toward the outside of the plate. It is clear that the tip of the reaction zone opens, creating a flow path for the gas inside the flame sheet to follow that avoids interaction with the OH radical, even though the heat release (HR) zone is mostly unaffected. In this case we are using the OH* chemiluminescence as the measure of the heat release zone. This structural change gives one possible mechanism by which CO can avoid oxidation.

Figure 5-14(b) presents qualitative results that include the PLIF signal and the Abel inverse transform of the OH*. The OH* transformed images have been used as a good marker of the HR zone of the flame, and other approaches using OH PLIF and CH_2O PLIF [99] have been used in order to not rely on the Abel inverse transform to find the HR zone. Some of the periodic structure of the fluorescence is likely due to our non-uniform laser sheet but the intensity can clearly be seen to gradually decrease as the flow field is disturbed. In general, the overall OH intensity decreases as the plate approaches the burner, which implies that smaller amounts of OH radical exist at small H/D distance. All the images were obtained with only varying the plate position. As the flame gets closer to the plate heat loss should drive the mean temperature of the flame down, and, because the fluorescence signal tends to increase as the temperature decreases (Figure 4-12), a relative decrease in the concentration of the OH is the only reasonable explanation for decreasing fluorescence intensity. This, combined with the fact that the velocities were kept low so that the flow behaves with similar characteristics of a laminar stagnation flow, gives a reason for the overall oxidation of the CO molecule to decrease, due to the lower OH concentration and shorter residence time for reaction through the OH layer as the plate approaches the burner. The tip of the OH radical zone opens because the plate acts a chiller for the flame, radiating energy and bringing the surface temperature to approximately 500K. Other work mentions that the OH radical is not expected to exist below 1000K [100], which is why the OH reaction zone opens in the cool gas layer near the surface before the HR zone changes its shape.

The images also show that OH fluorescence changes with electric field distributing outwardly with negative fields and gathering with a positive field. At

relatively high burner to plate spacing the electric field has minor influence on the OH PLIF intensity but it does affect the location of the OH as the fields change the location of the flame sheet. When the electric field is applied upward, the ion driven wind pulls the flame in the direction of the flow field and the reaction becomes more vigorous toward the plate. OH distributes strongly near the plate in this case. At closer plate distances the field affects the OH intensity as well as its position. When the electric field is negative, the downward directed positive ions produce a downward blowing wind that causes the reaction sheet to widen. In H/D = 3.5, there is the most dramatic effect of the electric field as regards the relative magnitude of OH fluorescence but relatively little change in the location of the OH relative to the flame sheet. This result is reflected in the large relative change in CO for this case with negative field applied. As with the CO measurements, these images show that the effects of changes in plate height have a larger effect on the OH distribution than does the electric field.
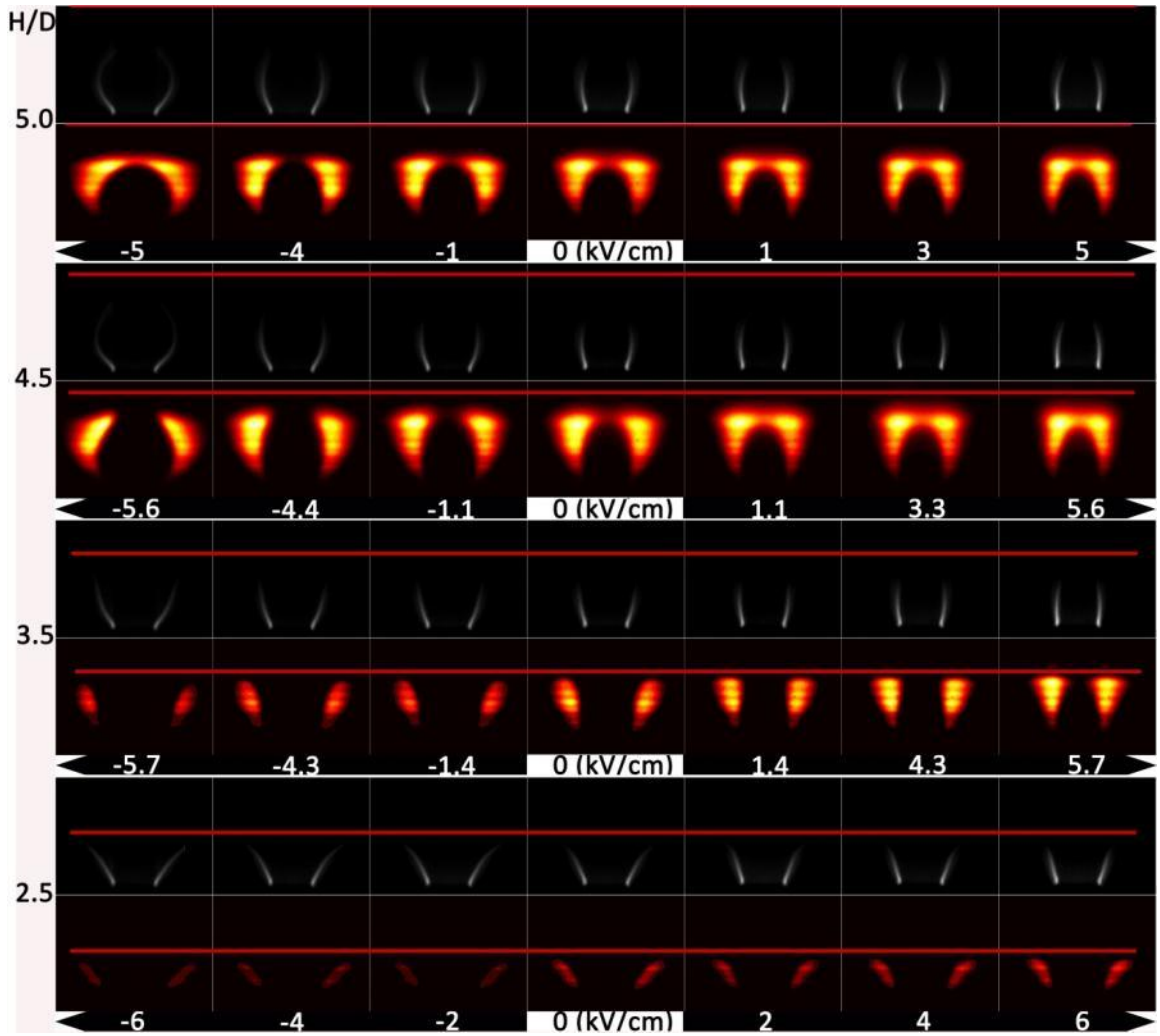
(a)
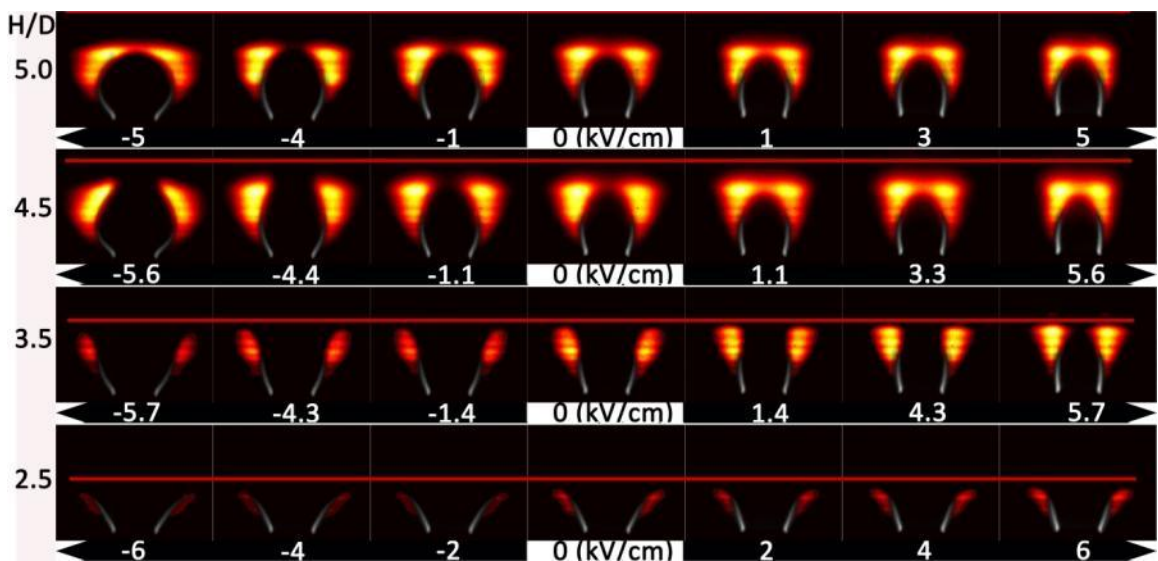
(b)

Fig. 5-14 (a) tomographically reconstructed OH* and OH planar laser induced

fluorescence at each quenching distance with changing electric field; (b) Combined

images from (a) for location comparison.
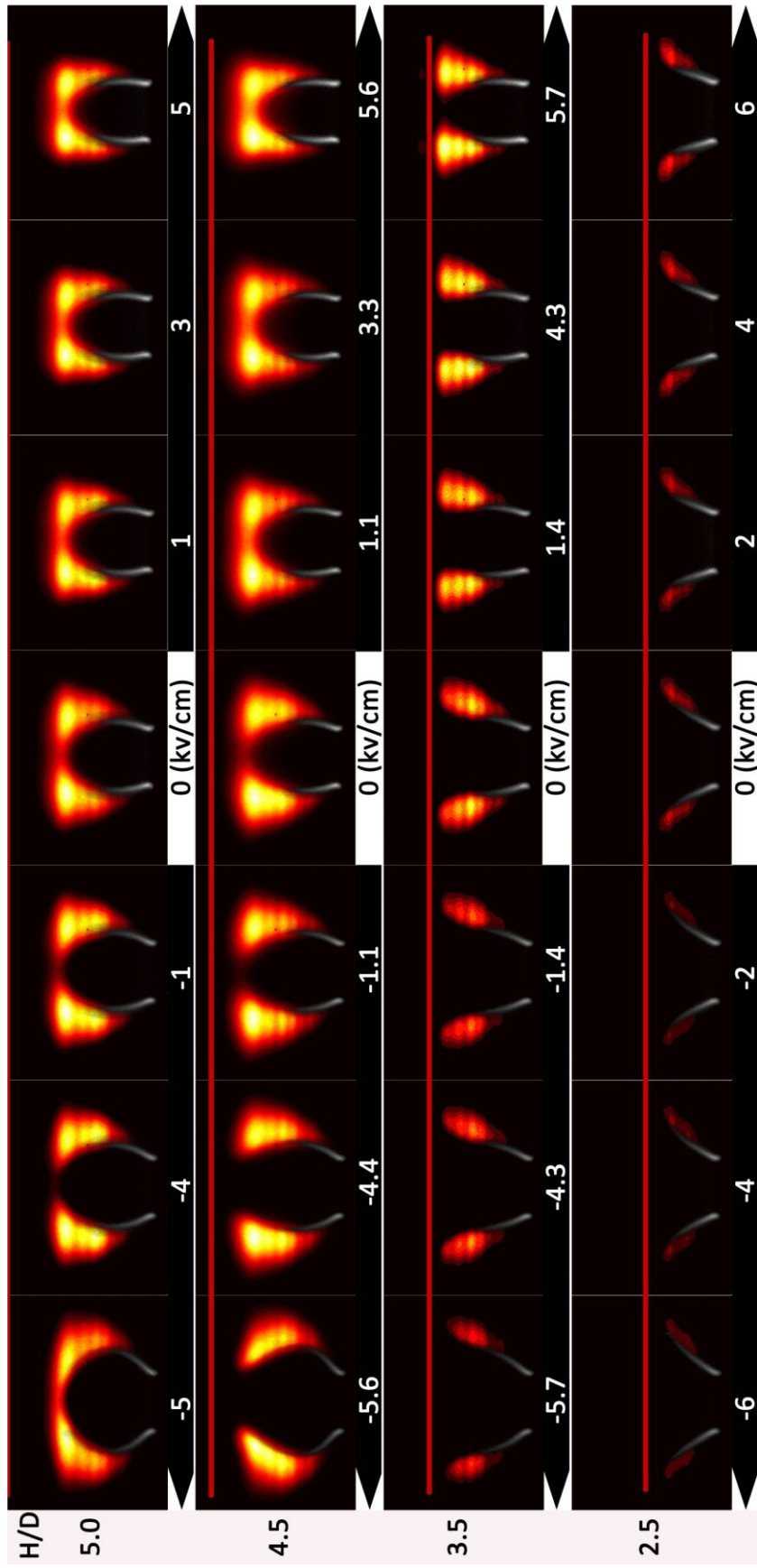
5.4 Temperature thermometry

5.4.1 Thermocouple flame temperature

While it is not possible to use a thermocouple to measure flame temperature when an electric field is operating, it is possible to confirm some of the suggestions of thermal influence by the plate using a thermocouple at zero field conditions. The result of thermocouple flame temperature is shown in Figure 5-15, which has a real flame photograph and the measured temperature in degree Celcius overlaid. The impinging plate is located at 10 mm height (H/D = 5), shown as red, and the burner exit is at zero in height (where the purple line is). The brightest part in the flame reaction zone in the picture is located about radius 2-3 mm, where the thermocouple acquired the maximum temperature around 1030 ^{o}C (or 1300 K). This result only gives a concept of the actual flame temperature since the thermocouple itself is large enough to interfere with the small reaction zone. Also, the measurement does not have high spatial resolution with the thermocouple averaging the flame temperature with that of the sourroundings. Nevertheless, the measurement shows the extent of the hot gas zone and that it is consistent with the OH PLIF measurements and the Schlieren imaging. It also confirms that the quench zone layer near the plate is approximately 1 mm in thickness.
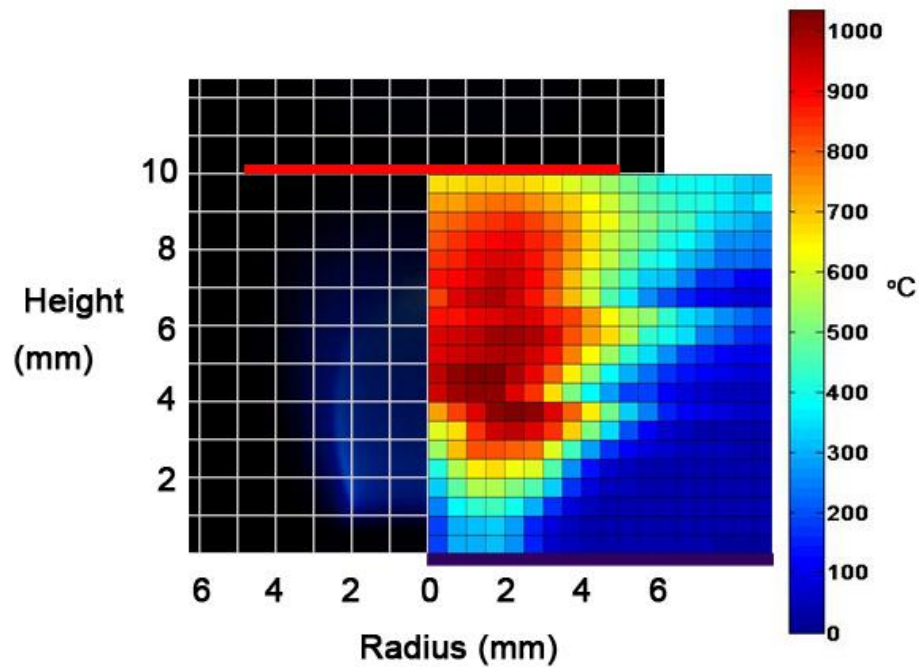
Fig. 5-15 Photographed flame image (left) with temperature measured with thermocouple

(right).

5.4.2 Two line OH PLIF thermometry

To further evaluate the thermal structure of the impinging flame and to estimate

the heat loss to the plate, a more comprehensive temperature measurement was developed

using the OH PLIF data. Figure 5-16 (a) and (b) shows the OH PLIF images taken with

PI-MAX4 ICCD camera at two different emission lines, R1(3) and R1(10) when the plate

is located 9 mm downstream of the burner (H/D = 4.5). All the OH PLIF images are

corrected for variation in laser intensity to avoid measurement errors. The laser intensity

is recorded for each single measurement. The two white lines represent the location of the

impinging plate and the burner exit. It is interesting to notice that the overall OH PLIF

intensity on the right side of the flame is slightly stronger than that on the left side while the laser is directed from left hand side to the right hand side. It is possible that the laser beam sheet convergence is not perfectly parallel and may be narrower on one side than the other, but an opposite intensity phenomenon is observed at 11 mm for R1(3) transition shown in Figure 5-16(c) and which is the only case among all of the images between two lines. It is possible that this variation is just a characteristic of the burner, but in any case this phenomenon represents less than 10% difference (and there is no difference when the line intensities are ratioed). Nevertheless, the asymmetry is an open question since there is almost no research published on OH temperature over a symmetric geometry in a combustion flow.

The closer look of the OH PLIF temperature profile at plate-to-burner distance 4.5 and 1.5 are shown in Figure 5-17. The higher temperature region is located at the inner side around the reaction zone. Figure 5-17 shows the temperature derived from the OH fluorescence images as having a value of about 1700-1800 Kelvin. Figure 5-17 and 5-18 show that the OH cloud has a similar temperature distribution independent of the plate-to-burner distance. The only difference is that the flame geometry is perturbed and opened up by the impinging plate and the reaction is opened and facing upward; this phenomenon can be observed from Figure 5-17a in comparison to 5-17b. This consistent OH temperature distribution with the plate-to-burner distance decrease implies that the plate does not cool the peak flame temperature. Instead, with the plate getting closer the burner, the flame is interrupted by the impinging plate and which changes substantially the reaction zone geometry.
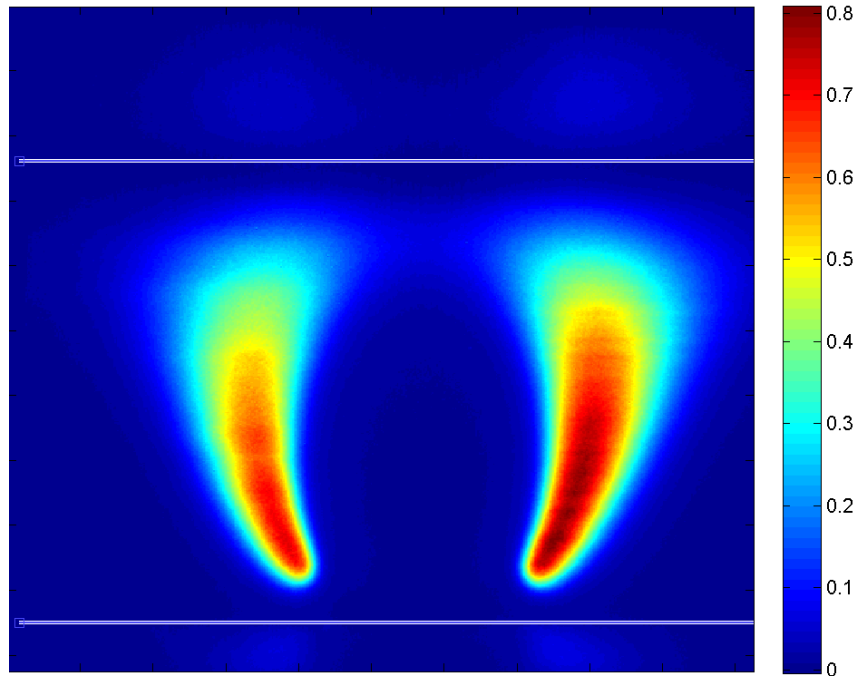
(a) R1(3) at H/D=4.5
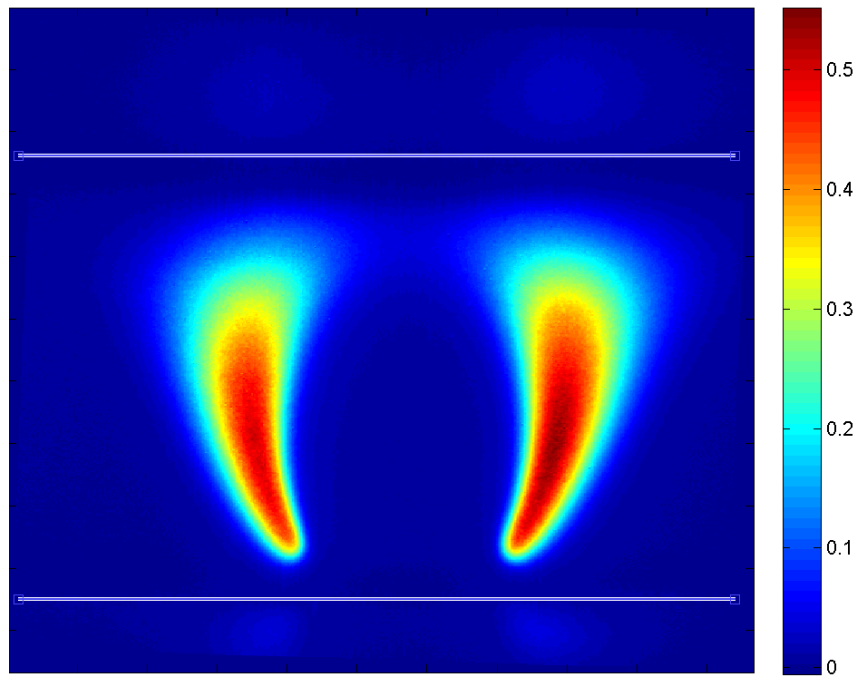
(b) R1(10) at H/D=4.5
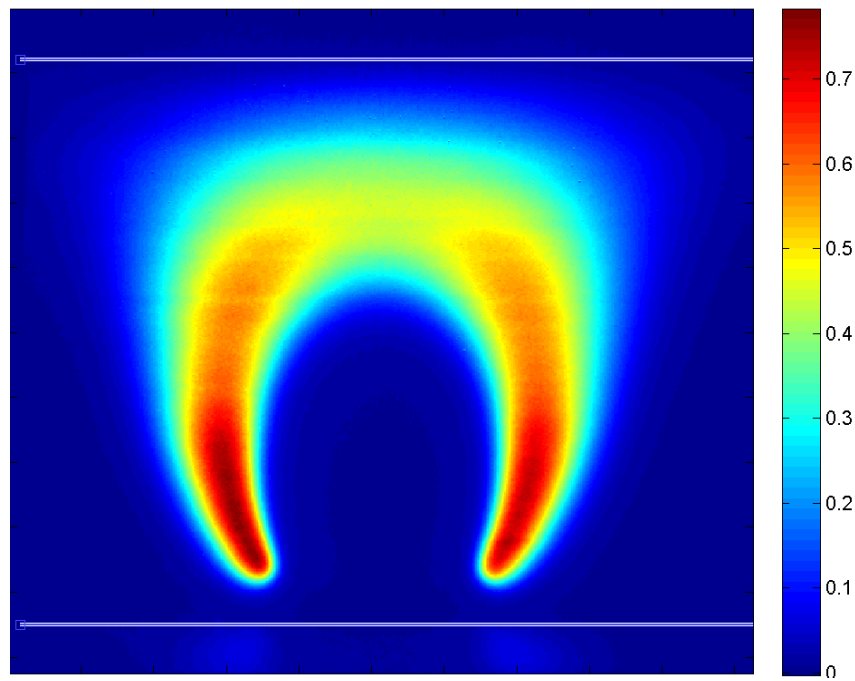
(c) Ri(3) at H/D=5.5

Fig. 5-16 OH PLIF images taken with PIMAX
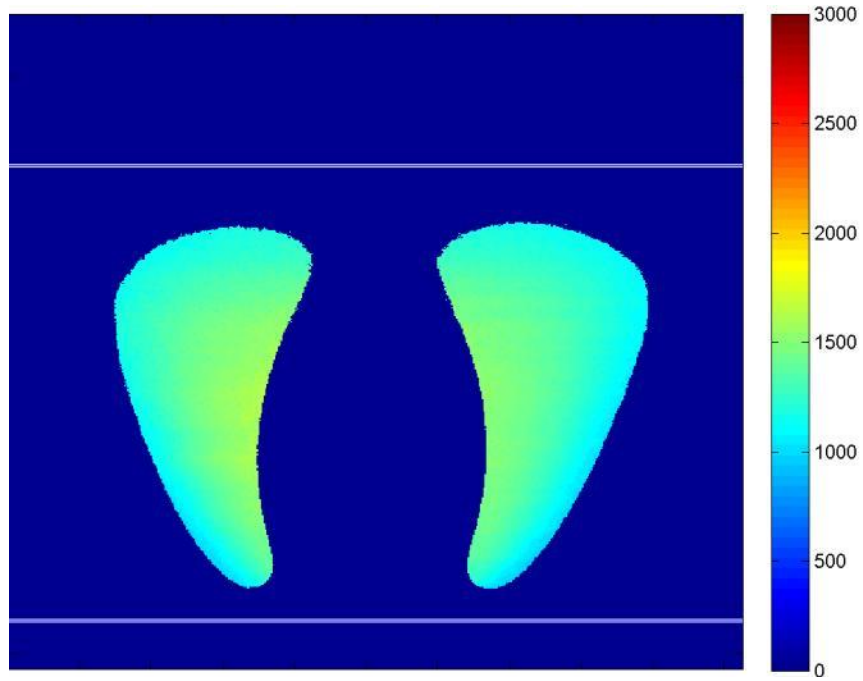
(a) H/D=4.5
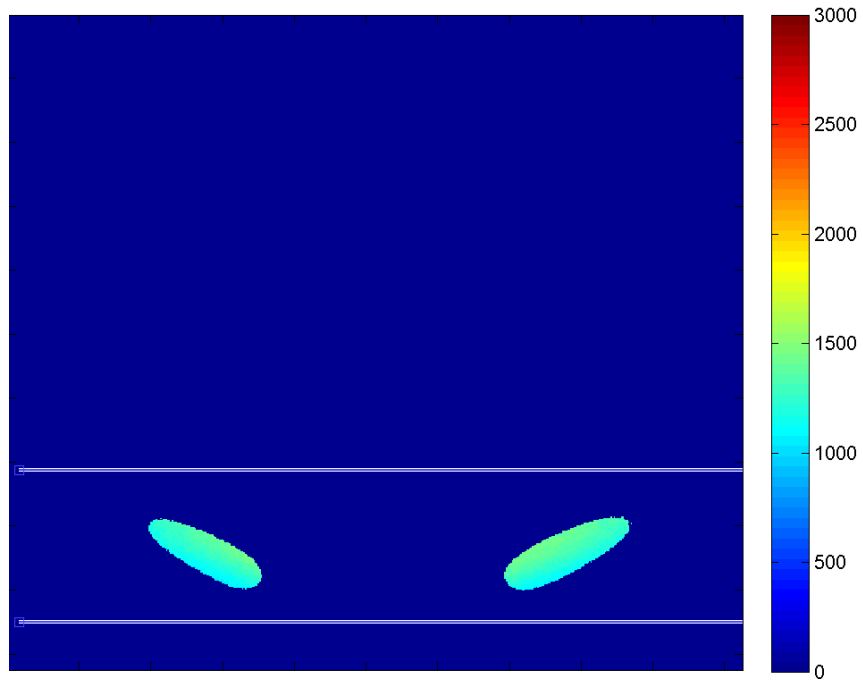
(b) H/D=1.5

Fig. 5-17 OH temperature measured at 9 mm. The unit is in Kelvin.
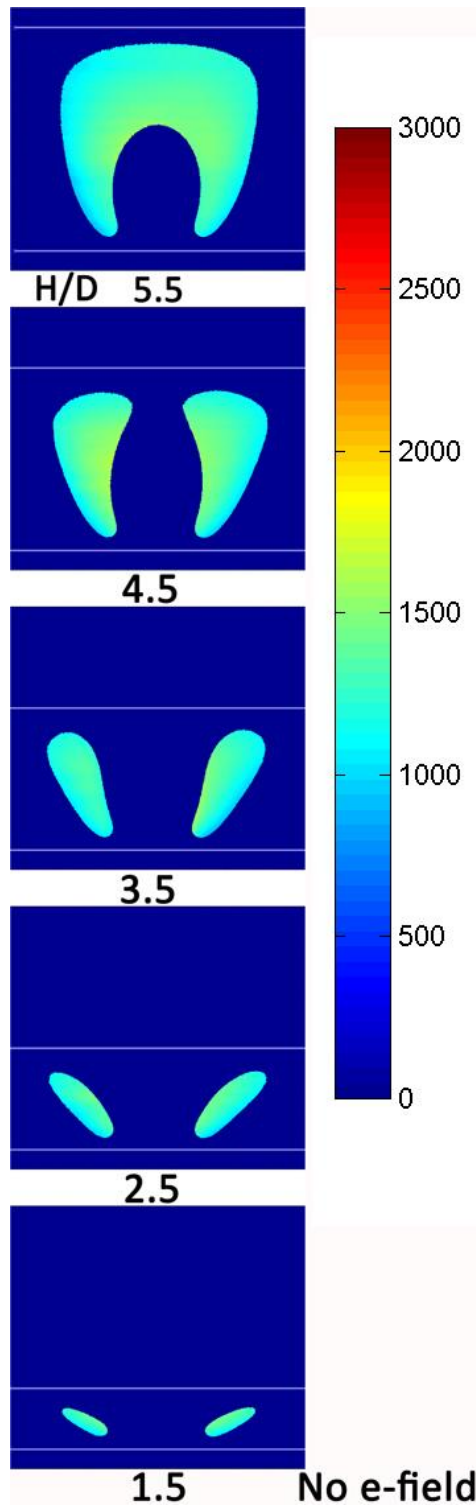
Fig. 5-18 OH PLIF temperature measured between R1(3) and R1(10) at different plate-

to-burner H/D distance with no electric field

5.5 Top View - Thermal study over the impinging plate

The results of the OH PLIF and other imaging indicate that the heat loss to the plate does not have a major global effect on the flame temperature but that the more dramatic influence is an interruption in the flame structure that leads to poorer combustion performance. To help quantify changes in heat loss to the plate, measurements were made of the thermal response by the plate to the flame and the electric field acting on the flame.

5.5.1 Heat propagation measurement
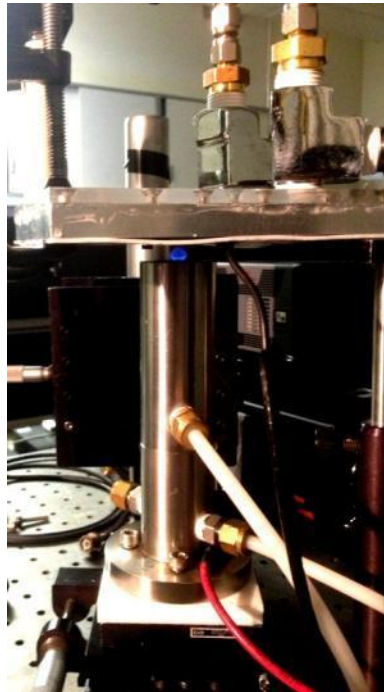
Fig. 5-19 Temperature measurements over the plate

Two thermocouples embedded in the plate and measuring at the same time became a good reference with each other. Thermocouple 1 and 2 both had very similar

results (Figure 5-20a and 5-20b) in measuring the amount of time required for raising one $^\circ$C. At H/D 5.5 the time consuming fluctuation has the least effect either with positive or negative electric field since the plate has not reached or influenced the flame. H/D=4.5 shows the strongest effect and obvious results; the time reduces with a positive field where the ion wind has upward direction entrainment while the time keeps almost at the same level with a negative field as the hot gas is pushed by the ion wind away from the plate. An obvious trend can be observed in Figure 5-21a and 5-21b, which shows the relative time at zero electric field. A similar trend can be observed at H/D 3.5 with less variation in time. When the plate is lowered to H/D=2.5 more time is needed to bring the plate up in temperature then for all the other plate locations. The overall local impinging plate temperature measurement gives some insight that the electric field has the potential to affect and change the plate temperature distribution but only in a band of heights where the flame is far enough from the burner to allow ion wind influence and not so far from the burner to keep the flame shape from being affected by the plate.
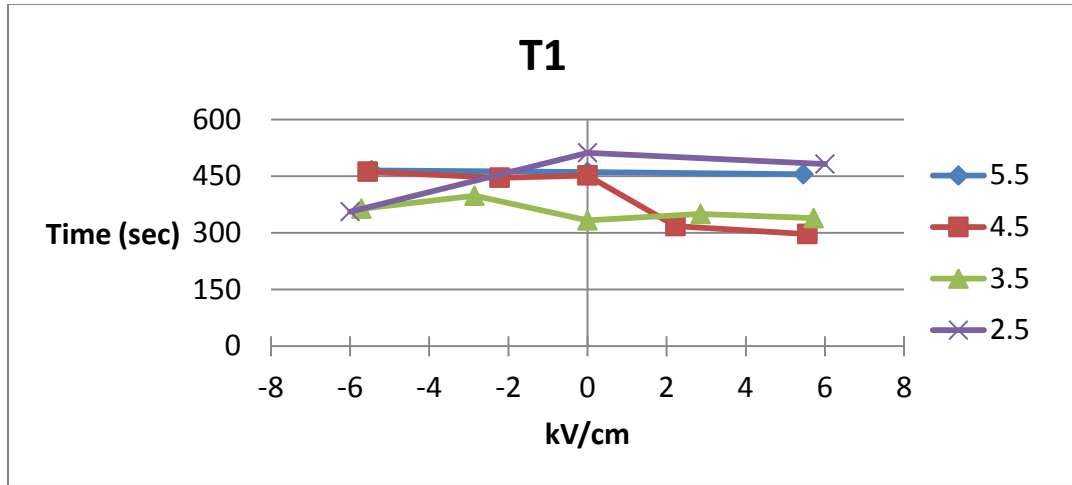
(a)
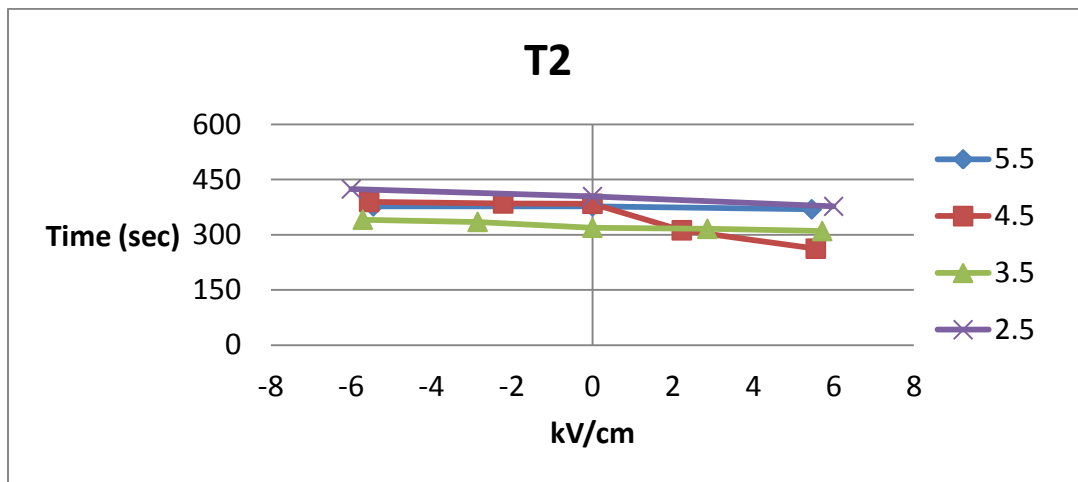
(b)

Fig. 5-20 Temperature measurements (a) Thermocouple 1 (b) Thermocouple 2
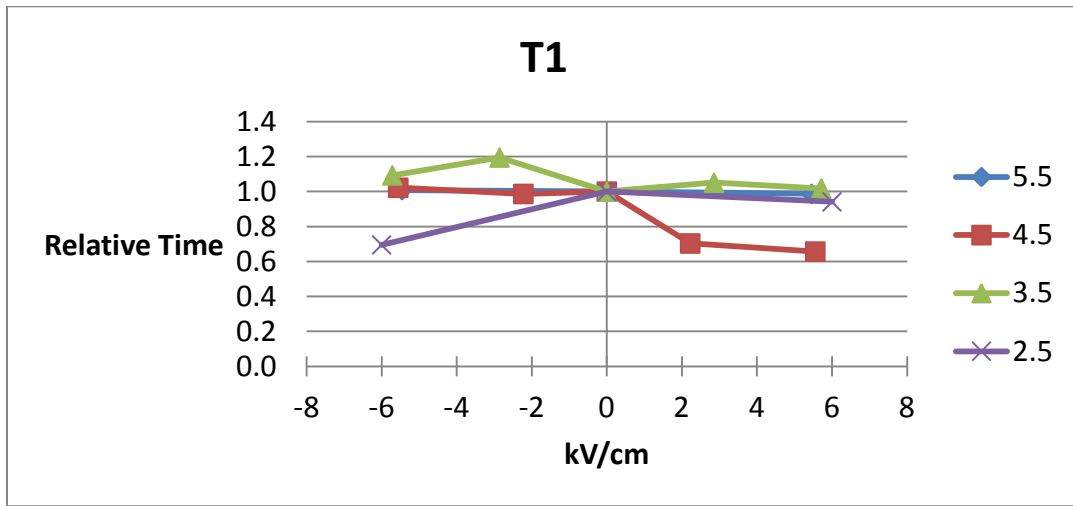
(a)
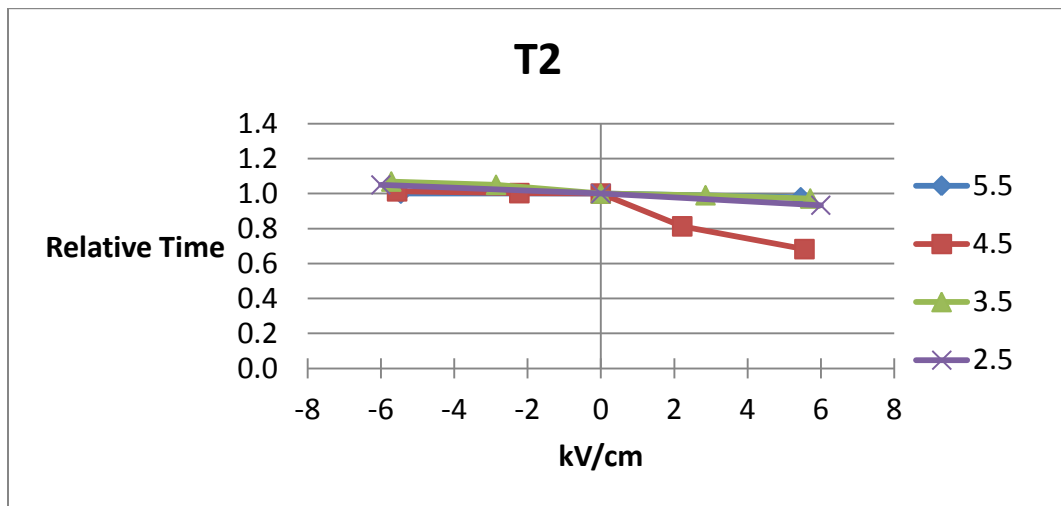
(b)

Fig. 5-21 Relative temperature at zero field (a) Thermocouple 1 (b) Thermocouple 2

5.5.2 IR imaging

While the temperature provided by the two thermocouples was consistent, it was clear from these measurements that the flame interacting with the plate would affect the thermal profile on the plate as well as the specific temperature values. The IR camera study provided more complete thermal mapping of this phenomenon.

5.5.2.1 Temperature profile

A sequence of IR image was captured at different impinging plate height and changing with electric field applied. Figure 5-22 is an illustration when plate is located at 9 mm (H/D=4.5). From the strongest positive field direction 5.6kV/cm to 2.2 kV/cm to no field (Figure 5-22a, b and c), the temperature profiles distribute from higher at the center and gradually reduces. With the increasing negative field from -2.2kV.cm to -5.6kV/cm (Figure 5-22d, and e), the peak temperature at the center decreased. The spot temperature is the cross symbol which is set locating at the center of the burner. It is observed that the spot temperature is the peak temperature of the plate; therefore, the plate temperature at the flame center is an averaged temperature with the surrounded reaction region. Clarifying how the plate temperature profile along the burner center distributes under electric field effect would bring a clear insight.
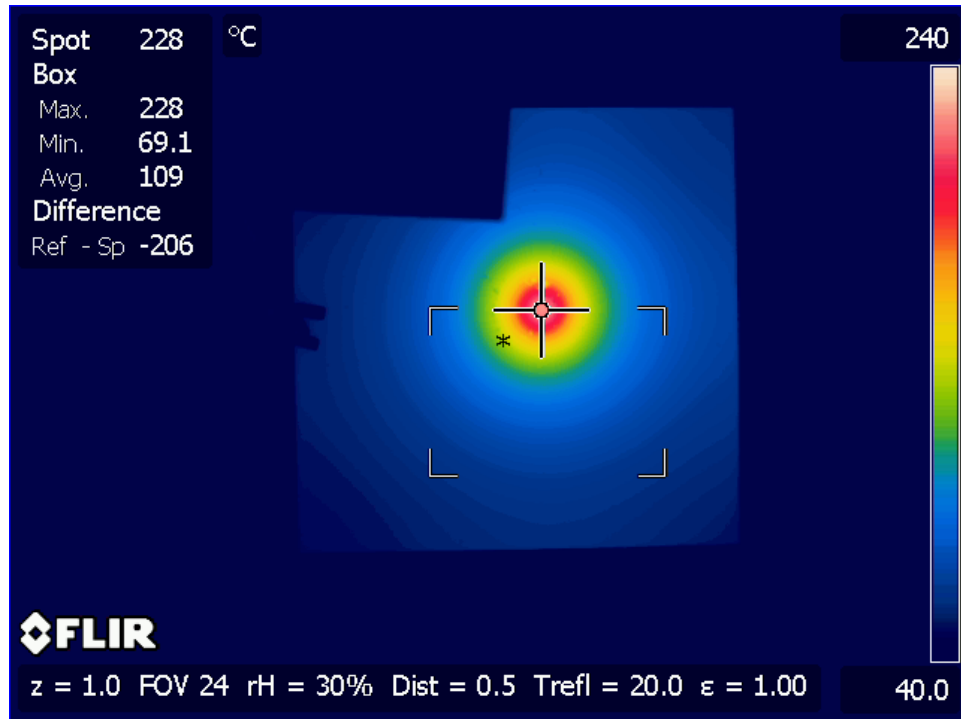
(a) 5.6 kV/cm applied
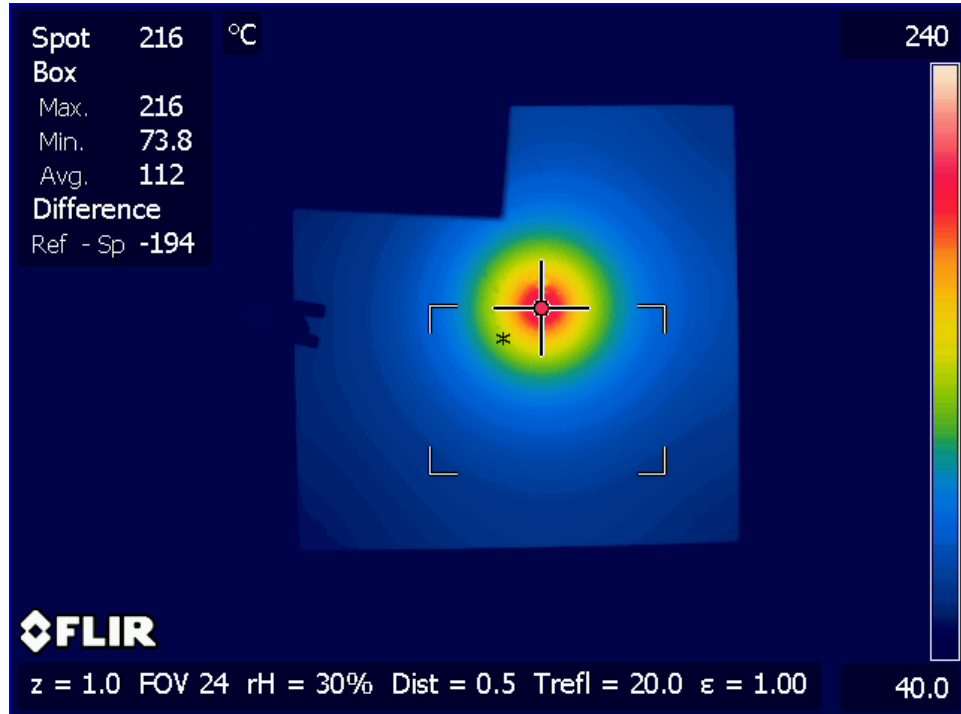
(b) 2.2 kV/cm applied
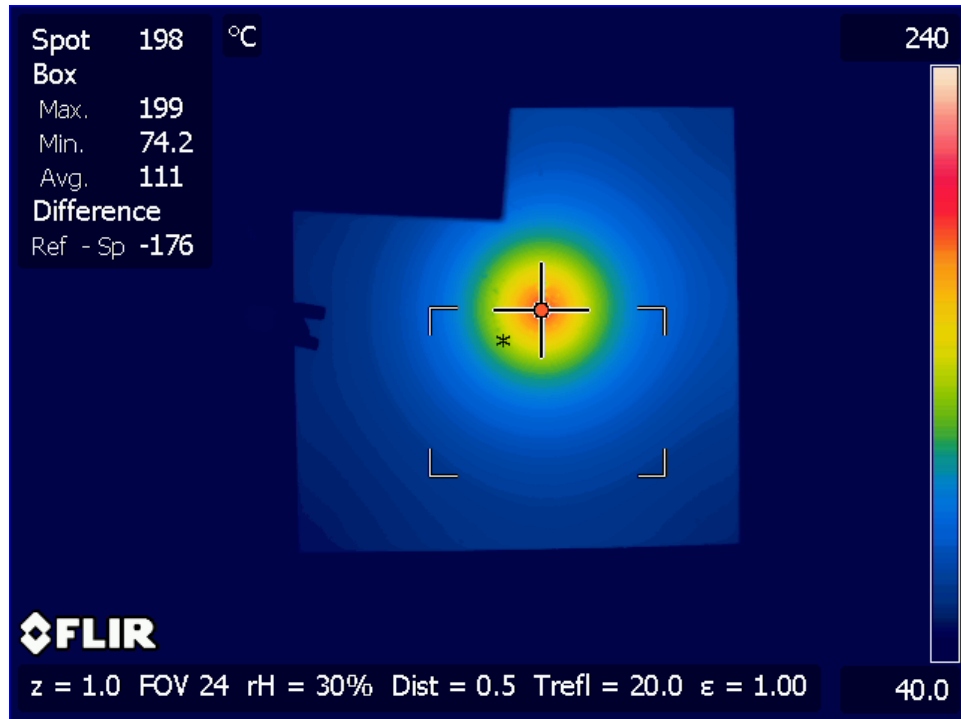
(c) No electric field applied
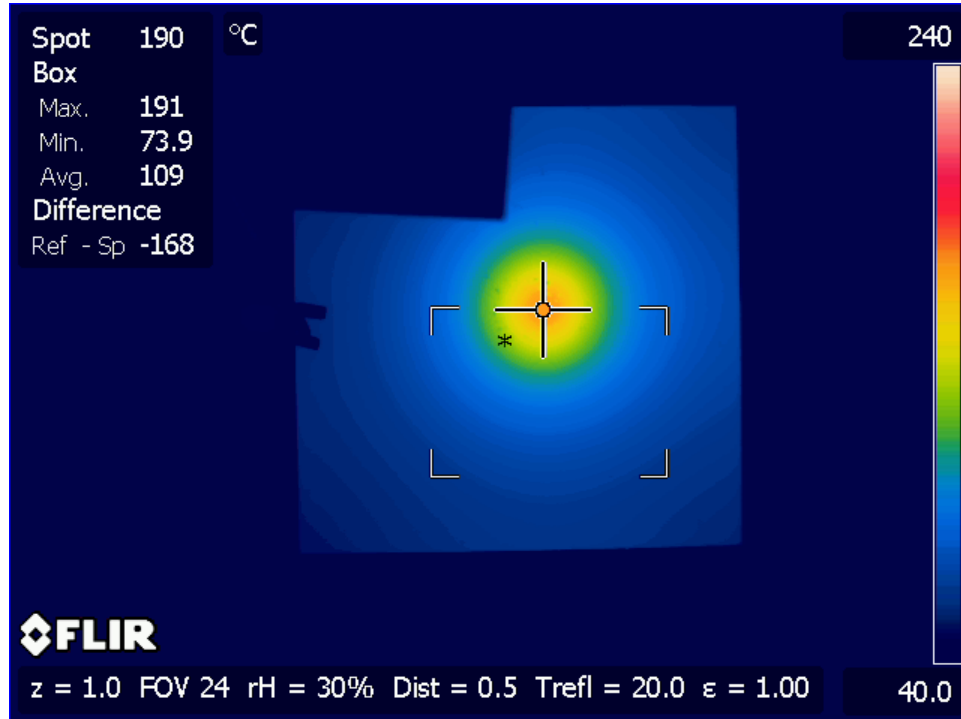
(d) -2.2 kV/cm applied

(e)
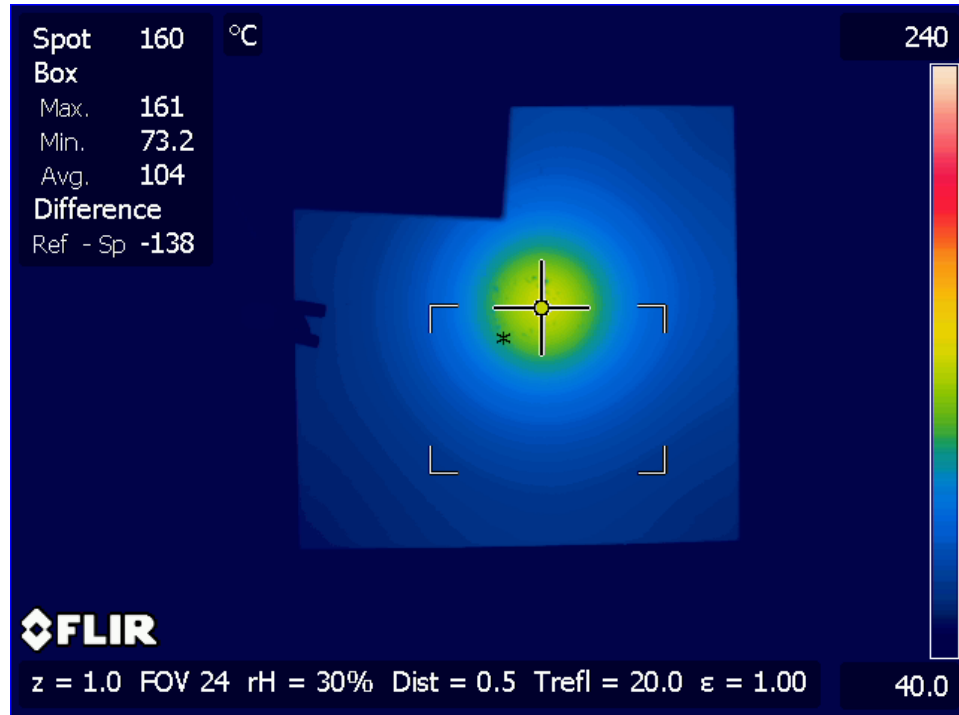
(f) -5.6 kV/cm applied

Fig. 5-22 IR image of plate temperature in degree Celsius changing with different

electric field applied at 9 mm.

Figure 5-23 converts the acquired thermal map from the 2-D image of the IR camera into a local temperature profile across the plate when it is 9 mm from the burner. The overall temperature distribution is approximately Gaussian for the cylindrically symmetric thermal system with a central hot spot. With a negative field in Figure 5-23b, the peak temperature is lower and the profile is broader while the positive field case has higher peak temperature and narrower profile (Figure 5-23c). The little dips on the left side of the peak in the profiles occur because of defects in the black paint on the plate gives variation of local emissivity. This information suggested that the heat transfer over

the quenching plate can be altered or improved by the electric field and, moreover, whether or not the electrically controlled flame might provide better thermal efficiency in terms of heat transfer to surfaces.
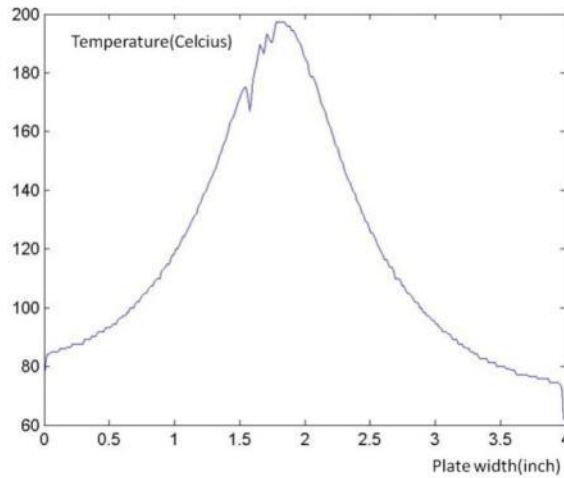
(a) No electric field
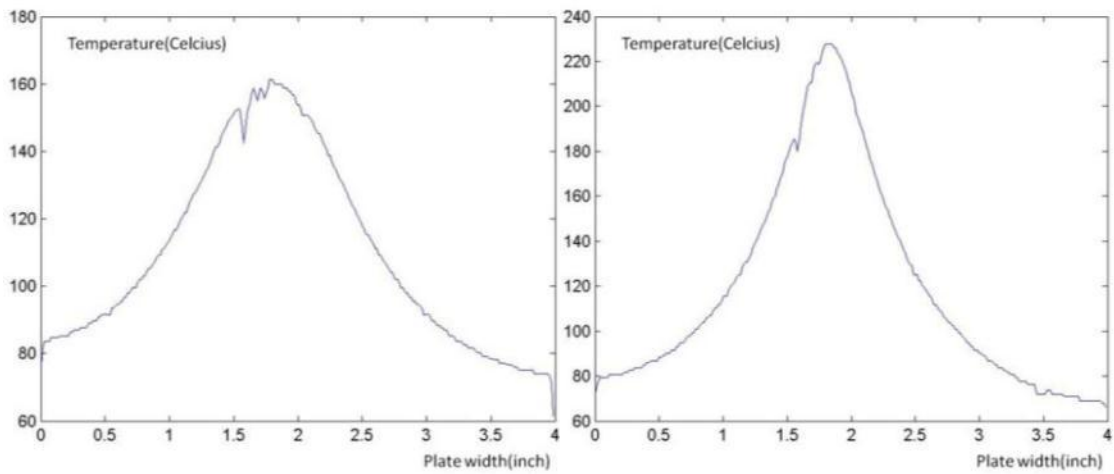
(b)-5.6kV/cm applied   (c) 5.6kV/cm applied

Fig. 5-23 Temperature profiles along the plate at 9 mm (a) no field (b) -5.6 kV/cm

applied (c) 5.6 kV/cm applied

Measurement at various heights (3, 5, 7, 9, 11 mm) shows that temperature decreases with the field strength (Figure 5-24). Maximum temperature of each condition at each height and field strength is recorded, and Figure 5-25 plots the relative maximum temperature at zero electric field at each distance between the plate and the burner. On the positive field strength side, the maximum temperature increases quickly in the beginning at 2kV/cm and keeps rising with the field strength applied. The reaction zone is narrowed due to the ion wind and the flame's hot gas is being pulled up toward the plate. Both of these effects produce an increased local heat flux. On the negative field strength side, the reaction zone of the flame is shifted wider with the increasing of the field strength. Therefore, the maximum temperature decreases. The curve shows that the reducing trend initially decreases with similar slope until -3kV/cm, and then drops more rapidly with more negative field applied. As the plate reaches 3mm, the lowest limit of its position, the electric field effect on the maximum temperature of the plate does not vary as dramatically as for plate positions that permit more electric field influence on the flame. This is because the plate is so close to the flame that the reaction zone of the flame has already opened widely. That is, the jet momentum modification caused by the proximity of the quenching plate is more substantial than the momentum modification caused by the ion driven wind. Since we have seen that the ion-driven wind effects decrease with decreasing plate height and the physical effects of the plate increase with decreasing plate height it is clear that there will be a trade-off between these two influences. These results need more evidence to explain completely how the electric field is able to control and manipulate the flame's heat flux to the plate.
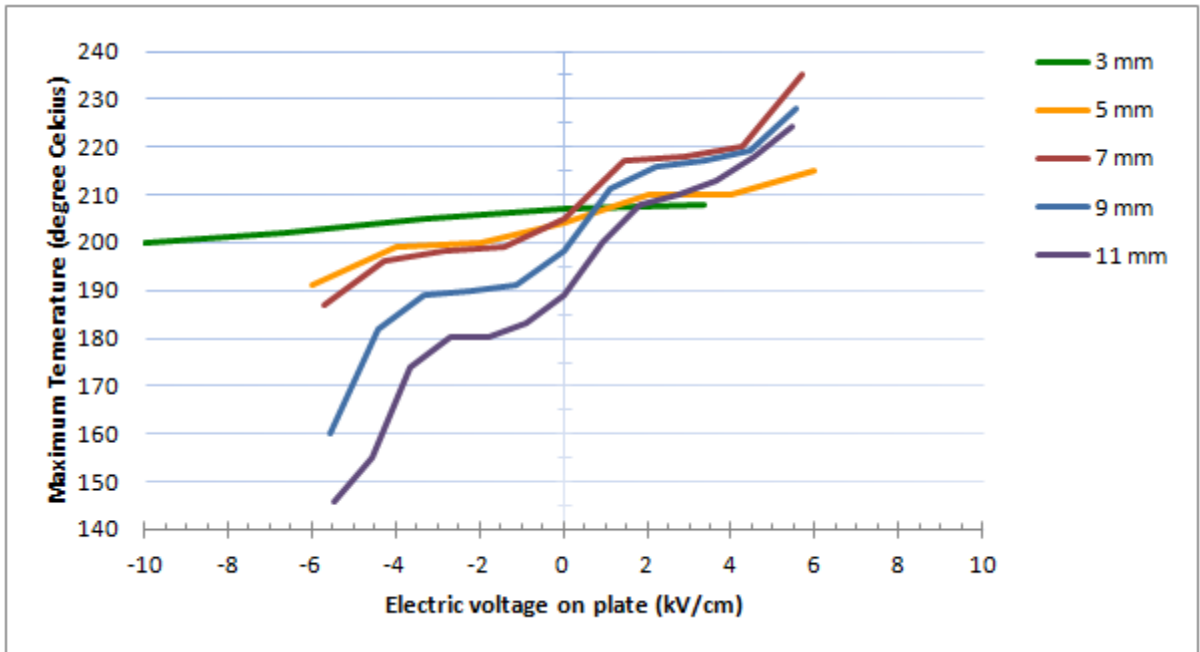
Fig. 5-24 The maximum temperature measured from the plate with different electric field

applied
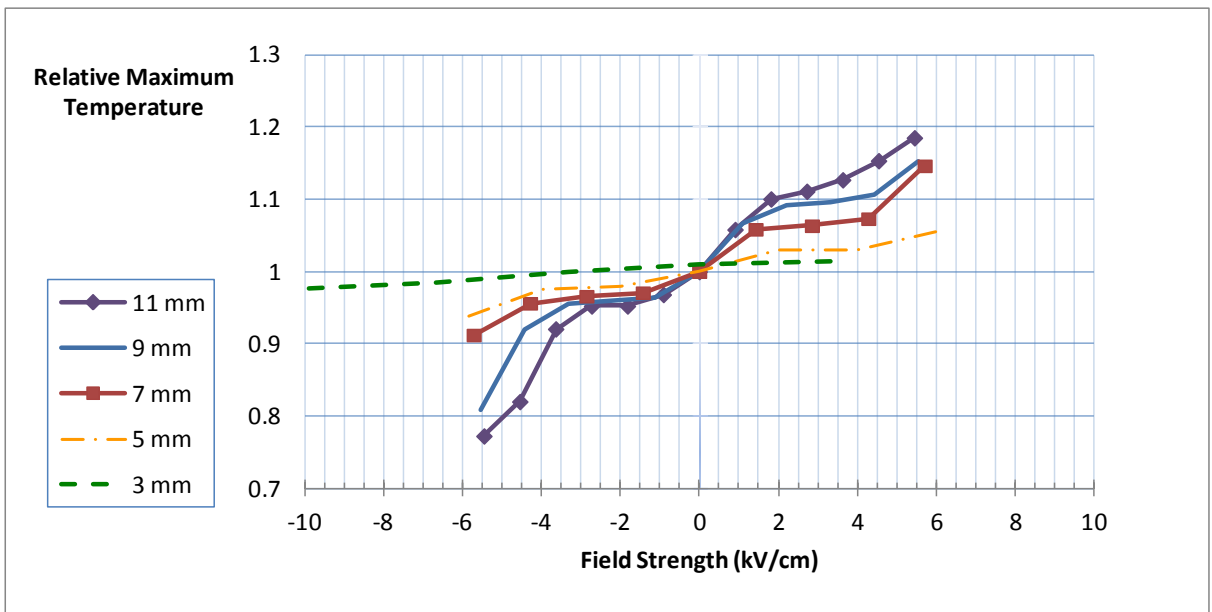
Fig. 5-25 maximum plate temperature with electric fields

5.5.2.2 Heat transfer

The overall heat transfer around the plate includes forced convection of hot flame products onto the bottom surface of the plate, conduction through the plate, the heat convection out from the surface into the air, and radiation from all the surfaces, as the system reaches thermal equilibrium (Figure 5-26) [101]. Based on straightforward heat transfer analysis it is easy to conclude that the radiation from the paint provides a reliable measure of the impinging heat from the flame on the backside of the plate. The heat transfer around the boundary near the plate can be written as:

Heat into the plate = Radiation + Convection
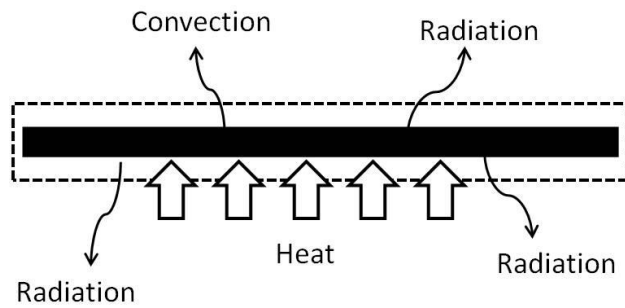
Fig. 5-26 Heat transfer near the boundary around the plate

5.5.2.3 Data processing

The experimental setup requires ceramic posts as an insulated non-conductive connector onto the plate in order to prevent the current from conducting through the metal optical table. The top view of the IR image has a corner blocked by an optical mount, as shown in Figure 5-27a. In order to acquire a full map of the temperature over the plate, a mirroring interpolation method is applied to reveal the corner temperature

map by assuming the temperature has symmetric distribution over the plate. Figure 5-27b shows a mirrored full map temperature image. An overall processed IR distribution image changing with electric field and the plate-to-burner distance is shown in Figure 5-28.

(a) Original image   (b) Processed image
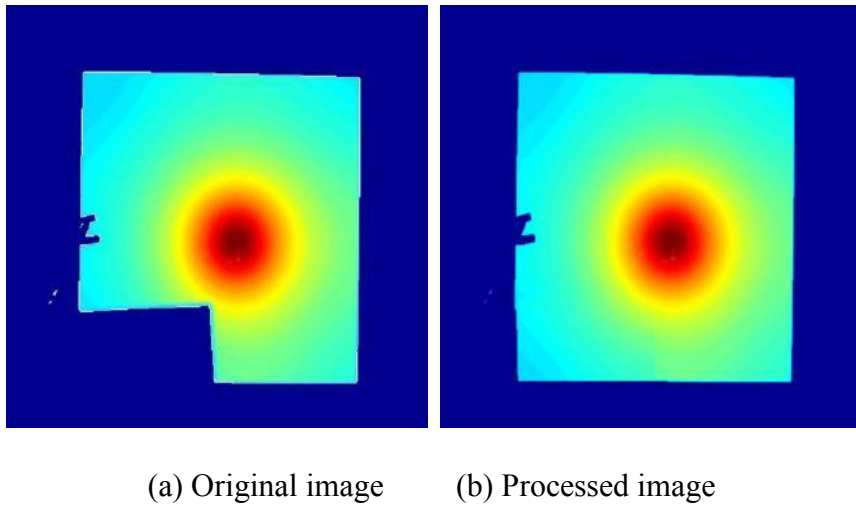
Fig. 5-27 IR image before and after mirroring the temperature to the corner
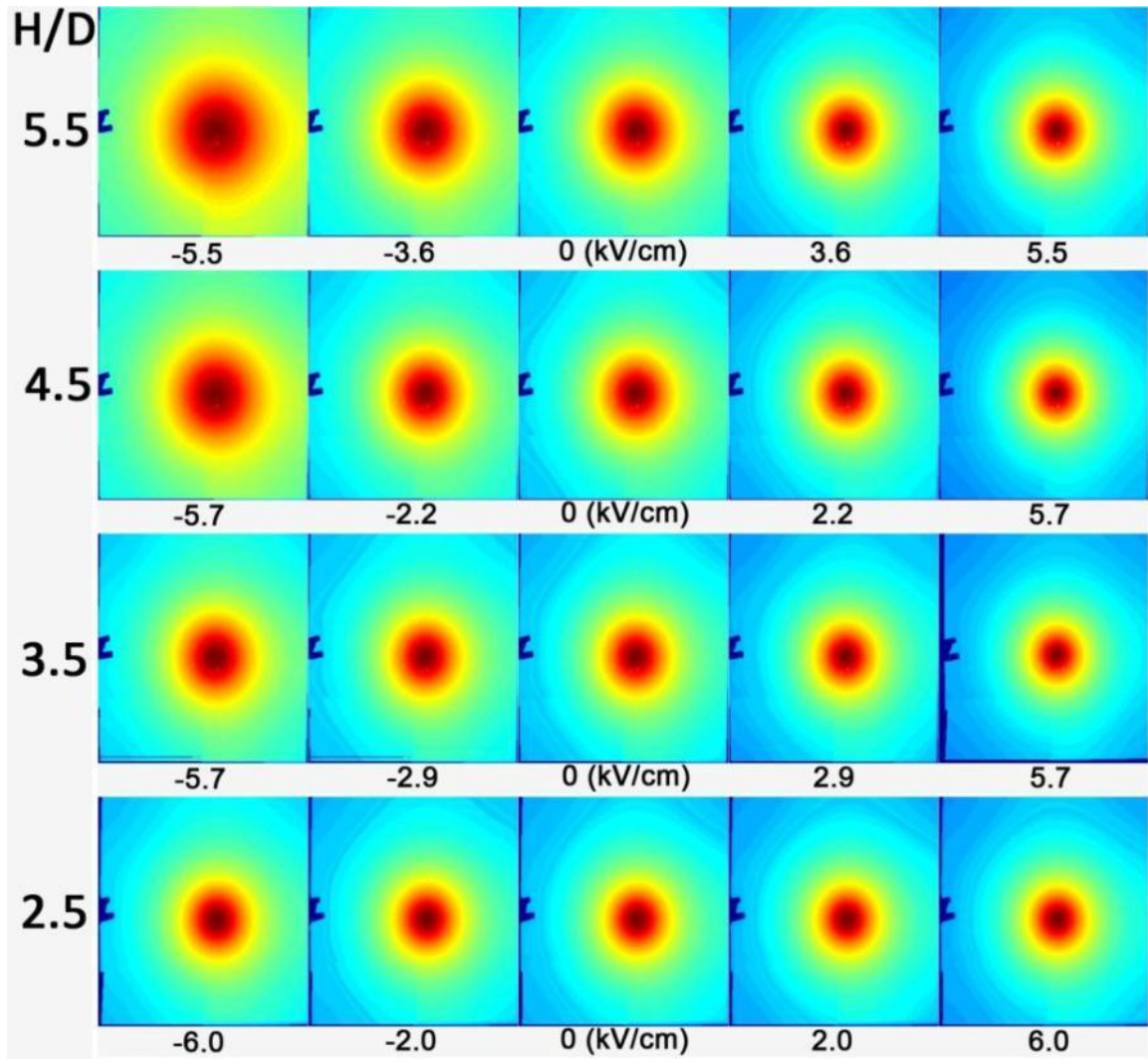
Fig. 5-28 The overall IR temperature distribution changing with burner-to-plate distance

under electric field effect

5.5.2.4 Heat concentration analysis

The Figure 5-29 shows the total amount of heat dissipated from the plate in percentage with respect to the total thermal power assumed to have been generated by the flame and that is available at the bottom of the plate, 25 watts. The heat loss is considered including free air convection from the plate top, coefficient set as 12 W/m^{2}K, and radiation from both sides of the plate, the emissivity is set at 1. Based on these values, the temperature profile is consistent with 5~6 Watts (20-24% of 25 Watts) of heat transferred to, and lost from, the plate at steady state. It appears that when the impingement is close to the heat source (from 5 mm towards 3mm) the total amount of heat loss over the plate is less affected by the electric field. The overall heat loss at the two sides in the strongest electric field cases have a tendency of decreasing at the same plate height. It is worth noticing that at 11 mm the heat loss grows from the negative field to the positive field, suggesting that the largest effects occur when the plate has not begun to interact with flame significantly. Interestingly, we see a similar behavior in our carbon monoxide release results where the electric field is effective only in a relatively narrow range of plate distances from the flame[69].
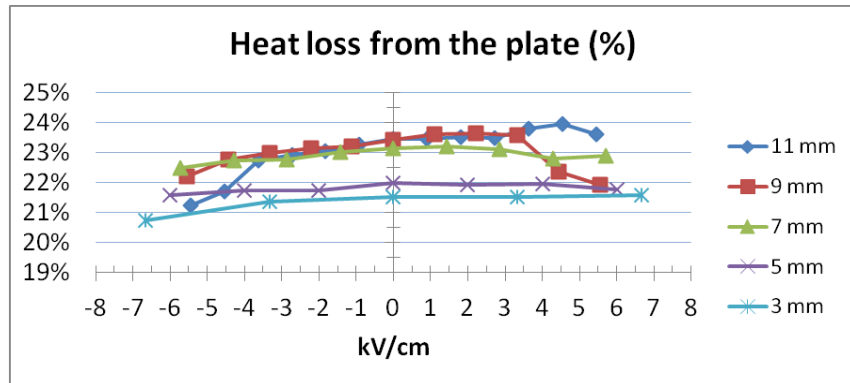
Fig. 5-29 The heat losses from the plate with electric field at different heights

Figure 5-29 conveys the information that the total heat loss is not affected by the electric field near quenching, i.e., for cases below 9 mm. It is clear from Figure 5-23, however, that the temperature profile does change with field so it must be that the electric field is affecting the distribution of heat flux rather than its overall value. To quantify this situation involves the radial analysis of heat loss, as shown in Figure 5-30. There are six rings mapped from the hottest spot, these six rings are different percentages of the total heat losses from the plate and we study how the heat flux change between these cases. A series of results are shown in Figure 5-31a to 5-31f from 80% to 20% of the heat loss. The overall heat flux intensity is growing as the rings move toward the hottest center. The heat flux loss varies under electric field control at 80% to 50% of heat loss or around 400 to 700 watts per meter square, 40% is around 800-900, 30% is around 1000-1100, and 20% can be high up to 1400 W/m^2. These results show that the electric field is capable of changing the concentration of the flux rather than the total transferred. In hindsight this is

reasonable since the plate is much larger than the flame allowing substantial time for the heat to transfer. The result might be far different for a small target. Figure 5-32 profiles true sizes of heat flux mapping with these six rings; the negative electric field spreads out the heat while the positive field concentrates the heat at the center. A close look of the 20% heat loss (Figure 5-33) normalized by the heat flux at zero-field at each height shows how the electric field changes the heat flux between plate locations. It has strong effect at 11 mm and less effect at lower locations when the plate starts quenching the flame and changing its shape. The 3 mm case is complex since the plate is very low affecting both the heat release and combustion and the heat transfer; further study is needed to fully understand the processes involved for this case[102].
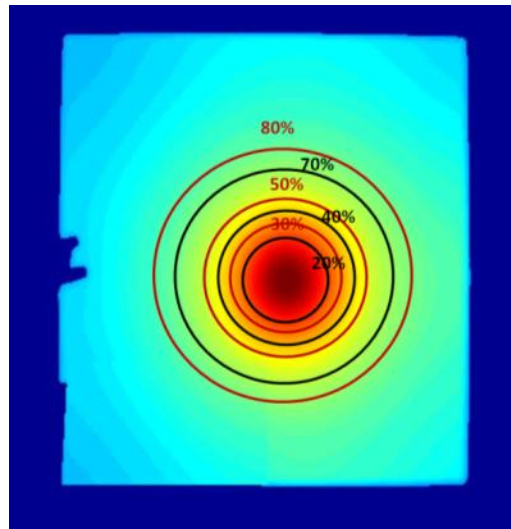
Fig. 5-30 Analyzing the heat map with different percentage rings from heat losses
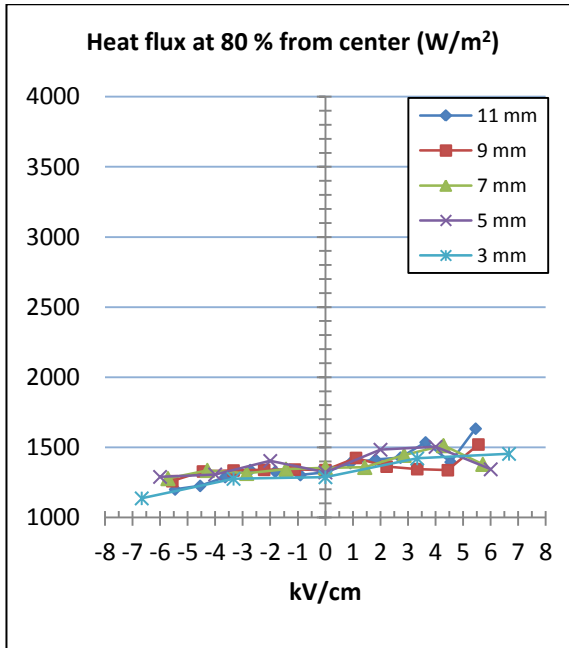
(a) Heat flux at 80% heat loss
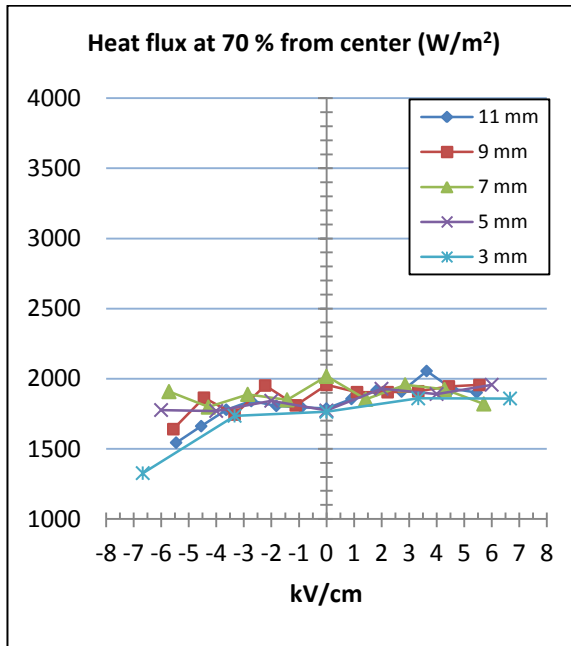
(b) Heat flux at 70% heat loss
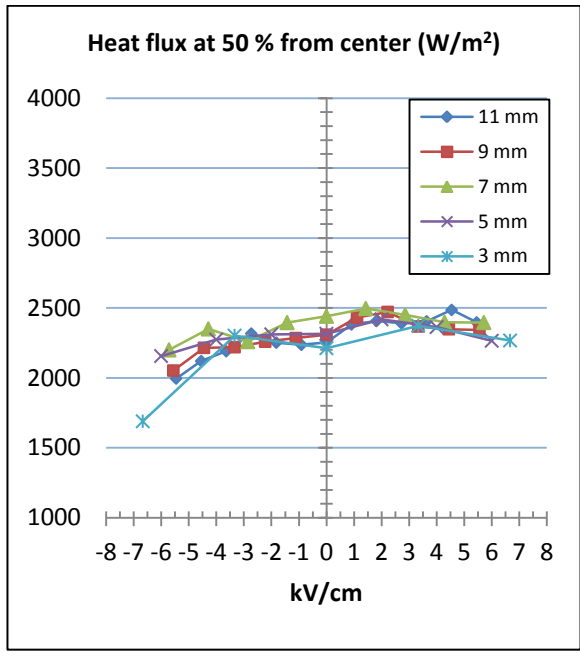
(c) Heat flux at 50% heat loss
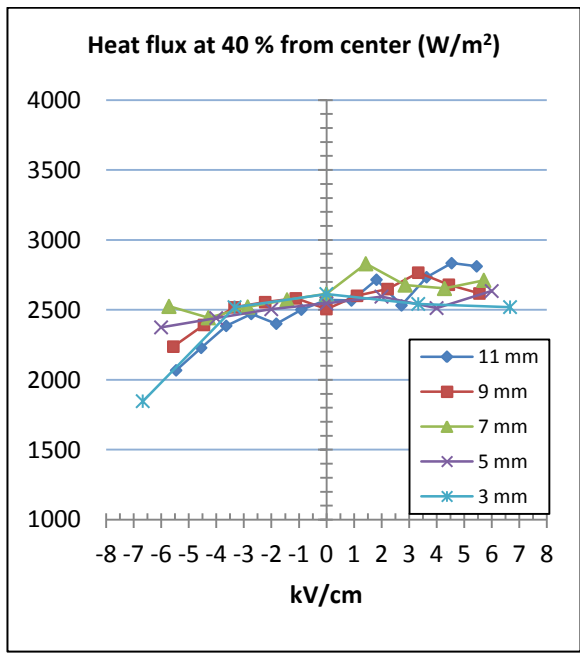
(d) Heat flux at 40% heat loss
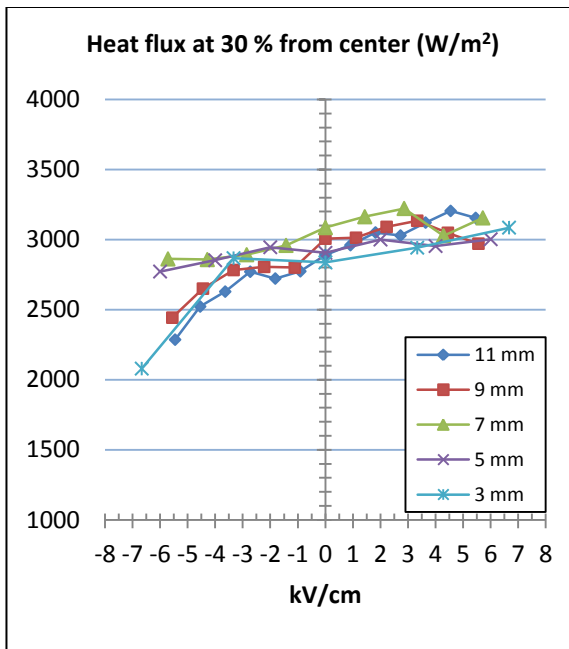
(e) Heat flux at 30% heat loss
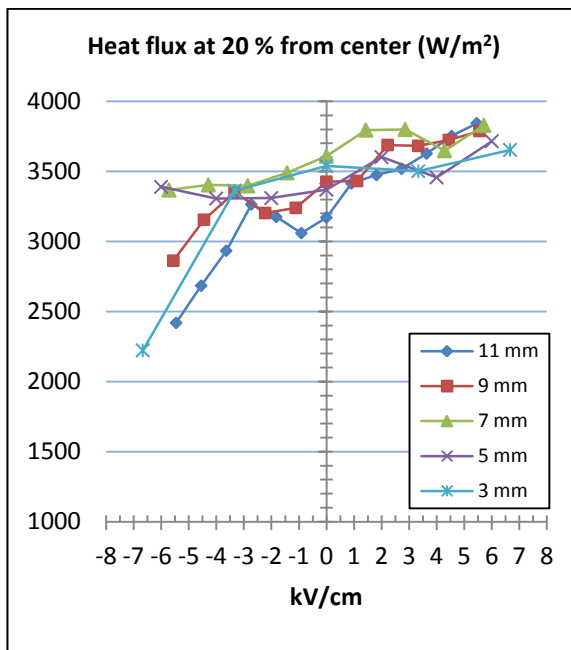
(f) Heat flux at 20% heat loss

Fig. 5-31 The heat flux at different heat losses in percentages with electric field effect
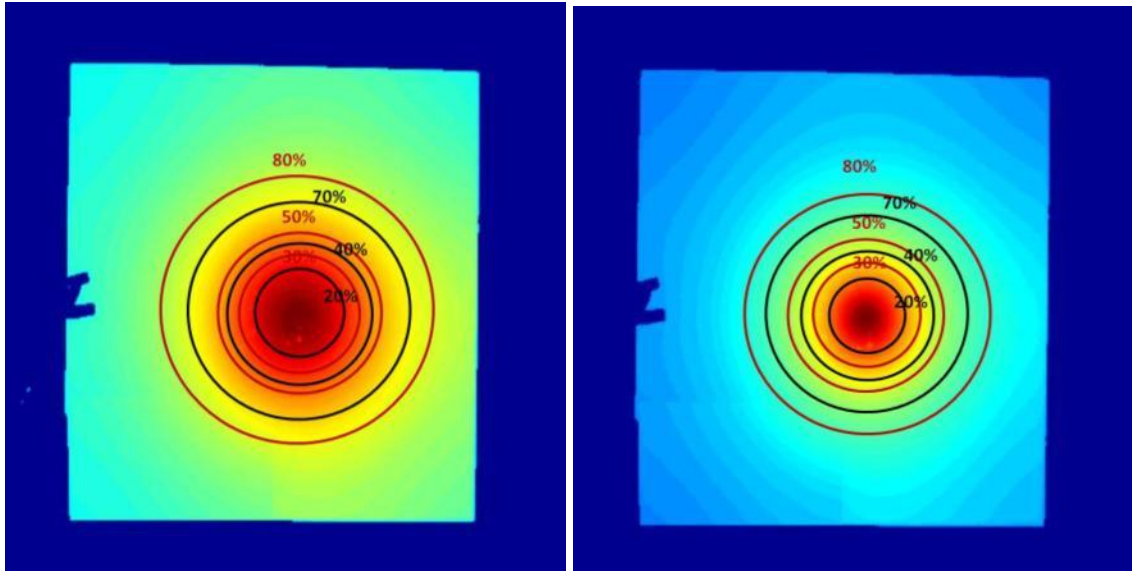
(a) -5.6kV/cm   (b) 5.6kV/cm

Fig. 5-32 The heat map with 20%-80% of total heat losses with different field at 9 mm
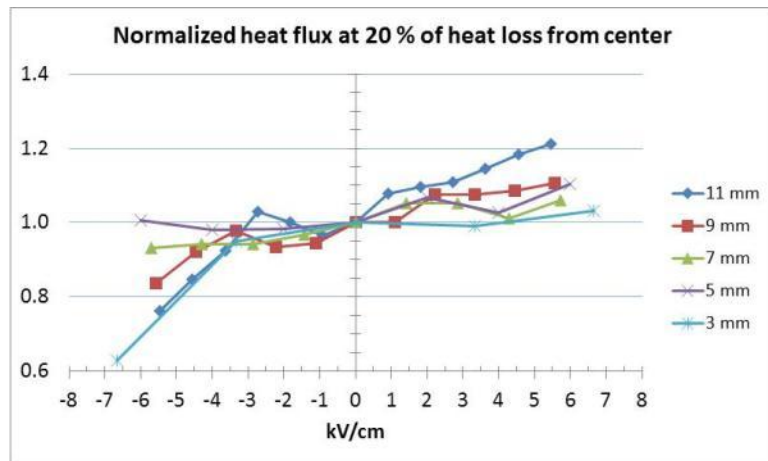
Fig. 5-33 Normalized heat flux at zero field at 20% of heat loss

Since 20% of total heat loss occurs from a disk around 9-12 mm in radius from the hottest spot. It is interesting to have a further look at smaller rings from 5-10mm as shown in Figure 5-34a. The 11 mm plate height is used because it shows the largest effects from the electric field in comparison with other heights. Not surprisingly, for a centered flame source, the results show the smaller the ring, the higher the heat flux. The heat flux under the negative field shows smaller changes than occur in the positive field. The results for the radii 5 and 7 mm are distinguishable from each other for different quenching heights, which are shown in Figure 5-34b and 5-34c, and so these heat fluxes are used as characteristics of heat flux focus. As the plate is lowered from 11 mm to 7 mm the heat flux variation is changed from around 52% at 11mm to 23-32% at 7mm. The heat flux variation is below 20% when the plate is below 5 mm in height. The fluctuations within the curve are obvious at different electric field conditions for the same height; this occurs because the rings are within the most concentrated region so small changes lead to large effects.
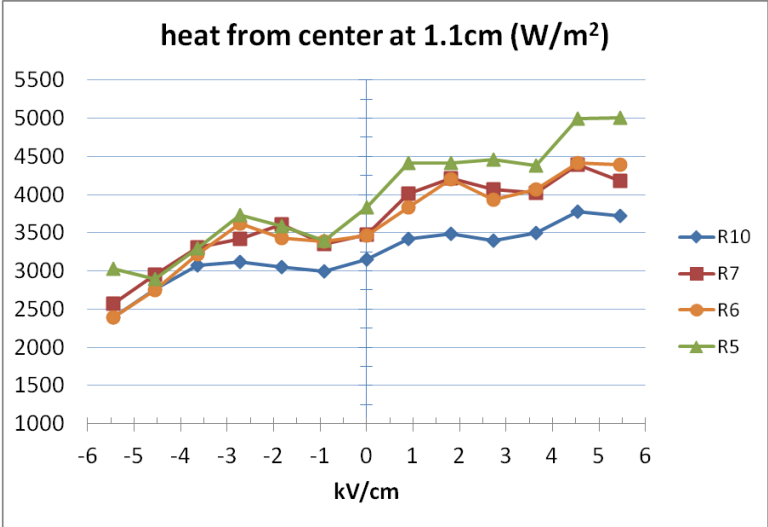
(a) Heat flux at 11mm with different radius

(b) at radius 7 mm

Heat flux at R5 from center
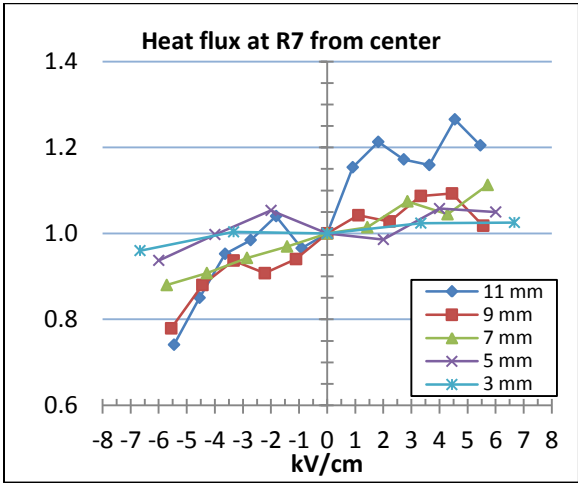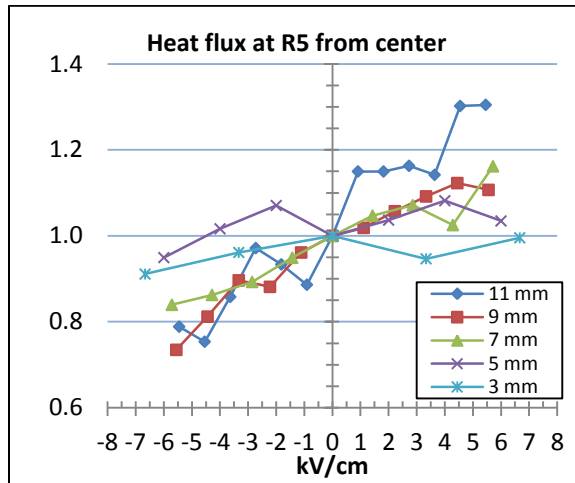
(c) at radius 5 mm

Fig. 5-34 Heat flux changes with electric field in radius

5.4.2.5 Thermal analysis summary

Figure 5-35 is the trend of an integrated overall heat flux at different heat losses in percentages with electric fields from Figure 5-30 with various plate-to-burner distance. The temperature and heat transfer over a quenching plate with the effect from electric field flames is investigated with the maximum electric field that can be applied without breakdown. The plate shows a broadened and lower peak temperature for the negative field (i.e., for a downward ion driven wind) and the opposite effects for the positive field and upward directed wind. The overall heat flux to the plate is not particularly sensitive to the electric field but the level of heat focusing on the plate is changing with the electric field. For the region responsible for 20% of the heat loss from the plate, the heat flux increases from 2400 W/m^2 up to 3800 W/m^2 at 11 mm with the addition of the field. Similar phenomenon can be observed during quenching though these changes are not as

significant as in the case before quenching. Further exploration is required to understand the heat propagation and distribution on the bottom side of the plate.
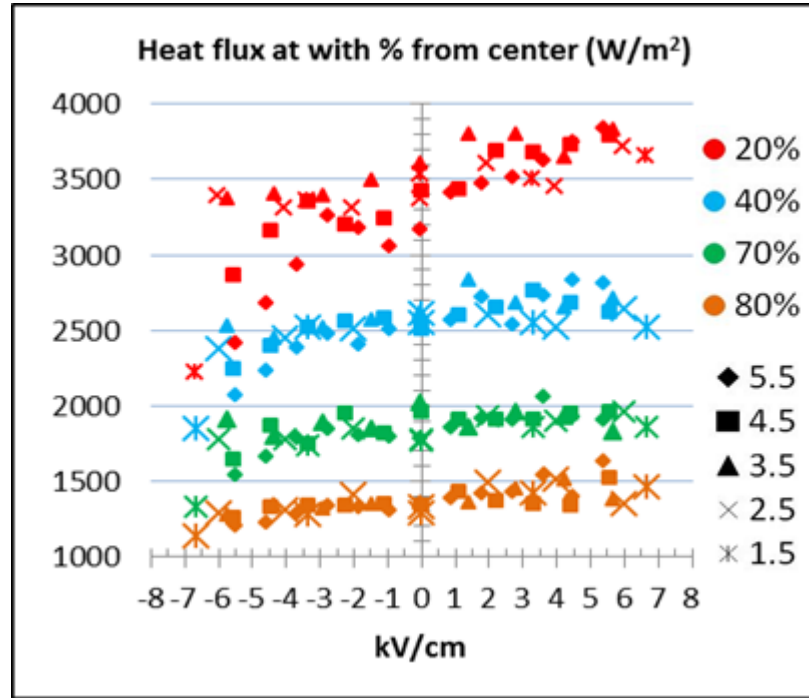
Fig. 5-35 Integrated heat flux at different heat losses in percentages with electric field effect trend from 5-28 with plate-to-burner distance

As one piece of additional insight, the Schlieren image, Figure 5-6, of the hot gas around the flame impinging on the plate demonstrated that part of the insensitivity of the heat flux to the electric field is because the thermal plume is far larger than the flame, and so the field has less dominance on it, while the near flame core is affected substantially by the field.

5.6 INVERSE JET EFIELD FLAME

Prior studies have shown that the body force produced by an electric field is comparable in these small flames to the body force associated with buoyancy[19,21,66]. This fact is one of the principal reasons for the microgravity E-FIELD Flames study as part of NASA's ACME project described earlier so that the confounding influences of buoyancy can be eliminated. In order to show how buoyancy can qualitatively affect the kinds of outcomes described above, a photographic study of the coflow flame in the inverted configuration was completed. One of the largest effects of this flame inversion (and flip of the buoyant force) appears in the sooting aspects of the flame. Electric field influences on sooting flames are very difficult to unravel since the soot can act as a charge emitter. These results help show the importance of microgravity study to determine the fundamental potential of electric fields to control flames near surfaces.

The photograph of an inverted flame under the influence of an electric field is shown in Figure 5-36. When there is no electric field applied over the flame, it is observed that the soot generated in the post combustion zone is buoyed upward into the flame, as shown in H/D=6.5 and 5.5 most obviously. When the impinging plate starts to interfere with the flame and the two sides of the reaction wings start attaching over the plate at H/D=4.5, the amount of soot carried by buoyancy back into the flame is reduced. At H/D below 3.5 cases, there is no soot observed in the flame.

Interestingly with a negative field at H/D above 4.5 cases, the soot moves through the openings between the two strong reaction wings. With increasing field, the soot is driven back into the flame jet center because the stronger downward directed ion wind

changes the flame reaction zones which became more concentrated and close to each other. Therefore, at the limit negative electric field condition, soot does not have the chance to escape back into the post jet region. In the positive field case at H/D=5.5 and 6.5 distances, the soot sits inside the flame jet region until the neutral buoyant force reaches its balance; since the ion wind is directed upward the flame reaction zone changes upward in location[5,19,66]. Similar to the no field observation, at the H/D=3.5 and lower cases in both field directions, and positive field direction at H/D=4.5, there is no soot buoyant phenomenon. Research has shown that the ion generation in diffusion flames has no relation to soot even with the increasing of carbons[12]. This means that the variation in the flame shape and soot behavior results from the change in buoyancy driven wind as compared to the case where the flame is in the upright condition. This is just a proof-of-concept study to motivate future microgravity experiments since any changes in the heat flux and CO release behavior will be orientation dependent. The findings and understanding of the upright flame are not affected by this difference.
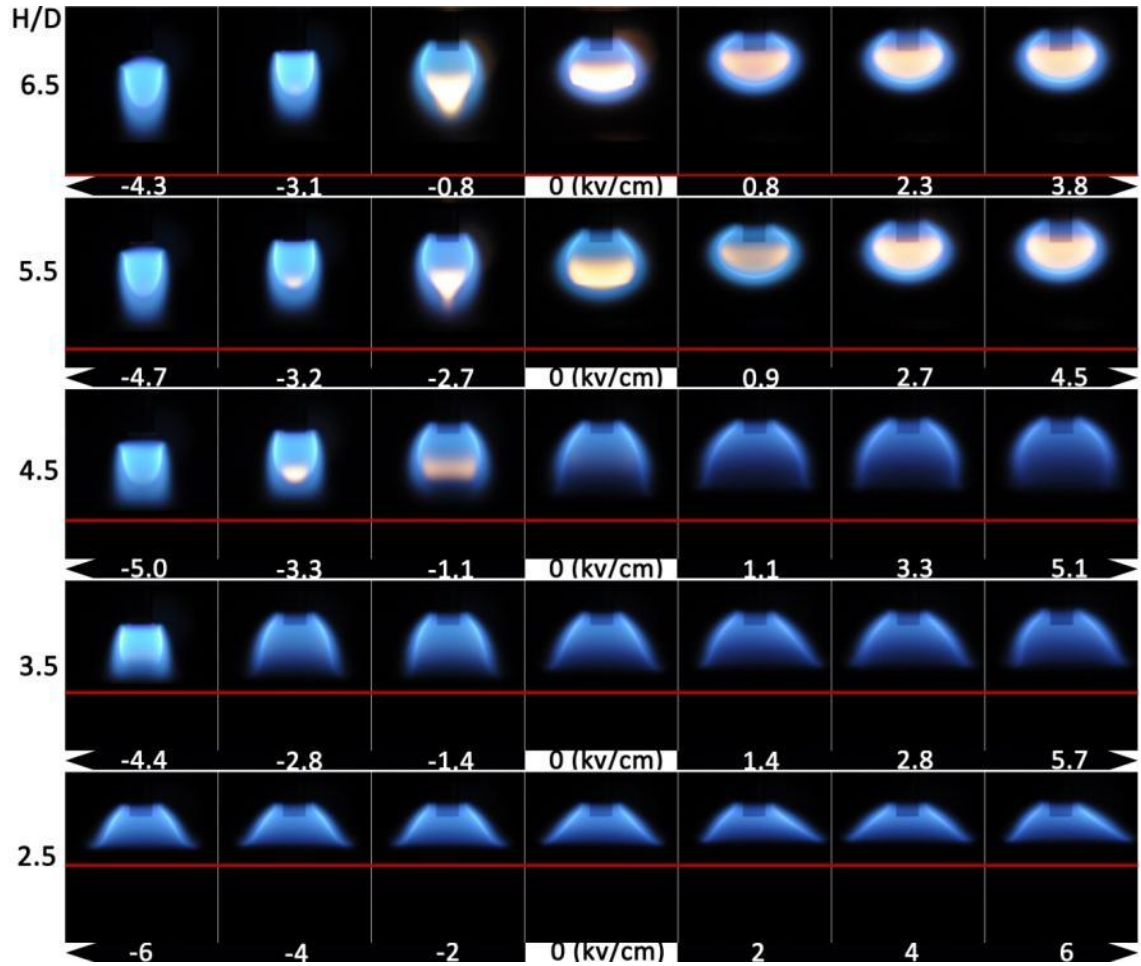
Fig. 5-36 The overall inverted jet photograph with electric field applied and different

plate-to-burner distance.

H/D							
6.5	-4.3	-3.1	-0.8	0 (kv/cm)	0.8	2.3	3.8
5.5	-4.7	-3.2	-2.7	0 (kv/cm)	0.9	2.7	4.5
4.5	-5.0	-3.3	-1.1	0 (kv/cm)	1.1	3.3	5.1
3.5	-4.4	-2.8	-1.4	0 (kv/cm)	1.4	2.8	5.7
2.5	-6	-4	-2	0 (kv/cm)	2	4	6
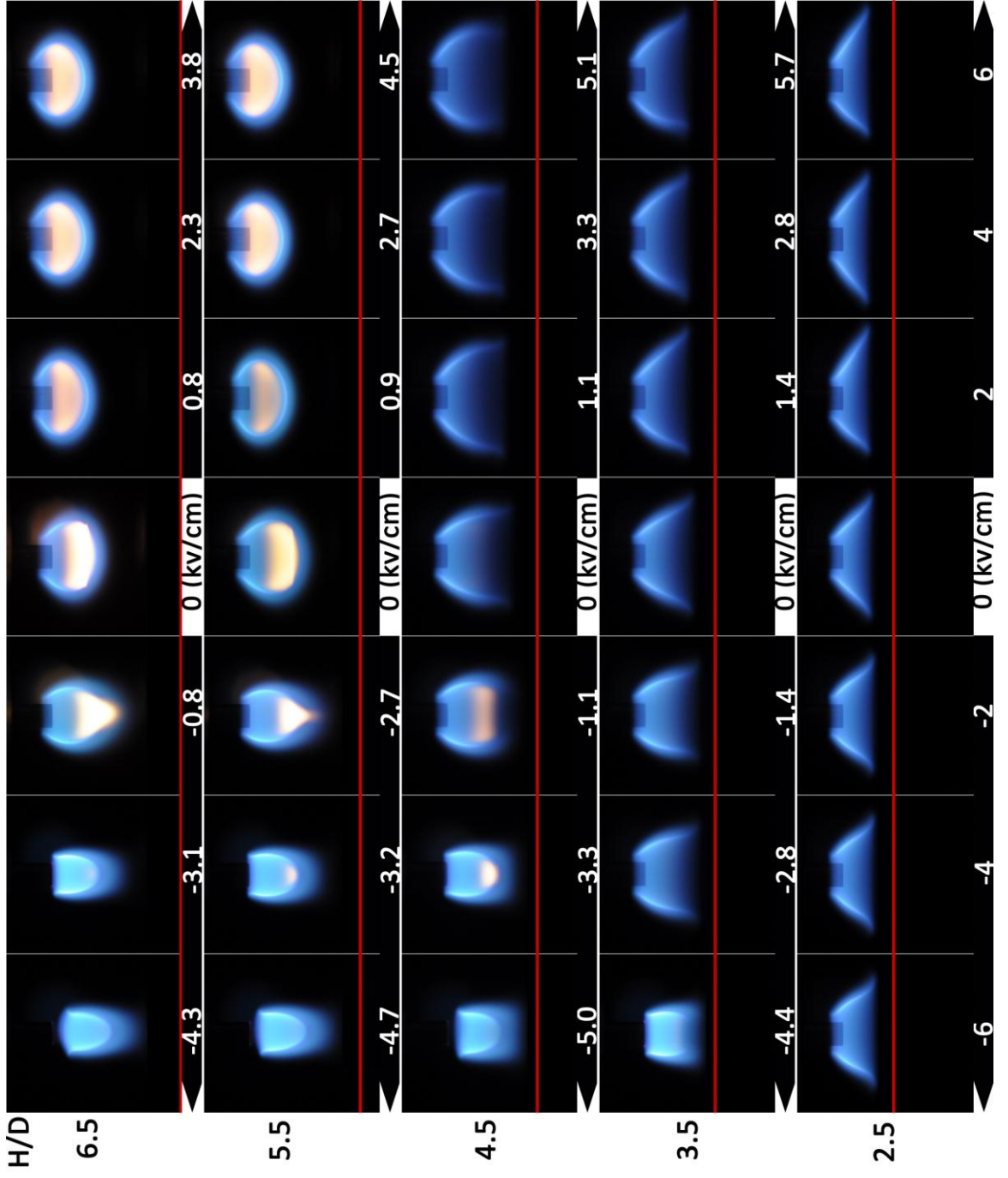
Chapter 6

Conclusions and Recommendations

This dissertation investigates the electric field flame response on a flame near an impinging surface. The research is accomplished using methane as the fuel under the conditions of a laminar coflow diffusion flame. The close distance impingement evaluation includes identifying flame reaction geometry, flow field geometry, ion current measurements, carbon monoxide emission measurements, and heat flux measurements, along with a brief evaluation of inverted jet geometry to determine the relative influence of gravity-driven buoyancy. The specific findings are as follows:

1. Because the flame response time can be the controlling factor, there are conditions where a slower responding power supply can provide reliable performance in an electrically actuated flame system. In particular, these conditions include steady averaged VCC sweeps and step changes between saturated ion current conditions. Economical designs, which may involve removing active current sinking components, can

compromise a power supply's ability to respond on the millisecond time scales that have made the electric actuation of flames a unique approach to combustion sensing and control. For flame-generated chemi-ion current measurements (nano/microamp), the performances of low-cost high-voltage power supplies characteristics are suitable in sensitive environments. These findings will certainly contribute to more effective use of the data to be obtained during the International Space Station ACME experiments but because the focus of this dissertation is on steady-state behavior, the temporal response of the power supply is not critical.

2. Carbon monoxide release from the impinging electric field actuated flame has a strong relationship with the amount of oxidant entrainment near the reaction zone and the reaction zone geometry. A combined schlieren image with OH* and OH location (Figure 6-1) shows that the OH sits inside the thermal flame jet plume. Electric field application in the negative field direction leads to a downward ion wind which causes the impinging flame tip to open. Some of the carbon monoxide in the stagnation region inside the OH layer then escapes along the wall in the boundary layer while some oxidizes with the nearby OH. The upward ion wind entrains more air into the reaction when the field is in the positive direction. In this case, the carbon monoxide in the stagnation flow region has to pass through more of the OH cloud as it leaves the reaction zone. With oxidation, carbon monoxide decreases. At lower

relative flame to plate distance H/D, the amount of CO escaping from the viscous region is competing with the amount of CO reacting with OH because the flame jet has a decoupling effect with the stagnation region. Further measurement on CO emission release rate (and perhaps in situ measurements of CO concentration in the flame) will help identify the relationships.

3. The shape and orientation of the reaction zone affects the way that the flame impinges on the surface, thereby affecting the resulting heat flux. Schlieren imaging of the thermal plume and flow field, combined with OH thermometry, Figure 6-2, shows that the flame temperature is approximately the same at different impinging distance. This shows that the plate does not substantially cool the flame peak temperature but instead affects the overall reaction behavior by spatially disturbing the jet flame.

4. The level of heat flux concentration can be improved by electric field actuation of the flame, and the field can also possibly reduce CO emission. The temperature gradient location from the stagnation region to flow boundary region changes not only with the impinging height but also with electric field. The heat flux increases dramatically in the positive field direction, and, at the same time, the measured quantitative carbon monoxide concentration has a decreasing trend at specific impinging distance (H/D <3.5). Because the level of CO generation

depends on impinging distance, locating the impinging plate at larger distance and applying a positive field can achieve very similar heat flux as occurs naturally at a lower burner to plate distance. For example, the impinging plate at H/D=4.5 with 2kv/cm and H/D=3.5 and no field have comparable heat flux (at 20%), but the carbon monoxide is more than approximately 2.4 times greater at the lower H/D and no field case. Additional tests by changing the impinging surface geometry and design can help quantify the electric field effect on heat flux and carbon monoxide release more generally.
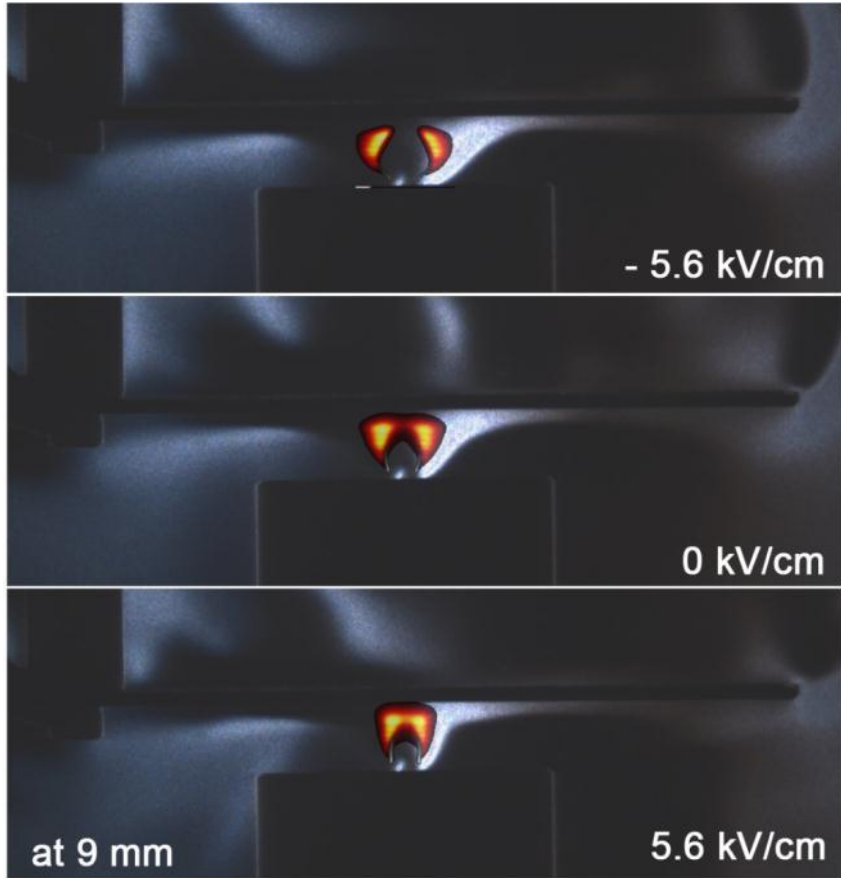
(a) Over all flow field view
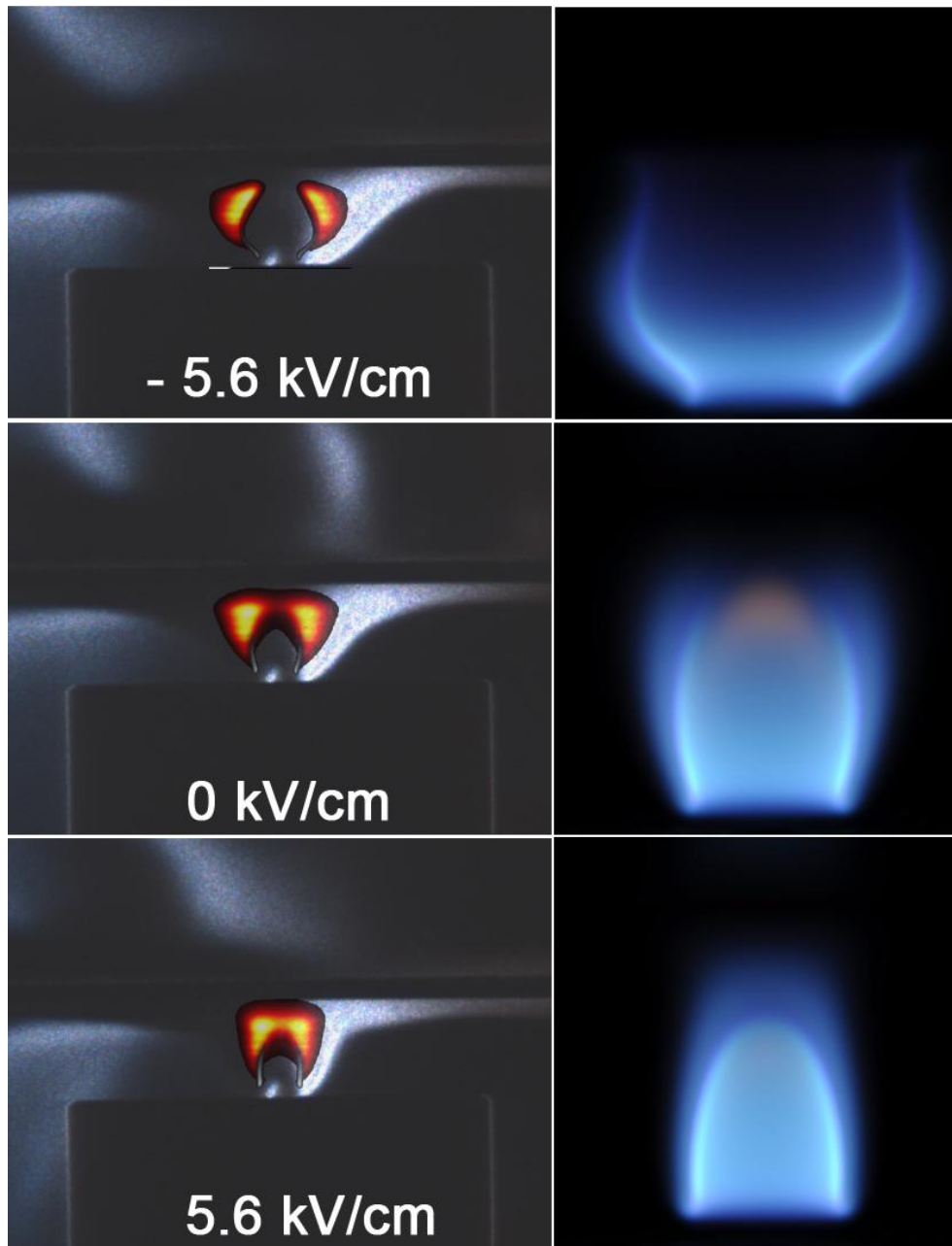
(b) A closer view with real flame images

Fig. 6-1 Schlieren image with OH* and OH.
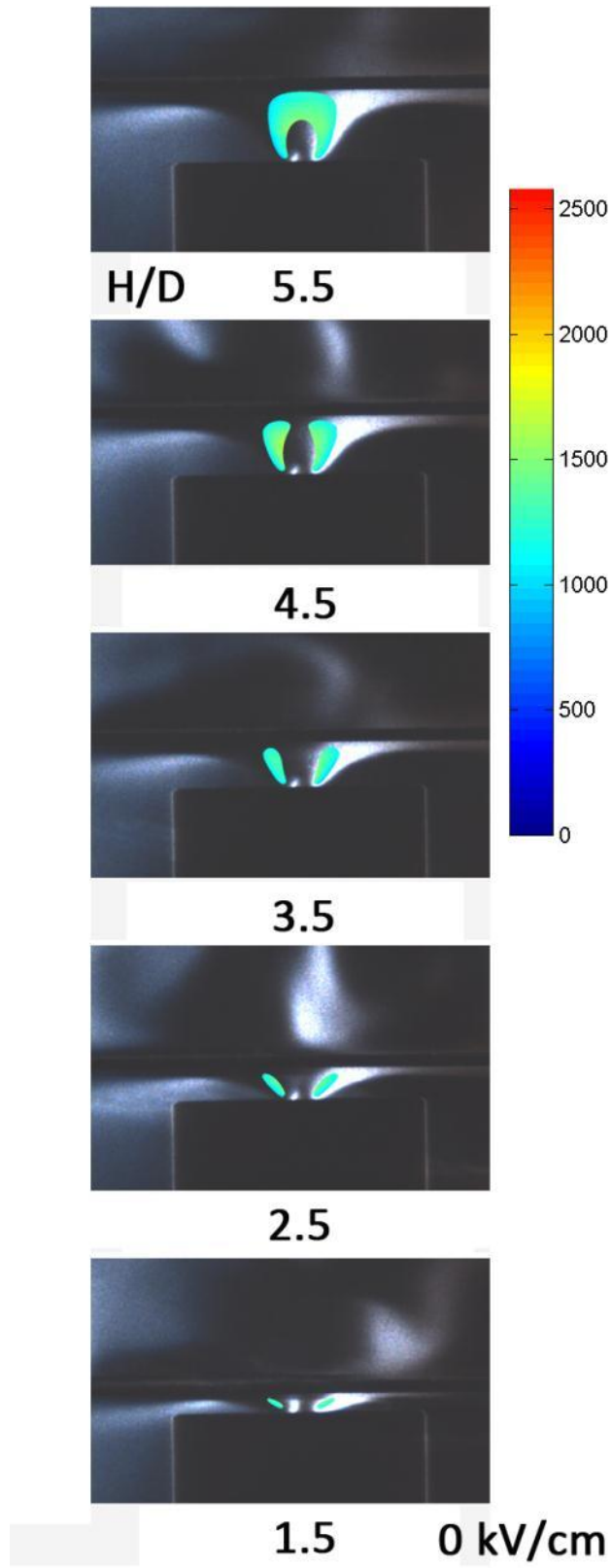
Fig. 6-2 Schlieren image with OH thermometry.

Recommendations

Impinging flames are used in home gas stoves, water heaters, furnaces, as well as in a wide range of industrial processes, for example as shown for metal treatment in Figure 6-3[10]. Based on the results in this dissertation, the possible application of electric fields to reduce carbon monoxide and enhance heat transfer/heat flux to surfaces can be further related and explored. By using the electric field, the heat flux and heat concentration on plates can be improved. Therefore, with a well-designed flame geometry at specific impinging distance, the heat transfer can be altered and enhanced by simply controlling the electric field. At the same time it may be possible to reduce the amount of carbon monoxide generation, which can create a safer flame impingement environment.
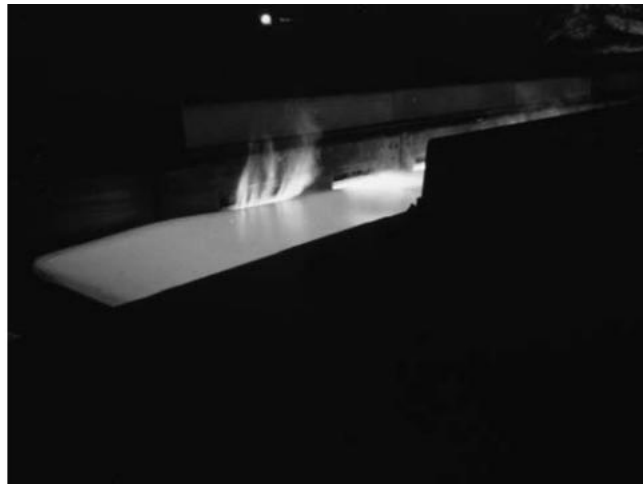
Fig. 6-3 Metal strip heating by an impinging flame[10].

A soot reduction phenomenon is observed in some of the flame images, Figure 3-8, at the specific burner to plate distance when the flame tip is not disturbed by the impinging plate. At H/D=5.5 the soot around the flame tip can be eliminated when the

electric field is applied at -5.5 kV/cm. This possible soot reduction mechanism when electric fields are applied can be further investigated. It is important to keep in mind, however, that the influence of the electric field as an actuator in combustion is a relatively subtle one that relies on very distinct regimes where small changes to the flame at its initiation have larger influences downstream in the reaction. Electrical properties of impinging flames appear to have broader potential as a sensor indicating flame behavior even when surfaces are relatively distant, and this is another subject for further research.

Bibliography

[1]   Y.C. Chien, Development of a Chemiluminescence Diagnostic System for Combustion Measurements, National Cheng Kung University Department of Aeronautics & Astronautics, 2007. http://etds.lib.ncku.edu.tw/etdservice/view_metadata?etdun=U0026-0812200913581686.

[2]   Climate change in the Arctic, Wikipedia, the Free Encyclopedia. (2012). http://en.wikipedia.org/w/index.php?title=Climate_change_in_the_Arctic&oldid=526101414 (accessed December 9, 2012).

[3]   Global warming, Wikipedia, the Free Encyclopedia. (2012). http://en.wikipedia.org/w/index.php?title=Global_warming&oldid=527030771 (accessed December 9, 2012).

[4]   D. Dunn-Rankin, F. Weinberg, Yuan, Z.G., Stocker, D., Electric field control of flames_ Science Requiments Document, (n.d.).

[5]   M. Papac, Electrical aspects of gaseous fuel flames for microgravity combustion, 2005.

[6]   S. Karnani, Electric field-driven flame dynamics, University of California, Irvine, 2011.

[7]   Carbon monoxide poisoning, Wikipedia, the Free Encyclopedia. (2012).

[8]   Smoke Inhalation Symptoms, (n.d.). http://www.emedicinehealth.com/smoke_inhalation/page3_em.htm.

[9]   Combustion incompletion, Wikipedia, the Free Encyclopedia. (n.d.). http://en.wikipedia.org/wiki/Combustion#Incomplete.

[10] C.E. Baukal, Industrial Combustion Testing, 1st ed., CRC Press, 2010.

[11] Carbon monoxide poisoning, (n.d.). http://en.wikipedia.org/wiki/Carbon_monoxide_poisoning.

[12] J. Lawton, F.J. Weinberg, Electrical Aspects of Combustion, Oxford University Press, 1970.

[13] R.M. Fristrom, A.A. Westenberg, Flame structure, McGraw-Hill, 1965.

[14] H.A. Wilson, The electrical properties of flames: and of incandescent solids, University of London press, ltd., 1912.

[15] T. Pedersen, R.C. Brown, Simulation of electric field effects in premixed methane flames, Combustion and Flame. 94 (1993) 433–448. doi:10.1016/0010-2180(93)90125-M.

[16] F.J. Weinberg, D. Dunn-Rankin, F.B. Carleton, S. Karnani, C. Markides, M. Zhai, Electrical aspects of flame quenching, Proceedings of the Combustion Institute. 34 (2013) 3295–3301. doi:10.1016/j.proci.2012.07.007.

[17] A.P. Chattock, On the electrification needle-points of air, Philosophical Magazine. (1891) 285.

[18] J. Josh, Quantitative Chemiluminescence from Small Diffusion Flames, 2012.

[19] M.J. Papac, D. Dunn-Rankin, Canceling Buoyancy of Gaseous Fuel Flames in a Gravitational Environment Using an Ion-Driven Wind, Annals of the New York Academy of Sciences. 1077 (2006) 585–601. doi:10.1196/annals.1362.038.

[20] S. Karnani, D. Dunn-Rankin, F. Takahashi, Z.-G. Yuan, D. Stocker, Simulating Gravity in Microgravity Combustion Using Electric Fields, Combustion Science and Technology. 184 (2012) 1891–1902. doi:10.1080/00102202.2012.694740.

[21] B.A. Strayer, J.D. Posner, D. Dunn-Rankin, F.J. Weinberg, Simulating microgravity in small diffusion flames by using electric fields to counterbalance natural convection, Proc. R. Soc. Lond. A. 458 (2002) 1151–1166. doi:10.1098/rspa.2001.0929.

[22] E.N. Volkov, V.N. Kornilov, L.P.H. de Goey, Experimental evaluation of DC electric field effect on the thermoacoustic behaviour of flat premixed flames, Proceedings of the Combustion Institute. 34 (2013) 955–962. doi:10.1016/j.proci.2012.06.175.

[23] E.V. Vega, S.S. Shin, K.Y. Lee, NO emission of oxygen-enriched CH4/O2/N2 premixed flames under electric field, Fuel. 86 (2007) 512–519. doi:10.1016/j.fuel.2006.07.034.

[24] F.J. Weinberg, Advanced combustion methods, Academic Press Inc.,Orlando, FL, 1986.

[25] A. Sakhrieh, G. Lins, F. Dinkelacker, T. Hammer, A. Leipertz, D.W. Branston, The influence of pressure on the control of premixed turbulent flames using an electric field, Combustion and Flame. 143 (2005) 313–322. doi:10.1016/j.combustflame.2005.06.009.

[26] F. Altendorfner, J. Kuhl, L. Zigan, A. Leipertz, Study of the influence of electric fields on flames using planar LIF and PIV techniques, Proceedings of the Combustion Institute. 33 (2011) 3195–3201. doi:10.1016/j.proci.2010.05.112.

[27] J. Kuhl, G. Jovicic, L. Zigan, A. Leipertz, Transient electric field response of laminar premixed flames, Proceedings of the Combustion Institute. 34 (2013) 3303–3310. doi:10.1016/j.proci.2012.07.016.

[28] J. Schmidt, S. Kostka, A. Lynch, B. Ganguly, Simultaneous particle image velocimetry and chemiluminescence visualization of millisecond-pulsed current–

voltage-induced perturbations of a premixed propane/air flame, Exp Fluids. 51 (2011) 657–665. doi:10.1007/s00348-011-1078-2.

[29] K. Yamashita, S. Karnani, D. Dunn-Rankin, Numerical prediction of ion current from a small methane jet flame, Combustion and Flame. 156 (2009) 1227–1233. doi:10.1016/j.combustflame.2009.02.002.

[30] D.. Mishra, Emission studies of impinging premixed flames, Fuel. 83 (2004) 1743–1748. doi:10.1016/j.fuel.2004.02.019.

[31] K.N.C.B. Y. Zhang, Characterization of impinging jet flames, Combustion and Flame - COMBUST FLAME. 116 (1999) 671–674. doi:10.1016/S0010-2180(98)00084-4.

[32] T.K. Ng, C.W. Leung, C.S. Cheung, Experimental investigation on the heat transfer of an impinging inverse diffusion flame, International Journal of Heat and Mass Transfer. 50 (2007) 3366–3375. doi:10.1016/j.ijheatmasstransfer.2007.01.046.

[33] L.L. Dong, C.S. Cheung, C.W. Leung, Characterization of impingement region from an impinging inverse diffusion flame jet, International Journal of Heat and Mass Transfer. 56 (2013) 360–369. doi:10.1016/j.ijheatmasstransfer.2012.08.064.

[34] N. Zuckerman, N. Lior, Jet Impingement Heat Transfer: Physics, Correlations, and Numerical Modeling, in: J.P.H., Avram Bar-Cohen and Young I. Cho George A. Greene (Ed.), Advances in Heat Transfer, Elsevier, 2006: pp. 565–631. http://www.sciencedirect.com/science/article/pii/S0065271706390065 (accessed February 11, 2014).

[35] R. Viskanta, Heat transfer to impinging isothermal gas and flame jets, Experimental Thermal and Fluid Science. 6 (1993) 111–134. doi:10.1016/0894-1777(93)90022-B.

[36] S.H. Kang, R. Greif, Flow and heat transfer to a circular cylinder with a hot impinging air jet, International Journal of Heat and Mass Transfer. 35 (1992) 2173–2183. doi:10.1016/0017-9310(92)90061-V.

[37] M.F.G. Cremers, M.J. Remie, K.R.A.M. Schreel, L.P.H. de Goey, Thermochemical heat release of laminar stagnation flames of fuel and oxygen, International Journal of Heat and Mass Transfer. 53 (2010) 952–961. doi:10.1016/j.ijheatmasstransfer.2009.11.025.

[38] L.L. Dong, C.S. Cheung, C.W. Leung, Heat transfer characteristics of an impinging inverse diffusion flame jet. Part II: Impinging flame structure and impingement heat transfer, International Journal of Heat and Mass Transfer. 50 (2007) 5124–5138. doi:10.1016/j.ijheatmasstransfer.2007.07.017.

[39] Z. Zhao, T.T. Wong, C.W. Leung, Impinging premixed butane/air circular laminar flame jet—influence of impingement plate on heat transfer characteristics, International Journal of Heat and Mass Transfer. 47 (2004) 5021–5031. doi:10.1016/j.ijheatmasstransfer.2004.06.022.

[40] M.J. Remie, M.F.G. Cremers, K.R.A.M. Schreel, L.P.H. de Goey, Analysis of the heat transfer of an impinging laminar flame jet, International Journal of Heat and

Mass Transfer. 50 (2007) 2816–2827.
doi:10.1016/j.ijheatmasstransfer.2006.10.053.

[41] T.H. Vandermeer, Heat transfer from impinging flame jets, Ph.D. Thesis Technische Hogeschool, Delft (Netherlands). (1987). http://adsabs.harvard.edu/abs/1987PhDT........19V (accessed February 12, 2014).

[42] M.J. Remie, G. Särner, M.F.G. Cremers, A. Omrane, K.R.A.M. Schreel, M. Aldén, et al., Extended heat-transfer relation for an impinging laminar flame jet to a flat plate, International Journal of Heat and Mass Transfer. 51 (2008) 1854–1865. doi:10.1016/j.ijheatmasstransfer.2007.06.042.

[43] M. (Martin) Remie, Heat transfer of oxy-fuel flames to glass, info:eu-repo/semantics/doctoralthesis, Technische Universiteit Eindhoven, 2007.

[44] H. Martin, Heat and Mass Transfer between Impinging Gas Jets and Solid Surfaces, in: James P. Hartnett and Thomas F. Irvine (Ed.), Advances in Heat Transfer, Elsevier, 1977: pp. 1–60. http://www.sciencedirect.com/science/article/pii/S0065271708702211 (accessed December 5, 2014).

[45] I.G. Currie, Fundamental Mechanics of Fluids, Fourth Edition, CRC Press, 2012.

[46] A. Milson, N.A. Chigier, Studies of methane and methane-air flames impinging on a cold plate, Combustion and Flame. 21 (1973) 295–305. doi:10.1016/S0010-2180(73)80052-5.

[47] A.C. Eckbreth, Laser Diagnostics for Combustion Temperature and Species, CRC Press, 1996.

[48] S.B. Gupta, B.P. Bihari, M.S. Biruduganti, R.R. Sekar, J. Zigan, On use of chemiluminescence for combustion metrics in natural gas fired reciprocating engines, Proceedings of the Combustion Institute. 33 (2011) 3131–3139. doi:10.1016/j.proci.2010.05.032.

[49] A.M.H.H. Verhasselt, Experimental evaluation of an electric field as actuator in thermoacoustic control, 2007.

[50] J.W. Daily, Saturation effects in laser induced fluorescence spectroscopy, Appl. Opt. 16 (1977) 568–571. doi:10.1364/AO.16.000568.

[51] D. Stepowski, M.J. Cottereau, Direct measurement of OH local concentration in a flame from the fluorescence induced by a single laser pulse, Appl. Opt. 18 (1979) 354–356. doi:10.1364/AO.18.000354.

[52] G. Kychakoff, R.D. Howe, R.K. Hanson, J.C. McDaniel, Quantitative visualization of combustion species in a plane, Appl. Opt. 21 (1982) 3225–3227. doi:10.1364/AO.21.003225.

[53] M. Aldén, H. Edner, G. Holmstedt, S. Svanberg, T. Högberg, Single-pulse laser-induced OH fluorescence in an atmospheric flame, spatially resolved with a diode array detector, Appl. Opt. 21 (1982) 1236–1240. doi:10.1364/AO.21.001236.

[54] L. Ma, W. Cai, Numerical investigation of hyperspectral tomography for simultaneous temperature and concentration imaging, Appl. Opt. 47 (2008) 3751–3759. doi:10.1364/AO.47.003751.

[55] W. Ren, D.F. Davidson, R.K. Hanson, IR laser absorption diagnostic for C2H4 in shock tube kinetics studies, International Journal of Chemical Kinetics. 44 (2012) 423–432. doi:10.1002/kin.20599.

[56] K.B. Chung, F.C. Gouldin, G.J. Wolga, Experimental reconstruction of the spatial density distribution of a nonreacting flow with a small number of absorption measurements, Appl. Opt. 34 (1995) 5492–5500. doi:10.1364/AO.34.005492.

[57] C.J. Dasch, One-dimensional tomography: a comparison of Abel, onion-peeling, and filtered backprojection methods, Appl. Opt. 31 (1992) 1146–1152. doi:10.1364/AO.31.001146.

[58] ZOLO Technologies, Overview of the ZoloBOSS applications and benefits, (n.d.). http://zolotech.com/.

[59] S.H. Pyun, W. Ren, K.-Y. Lam, D.F. Davidson, R.K. Hanson, Shock tube measurements of methane, ethylene and carbon monoxide time-histories in DME pyrolysis, Combustion and Flame. 160 (2013) 747–754. doi:10.1016/j.combustflame.2012.12.004.

[60] J. Vanderover, M.A. Oehlschlaeger, A mid-infrared scanned-wavelength laser absorption sensor for carbon monoxide and temperature measurements from 900 to 4000 K, Appl. Phys. B. 99 (2010) 353–362. doi:10.1007/s00340-009-3849-5.

[61] J. Vanderover, W. Wang, M.A. Oehlschlaeger, A carbon monoxide and thermometry sensor based on mid-IR quantum-cascade laser wavelength-modulation absorption spectroscopy, Appl. Phys. B. 103 (2011) 959–966. doi:10.1007/s00340-011-4570-8.

[62] A. Karpf, G.N. Rao, Enhancement of trace gas detection by integrating wavelength modulated spectra across multiple lines, Appl. Opt. 49 (2010) 1406–1413. doi:10.1364/AO.49.001406.

[63] A.N. Eraslan, R.C. Brown, Chemiionization and ion-molecule reactions in fuel-rich acetylene flames, Combustion and Flame. 74 (1988) 19–37. doi:10.1016/0010-2180(88)90084-3.

[64] K.T. Walsh, M.B. Long, M.A. Tanoff, M.D. Smooke, Experimental and computational study of CH, CH*, and OH* in an axisymmetric laminar diffusion flame, Symposium (International) on Combustion. 27 (1998) 615–623. doi:10.1016/S0082-0784(98)80453-0.

[65] J. Hu, B. Rivin, E. Sher, The effect of an electric field on the shape of co-flowing and candle-type methane–air flames, Experimental Thermal and Fluid Science. 21 (2000) 124–133. doi:10.1016/S0894-1777(99)00062-X.

[66] M.J. Papac, D. Dunn-Rankin, Modelling electric field driven convection in small combustion plasmas and surrounding gases, Combustion Theory and Modelling. 12 (2007) 23–44. doi:10.1080/13647830701383814.

[67] J. Prager, U. Riedel, J. Warnatz, Modeling ion chemistry and charged species diffusion in lean methane–oxygen flames, Proceedings of the Combustion Institute. 31 (2007) 1129–1137. doi:10.1016/j.proci.2006.07.141.

[68] Y. Koji, Y.C. Chien, K. Sunny, D. Dunn-Rankin, The Influence of Electric Field Power Systems on Flame Behavior, in: 8th National Combustion Meeting, Utah, 2013.

[69] Y.C. Chien, K. Yamashita, D. Dunn-Rankin, Electrical Aspects of Impinging Flames, in: 24th International Colloquium on the Dynamics of Explosions and Reactive Systems, 2013.

[70] G.S. Settles, Schlieren and shadowgraph techniques: visualizing phenomena in transparent media, Springer, 2001.

[71] Hitran-PC_4.0_Manual, (n.d.).

[72] Mishal Rosi Francis, DETECTING ELECTRIC FIELD EFFECTS ON FLAMES USING MID-IR PHOTODIODES, 2012.

[73] Y.C. Chien, D. Dunn-Rankin, Electric Field Effects on Carbon Monoxide Release from Impinging Flames, in: 8th US National Combustion Meeting, Utah, 2013.

[74] R.R. Skaggs, J.H. Miller, Tunable diode laser absorption measurements of carbon monoxide and temperature in a time-varying, methane/air, non-premixed flame, Symposium (International) on Combustion. 26 (1996) 1181–1188. doi:10.1016/S0082-0784(96)80334-1.

[75] R.K. Hanson, Combustion diagnostics: Planar imaging techniques, Symposium (International) on Combustion. 21 (1988) 1677–1691. doi:10.1016/S0082-0784(88)80401-6.

[76] R.J. CATTOLICA, S.R. VOSEN, Two-Dimensional Fluorescence Imaging of a Flame-Vortex Interaction, Combustion Science and Technology. 48 (1986) 77–87. doi:10.1080/00102208608923885.

[77] K.C. Smyth, J.E. Harrington, E.L. Johnsson, W.M. Pitts, Greatly enhanced soot scattering in flickering CH4/Air diffusion flames, Combustion and Flame. 95 (1993) 229–239. doi:10.1016/0010-2180(93)90064-A.

[78] J. Warnatz, The structure of laminar alkane-, alkene-, and acetylene flames, Symposium (International) on Combustion. 18 (1981) 369–384. doi:10.1016/S0082-0784(81)80042-2.

[79] I. Glassman, Combustion, Academic Press, 1997.

[80] K.C. Smyth, J.H. Miller, R.C. Dorfman, W.G. Mallard, R.J. Santoro, Soot inception in a methane/air diffusion flame as characterized by detailed species profiles, Combustion and Flame. 62 (1985) 157–181. doi:10.1016/0010-2180(85)90143-9.

[81] S.A. Kaiser, M.B. Long, Quantitative planar laser-induced fluorescence of naphthalenes as fuel tracers, Proceedings of the Combustion Institute. 30 (2005) 1555–1563. doi:10.1016/j.proci.2004.08.263.

[82] J.B. Schmidt, B.N. Ganguly, Point-to-plane pulsed discharge initiated flame structure modification in propane–air flame, Journal of Physics D: Applied Physics. 45 (2012) 045203. doi:10.1088/0022-3727/45/4/045203.

[83] D. Escofet-Martin, Y.C. Chien, D. Dunn-Rankin, OH PLIF of an impinging flame, in: 2014 Spring Meeting of the Western States Section of the Combustion Institute, 2014: p. 7.

[84] J.Luque, D.R. Crosley, LIFBASE: Database and spectral simulation program, 1999. http://www.sri.com/engage/products-solutions/lifbase.

[85] R. Sadanandan, M. Stöhr, W. Meier, Simultaneous OH-PLIF and PIV measurements in a gas turbine model combustor, Appl. Phys. B. 90 (2008) 609–618. doi:10.1007/s00340-007-2928-8.

[86] J.M. Seitzman, G. Kychakoff, R.K. Hanson, Instantaneous temperature field measurements using planar laser-induced fluorescence, Opt. Lett. 10 (1985) 439–441. doi:10.1364/OL.10.000439.

[87] R. Devillers, G. Bruneaux, C. Schulz, Development of a two-line OH-laser-induced fluorescence thermometry diagnostics strategy for gas-phase temperature measurements in engines, Appl. Opt. 47 (2008) 5871–5885. doi:10.1364/AO.47.005871.

[88] Wenhong Qin, Ying-Ling Chen, J. W. L. Lewis, Time-resolved temperature images of laser-ignition using OH two-line laser-induced fluorescence (LIF) thermometry, Journal of the International Flame Research Foundation. Ariticla Number 200508 (2005) 20.

[89] J.M. Seitzman, R.K. Hanson, Two-line planar fluorescence for temporally resolved temperature imaging in a reacting supersonic flow over a body, Appl. Phys. B. 57 (1993) 385–391. doi:10.1007/BF00357380.

[90] B.E. Battles, R.K. Hanson, Laser-induced fluorescence measurements of NO and OH mole fraction in fuel-lean, high-pressure (1–10 atm) methane flames: Fluorescence modeling and experimental validation, Journal of Quantitative Spectroscopy and Radiative Transfer. 54 (1995) 521–537. doi:10.1016/0022-4073(95)00020-L.

[91] F.P. Incropera, D.P. DeWitt, T.L. Bergman, A.S. Lavine, Fundamentals of Heat and Mass Transfer 5th Edition with IHT2.0/FEHT with Users Guides, Wiley, 2001.

[92] FLIR Systems, FLIR User's manual for B6XX series, P6XX series, SC6XX series, (2010). http://www.flir.com/.

[93] F. Borgatelli, D. Dunn-Rankin, Behavior of a small diffusion flame as an electrically active component in a high-voltage circuit, Combustion and Flame. 159 (2012) 210–220. doi:10.1016/j.combustflame.2011.06.002.

[94] S. Karnani, D. Dunn-Rankin, F. Takahashi, Z.-G. Yuan, D. Stocker, Simulating Gravity in Microgravity Combustion Using Electric Fields, Combustion Science and Technology. 184 (2012) 1891–1902. doi:10.1080/00102202.2012.694740.

[95] J. Tinajero, D. Dunn-Rankin, J. Bai, M. Plascencia, Ground-Based Schlieren Experiments of Chemi-ion Driven Flows in a Time Varying Electric Field, in: American Society for Gravitational and Space Research (ASGSR) Annual Meeting, Pasadena, CA, 2014.

[96] L.G. Blevins, J.P. Gore, Computed structure of low strain rate partially premixed CH4/air counterflow flames: implications for NO formation, Combustion and Flame. 116 (1999) 546–566. doi:10.1016/S0010-2180(98)00059-5.

[97] L.G. Blevins, M.W. Renfro, K.H. Lyle, N.M. Laurendeau, J.P. Gore, Experimental study of temperature and CH radical location in partially premixed CH4/air coflow flames, Combustion and Flame. 118 (1999) 684–696. doi:10.1016/S0010-2180(99)00023-1.

[98] Y.K. Jeong, C.H. Jeon, Y.J. Chang, Evaluation of the equivalence ratio of the reacting mixture using intensity ratio of chemiluminescence in laminar partially premixed CH4-air flames, Experimental Thermal and Fluid Science. 30 (2006) 663–673. doi:10.1016/j.expthermflusci.2006.01.005.

[99] B.O. Ayoola, R. Balachandran, J.H. Frank, E. Mastorakos, C.F. Kaminski, Spatially resolved heat release rate measurements in turbulent premixed flames, Combustion and Flame. 144 (2006) 1–16. doi:10.1016/j.combustflame.2005.06.005.

[100] B.K. McMillin, J.M. Seitzman, R.K. Hanson, Comparison of NO and OH planar fluorescence temperature measurements in scramjet model flowfield, AIAA Journal. 32 (1994) 1945–1952. doi:10.2514/3.12237.

[101] M. (Marcel) Cremers, Heat transfer of oxy-fuel flames to glass:the role of chemistry and radiation, URN:NBN:NL:UI:25-609422, Technische Universiteit Einhoven, 2006. http://repository.tue.nl/609422.

[102] M.J. Remie, G. Särner, M.F.G. Cremers, A. Omrane, K.R.A.M. Schreel, L.E.M. Aldén, et al., Heat-transfer distribution for an impinging laminar flame jet to a flat plate, International Journal of Heat and Mass Transfer. 51 (2008) 3144–3152. doi:10.1016/j.ijheatmasstransfer.2007.08.036.

Appendix

A. Burner Insulation Base Drawing

0.150

3.00

3.00

0.500

0.500

0.200

0.375

Teflon

UNLESS OTHERWISE SPECIFIED:

DIMENSIONS ARE IN INCHES
TOLERANCES:
FRACTIONAL±
ANGULAR: MACH± BEND ±
TWO PLACE DECIMAL ±
THREE PLACE DECIMAL ±

INTERPRET GEOMETRIC
TOLERANCING PER:

MATERIAL
Teflon

FINISH

DO NOT SCALE DRAWING

NEXT ASSY   USED ON

APPLICATION

	NAME	DATE
DRAWN	Alice	9/14/13
CHECKED		
ENG APPR.		
MFG APPR.		
Q.A.		
COMMENTS:		

TITLE:

Square Burner Base

SIZE | DWG. NO.   REV
A | Square burner base

SCALE: 1:1   WEIGHT: SHEET 1 OF 1

5   4   3   2   1

Appendix

B. Matlab Code for High Voltage

Power Supply Measurement

MATLAB

```matlab
clear all
R = 4645e2;   %sense resistor [\Omega]


voltage= input('Enter HV: ');
if isempty(voltage)
voltage=[0,0:-200:-11000,0:200:10000,5000,0];
% voltage=[0,0:-200:-9000,0];
%voltage=[0,0:-1000:-5000, -5400,-5600,-6000,-6200,-6400, -5400,-5600,-
6000,-6200,-6400, -5400,-5600,-6000,-6200,-6400, -5400,-5600,-6000,-
6200,-6400, -5400,-5600,-6000,-6200,-6400, -5400,-5600,-6000,-6200,-
640 , -5400,-5600,-6000,-6200,-6400, 0];
%voltage=[0,0];
end


volt = -voltage/2000;   %reduces voltage by a factor of 2000 to
accomodate
%analog output and flips it to accomodate op-amp
%volt = voltage/1000;   %reduces voltage by a factor of 1000 to
accomodate analog output
i = 2;   %initializes iteration number
l = 1;   %initialize storage count

syms fuel time flow today
fuel=input('fuel: ','s');
fuelflow=input('flow: ');
time=input('time:','s');
today = date;

pathname = 'C:\Documents and Settings\LFA\My Documents\efield\test\';
mkdir(pathname,today);
pathname1 = [pathname,today,'\'];
mkdir(pathname1,time);

pathname2=[pathname1,time,'\'];
mkdir(pathname2,'transient');
pathname3=[pathname2,'transient\'];
distance=input('Enter the distance between the burner and the mesh [cm]
');


%Initialize Data Acquisition
if (~isempty(daqfind))
    stop(daqfind)
end
% daqhardwareinfo = daqhwinfo
% daqinstalledadaptors = daqhardwareinfo.InstalledAdaptors


% daqmccinfo.ObjectConstructorName{:}
ai = analoginput('nidaq', 'Dev1');
ao = analogoutput('mcc',0);
```

```
% daqhwinfo(ai)
% daqhwinfo(ao)
% aiInfo = propinfo(ai);
% aiInfo.SampleRate
% aoOut = propinfo(ao, 'TriggerType')
chI= addchannel(ai, [0 1 2], {'IonCurrent';'Mesh';'PMT'});
chO= addchannel(ao,[0 1],{'Output'});

Fs = 3000;                         % Sample frequency
%Data is oversampled to prevent alias frequencies from influencing data
%set. Specifically, I came across noise from the high voltage amplifier.
T = 1/Fs;                          % Sample time
L = Fs*1;                          % Signal length
t = (0:L-1)*T;                     % Time vector

set(ai,'InputType','Differential')
set(ai,'SampleRate',Fs);
set(ai,'SamplesPerTrigger',L);    %Sampling time
set(ao,'SampleRate',400);
%End Initialization


%Transient information, collection and processing
for i=2:1:length(voltage)

out = volt(i);
putdata(ao,out*ones(400,2)) ;
start(ao)
beep
wait(ao,10)
start(ai)
data = getdata(ai);

data1=data; %rawdata will remain the raw unmodified data set
data(:,1) = -data(:,1)/R*1e6; %Compensating for OPamp inversion, and
converting to microamps
data(:,2) = -data(:,2)*2;      %Compensating for OPamp inversion, and
scaling -- Mesh Voltage
[b,a] = butter(6,0.06667,'low'); %Because of the conditions, I assumed
I wouldn't find transient
%features over 100Hz
data(:,4) = filtfilt(b,a,data(:,1)); %This filter compensates for phase
distortion
data(:,5) = filtfilt(b,a,data(:,3)); %This filter compensates for phase
distortion

%search = find(abs(data(:,1))>0);   %useless unless a delay between
voltage and collection is used
q = num2str(voltage(i));
transave = strcat(fuel,'_trans_', q,'kV.mat');
fullname1 = [pathname3,transave];
save(fullname1)


    for chan=1:5
```

```matlab
                disp(' ');
%               disp(channels(chan));
                m(i-1,2*chan-1)=mean(data((1):end,chan));
%               disp(strcat('average: ',num2str(m(i,2*chan-1))));
                m(i-1,2*chan)=std(data((1):end,chan));
%               disp(strcat('std: ',num2str(m(i,2*chan))));
    end


  figure(1);
  plot(data(:,4));
  grid on
  ylabel('IonCurrent [\muA]');
  xlabel('sample number');
  title(['Transient ion current Filtered ',q,'kV/cm'])

  figure(2);
  plot(data1(:,1));
  grid on
  ylabel('Measured Voltage [V]');
  xlabel('sample number');
  title(['Transient Voltage ',q,'kV/cm'])

%     figure(3);
%     plot(data(:,5));
%     grid on
%     ylabel('Photoresponse [A.U.]');
%     xlabel('sample number');
%     title(['Transient photoresponse Filtered',q,'kV'])

figure(4)
grid on
hold on
errorbar(m(i-1,3)/distance,m(i-1,1),m(i-1,2),'.k');
ylabel('Ion Current [\muA]');
xlabel('Field Strength [kV/cm]');
hold on



% The following lines remove the mean component and calculate the FFT
of the
% ion current signal
A=data(:,1)-mean(data(:,1));
NFFT = 2^nextpow2(L); % Next power of 2 from length of y
Y = fft(A,NFFT)/L;
f = Fs/2*linspace(0,1,NFFT/2);
figure(5)
plot(f,2*abs(Y(1:NFFT/2)))
title('Single-Sided Amplitude Spectrum of y(t)')
xlabel('Frequency (Hz)')
ylabel('|Y(f)|')



figure(6)
```

```
grid on
hold on
errorbar(m(i-1,3)/distance,m(i-1,9),m(i-1,10),'.k');
ylabel('Transient filtered PMT response [A.U.]');
xlabel('Field Strength [kV/cm]');
hold on


end


figure(7)
grid on
hold on
errorbar(m(1:size(m),3)/distance,m(1:size(m),1),m(1:size(m),2),'.k');
ylabel('Absolute Ion Current [\muA] -- unfiltered');
xlabel('Field Strength [kV/cm]');

figure(8)
grid on
hold on
errorbar(m(1:size(m),3)/distance,m(1:size(m),7)/fuelflow,m(1:size(m),8)
/fuelflow,'.g');
ylabel('Ion Current [\muA*min/ml CH_4] -- filtered');
xlabel('Field Strength [kV/cm]');

figure(9)
grid on
hold on
errorbar(m(1:length(m),3)/distance,m(1:length(m),9),m(1:length(m),10),'
.b');
ylabel('PMT [A.U.] -- filtered');
xlabel('Field Strength [kV/cm]');

filename2 = strcat(fuel,'_', time,'.mat');
fullname2 = [pathname2,filename2];
save(fullname2)
disp('switch everything off!');
pause
```

Appendix

C. Tomography Analysis Paper

Tomographic analysis of quantum cascade laser absorption by carbon monoxide

Chien, Y.C., Garman, J., and Dunn-Rankin, D.

Mechanical and Aerospace Engineering Department,
University of California, Irvine, CA 92697-3975, USA.

Abstract

This study investigates the potential for quantum cascade laser (QCL) absorption by carbon monoxide to be used as a possible sensor for combustion control. Specifically, the research examines the potential application of spatially monitoring carbon monoxide concentration by using a QCL within the 4.44-4.54 microns wavelength range. Based on the expected absorption from an ideal distribution, the study compares a numerical prediction of the spatial distribution of carbon monoxide concentration in a coarse grid, based on the line-of-sight integrated values that would be detected in an ideal absorption system. The results give insights into the effective methodology for analysis and the number of lines of sight needed to identify islands of CO in a combustion system.

1. Introduction

Laser-based techniques provide the combustion field with the capability for remote, nonintrusive, in-situ, spatially and temporally precise measurements of important chemical parameters [1]. Laser absorption spectroscopy, in particular, has high signal strength, species specificity, and relative simplicity of equipment and data interpretation characteristics, so it is especially outstanding among the laser-based techniques [2]. Laser absorption spectroscopy allows the study of internal structure or distributions such as temperature and concentrations of a variety of molecules by path-integrated measurement if effective tomographic reconstructions are available. It is often worth the additional effort of tomography because absorption spectroscopy measurements are well suited for application to environments that are hostile since absorption signals can be robust if the laser wavelength matches a strong molecular-absorption line. The tomographic techniques require reconstruction along the line-of-sight to retrieve the spatial distributions of interest from the measured data [3]. There are some popular approaches for this retrieval, including Abel, onion-peeling, and backprojection methods [4]. For the particular use in hostile combustion exhaust, there is a commercial instrument, ZoloBOSS, that uses similar techniques. This instrument is being touted as one that can act as a combustion

monitor with the goal of burning coal in power plants more efficiently [5]. The ZoloBOSS method uses QCL lasers and a special tomographic method. The evaluation of these elements in general (though not the ZoloBOSS, itself) for their potential application in combustion control is the main subject of this paper.

Quantum cascade lasers operate in the mid-infrared region, λ= 4 to 20μm, and represent a good light source for detecting gas species and temperature because they provide access to the fundamental rotational-vibrational transitions of molecular species. By using the mid-IR, the sensitivity can be improved by several orders of magnitude compared to near-IR laser approaches that rely on overtone detection. In effect, the mid-IR provides much stronger absorption lines for many more molecules of combustion interest. Quantum cascade lasers have been used to detect gas species such as CO, CO_2, NO, NO_2, NH_3, CH_4 and N_2O [6].

The ZoloBOSS tomography algorithm depicts the spatial distribution of species concentration by measurement of the path average of the data [7]. It is a commercial technique that uses an optimization algorithm rather than an integration to provide the tomographic inversion. This method works well for sparse data sets and can provide reliable results under the assumptions of widely separated absorption lines (so there are no interferences between species) and slowly varying species concentrations (i.e., no small pockets of species at scales below the line of sight spacing). In some practical environments, particularly regions within the combustion zone, these assumptions may not be valid. When measuring absorption lines under these more strenuous conditions, the detected absorption spectra may have different species interferences with each other. Therefore, the acquired spectra will not come only from one species but any analysis needs to consider other absorbing species in the same wavelength region. In the combustion environment, water lines are one of the major interfering species. To begin exploring the effects of these interferences on the tomographic analysis of spatial distributions, this paper uses CO as the target species and models the ideal measurement of it in a combustion environment using a typical QCL.

2. Spectral survey and line selection

In order to understand the spectroscopic behavior, we use HitranPC which is software that draws on a compilation of spectroscopic parameters from the Hitran database to estimate the molecular line strengths for the relevant gas molecules. Initially, we simulated the main interfering species over the region from 4.44-4.54 microns, as shown in **Fig.** 1. The species shown are CO, CO_2, H_2O and N_2O at the relatively high temperature of 1000K. We selected this wavelength region because we were loaned a laser for companion experiments (to be reported in a future work) spanning this wavelength range. It is important to consider the temperature of the system under study since the relative line strengths can depend on this parameter.
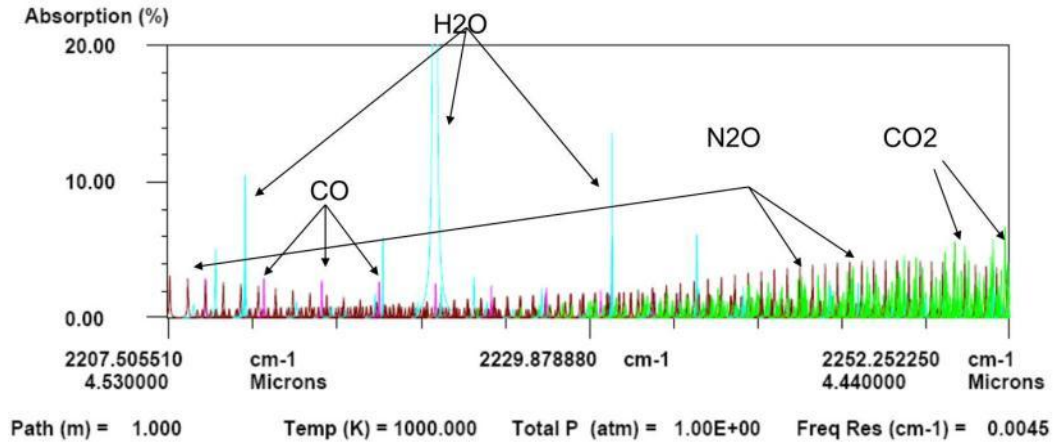
Figure 1. The potential interference species over the laser operation range (from HitranPC)

Fig. 2 is a composite spectrum based on **Fig.** 1; it includes absorption contributions from all species for a given wavelength. When the spectrum is scanned with a laser of infinitely narrow linewidth, the composite spectrum is the signal one should detect.
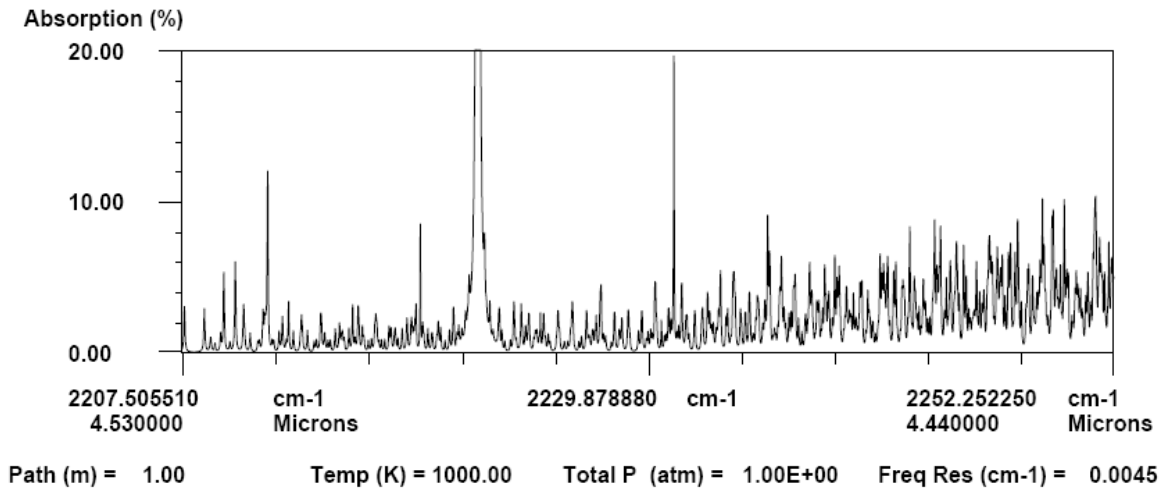
Figure 2. The composite spectrum over the laser operation range (from HitranPC).

For achieving the goal of a calibration spectral survey at 700K in a test cell filled with CO and water only at room temperature, **Fig.** 3 shows the predicted absorption of CO and water with a 0.1 meter pathlength in the same wavelength region shown in **Fig.** 2. According to the ideal gas law, when pressure is 1 atm at room temperature (300K), the pressure rises to 7/3(2.33) atm at 700K. The CO concentration is selected as 400ppm, based on a desired 10% absorption maximum at 700K and as a typical value for core combustion zones. Similarly, the H_2O concentration is selected as 0.6% at the same condition. This concentration is a little lower than might be encountered in combustion systems, but it provides a reliable interference.

174
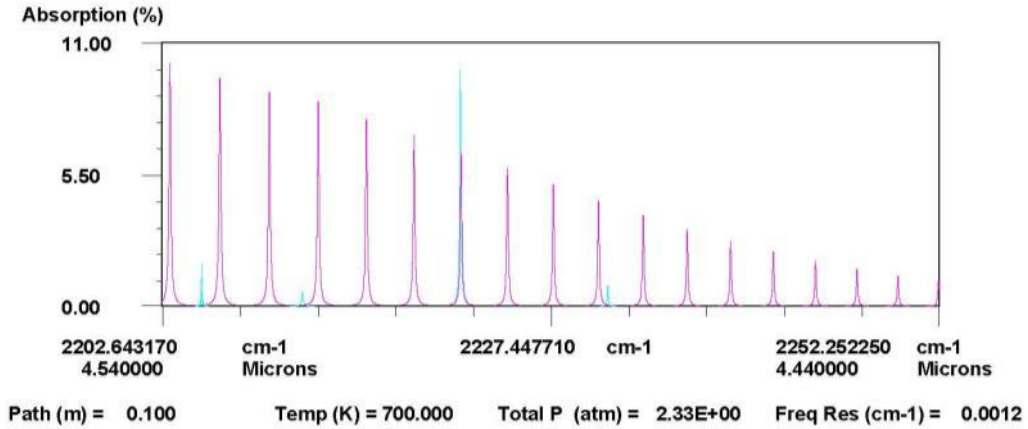
Figure 3. Spectrum of CO (pink) and H_2O (blue) between 4.44 to 4.54 microns at 700K. A 0.1 meter pathlength was assumed and the concentration for CO is set at 400ppm while water is 0.6%.

After the entire inspection of the absorption of CO under high resolution over the region accessible to the QCL selected, there exists only R-branch lines in this region, and fortunately they are water interference free.

Line Position(cm-1)	Intensity(cm-1mol-1)	v"	v'	Rotational	Transition	Transmission (%)
2203.161	1.28E-19	0	1	R	16	92.31%
2206.3535	9.92E-20	0	1	R	17	93.92%
2215.7044	4.02E-20	0	1	R	20	97.24%
2221.7483	1.98E-20	0	1	R	22	98.55%
2224.7127	1.35E-20	0	1	R	23	98.98%
2227.6386	9.01E-21	0	1	R	24	99.31%
2230.5258	5.90E-21	0	1	R	25	99.54%
2233.3743	3.78E-21	0	1	R	26	99.70%
2236.1838	2.38E-21	0	1	R	27	99.81%
2238.9541	1.47E-21	0	1	R	28	99.88%
2241.6853	8.85E-22	0	1	R	29	99.93%
2244.377	5.25E-22	0	1	R	30	99.95%
2247.0292	3.05E-22	0	1	R	31	99.97%
2249.6417	1.74E-22	0	1	R	32	99.98%
2252.2144	9.73E-23	0	1	R	33	99.99%

Figure 4. List of the line position, intensity, rotational and vibrational transitions, and transmission percentage for CO lines in figure 3. Only R-branch lines appear in the spectrum over the range.

We also need to use the absorption data to determine temperature. In order to find the most sensitive line pair to the temperature change, we ratio the absorption intensities of each line with each other from 300K to 500K till 700K (**Fig.** 5). We calculated the ratio change from 300K to

500K and also from 500K to 700K. The ratio change that produces the maximum value represents the most sensitive lines to temperature change in this range of temperature.

	R16	R17	R20	R22	R23	R24	R25	R26	R27	R28	R29	R30	R31	R32	R33
R16	1	R17/R16	R20/R16	R22/R16	R23/R16	R24/R16	R25/R16	R27/R16	R27/R16	...	...				
R17		1	R20/R17	R22/R17	R23/R17	...	...								
R20			1	R22/R20	R23/R20	...	...								
R22				1	...	...	...								
R23					1	...	...								
R24						1									
R25							1								
R26								1							
R27									1						
R28										1					
R29											1				
R30												1			
R31													1		
R32														1	
R33															1

Figure 5. Ratio of the intensities of rotational transitions at different line positions to select the most sensitive lines.

In a practical case, it will not be possible to attribute all decrease in laser intensity to absorption. Beam steering, window losses, scattering from particles, and detector response characteristics all will affect the absolute signal value. To eliminate this problem, it is common to use the ratio of absorption at two different lines as the normalized measurement with internal consistency. In addition, as we describe above, the temperature can affect the results substantially. It is likewise possible to determine the temperature by comparing the relative absorption for two different lines. To accomplish the effective normalization and simultaneously the temperature measurement, we determined the most sensitive absorption ratio of positions (wavelengths), R22/R16 (2221.7 cm^{-1}/ 2203.2 cm^{-1}), of carbon monoxide within the operating range of the quantum cascade laser. Figure 6 shows that the R22/R16 ratio is the most sensitive with the temperature change, having the largest difference in slope.

This wavelengths ratio was selected because the ratio of these two lines is sensitive to temperature change whether from 300 K to 500 K or 500 K to 700 K. The relative change of transmission between these two R-band transitions with temperature is higher than between other pairs. In addition, there is no interference effect of water lines at these two positions.

	R16	R17	R20	R22	R23	R24	R25	R26	R27	R28	R29	R30	R31	R32	R33
R16	0	0.14431	0.40684	0.4427	0.4324	0.40498	0.3697	0.33028	0.28958	0.25	0.21	0.18	0.15	0.12	0.1
R17		0	0.36491	0.43662	0.43654	0.41548	0.38361	0.34552	0.30475	0.26	0.22	0.19	0.16	0.13	0.1
R20			0	0.29922	0.36873	0.39552	0.39383	0.37313	0.34084	0.3	0.26	0.22	0.19	0.15	0.13
R22				0	0.19256	0.30667	0.36246	0.37741	0.36536	0.34	0.3	0.26	0.22	0.18	0.15
R23					0	0.19641	0.3076	0.35813	0.36757	0.35	0.32	0.28	0.24	0.2	0.17
R24						0	0.20161	0.31105	0.35692	0.36	0.34	0.31	0.27	0.23	0.19
R25							0	0.20662	0.31401	0.36	0.35	0.33	0.29	0.25	0.21
R26								0	0.21132	0.32	0.35	0.35	0.32	0.28	0.24
R27									0	0.22	0.32	0.35	0.34	0.31	0.27
R28										0	0.22	0.32	0.35	0.33	0.3
R29											0	0.22	0.32	0.35	0.33
R30												0	0.23	0.32	0.34
R31													0	0.23	0.32
R32														0	0.24
R33															0

Figure 6. The results of the ratios from figure 6. R22/R16 is the most sensitive to the temperature change from 300K to 500K, and 500K to 700K.

3. Concentration analysis method and numerical approach

In molecular absorption spectroscopy, the intensity of the laser radiation changes when it passes through a medium. The decrease in intensity is governed by the well-known Beer-lambert law or Beer's law:

$$A = P = \ln\left[\frac{I_0}{I}\right] = -\ln\left[\frac{I}{I_0}\right] = \varepsilon c l = \alpha l$$

(1)

where I_0 is the intensity of incident light, I is the intensity of transmitted light. A is the absorbance across the transition centered at the specific wavelength (it is also sometimes known as the projection of the property field); ε is molar absorptivity; c is the concentration of the sample species; l is the pathlength; α is the absorption coefficient. For absorption spectroscopy to provide a single valid measurement of concentration, the medium must be uniform. If the absorption coefficient (either the absorptivity or the species concentration) varies along the

path, the change will be reflected in the absorbance but the result cannot be attributed unequivocally to average species concentration.

We explicitly investigate and compare two different uniformity assumptions of methods that employ the Beer-Lambert law in order to understand how the path along which the laser passes is related to an assumed homogenous distribution of species. For example, a concentration field of carbon monoxide is distributed as a 2-D Gaussian profile, as shown in **Fig.** 7 from the top view. We need consider only one quarter of the plane due to the cylindrical symmetry of the distribution. For this case, we assume that the concentration of CO does not vary in the out-of-plane direction (i.e., over the laser beam width we assume a uniform concentration and absorptivity).
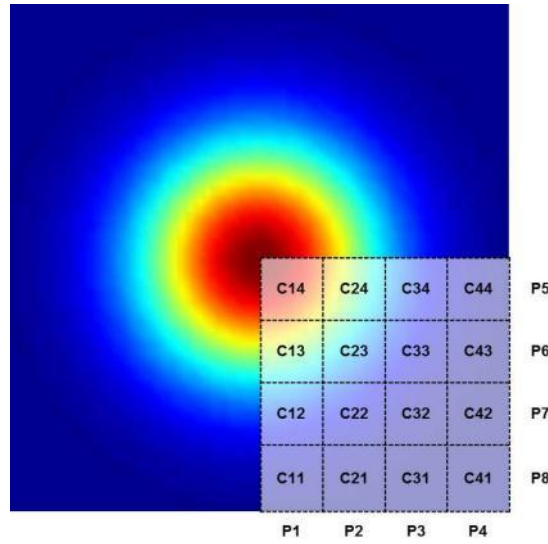
Figure 7. Top view of the Gaussian profile of CO. Overlaid is a grid in the lower quadrant. Only a quarter of the plane is needed because the distribution is symmetric.

In Figure 7 we divided the quarter plane as 4 by 4 grids, and each grid represents one concentration named C11, C12, C13 and C14. The projection (i.e., integrated absorbance over the path) of the first line is P1. Projection 1 and projection 5 should be equal because the distribution is axisymmetric. Similarly, P2 equals to P6; P3 equals P7; P4 equals P8. Moreover, C11 equals C44, C12 equals C34, and so on. We are using this highly symmetric configuration as a test case. In a real system none of these equalities will hold and all projections and concentrations will be different from each other.

When a laser is passed through the C11-C14 field, we take it as passing approximately through four different concentrations of carbon monoxide. By using the Beer-lambert law, the calculation is as follows:

$$P_{11} = \ln(\frac{I_{10}}{I_{11}}) = \varepsilon c_{11} \delta x \tag{2}$$

$$P_{12} = \ln(\frac{I_{11}}{I_{12}}) = \varepsilon c_{12} \delta x \tag{3}$$

Similarly, we can calculate the projection of P_{13}, and P_{14}.

In order to get the total integrated projection over the four different concentrations, we combine all of the individual sub-projections together.

$$P1 = \ln(\frac{I_{10}}{I_{11}}) + \ln(\frac{I_{11}}{I_{12}}) + \ln(\frac{I_{12}}{I_{13}}) + \ln(\frac{I_{13}}{I_{14}}) = \ln(\frac{I_{10}}{I_{11}} \times \frac{I_{11}}{I_{12}} \times \frac{I_{12}}{I_{13}} \times \frac{I_{13}}{I_{14}}) = \ln(\frac{I_{10}}{I_{14}})$$
$$= \varepsilon c_{11} \delta x + \varepsilon c_{12} \delta x + \varepsilon c_{13} \delta x + \varepsilon c_{14} \delta x = \varepsilon \left[(c_{11} + c_{12} + c_{13} + c_{14}) \delta x \right]$$
(4)

And from this equation, we get the equation of the inverse of the transmission I_{10}/I_{14},

$$\frac{I_{10}}{I_{14}} = \exp(\varepsilon \left[(c_{11} + c_{12} + c_{13} + c_{14}) \delta x \right])$$
(5)

Naturally, since the concentrations are considered uniform over a fairly coarse grid, it will be valuable to determine what these concentrations actually represent. Two options to consider are the midpoint value or the average value. These two will converge for high enough grid resolution, but for realistic systems the number of laser paths will be relatively small. In the following we evaluate these two definitions for the concentration in a grid.

A. Mid-point method

The mid-point method is considering the local concentration in the middle of each resolution grid and it alone represents the concentration of the grid. **Fig.** 8 shows the 4 by 4 grids, and the blue arrows represent the laser pathway, the circles (red) in the middle of each grid are taken as the discrete carbon monoxide concentration in each grid. Therefore, the δ displacement in the Gaussian distribution then is determined by the width between the start point at the center and the middle point in each grid. They are δx, 3δx, 5δx and 7δx from the center point to each mid-point. The same occurs for δy in the y direction.
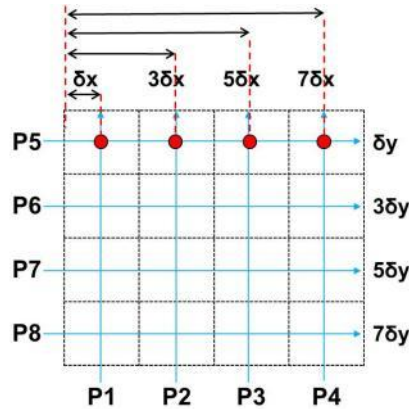
Figure 8. The mid-point method is taking the concentration at precisely the middle point inside each grid. The δx is the distance from the center of the Gaussian distribution.

B. Average method

The average method is illustrated in **Fig.** 9(a), which takes a hundred points of CO concentration in each grid, and then takes the average of them to represent the concentration in the grid. The Gaussian displacement δ here is defined by the width of each grid. And inside each measurement grid there are N by N points. δx' is the space between the internal point values (**Fig.** 9(b)).

(a)   (b)
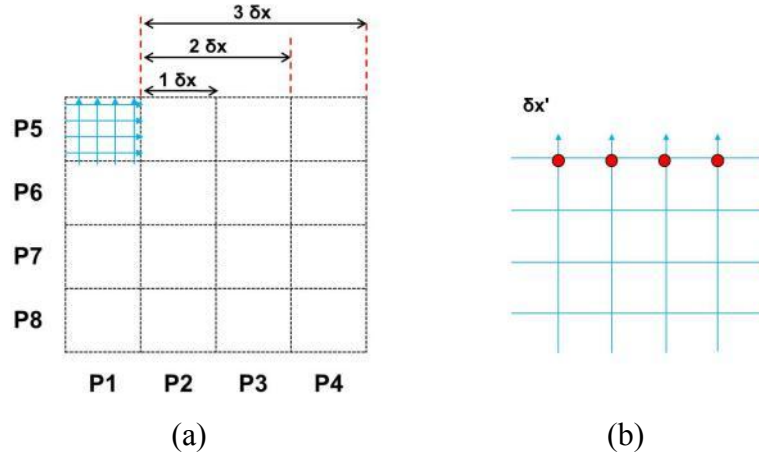
Figure 9. (a) The average method is taking the average of 100 points inside each grid. (b) Inside one grid, there are N by N points representing the intersections of the narrowly spaced lines spaced at δx' or δy'.

The actual value (the presumed precise value that would occur with narrow laser beam traversing the space) is calculated only through the pathway in the middle line of each grid. One thousand data points in each grid along the centerline are used to get the true projection value. Although the illustrations describe a 4 by 4 grid condition, we have also analyzed an 8 by 8 grid configuration.

C. Methane jet flame with tomographic reconstructions

When considering the potential of the absorption measurement over a real system, a tomographic reconstruction will be necessary. To examine the potential pitfalls of such reconstructions we analyze first the absorption information potential in a methane jet flame. In order to avoid experimental fluctuations for this idealized evaluation, a simulated methane coflow flame (using the CHEMKIN coflow configuration) is used for the reconstruction algorithm calculation tests.

Fig. 10 shows the results of the calculation for a 10mm diameter burner. We chose this configuration because we will later compare the findings in an experiment that is already functioning. We make the assumption that the distributions in the jet burner are axisymmetric. Therefore, we need only take data from half of the burner as in **Fig.** 11(a) and revolve the values around the Z-axis to simulate the full jet flame.

As mentioned earlier, if there are concentration gradients that are steep relative to the thickness of the laser beam used for the absorption measurement, there will be spatial averaging issues in the cross beam dimension as well as those along the beam path. Hence, we take actual values into account when doing the calculation rather than taking the average. The flame simulation data we have has higher spatial resolution then the typical laser beam size. The calculation resolution is 5mm/100points (radius/data points) in X or Y directions. Therefore, we take 5mm and 10 grids over the XY plane and 7mm for 7 grids in the height. This means that the laser beam size is simulated as 0.5mm x 0.5mm x 1mm. Specifically, we take 10 x 10 x 7 (X-Y-Z) as the resolution grid over a quarter of the burner, and then compute the average of CO concentration inside each grid. We use only the first layer of gas from the exit base of the burner as the vertical slice, as shown in **Fig.** 11(b) and **Fig.** 11(c). **Fig.** 11(b) shows the XYZ axis with respect to the first layer as a disc while **Fig.** 11(c) shows a top view of the burner. The n by n matrix of grids is 10 by 10 in this paper.

After getting the n by n CO concentration values from the base layer simulation, we are able to calculate the transmission using the Hitran database through the online software provided by SpectraCalc [9]. The strongest and most sensitive line at 2203 cm^{-1} is selected. The pathlength is 0.5mm over the burner along the X-Y plane, and the temperature is selected as the average value within each grid. It is important to note this further complication. Since there is a variation in the temperature as well as in the species concentration, the absorbance is affected in two ways. The convolution of these effects can be problematic and so it is valuable to explore them in this idealized system.
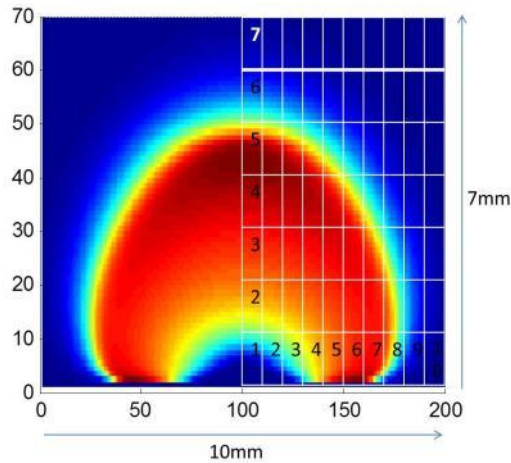
Figure 10. A 10 mm simulated methane jet flame of CO concentration and the resolution grids are taking as 10 by 7 (radius by height).

(a)   (b)   (c)
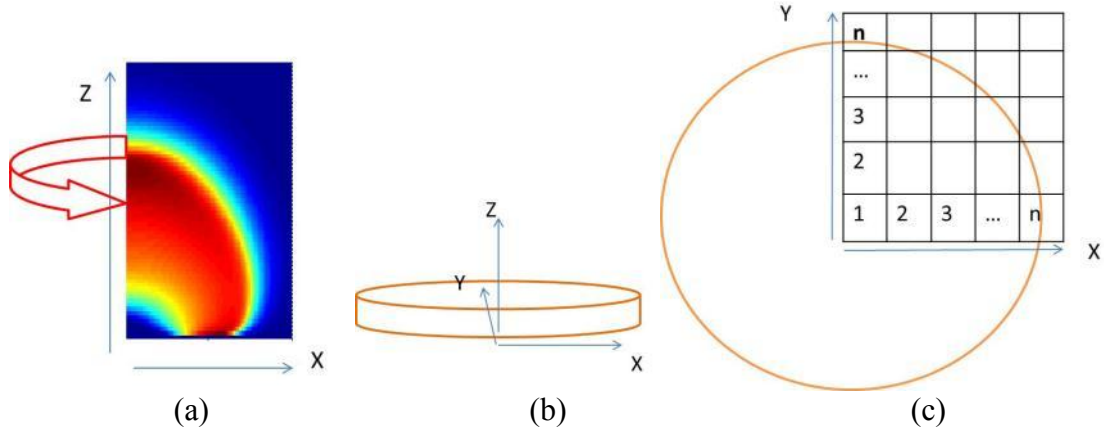
Figure 11. (a) The half plane of the jet revolves a circle makes a real jet data. (b) Taking a disc from the exit of the jet and shows the defined X-Y-Z axis in direction. (c) From the top view of the burner and shows taking the data of a quarter of the burner due to the symmetric distribution.

After having the transmission value from each position, we can calculate the total projection along the pathlength by using equation (6). This projected value from the data is a simulation for the real case when getting measurements from a QCL. The above describes the forward problem, but the real challenge is the inverse problem where the concentrations are desired. Typically, with proper treatment of the temperature effect, an Abel inversion can redistribute the concentration of the projection data.

The idea of Abel inversion is observing the object along the arrow lines shown in **Fig.** 12 and the integrated value is the projection value. By using the inverse Abel, it is possible to retrieve the original distribution.

$$P(r) = 2\int_{r}^{\infty} F[(r^2 + y^2)^{1/2}]dy$$

(6)
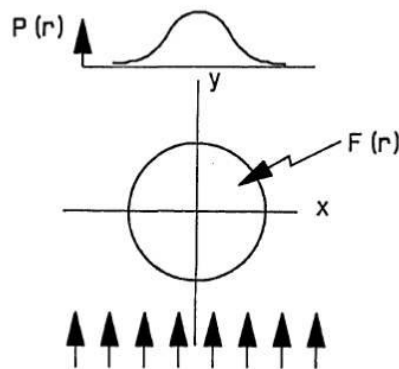
Figure 12. The graph of the idea of the Abel inversion [4].

The projected data can be reconstructed by Abel inversion [4, 8], and the distribution is,

$$F(r) = -\frac{1}{\pi}\int_{r}^{\infty} \frac{P'(r')}{(r'^2 - r^2)^{1/2}}dr'$$

182

(7)

F(r) represent the distribution; *P'* is the projection value; *r* is the radius. The Abel inversion is, however, more complicated than it appears, particularly near the centerline of the distribution. There have been many works on this method, fortunately, and so the reader is referred to them for additional information. For the current work, the main point is that there is a theoretical inversion method well-known for symmetric distributions that can be employed.

4. Results and Discussion

The projection result of the two reconstruction methods, using values by the midpoint and the average of the 2-D Gaussian profile is shown in **Fig.** 13 and 14. Fig 13 is the projection result of a 4 by 4 resolution grid calculated from equation (7). **Fig.** 14 shows the outcome from an 8 by 8 resolution grid; in this case the results get closer to the actual value than do the 4 by 4 ones, as expected. The results also show that the average value gives a better result, but they are all fairly close to the actual value. It seems that this spatial averaging is not the major challenge with the system. It also appears that the results would be better interpreted as average concentration values rather than as specific values at a specific location.

	Midpoint	R^2	Average	R^2	Actual
P1	3.2082	5.86E-3	3.1464	2.19E-4	3.1316
P2	1.9430	3.72E-5	1.9485	3.6E-7	1.9491
P3	1.2407	2.34E-4	1.2533	7.29E-6	1.2560
P4	1.0407	1.54E-3	1.0454	5.69E-5	1.0464
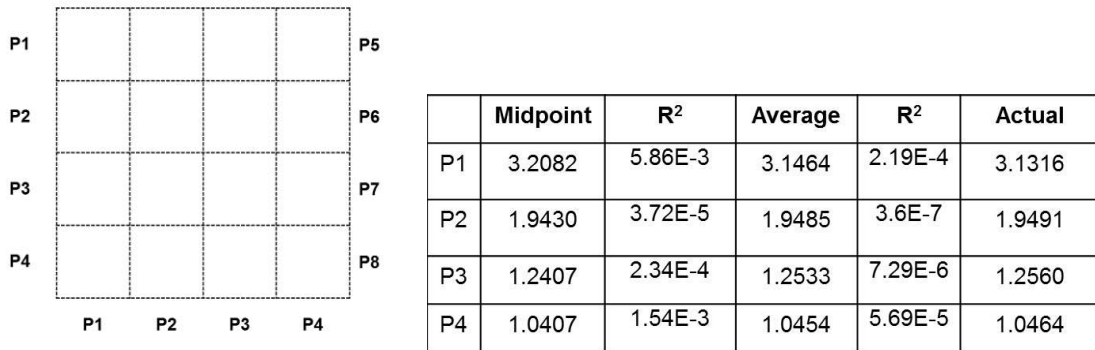
Figure 13. The projection positions corresponds to the 4 by 4 grids and the projection values from different calculations.

	Midpoint	R^2	Average	R^2	Actual
P1	3.4155	0.00076176	3.3958	6.241E-05	3.3879
P2	2.9072	0.00023716	2.8967	2.401E-05	2.8918
P3	2.2380	9.61E-06	2.2367	3.24E-06	2.2349
P4	1.6960	8.41E-06	1.6990	1E-08	1.6989
P5	1.3512	0.000016	1.3548	1.6E-07	1.3552
P6	1.1607	9.61E-06	1.1634	1.6E-07	1.1638
P7	1.0662	3.61E-06	1.0678	9E-08	1.0681
P8	1.0242	1E-06	1.0251	1E-08	1.0252
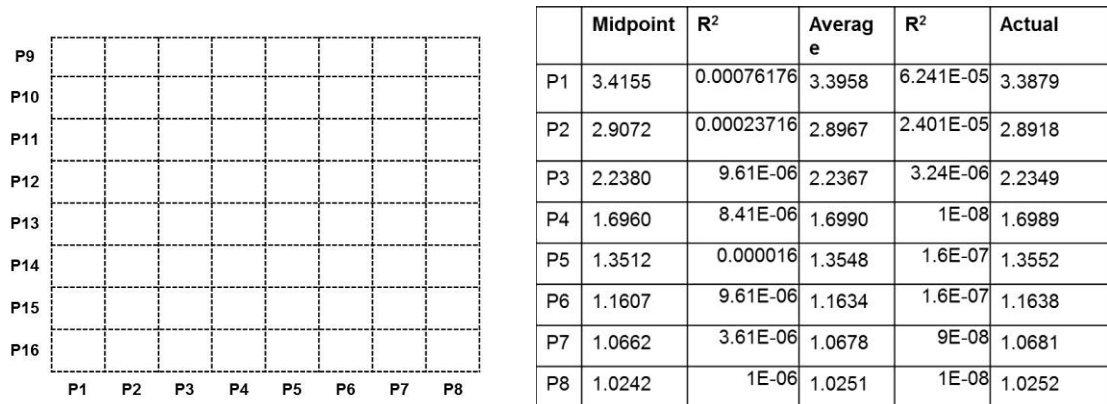
Figure 14. The projection positions correspond to the 8 by 8 grid and the projection values from different calculations.

 Fig. 15 is the simulated methane jet flame taking 0.05 cm height from the bottom of the flame, and taking resolution as 10 by 10 in the X-Y plane of the flame, and 1 mm in the height. The transmission data at the chosen sensitive line 2203 cm^{-1} is acquired from HitranPC, and the projection data is calculated. The projection data is then processed by Abel inversion to get the estimated distribution, as shown in **Fig.** 16. The results compare the original simulated carbon monoxide data and the estimated measured distribution (**Fig.** 16). Both show the same trend. They present a donut shape, with the concentration starting lowest from the outside rings. The concentration rises as the radius reduces. After the concentration reaches a maximum near the centerline, it drops again in the core of the jet. The Abel inversion method cannot resolve the center well because it diverges there, but it captures the distribution well except there.
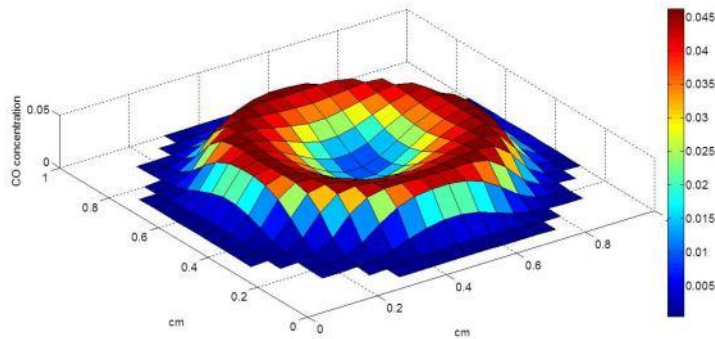
Figure 15. The simulated CO concentration distribution of the first layer of disc from exit of the jet.
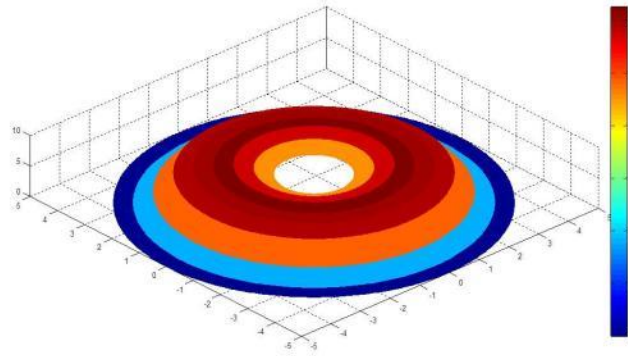
Figure 16. The CO concentration distribution doing projection then taking Abel inversion.

5. Conclusion and Future work

The most sensitive carbon monoxide line pair to the temperature change from 300K to 700K over the QCL operating range 4.44-4.54 microns is selected at R22/R16 (2221.7cm^{-1}/2203 cm^{-1})

according to the HitranPC spectral line database. An investigation over an idealized Gaussian carbon monoxide concentration profile comparing between the mid-point and average methods is demonstrated. Both of the methods show fairly close results with the actual value, while the averaging value gives the slightly better result. The potential analysis of tomographic reconstruction over a methane jet flame predicts the same trend of the distribution but is not able to resolve the center of the jet. This project involves two experiments that are not yet ready for measurement. The first is a glass cell with fixed concentrations of CO and water to confirm the selected lines for the QCL measurement. The second is a small methane jet flame, just as is simulated above. We will then compare the actual QCL performance to the simulated result above to determine what practical issues we have not properly addressed.

Acknowledgement

References

[1] Laser Diagnostics for Combustion Temperature and Species, Alan C. Eckbreth, 2nd edition, 1996.

[2] L. Ma, W. Cai, "Numerical investigation of hyperspectral tomography for simultaneous temperature and concentration imaging," Applied Optics, vol. 47, No. 21, pp. 3751-3759, July 2008.

[3] K. B. Chung, F. C. Gouldin, G. J. Wolga, "Experimental reconstruction of the spatial density distribution of a nonreacting flow with a small number of absorption measurements", Applied Optics, vol. 34, No. 24, pp. 5492-5500, August 1995.

[4] C. J. Dasch, "One-dimensional tomography: a comparison of Abel, onion-peeling, and filtered backprojection methods", Applied Optics, vol. 31, No. 8, pp. 1145-1152, March 1992.

[5] Overview of the ZoloBOSS applications and benefits, http://www.zolotech.com/pdfs/2008-ZoloBOSS.pdf, ZOLO Technologies.

[6] A. Karpf, G. N. Rao, "Enhancement of trace gas detection by integrating wavelength modulated spectra across multiple lines", Applied Optics, vol. 49, No. 8, pp. 1406-1413, March 2010.

[7] ZoloBOSS Tomography Algorithm – An Overview, http://www.zolotech.com/pdfs/zoloboss-tomography.pdf, ZOLO Technologies.

[8] K. Bockasten, "Transformation of Observed Radiances into Radial Distribution of the Emission of a Plasma", Journal of the optical society of America, vol. 51, No. 9, pp. 943-947, July 1960.

[9] Spectral Calc.com, http://www.spectralcalc.com, GATS, Inc.

Appendix

D.   Heat Propagation Measurement System Drawings

Dimensions and annotations (engineering drawing "Cooling - Lid"):

- 5.75
- 1.219
- 0.250
- 0.250
- 1.188
- 0.250
- 2.750
- 3.093
- 1.000
- 5.50
- 1.219
- 2.000
- 0.219
- Pipe thread 1/2-14
- 2 x ⌀ 0.719
- 7 x ⌀ 0.136 THRU ALL
- 8-32 UNC THRU ALL
- ⌀ 0.325 X 82°, Near Side
- 2 x ⌀ 0.136 THRU ALL
- 8-32 UNC THRU ALL

Title block:

	NAME	DATE
DRAWN	Alice	4/06/14
CHECKED		
ENG APPR.		
MFG APPR.		
Q.A.		
COMMENTS:		

UNLESS OTHERWISE SPECIFIED:
DIMENSIONS ARE IN INCHES
TOLERANCES:
FRACTIONAL±
ANGULAR: MACH± BEND±
.00 ±.01
.000 ±.005

INTERPRET GEOMETRIC
TOLERANCING PER:

MATERIAL
Acrylic

FINISH

DO NOT SCALE DRAWING

TITLE:

Cooling - Lid

SIZE **A**
DWG. NO. **1**
REV

SCALE: 1:2   WEIGHT: SHEET 1 OF 3

2   1

NEXT ASSY   USED ON
APPLICATION

Cooling - bottom

SIZE A | DWG. NO. | REV

SCALE: 1:2 | WEIGHT: | SHEET 3 OF 3

0.063

2 x Ø 0.136 ▼ 0.340
8-32 UNC ▼ 0.330

5.75
2.875
0.250

3.875
0.500
0.500
0.813
2.750
0.500
0.750

5.50
2.250
1.000

3.875
1.063

4 x Ø 0.136 ▼ 0.310
8-32 UNC ▼ 0.330

UNLESS OTHERWISE SPECIFIED:

DIMENSIONS ARE IN INCHES
TOLERANCES:
FRACTIONAL±
ANGULAR: MACH± BEND ±
.00 ±.01
.000 ±.005

INTERPRET GEOMETRIC
TOLERANCING PER:

MATERIAL Teflon

FINISH

DO NOT SCALE DRAWING

	NAME	DATE
DRAWN	Alice	4/06/14
CHECKED		
ENG APPR.		
MFG APPR.		
Q.A.		
COMMENTS:		

TITLE:

NEXT ASSY | USED ON
APPLICATION

Appendix

E.   Solidworks Thermo Map Study

A supervised master project.

University of California, Irvine

Department of Mechanical and Aerospace Engineer

M.S Project Report

Studying the Temperature Profile of a Heated Plate in Solid Works

Advisor: Professor. Derek Dunn-Rankin

Samboroth Kong

September 27, 2013

1

Content

Background

- Experiment Concept
- Goal of Simulation

Methods

- Introduction to SolidWorks
- Boundary Conditions

Geometry of Heat Source

- Size
- Power
- Boundary conditions

Results

- Hole
- Large Hole
- Puck
- Multiple Cylinders
- Optimize comparison with experimental plot

Conclusion

- Summary of the work
- Motivation
- Future work- Different Plate Shape, Plate size etc.

2

I.   Background

The study of the chemical in the smoke becomes more interesting in the science department since people who absorb the smoke would pass out easily after certain amount of time. The question was raised on what exactly release the poison smoke. This kind of curiosity has lead experimenters to test out the temperature profile of the steel plate that is a good representation of the steel structure of a building. The temperature profile of the heated steel plate will help experimenters to understand the behavior of the temperature distribution throughout the plate with the assumption that the temperature will distribute in the steady state manner, time independent.

The square painted plate is used as the sample and then it is heated with the methane flame. An infrared camera was used to take the picture of the top plate to see the temperature distribution on the plate. In order to get the good picture with good emissivity, the experimenter painted the plate black on the top side.

In order to verify the accuracy of the experiment, the theoretical calculation should be conducted. Therefore, in this case SolidWorks simulation is used to do the theoretically study of the temperature distribution on the heated plate with the purpose of matching the result with the experimental plot and go back to understand the experimental result.

II.   Methods

SolidWorks is one of the most power tool in twenty first century for engineering to perform 3D drawing, simulation which include stress, thermal, fatigue, buckle, and so on that allow the engineers to get the better estimation as much as the understand how the sample of the piece behave before the real piece will me be made. Therefore, in this case we used thermal study in the simulation to study the heated plate temperature distribution. Before proceed with the thermal study, the boundary conditions are needed to be defined on the plate. The natural convection were applied on all the six faces of the plate with 25 W/m^2 as the heat transfer coefficient and radiation were applied to both flat sides of the plate with emissivity of one with assumption that the plate is a black body.

III.   Geometry of the Heat Source

Geometry of the heat source that represents the flame is one of the important factors in the temperature profile of the plate. And the next important factors that affect the temperature distribution of the plate are the power supply that is input into the heat source to provide the temperature profile. Since there are more variables in term of the geometry of the heat source, the study of difference heat sources will be considered first.

First of all, a hole was cut in the middle of the plate with 6 mm diameter that represents the flame. Since the hole is the heat source, the heat power was only applied on the outer surface of the hole that was cut out from the plate. The thermal study of the plate with the hole shows that the hottest temperature is about 8000 degree Fahrenheit with 40 Watt power. The reason for the high temperature is that the plate has put on 40 Watt of power, so the temperature of the heat source has to be very high in order to deliver 40 Watt of heat source through the plate. However, the hottest temperature of the plate that represents the heat source on the plate is way higher than

3

the hottest temperature of the heat source from the experiment. Since the hole gives much higher temperature, the hole is not a good representation of the heated plate from the experiment.

Second of all, the second piece was made to be the heat source with one piece of cylinder with the same thickness as the plate. The one piece heat source was placed on top and in the middle of the plate. The plate material is stainless steel, so as the assigned material in SolidWorks in order to keep study as closely as the experiment. The one-piece heat source was assigned to be stainless steel at first, but since the thermal conductivity of the stainless steel is very low it affects the heat transfer from the heat source to plate. The low conductivity of the stainless steel from the heat source did not transfer the heat power that put into the heat source to the plate as efficient as it should be and as the result the temperature is still very high. Therefore, the copper heat source was used as the material of the heat source to avoid the effect of the low conductivity of the material that affect the temperature distribution on the plate. After the copper was used the heat source material, there size and the power input into the heat source are the new variables that effect the temperature distribution on the plate. At first, the size of the heat source had been varied from 6 mm diameter, 12 mm, diameter, 18 mm diameter, 24 mm diameter, and 30 mm diameter with the same heat power which is 40 Watt. The temperature of the plate is getting lower as we expected with the bigger heat source, but they were not still closed enough to the experimental temperature yet. Thus, the power input into the heat source had been varied in order to change the temperature distribution on the plate since the size of the heat source did not give enough effect that potentially matching the result with the experimental result. Lower heat power was applied to different diameter of the heat source and of course the larger heat source will drop the temperature faster with the lower the heat power compare the smaller heat source. The results of all the trial will be under the result section.

Third of all, multiple pieces of heat source was assembled together in order to become one heat source. For this multiple heat source, the cylinder shape is still used with different diameter. The multiple heat sources allow us to divide heat power into more pieces which would change the temperature of the plate. The number of heat source pieces were tried out from 4 pieces, 6 pieces, 8 pieces and 10 pieces and they number of the pieces did not give much effect on the temperature of the plate, so the 4 pieces was chosen to be used to see the result of the iteration in term of power distribution among the 4 pieces, different power, and the size of the 4-piece together. There are 3 different variations that we can change in the heat source in order to change the temperature distribution on the plate. First, the total size of the assembled four pieces was increased with the same power input and the uniform distribution among each piece. Second, the total heat power input was lower with the same size, and the uniform distribution among each piece. Third, the power distribution was varied with the higher power input in the middle and less or none in the other three pieces without the same power input and the constant size of the total heat source.

All three variations above are part of trial and error testing to see which variation has the most sensitive effect on the temperature of the plate. Therefore, the last trial the 6 mm size heat source was used in order to get the same proportion between the experimental result and the SolidWorks result. Thus, the heat power will be the most important factor that can change the temperature on the plate. Therefore, another trial and error continued with the lower power input with 6 mm diameter. After the third trial, the result showed that the 4-piece heat source did not give much effect on the temperature on the plate with different size and different distribution

4

among the pieces with lower heat power, so the 4-piece would not be considered in the final result anymore. Then, the only heat source that would be considered is one piece cylinder with different power source. At the same time, the actual heat power from the flame in the experiment was calculated to get the exact power that the flame provides the plate which is equaled to 0.7 Watt. Furthermore, the exact power source was applied to the SolidWorks to see the temperature distribution on the plate and then compare to the experimental result.

IV.   Results

The result from drilling a hole in the middle of the plate which represents the heat source with the same heat power at 40W with increasing diameter from 6 mm, 12mm, 18mm, and 24mm represents in the table below. And then there is a comparison between two thermal studies with the same diameter, 24mm, and different heat power. The diameter increases multiple times with slower effect on the temperature on the plate than the lower the decreasing of the heat power input. The pictures of the SolidWorks below are the example of the thermal study that has been done on the heated plate with the hole in the middle.

Table1: The comparison with different diameter size.

Heat Source	Hole				
Power Input	40W	40W	40W	40W	25W
Diameter	6mm	12mm	18mm	24mm	24mm
Temperature	1639K	1280K	1100K	984K	754K

Figure1: Plate with 24mm Hole, and 40 W power- input
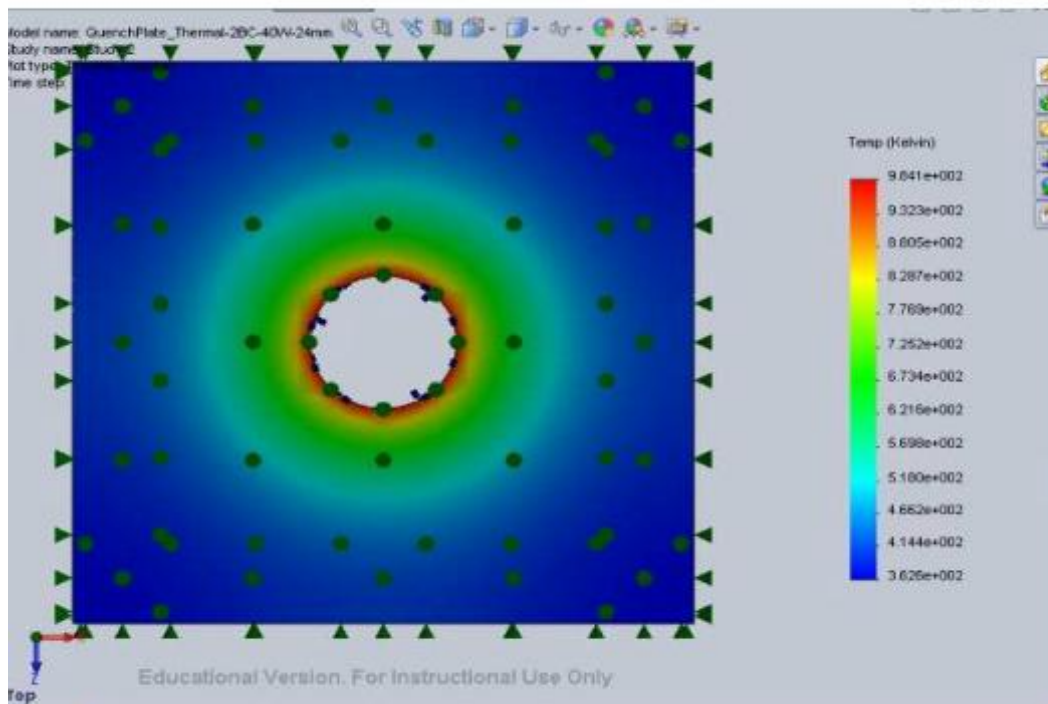
Figure 2: Plate with 24mm-Hole and 25 W power-input.
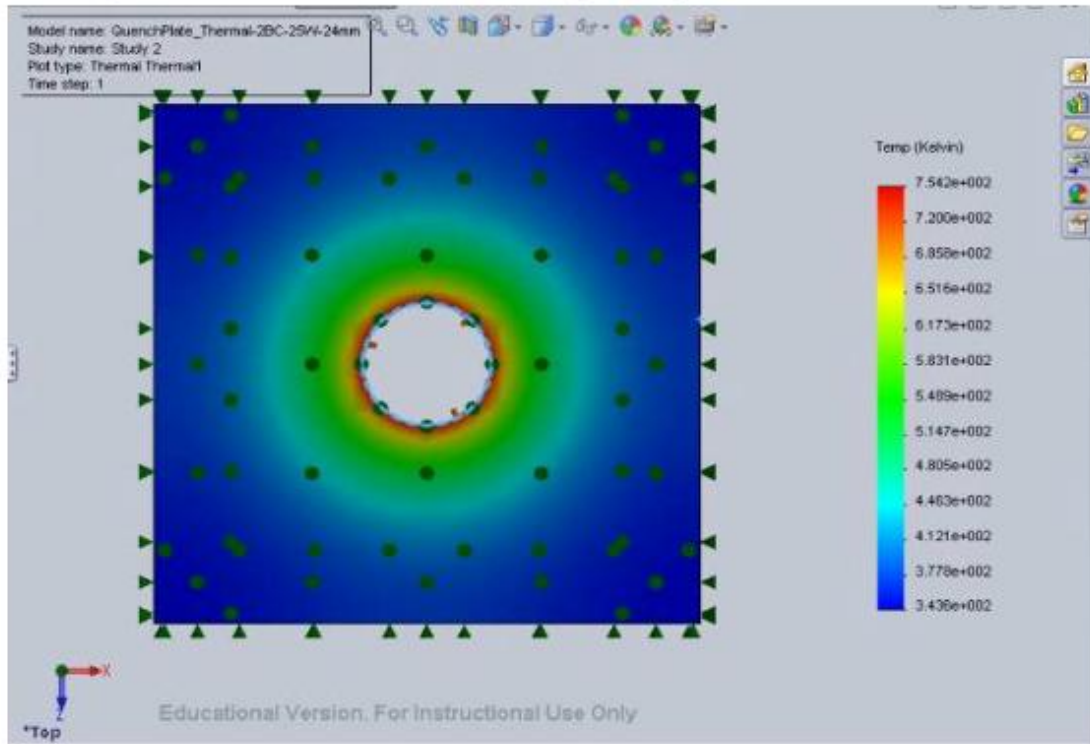
The result from comparison between different materials of the heat source is in the table below. Between stainless and copper for the temperature drop about 100 degree Kelvin with everything else stay constant. Copper has higher thermal conductivity, so the heat that applied into the heat source will be mostly transferred to the plate with very minimal lost compare to stainless steel. Therefore, copper will be used as the heat source material from now on for the sake of study of the plate temperature.

Table 2: The comparison between stainless steel and copper material of heat source

Heat Source	Cylinder							
Power Input(W)	40	40	25	25	40	40	25	25
Type of Material	Stainless	Copper	Stainless	Copper	Stainless	Copper	Stainless	Copper
Diameter(mm)	24	24	24	24	24	24	24	24
Number of Pieces	1	1	1	1	4	4	4	4
Temperature(K)	1204	1109	939	879	1467	1207	1144	965

6

Figure 3: Plate with 25W Stainless Steel Cylinder Heat Source and 24mm Diameter
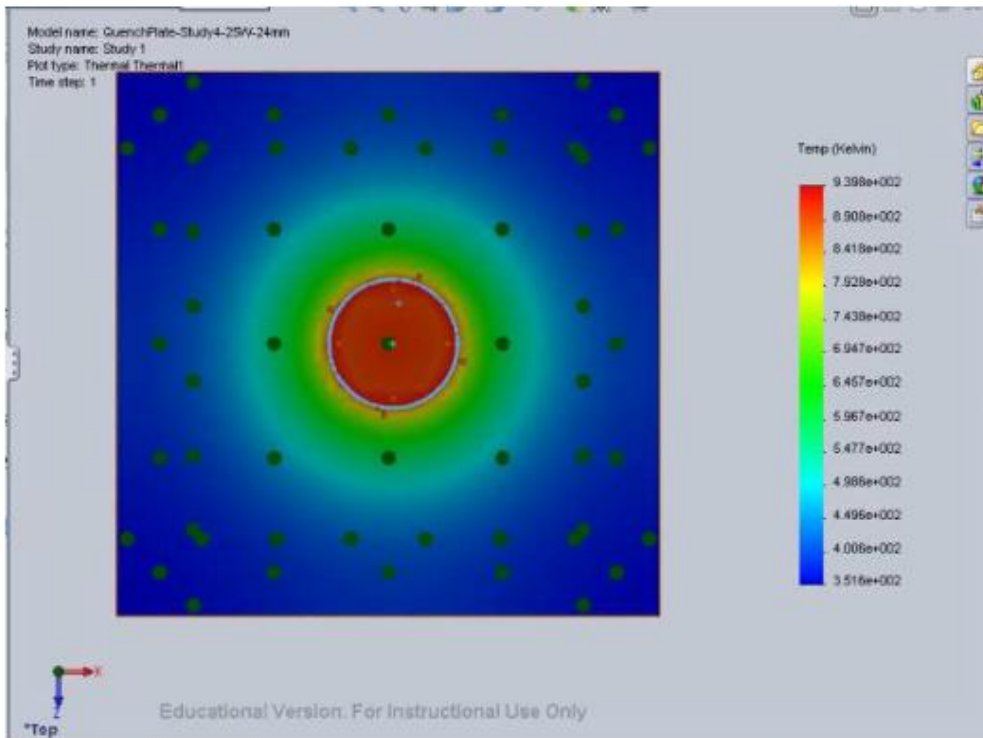
Figure 4: Plate with 25W Copper Cylinder Heat Source and 24mm Diameter.
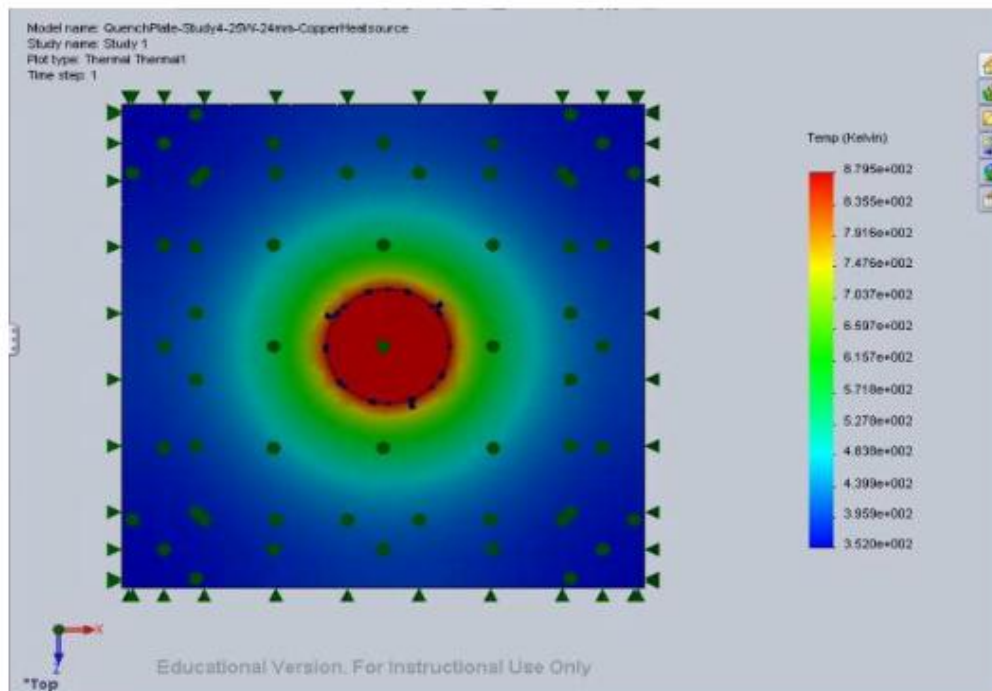
This is part of the second trial that one piece of cylinder was used as the heat source with 40W heat power and diameter was increased to see the different in the temperature of the plate. And here we can see that the temperature of the plate would change in the fair amount at 24 mm diameter that leaded to more investigating the bigger diameter with lower heat power. It is interesting to see how much the temperature of the plate would change when the diameter of the heat source gets even bigger with a lower heat power. Those results of that study will be show in Table 4 below.

Table 3: Comparison effect of the diameter of the Cylinder Heat Source

Heat Source	Cylinder			
Power Input(W)	40	40	40	40
Type of Material	Stainless	Stainless	Stainless	Stainless
Diameter(mm)	6	12	18	24
Number of Pieces	1	1	1	1
Temperature (K)	2653	1769	1413	1204

Table 4: The temperature results from bigger diameter along with lower heat power.

Heat Source	Cylinder											
Power Input (W)	40W	25W	25W	25W	20W	20W	18W	18W	15W	15W	12W	12W
Type of Material	Copper	Copper	Copper	Copper	Copper	Copper	Copper	Copper	Copper	Copper	Copper	Copper
Diameter(mm)	24mm	24mm	30mm	36mm	30mm	36mm	30mm	36mm	30mm	36mm	30mm	36mm
Number of Pieces	1	1	1	1	1	1	1	1	1	1	1	1
Temperature(K)	1109	879	788.5	720.7	707.9	649.9	673.3	619.7	618.8	572.3	560.9	522.4

This part is the part where the number of pieces of the heat source had been increased in order to see how much the effect can on the temperature of the plate. The results show in Table 5 and then Table 6 is the study of 4-piece heat source with different diameter and different power input since the table 5 clearly shows that the number of pieces did not have much effect on the temperature of the plate. Table 6 is the summary of the results of the uniform distributed 4-piece heat source with different total heat input and different diameters. In table 6, the combination of the 12W heat power and the 36 mm 4-piece diameter heat source gives the closest temperature of 560 degree Kelvin to the experimental temperature which is 525 degree Kelvin. However, the diameter is very large compare to the experimental heat source where the diameter of the flame is about 6 mm from the IR camera. One of the goals in this study is to match the experimental temperature and the picture from SolidWorks to the picture from the IR camera, so in this case the diameter is much bigger than the experimental picture.

8 |

Table 5: Effect on the Temperature of the Plate with increased number of pieces assemble in the heat source

Heat Source	Cylinder		
Power Input(W)	24	24	24
Type of Material	Copper	Copper	Copper
Diameter(mm)	30	30	30
Number of Pieces	4	6	8
Temperature(K)	843	851.7	856.1

Table 6: Effect on the Temperature of the Plate with increased diameter of the 4-piece heat source and decreased power input

Heat Source	Cylinder					
Power Input (W)	20	20	16	16	12	12
Type of Material	Copper	Copper	Copper	Copper	Copper	Copper
Diameter(mm)	30	36	30	36	30	36
Number of Pieces	4	4	4	4	4	4
Temperature (K)	770.6	706.3	691.3	636.6	604.4	560.8

Tables 7,8,9 are the results of the effect on the temperature at three different cylinder diameters, 24mm, 18mm, and 12mm at 4 different heat power which are 12, 10, 8 and 6 Watt. At each power input, between 24mm and 18 mm the temperature is about 50 degree Kelvin different. However, at the same power input between 18mm and 12 mm, the temperature different is about 100 degree Kelvin. The temperature is getting less sensitive at the same heat power as the diameter getting larger. The temperature gets much closed to the experimental temperature, but the diameter is still too large compare to the experimental picture.

Table 7: Effect on the Plate at 24mm diameter cylinder heat source with decreasing heat power.

Heat Source	Cylinder			
Power Input (W)	12	10	8	6
Type of Material	Copper	Copper	Copper	Copper
Diameter(mm)	24	24	24	24
Number of Pieces	1	1	1	1
Temperature(K)	613.1	565.1	515	463.2

9

Table 8: Effect on the Plate at 18mm diameter cylinder heat source with decreasing heat power

Heat Source	Cylinder			
Power Input (W)	12	10	8	6
Type of Material	Copper	Copper	Copper	Copper
Diameter(mm)	18	18	18	18
Number of Pieces	1	1	1	1
Temperature(K)	687.9	628.9	567.3	503.2

Table 9: Effect on the Plate at 12mm diameter cylinder heat source with decreasing heat power

Heat Source	Cylinder			
Power Input (W)	12	10	8	6
Type of Material	Copper	Copper	Copper	Copper
Diameter(mm)	12	12	12	12
Number of Pieces	1	1	1	1
Temperature(K)	807.7	731.3	651.2	567.4

From Table 10 to 14 are the results from the study of the 4-piece cylinder heat source with different diameter, different power source and different distribution among the pieces. It is expected that the higher the heat power in the middle gives lower temperature on the plate. After all the studies with 4-piece, we realized that it is not much of the effect with the 4-piece compare with the single piece cylinder. Therefore, the study of a single piece of heat source should be considered again.

Table 10: Effect on the Plate at 24mm diameter 4-piece cylinder heat source with decreasing heat power

Heat Source	Cylinder				
Power Input (W)	12	12	10	10	10
Type of Material	Copper	Copper	Copper	Copper	Copper
Diameter(mm)	24	24	24	24	24
Distribution(inner-outer)	Uniform	6-2-2-2	Uniform	7-1-1-1	4-2-2-2
Number of Pieces	4	4	4	4	4
Temperature(K)	663.1	614.2	608.2	530.4	582.9

Table 11: Effect on the Plate at 18 mm diameter 4-piece cylinder heat source with decreasing heat power and different distribution

10

Heat Source	Cylinder											
Power Input (W)	12	12	12	10	10	10	8	8	8	6	6	6
Type of Material	Copper	Copper	Copper	Copper	Copper	Copper	Copper	Copper	Copper	Copper	Copper	Copper
Diameter(mm)	18	18	18	18	18	18	18	18	18	18	18	18
Distribution(inner-outer)	Uniform	6-2-2-2	7-2.5-1.5-1	Uniform	7-1-1-1	4-2-2-2	Uniform	5-1-1-1	6.5-0.5-0.5-0.5	Uniform	3-1-1-1	4.5-0.5-0.5-0.5
Number of Pieces	4	4	4	4	4	4	4	4	4	4	4	4
Temperature(K)	747.4	660	688	681	585	650	611	544	510	537	503	467

Table 12: Effect on the Plate at 12 mm diameter 4-piece cylinder heat source with decreasing heat power and different distribution

Heat Source	Cylinder											
Power Input (W)	12	12	12	10	10	10	8	8	8	6	6	6
Type of Material	Copper	Copper	Copper	Copper	Copper	Copper	Copper	Copper	Copper	Copper	Copper	Copper
Diameter(mm)	12	12	12	12	12	12	12	12	12	12	12	12
Distribution(inner-outer)	Uniform	6-2-2-2	7-2.5-1.5-1	Uniform	7-1-1-1	4-2-2-2	Uniform	5-1-1-1	6.5-0.5-0.5-0.5	Uniform	3-1-1-1	4.5-0.5-0.5-0.5
Number of Pieces	4	4	4	4	4	4	4	4	4	4	4	4
Temperature(K)	881.2	834	803	796	720	771	705	652	625	610	582	554

Table 13: Effect on the Plate at 10 mm diameter 4-piece cylinder heat source with constant heat power and different distribution

Heat Source	Cylinder						
Power Input (W)	6	6	6	6	6	6	6
Type of Material	Copper	Copper	Copper	Copper	Copper	Copper	Copper
Diameter(mm)	10	10	10	10	10	10	10
Distribution(inner-outer)	Uniform	3-1-1-1	4.5-0.5-0.5-0.5	5.4-0.2-0.2-0.2	5.7-0.1-0.1-0.1	5.1-0.3-0.3-0.3	6-0-0-0
Number of Pieces	4	4	4	4	4	4	4
Temperature(K)	645.8	595	543	511	500	522	490

Table 14: Effect on the Plate at 6 mm diameter 4-piece cylinder heat source with constant heat power and different distribution

Heat Source	Cylinder						
Power Input (W)	6	6	6	6	6	6	6
Type of Material	Copper	Copper	Copper	Copper	Copper	Copper	Copper
Diameter(mm)	6	6	6	6	6	6	6
Distribution(inner-outer)	Uniform	3-1-1-1	4.5-0.5-0.5-0.5	5.4-0.2-0.2-0.2	5.7-0.1-0.1-0.1	5.1-0.3-0.3-0.3	6-0-0-0
Number of Pieces	4	4	4	4	4	4	4
Temperature(K)	755.5	688	619	576	562	590	548

Table 15 is the summary of the study of a single piece of cylinder heat source at different power input and the study of the exact heat input from the experimental flame which is 0.7 Watt. The exact power did not give the temperature as the IR camera showed. However, at 2.35Watt the temperature is 523 degree Kelvin which is exactly as the temperature of the plate from the experiment and picture from the IR camera and the SolidWorks is also matched.

Table 15: Effect on the Plate with a single piece of cylinder at different heat power

Heat Source	Cylinder				
Power Input (W)	6	6	0.7	0.7	2.35
Type of Material	Copper	Copper	Copper	Copper	
Diameter(mm)	10	6	6	3	3
Number of Pieces	1	1	1	1	1
Temperature(K)	599	696	346	366	523

Figure 5: Plate with 6W power, 10mm diameter and copper material
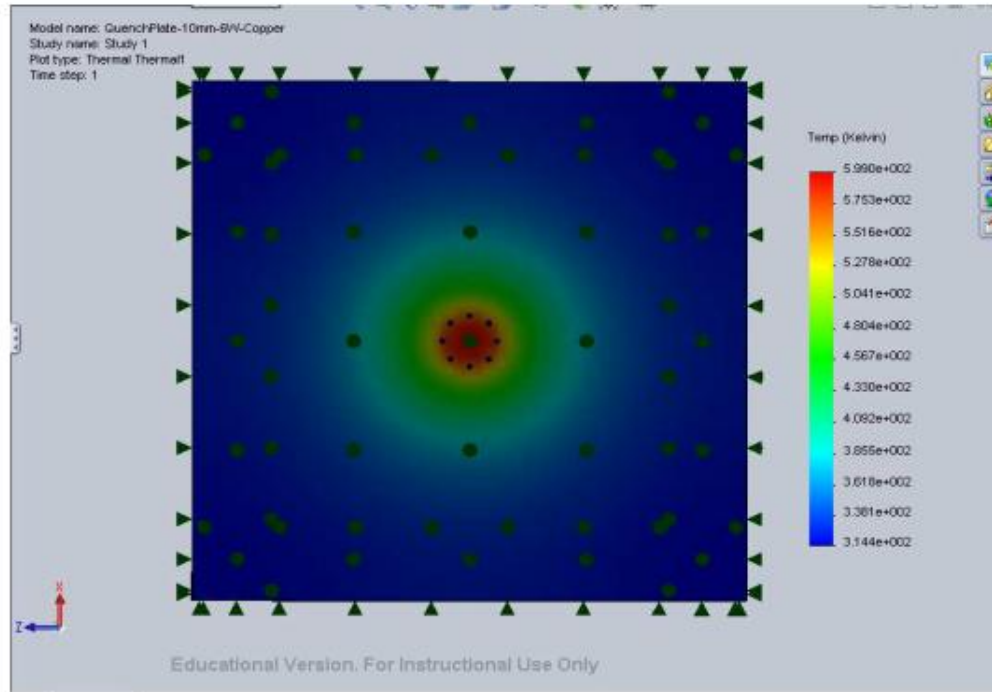
Figure 6: Plate with 6W, 6 mm diameter, and copper material
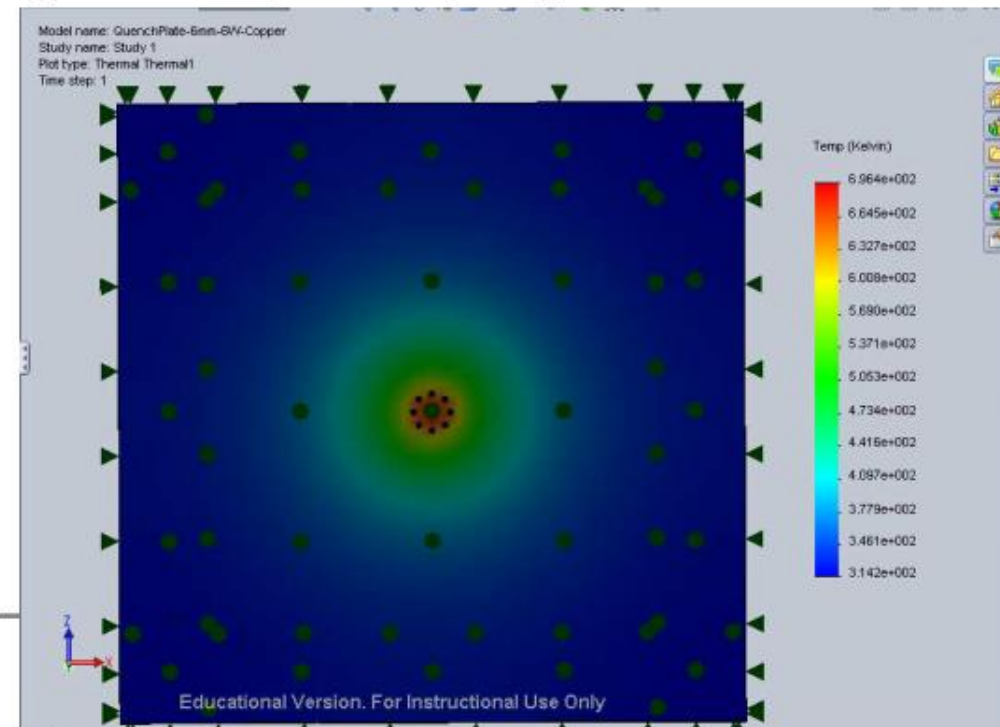
Figure 7: Plate with 0.7 W, 6 mm diameter and copper material
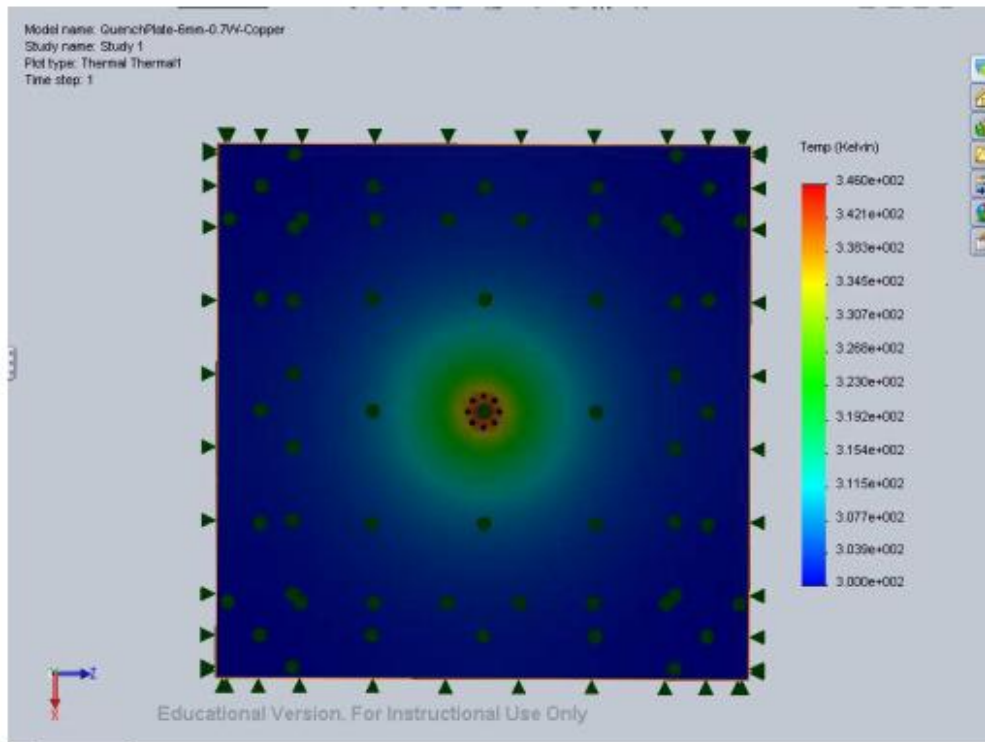
Figure 8: Plate with 0.7W, 3 mm diameter and copper material
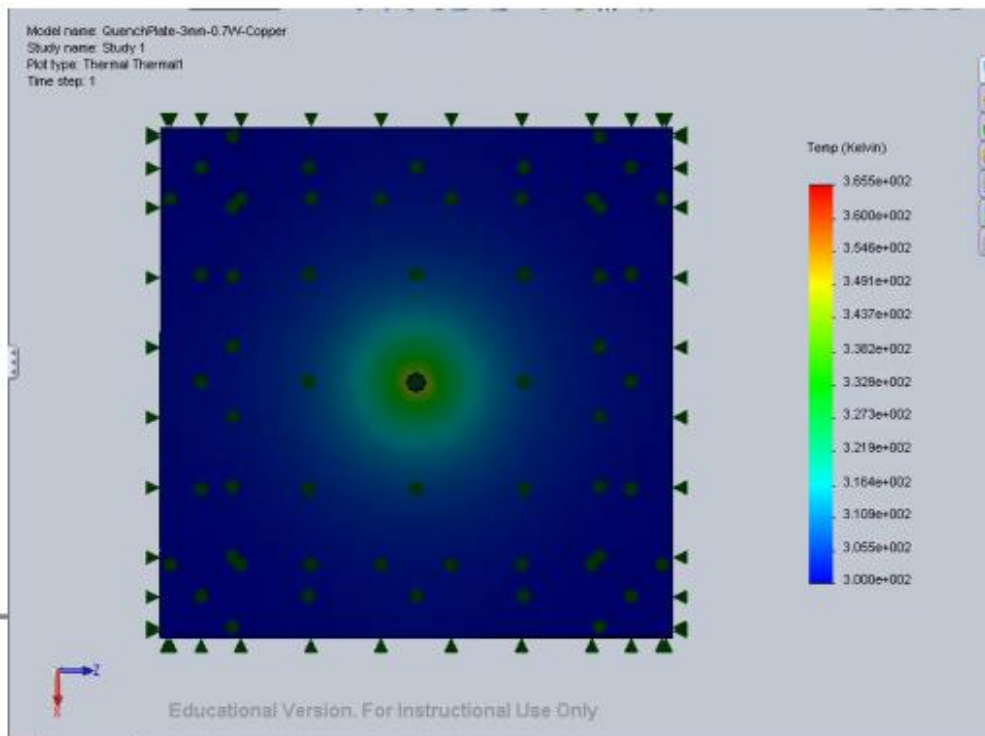
Figure 9: Plate with 2.35W, 3 mm diameter and copper material
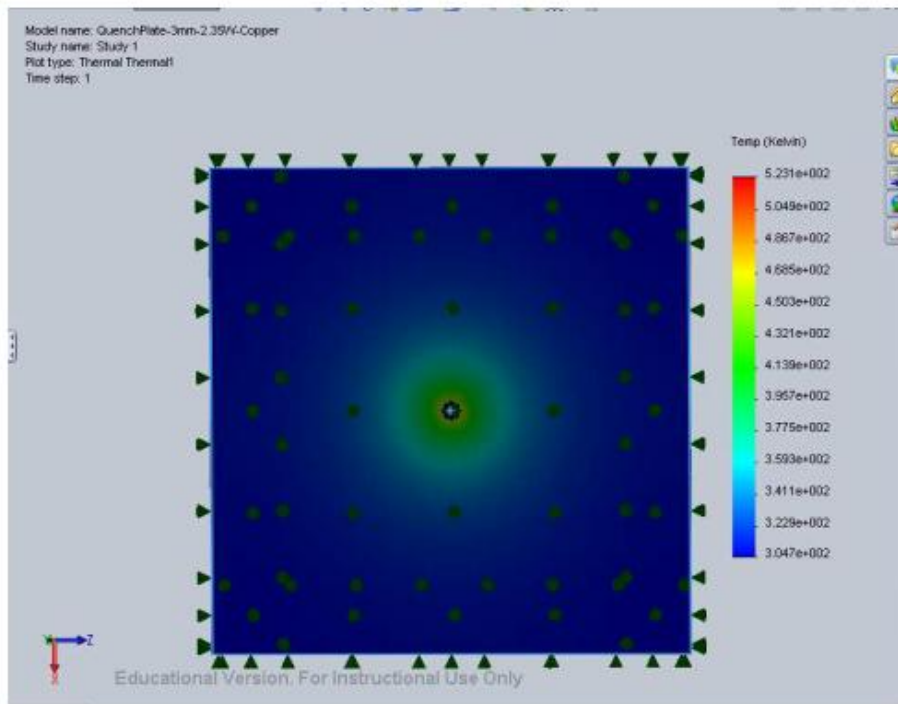
Plot 1: Temperature distribution on the top plate of 3mm diameter and 2.35W power input
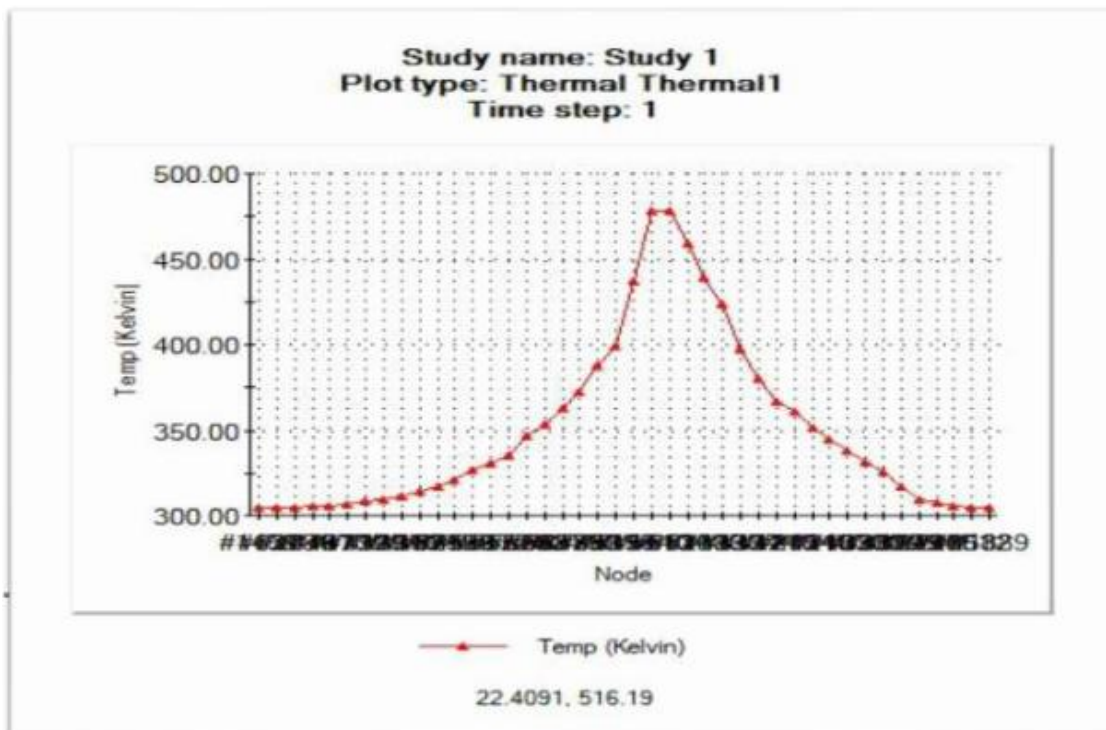
Plot 2: The Experimental Plot of the Temperature distribution of the plate in degree Celsius for the Zero volt
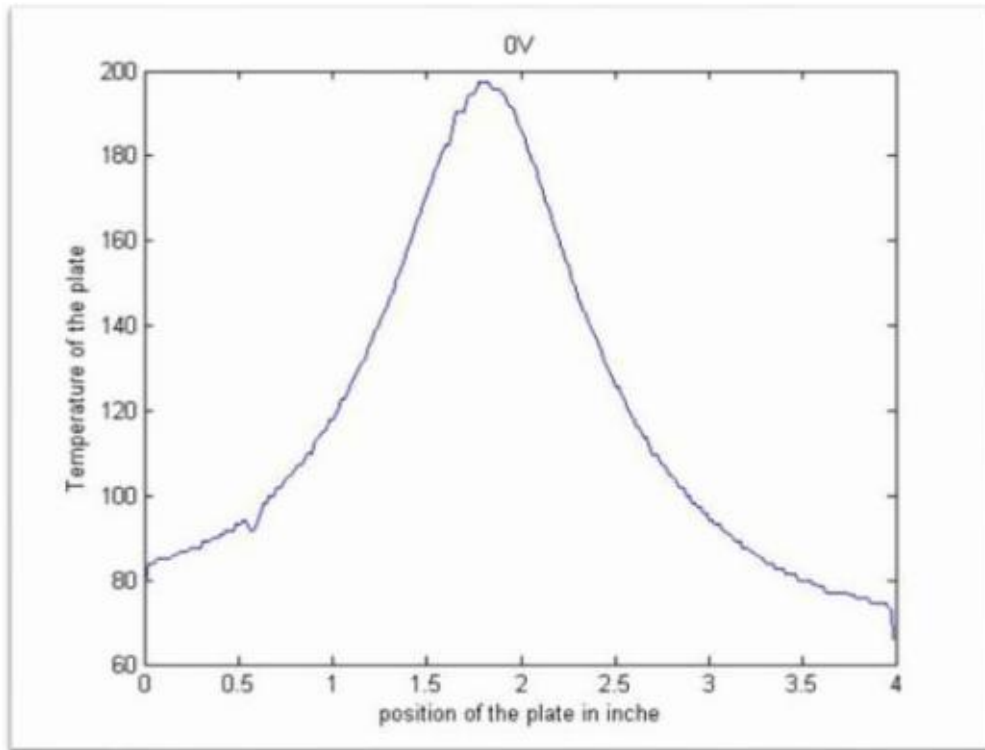
Figure 10: Picture from the IR camera of the top plate
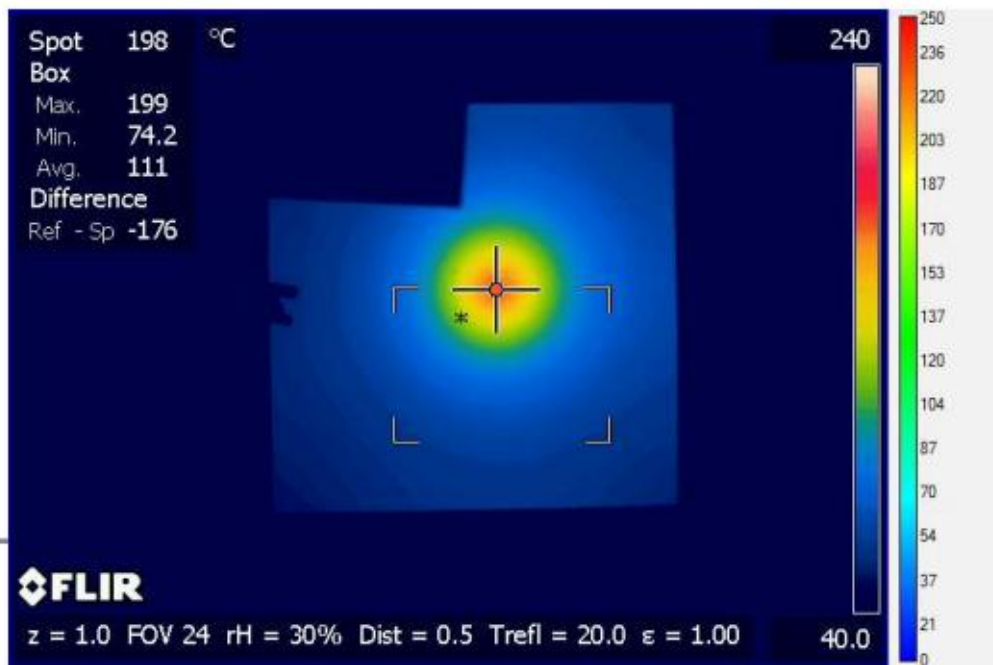
Figure 9 and 10 and plot 1 and 2, are the comparison of the experimental pictures and plots with the SolidWorks. The plots and the pictures match the closest with one another, so the last trial is the 3mm diameter with 2.35 Watt as the final result.

V.   Conclusion

In short, after many trials and errors in term of the geometry of the heat source, the power input, the material of the heat source, and power distribution, and number of pieces of the heat source, we have better understand how those factors affect the temperature distribution on the plate that represent the actual heated plate by the methane flame in the lab. So after the study in SolidWorks, it is clear that the flame did not give off the exact heat power as we thought it did. The heat power has the most effective on the temperature of the plate and the distribution on the plate than any other factors that were study above. However, there are still many other factors that we can play around such as the shape of the heat source that we can investigate more in deep in order to see the effect and to also try to get the best result out of these studies. The future study can be done by changing shape of the heat source, and matching the point by point from the plots from experiment to the SolidWorks plot.

Appendix

F. Chemkin Kinetics, Transport and Thermo files

Kinetic file

! GRI-Mech Version 3.0 7/30/99 CHEMKIN-II format
! See README30 file at anonymous FTP site unix.sri.com, directory gri;
! WorldWideWeb home page http://www.me.berkeley.edu/gri_mech/ or
! through http://www.gri.org , under 'Basic Research',
! for additional information, contacts, and disclaimer
ELEMENTS
O H C N AR E
END
SPECIES
H2   H   O   O2   OH   H2O   HO2   H2O2
C   CH   CH2   CH2(S)   CH3   CH4   CO   CO2
HCO   CH2O   CH2OH   CH3O   CH3OH   C2H   C2H2   C2H3
C2H4   C2H5   C2H6   HCCO   CH2CO   HCCOH   N   NH
NH2   NH3   NNH   NO   NO2   N2O   HNO   CN
HCN   H2CN   HCNN   HCNO   HOCN   HNCO   NCO   N2
AR   C3H7   C3H8   CH2CHO   CH3CHO
C2H5OH
E
HCO+
H3O+
C2H3O+
O2-
OH-
CHO2-
O-
!C2
OH*
CH*
END
!THERMO
! Insert GRI-Mech thermodynamics here or use in default file
!END
REACTIONS
2O+M<=>O2+M   1.200E+17   -1.000   .00
H2/ 2.40/ H2O/15.40/ CH4/ 2.00/ CO/ 1.75/ CO2/ 3.60/ C2H6/ 3.00/ AR/ .83/
O+H+M<=>OH+M   5.000E+17   -1.000   .00
H2/2.00/ H2O/6.00/ CH4/2.00/ CO/1.50/ CO2/2.00/ C2H6/3.00/ AR/ .70/
O+H2<=>H+OH   3.870E+04   2.700   6260.00
O+HO2<=>OH+O2   2.000E+13   .000   .00
O+H2O2<=>OH+HO2   9.630E+06   2.000   4000.00
O+CH<=>H+CO   5.700E+13   .000   .00
O+CH2<=>H+HCO   8.000E+13   .000   .00
O+CH2(S)<=>H2+CO   1.500E+13   .000   .00
O+CH2(S)<=>H+HCO   1.500E+13   .000   .00
O+CH3<=>H+CH2O   5.060E+13   .000   .00
O+CH4<=>OH+CH3   1.020E+09   1.500   8600.00

```
O+CO(+M)<=>CO2(+M)                              1.800E+10      .000     2385.00
    LOW/ 6.020E+14      .000     3000.00/
H2/2.00/ O2/6.00/ H2O/6.00/ CH4/2.00/ CO/1.50/ CO2/3.50/ C2H6/3.00/ AR/ .50/
O+HCO<=>OH+CO                                   3.000E+13      .000        .00
O+HCO<=>H+CO2                                   3.000E+13      .000        .00
O+CH2O<=>OH+HCO                                 3.900E+13      .000     3540.00
O+CH2OH<=>OH+CH2O                               1.000E+13      .000        .00
O+CH3O<=>OH+CH2O                                1.000E+13      .000        .00
O+CH3OH<=>OH+CH2OH                              3.880E+05     2.500     3100.00
O+CH3OH<=>OH+CH3O                               1.300E+05     2.500     5000.00
O+C2H<=>CH+CO                                   5.000E+13      .000        .00
O+C2H2<=>H+HCCO                                 1.350E+07     2.000     1900.00
O+C2H2<=>OH+C2H                                 4.600E+19    -1.410    28950.00
O+C2H2<=>CO+CH2                                 6.940E+06     2.000     1900.00
O+C2H3<=>H+CH2CO                                3.000E+13      .000        .00
O+C2H4<=>CH3+HCO                                1.250E+07     1.830      220.00
O+C2H5<=>CH3+CH2O                               2.240E+13      .000        .00
O+C2H6<=>OH+C2H5                                8.980E+07     1.920     5690.00
O+HCCO<=>H+2CO                                  1.000E+14      .000        .00
O+CH2CO<=>OH+HCCO                               1.000E+13      .000     8000.00
O+CH2CO<=>CH2+CO2                               1.750E+12      .000     1350.00
O2+CO<=>O+CO2                                   2.500E+12      .000    47800.00
O2+CH2O<=>HO2+HCO                               1.000E+14      .000    40000.00
H+O2+M<=>HO2+M                                  2.800E+18     -.860        .00
O2/ .00/ H2O/ .00/ CO/ .75/ CO2/1.50/ C2H6/1.50/ N2/ .00/ AR/ .00/
H+2O2<=>HO2+O2                                  2.080E+19    -1.240        .00
H+O2+H2O<=>HO2+H2O                              11.26E+18     -.760        .00
H+O2+N2<=>HO2+N2                                2.600E+19    -1.240        .00
H+O2+AR<=>HO2+AR                                7.000E+17     -.800        .00
H+O2<=>O+OH                                     2.650E+16    -.6707    17041.00
2H+M<=>H2+M                                     1.000E+18    -1.000        .00
H2/ .00/ H2O/ .00/ CH4/2.00/ CO2/ .00/ C2H6/3.00/ AR/ .63/
2H+H2<=>2H2                                     9.000E+16     -.600        .00
2H+H2O<=>H2+H2O                                 6.000E+19    -1.250        .00
2H+CO2<=>H2+CO2                                 5.500E+20    -2.000        .00
H+OH+M<=>H2O+M                                  2.200E+22    -2.000        .00
H2/ .73/ H2O/3.65/ CH4/2.00/ C2H6/3.00/ AR/ .38/
H+HO2<=>O+H2O                                   3.970E+12      .000      671.00
H+HO2<=>O2+H2                                   4.480E+13      .000     1068.00
H+HO2<=>2OH                                     0.840E+14      .000      635.00
H+H2O2<=>HO2+H2                                 1.210E+07     2.000     5200.00
H+H2O2<=>OH+H2O                                 1.000E+13      .000     3600.00
H+CH<=>C+H2                                     1.650E+14      .000        .00
H+CH2(+M)<=>CH3(+M)                             6.000E+14      .000        .00
    LOW  /  1.040E+26    -2.760    1600.00/
     TROE/   .5620  91.00  5836.00  8552.00/
H2/2.00/ H2O/6.00/ CH4/2.00/ CO/1.50/ CO2/2.00/ C2H6/3.00/ AR/ .70/
```

```
H+CH2(S)<=>CH+H2                              3.000E+13     .000        .00
H+CH3(+M)<=>CH4(+M)                           13.90E+15    -.534     536.00
    LOW  /  2.620E+33   -4.760   2440.00/
    TROE/  .7830   74.00  2941.00  6964.00 /
H2/2.00/ H2O/6.00/ CH4/3.00/ CO/1.50/ CO2/2.00/ C2H6/3.00/ AR/ .70/
H+CH4<=>CH3+H2                                6.600E+08    1.620   10840.00
H+HCO(+M)<=>CH2O(+M)                          1.090E+12     .480    -260.00
    LOW  /  2.470E+24   -2.570    425.00/
    TROE/  .7824  271.00  2755.00  6570.00 /
H2/2.00/ H2O/6.00/ CH4/2.00/ CO/1.50/ CO2/2.00/ C2H6/3.00/ AR/ .70/
H+HCO<=>H2+CO                                 7.340E+13     .000        .00
H+CH2O(+M)<=>CH2OH(+M)                        5.400E+11     .454    3600.00
    LOW  /  1.270E+32   -4.820   6530.00/
    TROE/  .7187  103.00  1291.00  4160.00 /
H2/2.00/ H2O/6.00/ CH4/2.00/ CO/1.50/ CO2/2.00/ C2H6/3.00/
H+CH2O(+M)<=>CH3O(+M)                         5.400E+11     .454    2600.00
    LOW  /  2.200E+30   -4.800   5560.00/
    TROE/  .7580   94.00  1555.00  4200.00 /
H2/2.00/ H2O/6.00/ CH4/2.00/ CO/1.50/ CO2/2.00/ C2H6/3.00/
H+CH2O<=>HCO+H2                               5.740E+07    1.900    2742.00
H+CH2OH(+M)<=>CH3OH(+M)                       1.055E+12     .500      86.00
    LOW  /  4.360E+31   -4.650   5080.00/
    TROE/  .600  100.00  90000.0  10000.0 /
H2/2.00/ H2O/6.00/ CH4/2.00/ CO/1.50/ CO2/2.00/ C2H6/3.00/
H+CH2OH<=>H2+CH2O                             2.000E+13     .000        .00
H+CH2OH<=>OH+CH3                              1.650E+11     .650    -284.00
H+CH2OH<=>CH2(S)+H2O                          3.280E+13    -.090     610.00
H+CH3O(+M)<=>CH3OH(+M)                        2.430E+12     .515      50.00
    LOW  /  4.660E+41   -7.440   14080.0/
    TROE/  .700  100.00  90000.0 10000.00 /
H2/2.00/ H2O/6.00/ CH4/2.00/ CO/1.50/ CO2/2.00/ C2H6/3.00/
H+CH3O<=>H+CH2OH                              4.150E+07    1.630    1924.00
H+CH3O<=>H2+CH2O                              2.000E+13     .000        .00
H+CH3O<=>OH+CH3                               1.500E+12     .500    -110.00
H+CH3O<=>CH2(S)+H2O                           2.620E+14    -.230    1070.00
H+CH3OH<=>CH2OH+H2                            1.700E+07    2.100    4870.00
H+CH3OH<=>CH3O+H2                             4.200E+06    2.100    4870.00
H+C2H(+M)<=>C2H2(+M)                          1.000E+17   -1.000        .00
    LOW  /  3.750E+33   -4.800   1900.00/
    TROE/  .6464  132.00  1315.00  5566.00 /
H2/2.00/ H2O/6.00/ CH4/2.00/ CO/1.50/ CO2/2.00/ C2H6/3.00/ AR/ .70/
H+C2H2(+M)<=>C2H3(+M)                         5.600E+12     .000    2400.00
    LOW  /  3.800E+40   -7.270   7220.00/
    TROE/  .7507   98.50  1302.00  4167.00 /
H2/2.00/ H2O/6.00/ CH4/2.00/ CO/1.50/ CO2/2.00/ C2H6/3.00/ AR/ .70/
H+C2H3(+M)<=>C2H4(+M)                         6.080E+12     .270     280.00
    LOW  /  1.400E+30   -3.860   3320.00/
```

```
      TROE/   .7820  207.50  2663.00  6095.00 /
H2/2.00/ H2O/6.00/ CH4/2.00/ CO/1.50/ CO2/2.00/ C2H6/3.00/ AR/ .70/
H+C2H3<=>H2+C2H2                         3.000E+13    .000        .00
H+C2H4(+M)<=>C2H5(+M)                    0.540E+12    .454     1820.00
      LOW  /  0.600E+42   -7.620   6970.00/
      TROE/   .9753  210.00   984.00  4374.00 /
H2/2.00/ H2O/6.00/ CH4/2.00/ CO/1.50/ CO2/2.00/ C2H6/3.00/ AR/ .70/
H+C2H4<=>C2H3+H2                         1.325E+06    2.530   12240.00
H+C2H5(+M)<=>C2H6(+M)                    5.210E+17    -.990    1580.00
      LOW  /  1.990E+41   -7.080   6685.00/
      TROE/   .8422  125.00  2219.00  6882.00 /
H2/2.00/ H2O/6.00/ CH4/2.00/ CO/1.50/ CO2/2.00/ C2H6/3.00/ AR/ .70/
H+C2H5<=>H2+C2H4                         2.000E+12    .000        .00
H+C2H6<=>C2H5+H2                         1.150E+08    1.900    7530.00
H+HCCO<=>CH2(S)+CO                       1.000E+14    .000        .00
H+CH2CO<=>HCCO+H2                        5.000E+13    .000     8000.00
H+CH2CO<=>CH3+CO                         1.130E+13    .000     3428.00
H+HCCOH<=>H+CH2CO                        1.000E+13    .000        .00
H2+CO(+M)<=>CH2O(+M)                     4.300E+07    1.500   79600.00
      LOW  /  5.070E+27   -3.420   84350.00/
      TROE/   .9320  197.00  1540.00 10300.00 /
H2/2.00/ H2O/6.00/ CH4/2.00/ CO/1.50/ CO2/2.00/ C2H6/3.00/ AR/ .70/
OH+H2<=>H+H2O                            2.160E+08    1.510    3430.00
2OH(+M)<=>H2O2(+M)                       7.400E+13    -.370        .00
      LOW  /  2.300E+18   -.900   -1700.00/
      TROE/   .7346   94.00  1756.00  5182.00 /
H2/2.00/ H2O/6.00/ CH4/2.00/ CO/1.50/ CO2/2.00/ C2H6/3.00/ AR/ .70/
2OH<=>O+H2O                              3.570E+04    2.400   -2110.00
OH+HO2<=>O2+H2O                          1.450E+13    .000     -500.00
 DUPLICATE
OH+H2O2<=>HO2+H2O                        2.000E+12    .000      427.00
 DUPLICATE
OH+H2O2<=>HO2+H2O                        1.700E+18    .000    29410.00
 DUPLICATE
OH+C<=>H+CO                              5.000E+13    .000        .00
OH+CH<=>H+HCO                            3.000E+13    .000        .00
OH+CH2<=>H+CH2O                          2.000E+13    .000        .00
OH+CH2<=>CH+H2O                          1.130E+07    2.000    3000.00
OH+CH2(S)<=>H+CH2O                       3.000E+13    .000        .00
OH+CH3(+M)<=>CH3OH(+M)                   2.790E+18    -1.430    1330.00
      LOW  /  4.000E+36   -5.920   3140.00/
      TROE/   .4120  195.0  5900.00  6394.00/
H2/2.00/ H2O/6.00/ CH4/2.00/ CO/1.50/ CO2/2.00/ C2H6/3.00/
OH+CH3<=>CH2+H2O                         5.600E+07    1.600    5420.00
OH+CH3<=>CH2(S)+H2O                      6.440E+17    -1.340    1417.00
OH+CH4<=>CH3+H2O                         1.000E+08    1.600    3120.00
OH+CO<=>H+CO2                            4.760E+07    1.228      70.00
```

```
OH+HCO<=>H2O+CO                          5.000E+13      .000        .00
OH+CH2O<=>HCO+H2O                         3.430E+09     1.180     -447.00
OH+CH2OH<=>H2O+CH2O                       5.000E+12      .000        .00
OH+CH3O<=>H2O+CH2O                        5.000E+12      .000        .00
OH+CH3OH<=>CH2OH+H2O                      1.440E+06     2.000     -840.00
OH+CH3OH<=>CH3O+H2O                       6.300E+06     2.000     1500.00
OH+C2H<=>H+HCCO                           2.000E+13      .000        .00
OH+C2H2<=>H+CH2CO                         2.180E-04     4.500    -1000.00
OH+C2H2<=>H+HCCOH                         5.040E+05     2.300    13500.00
OH+C2H2<=>C2H+H2O                         3.370E+07     2.000    14000.00
OH+C2H2<=>CH3+CO                          4.830E-04     4.000    -2000.00
OH+C2H3<=>H2O+C2H2                        5.000E+12      .000        .00
OH+C2H4<=>C2H3+H2O                        3.600E+06     2.000     2500.00
OH+C2H6<=>C2H5+H2O                        3.540E+06     2.120      870.00
OH+CH2CO<=>HCCO+H2O                       7.500E+12      .000     2000.00
2HO2<=>O2+H2O2                            1.300E+11      .000    -1630.00
  DUPLICATE
2HO2<=>O2+H2O2                            4.200E+14      .000    12000.00
  DUPLICATE
HO2+CH2<=>OH+CH2O                         2.000E+13      .000        .00
HO2+CH3<=>O2+CH4                          1.000E+12      .000        .00
HO2+CH3<=>OH+CH3O                         3.780E+13      .000        .00
HO2+CO<=>OH+CO2                           1.500E+14      .000    23600.00
HO2+CH2O<=>HCO+H2O2                       5.600E+06     2.000    12000.00
C+O2<=>O+CO                               5.800E+13      .000      576.00
C+CH2<=>H+C2H                             5.000E+13      .000        .00
C+CH3<=>H+C2H2                            5.000E+13      .000        .00
CH+O2<=>O+HCO                             6.710E+13      .000        .00
CH+H2<=>H+CH2                             1.080E+14      .000     3110.00
CH+H2O<=>H+CH2O                           5.710E+12      .000     -755.00
CH+CH2<=>H+C2H2                           4.000E+13      .000        .00
CH+CH3<=>H+C2H3                           3.000E+13      .000        .00
CH+CH4<=>H+C2H4                           6.000E+13      .000        .00
CH+CO(+M)<=>HCCO(+M)                      5.000E+13      .000        .00
     LOW  /  2.690E+28   -3.740   1936.00/
      TROE/   .5757  237.00  1652.00   5069.00 /
H2/2.00/ H2O/6.00/ CH4/2.00/ CO/1.50/ CO2/2.00/ C2H6/3.00/ AR/ .70/
CH+CO2<=>HCO+CO                           1.900E+14      .000    15792.00
CH+CH2O<=>H+CH2CO                         9.460E+13      .000     -515.00
CH+HCCO<=>CO+C2H2                         5.000E+13      .000        .00
CH2+O2=>OH+H+CO                           5.000E+12      .000     1500.00
CH2+H2<=>H+CH3                            5.000E+05     2.000     7230.00
2CH2<=>H2+C2H2                            1.600E+15      .000    11944.00
CH2+CH3<=>H+C2H4                          4.000E+13      .000        .00
CH2+CH4<=>2CH3                            2.460E+06     2.000     8270.00
CH2+CO(+M)<=>CH2CO(+M)                    8.100E+11      .500     4510.00
     LOW  /  2.690E+33   -5.110   7095.00/
```

```
      TROE/   .5907  275.00  1226.00  5185.00 /
H2/2.00/ H2O/6.00/ CH4/2.00/ CO/1.50/ CO2/2.00/ C2H6/3.00/ AR/ .70/
CH2+HCCO<=>C2H3+CO                    3.000E+13     .000        .00
CH2(S)+N2<=>CH2+N2                    1.500E+13     .000     600.00
CH2(S)+AR<=>CH2+AR                    9.000E+12     .000     600.00
CH2(S)+O2<=>H+OH+CO                   2.800E+13     .000        .00
CH2(S)+O2<=>CO+H2O                    1.200E+13     .000        .00
CH2(S)+H2<=>CH3+H                     7.000E+13     .000        .00
CH2(S)+H2O(+M)<=>CH3OH(+M)            4.820E+17   -1.160    1145.00
      LOW  /  1.880E+38    -6.360    5040.00/
      TROE/   .6027  208.00  3922.00  10180.0 /
H2/2.00/ H2O/6.00/ CH4/2.00/ CO/1.50/ CO2/2.00/ C2H6/3.00/
CH2(S)+H2O<=>CH2+H2O                  3.000E+13     .000        .00
CH2(S)+CH3<=>H+C2H4                   1.200E+13     .000     -570.00
CH2(S)+CH4<=>2CH3                     1.600E+13     .000     -570.00
CH2(S)+CO<=>CH2+CO                    9.000E+12     .000        .00
CH2(S)+CO2<=>CH2+CO2                  7.000E+12     .000        .00
CH2(S)+CO2<=>CO+CH2O                  1.400E+13     .000        .00
CH2(S)+C2H6<=>CH3+C2H5                4.000E+13     .000     -550.00
CH3+O2<=>O+CH3O                       3.560E+13     .000   30480.00
CH3+O2<=>OH+CH2O                      2.310E+12     .000   20315.00
CH3+H2O2<=>HO2+CH4                    2.450E+04    2.470    5180.00
2CH3(+M)<=>C2H6(+M)                   6.770E+16   -1.180     654.00
      LOW  /  3.400E+41    -7.030    2762.00/
      TROE/   .6190  73.20  1180.00  9999.00 /
H2/2.00/ H2O/6.00/ CH4/2.00/ CO/1.50/ CO2/2.00/ C2H6/3.00/ AR/ .70/
2CH3<=>H+C2H5                         6.840E+12     .100   10600.00
CH3+HCO<=>CH4+CO                      2.648E+13     .000        .00
CH3+CH2O<=>HCO+CH4                    3.320E+03    2.810    5860.00
CH3+CH3OH<=>CH2OH+CH4                 3.000E+07    1.500    9940.00
CH3+CH3OH<=>CH3O+CH4                  1.000E+07    1.500    9940.00
CH3+C2H4<=>C2H3+CH4                   2.270E+05    2.000    9200.00
CH3+C2H6<=>C2H5+CH4                   6.140E+06    1.740   10450.00
HCO+H2O<=>H+CO+H2O                    1.500E+18   -1.000   17000.00
HCO+M<=>H+CO+M                        1.870E+17   -1.000   17000.00
H2/2.00/ H2O/ .00/ CH4/2.00/ CO/1.50/ CO2/2.00/ C2H6/3.00/
HCO+O2<=>HO2+CO                       13.45E+12     .000     400.00
CH2OH+O2<=>HO2+CH2O                   1.800E+13     .000     900.00
CH3O+O2<=>HO2+CH2O                    4.280E-13    7.600   -3530.00
C2H+O2<=>HCO+CO                       1.000E+13     .000     -755.00
C2H+H2<=>H+C2H2                       5.680E+10    0.900    1993.00
C2H3+O2<=>HCO+CH2O                    4.580E+16   -1.390    1015.00
C2H4(+M)<=>H2+C2H2(+M)                8.000E+12     .440   86770.00
      LOW  /  1.580E+51    -9.300    97800.00/
      TROE/   .7345  180.00  1035.00  5417.00 /
H2/2.00/ H2O/6.00/ CH4/2.00/ CO/1.50/ CO2/2.00/ C2H6/3.00/ AR/ .70/
C2H5+O2<=>HO2+C2H4                    8.400E+11     .000    3875.00
```

HCCO+O2<=>OH+2CO	3.200E+12	.000	854.00
2HCCO<=>2CO+C2H2	1.000E+13	.000	.00
N+NO<=>N2+O	2.700E+13	.000	355.00
N+O2<=>NO+O	9.000E+09	1.000	6500.00
N+OH<=>NO+H	3.360E+13	.000	385.00
N2O+O<=>N2+O2	1.400E+12	.000	10810.00
N2O+O<=>2NO	2.900E+13	.000	23150.00
N2O+H<=>N2+OH	3.870E+14	.000	18880.00
N2O+OH<=>N2+HO2	2.000E+12	.000	21060.00
N2O(+M)<=>N2+O(+M)	7.910E+10	.000	56020.00

LOW / 6.370E+14 .000 56640.00/
H2/2.00/ H2O/6.00/ CH4/2.00/ CO/1.50/ CO2/2.00/ C2H6/3.00/ AR/ .625/

HO2+NO<=>NO2+OH	2.110E+12	.000	-480.00
NO+O+M<=>NO2+M	1.060E+20	-1.410	.00

H2/2.00/ H2O/6.00/ CH4/2.00/ CO/1.50/ CO2/2.00/ C2H6/3.00/ AR/ .70/

NO2+O<=>NO+O2	3.900E+12	.000	-240.00
NO2+H<=>NO+OH	1.320E+14	.000	360.00
NH+O<=>NO+H	4.000E+13	.000	.00
NH+H<=>N+H2	3.200E+13	.000	330.00
NH+OH<=>HNO+H	2.000E+13	.000	.00
NH+OH<=>N+H2O	2.000E+09	1.200	.00
NH+O2<=>HNO+O	4.610E+05	2.000	6500.00
NH+O2<=>NO+OH	1.280E+06	1.500	100.00
NH+N<=>N2+H	1.500E+13	.000	.00
NH+H2O<=>HNO+H2	2.000E+13	.000	13850.00
NH+NO<=>N2+OH	2.160E+13	-.230	.00
NH+NO<=>N2O+H	3.650E+14	-.450	.00
NH2+O<=>OH+NH	3.000E+12	.000	.00
NH2+O<=>H+HNO	3.900E+13	.000	.00
NH2+H<=>NH+H2	4.000E+13	.000	3650.00
NH2+OH<=>NH+H2O	9.000E+07	1.500	-460.00
NNH<=>N2+H	3.300E+08	.000	.00
NNH+M<=>N2+H+M	1.300E+14	-.110	4980.00

H2/2.00/ H2O/6.00/ CH4/2.00/ CO/1.50/ CO2/2.00/ C2H6/3.00/ AR/ .70/

NNH+O2<=>HO2+N2	5.000E+12	.000	.00
NNH+O<=>OH+N2	2.500E+13	.000	.00
NNH+O<=>NH+NO	7.000E+13	.000	.00
NNH+H<=>H2+N2	5.000E+13	.000	.00
NNH+OH<=>H2O+N2	2.000E+13	.000	.00
NNH+CH3<=>CH4+N2	2.500E+13	.000	.00
H+NO+M<=>HNO+M	4.480E+19	-1.320	740.00

H2/2.00/ H2O/6.00/ CH4/2.00/ CO/1.50/ CO2/2.00/ C2H6/3.00/ AR/ .70/

HNO+O<=>NO+OH	2.500E+13	.000	.00
HNO+H<=>H2+NO	9.000E+11	.720	660.00
HNO+OH<=>NO+H2O	1.300E+07	1.900	-950.00
HNO+O2<=>HO2+NO	1.000E+13	.000	13000.00
CN+O<=>CO+N	7.700E+13	.000	.00

```
CN+OH<=>NCO+H                              4.000E+13     .000        .00
CN+H2O<=>HCN+OH                            8.000E+12     .000     7460.00
CN+O2<=>NCO+O                              6.140E+12     .000     -440.00
CN+H2<=>HCN+H                              2.950E+05    2.450     2240.00
NCO+O<=>NO+CO                              2.350E+13     .000        .00
NCO+H<=>NH+CO                              5.400E+13     .000        .00
NCO+OH<=>NO+H+CO                           0.250E+13     .000        .00
NCO+N<=>N2+CO                              2.000E+13     .000        .00
NCO+O2<=>NO+CO2                            2.000E+12     .000    20000.00
NCO+M<=>N+CO+M                             3.100E+14     .000    54050.00
 H2/2.00/ H2O/6.00/ CH4/2.00/ CO/1.50/ CO2/2.00/ C2H6/3.00/ AR/ .70/
NCO+NO<=>N2O+CO                            1.900E+17   -1.520      740.00
NCO+NO<=>N2+CO2                            3.800E+18   -2.000      800.00
HCN+M<=>H+CN+M                             1.040E+29   -3.300   126600.00
 H2/2.00/ H2O/6.00/ CH4/2.00/ CO/1.50/ CO2/2.00/ C2H6/3.00/ AR/ .70/
HCN+O<=>NCO+H                              2.030E+04    2.640     4980.00
HCN+O<=>NH+CO                              5.070E+03    2.640     4980.00
HCN+O<=>CN+OH                              3.910E+09    1.580    26600.00
HCN+OH<=>HOCN+H                            1.100E+06    2.030    13370.00
HCN+OH<=>HNCO+H                            4.400E+03    2.260     6400.00
HCN+OH<=>NH2+CO                            1.600E+02    2.560     9000.00
H+HCN(+M)<=>H2CN(+M)                       3.300E+13     .000        .00
     LOW /   1.400E+26    -3.400     1900.00/
 H2/2.00/ H2O/6.00/ CH4/2.00/ CO/1.50/ CO2/2.00/ C2H6/3.00/ AR/ .70/
H2CN+N<=>N2+CH2                            6.000E+13     .000      400.00
C+N2<=>CN+N                                6.300E+13     .000    46020.00
CH+N2<=>HCN+N                              3.120E+09    0.880    20130.00
CH+N2(+M)<=>HCNN(+M)                       3.100E+12     .150        .00
     LOW /   1.300E+25    -3.160      740.00/
     TROE/    .6670   235.00   2117.00   4536.00 /
 H2/2.00/ H2O/6.00/ CH4/2.00/ CO/1.50/ CO2/2.00/ C2H6/3.00/ AR/ 1.0/
CH2+N2<=>HCN+NH                            1.000E+13     .000    74000.00
CH2(S)+N2<=>NH+HCN                         1.000E+11     .000    65000.00
C+NO<=>CN+O                                1.900E+13     .000        .00
C+NO<=>CO+N                                2.900E+13     .000        .00
CH+NO<=>HCN+O                              4.100E+13     .000        .00
CH+NO<=>H+NCO                              1.620E+13     .000        .00
CH+NO<=>N+HCO                              2.460E+13     .000        .00
CH2+NO<=>H+HNCO                            3.100E+17   -1.380     1270.00
CH2+NO<=>OH+HCN                            2.900E+14    -.690      760.00
CH2+NO<=>H+HCNO                            3.800E+13    -.360      580.00
CH2(S)+NO<=>H+HNCO                         3.100E+17   -1.380     1270.00
CH2(S)+NO<=>OH+HCN                         2.900E+14    -.690      760.00
CH2(S)+NO<=>H+HCNO                         3.800E+13    -.360      580.00
CH3+NO<=>HCN+H2O                           9.600E+13     .000    28800.00
CH3+NO<=>H2CN+OH                           1.000E+12     .000    21750.00
HCNN+O<=>CO+H+N2                           2.200E+13     .000        .00
```

217

HCNN+O<=>HCN+NO	2.000E+12	.000	.00
HCNN+O2<=>O+HCO+N2	1.200E+13	.000	.00
HCNN+OH<=>H+HCO+N2	1.200E+13	.000	.00
HCNN+H<=>CH2+N2	1.000E+14	.000	.00
HNCO+O<=>NH+CO2	9.800E+07	1.410	8500.00
HNCO+O<=>HNO+CO	1.500E+08	1.570	44000.00
HNCO+O<=>NCO+OH	2.200E+06	2.110	11400.00
HNCO+H<=>NH2+CO	2.250E+07	1.700	3800.00
HNCO+H<=>H2+NCO	1.050E+05	2.500	13300.00
HNCO+OH<=>NCO+H2O	3.300E+07	1.500	3600.00
HNCO+OH<=>NH2+CO2	3.300E+06	1.500	3600.00
HNCO+M<=>NH+CO+M	1.180E+16	.000	84720.00

H2/2.00/ H2O/6.00/ CH4/2.00/ CO/1.50/ CO2/2.00/ C2H6/3.00/ AR/ .70/

HCNO+H<=>H+HNCO	2.100E+15	-.690	2850.00
HCNO+H<=>OH+HCN	2.700E+11	.180	2120.00
HCNO+H<=>NH2+CO	1.700E+14	-.750	2890.00
HOCN+H<=>H+HNCO	2.000E+07	2.000	2000.00
HCCO+NO<=>HCNO+CO	0.900E+13	.000	.00
CH3+N<=>H2CN+H	6.100E+14	-.310	290.00
CH3+N<=>HCN+H2	3.700E+12	.150	-90.00
NH3+H<=>NH2+H2	5.400E+05	2.400	9915.00
NH3+OH<=>NH2+H2O	5.000E+07	1.600	955.00
NH3+O<=>NH2+OH	9.400E+06	1.940	6460.00
NH+CO2<=>HNO+CO	1.000E+13	.000	14350.00
CN+NO2<=>NCO+NO	6.160E+15	-0.752	345.00
NCO+NO2<=>N2O+CO2	3.250E+12	.000	-705.00
N+CO2<=>NO+CO	3.000E+12	.000	11300.00
O+CH3=>H+H2+CO	3.370E+13	.000	.00
O+C2H4<=>H+CH2CHO	6.700E+06	1.830	220.00
O+C2H5<=>H+CH3CHO	1.096E+14	.000	.00
OH+HO2<=>O2+H2O	0.500E+16	.000	17330.00

  DUPLICATE

OH+CH3=>H2+CH2O	8.000E+09	.500	-1755.00
CH+H2(+M)<=>CH3(+M)	1.970E+12	.430	-370.00

   LOW/ 4.820E+25 -2.80 590.0 /
   TROE/ .578 122.0 2535.0 9365.0 /

H2/2.00/ H2O/6.00/ CH4/2.00/ CO/1.50/ CO2/2.00/ C2H6/3.00/ AR/ .70/

CH2+O2=>2H+CO2	5.800E+12	.000	1500.00
CH2+O2<=>O+CH2O	2.400E+12	.000	1500.00
CH2+CH2=>2H+C2H2	2.000E+14	.000	10989.00
CH2(S)+H2O=>H2+CH2O	6.820E+10	.250	-935.00
C2H3+O2<=>O+CH2CHO	3.030E+11	.290	11.00
C2H3+O2<=>HO2+C2H2	1.337E+06	1.610	-384.00
O+CH3CHO<=>OH+CH2CHO	2.920E+12	.000	1808.00
O+CH3CHO=>OH+CH3+CO	2.920E+12	.000	1808.00
O2+CH3CHO=>HO2+CH3+CO	3.010E+13	.000	39150.00
H+CH3CHO<=>CH2CHO+H2	2.050E+09	1.160	2405.00

```
H+CH3CHO=>CH3+H2+CO                         2.050E+09    1.160     2405.00
OH+CH3CHO=>CH3+H2O+CO                        2.343E+10    0.730    -1113.00
HO2+CH3CHO=>CH3+H2O2+CO                       3.010E+12     .000    11923.00
CH3+CH3CHO=>CH3+CH4+CO                        2.720E+06    1.770     5920.00
H+CH2CO(+M)<=>CH2CHO(+M)                      4.865E+11    0.422    -1755.00
     LOW/ 1.012E+42  -7.63  3854.0/
     TROE/ 0.465  201.0  1773.0  5333.0 /
H2/2.00/ H2O/6.00/ CH4/2.00/ CO/1.50/ CO2/2.00/ C2H6/3.00/ AR/ .70/
O+CH2CHO=>H+CH2+CO2                          1.500E+14     .000      .00
O2+CH2CHO=>OH+CO+CH2O                         1.810E+10     .000      .00
O2+CH2CHO=>OH+2HCO                           2.350E+10     .000      .00
H+CH2CHO<=>CH3+HCO                           2.200E+13     .000      .00
H+CH2CHO<=>CH2CO+H2                          1.100E+13     .000      .00
OH+CH2CHO<=>H2O+CH2CO                        1.200E+13     .000      .00
OH+CH2CHO<=>HCO+CH2OH                        3.010E+13     .000      .00
CH3+C2H5(+M)<=>C3H8(+M)                       .9430E+13     .000      .00
     LOW/ 2.710E+74  -16.82  13065.0 /
     TROE/ .1527  291.0  2742.0  7748.0 /
H2/2.00/ H2O/6.00/ CH4/2.00/ CO/1.50/ CO2/2.00/ C2H6/3.00/ AR/ .70/
O+C3H8<=>OH+C3H7                             1.930E+05    2.680     3716.00
H+C3H8<=>C3H7+H2                             1.320E+06    2.540     6756.00
OH+C3H8<=>C3H7+H2O                           3.160E+07    1.800      934.00
C3H7+H2O2<=>HO2+C3H8                          3.780E+02    2.720     1500.00
CH3+C3H8<=>C3H7+CH4                          0.903E+00    3.650     7154.00
CH3+C2H4(+M)<=>C3H7(+M)                       2.550E+06    1.600     5700.00
     LOW/ 3.00E+63  -14.6  18170./
     TROE/ .1894  277.0  8748.0  7891.0 /
H2/2.00/ H2O/6.00/ CH4/2.00/ CO/1.50/ CO2/2.00/ C2H6/3.00/ AR/ .70/
O+C3H7<=>C2H5+CH2O                           9.640E+13     .000      .00
H+C3H7(+M)<=>C3H8(+M)                        3.613E+13     .000      .00
     LOW/ 4.420E+61  -13.545  11357.0/
     TROE/ .315  369.0  3285.0  6667.0 /
H2/2.00/ H2O/6.00/ CH4/2.00/ CO/1.50/ CO2/2.00/ C2H6/3.00/ AR/ .70/
H+C3H7<=>CH3+C2H5                            4.060E+06    2.190      890.00
OH+C3H7<=>C2H5+CH2OH                         2.410E+13     .000      .00
HO2+C3H7<=>O2+C3H8                           2.550E+10    0.255     -943.00
HO2+C3H7=>OH+C2H5+CH2O                        2.410E+13     .000      .00
CH3+C3H7<=>2C2H5                             1.927E+13   -0.320      .00
!
!Positive!
!
CH + O <=> HCO+ + E                          2.512E+11    0.000     7.118!ok
HCO+ + E <=> CO + H                          7.400E+18   -0.680     0.000!ok
HCO+ + H2O <=> H3O+ + CO                      1.506E+15    0.000     0.000!N
HCO+ + C2H5OH <=> H3O+ + CO + C2H4           6.000E+14    0.000     0.000!CHEMISTRY
ISSUE
H3O+ + E <=> H2O + H                         2.291E+18   -0.500     0.000!N
```

H3O+ + E <=> OH + H + H	7.949E+21	-1.370	0.000!NOt ok
H3O+ + E <=> H2 + OH	1.253E+19	-0.500	0.000!NOt ok
H3O+ + E <=> O + H2 + H	6.000E+17	-0.300	0.000!N
H3O+ + C <=> HCO+ + H2	6.022E+12	0.000	0.000!n
HCO+ + HCCOH <=> C2H3O+ + CO	1.259E+15	-0.048	0.000!n
HCO+ + CH3 <=> C2H3O+ + H	7.763E+14	-0.006	0.000 !N
C2H3O+ + E <=> HCCOH + H	2.291E+18	-0.500	0.000!N
H3O+ + HCCOH <=> C2H3O+ + H2O	1.204E+15	0.000	0.000!N
C2H3O+ + E <=> CO + CH3	2.403E+17	-0.050	0.000 !ok
C2H3O+ + O <=> HCO+ + CH2O	2.000E+14	0.000	0.000 !ok
!			
!Negative!			
O2- + H2 <=> H2O2 + E	6.022E+14	0.000	0.000 !ok
O2- + H <=> HO2 + E	7.226E+14	0.000	0.000 !ok
O2- + OH <=> OH- + O2	6.022E+13	0.000	0.000 !ok
O2- + H <=> OH- + O	1.084E+15	0.000	0.000 !ok
OH- + O <=> HO2 + E	1.204E+14	0.000	0.000 !ok
OH- + H <=> H2O + E	1.084E+15	0.000	0.000 !ok
OH- + C <=> HCO + E	3.001E+14	0.000	0.000 !ok
OH- + CH <=> CH2O + E	3.001E+14	0.000	0.000 !ok
OH- + CH3 <=> CH3OH + E	6.022E+14	0.000	0.000 !ok
CHO2- + H <=> CO2 + H2 + E	1.159E+14	0.000	0.000 !ok
OH- + HCO <=> CHO2- + H	2.959E+15	-0.140	-0.441 !not ok
O- + C <=> CO + E	3.011E+14	0.000	0.000 !ok
O- + H2 <=> OH- + H	1.987E+13	0.000	0.000 !ok
O- + CH4 <=> OH- + CH3	6.022E+13	0.000	0.000 !ok
O- + H2O <=> OH- + OH	8.431E+14	0.000	0.000!ok for
single			
O- + CH2O <=> OH- + HCO	5.601E+14	0.000	0.000 !ok
O- + CH2O <=> CHO2- + H	1.307E+15	0.000	0.000 !ok
O- + C2H6 <=> C2H5 + OH-	6.130E+15	-0.500	0.000 !ok
O- + H <=> OH + E	3.011E+14	0.000	0.000 !ok
O- + H2 <=> H2O + E	4.215E+14	0.000	0.000 !ok
O- + CH <=> HCO + E	3.011E+14	0.000	0.000 !ok
O- + CH2 <=> CH2O + E	3.011E+14	0.000	0.000 !ok
O- + CO <=> CO2 + E	3.914E+14	0.000	0.000 !ok
O- + O <=> O2 + E	8.431E+13	0.000	0.000 !ok
O- + C2H2 <=> HCCOH + E	7.226E+14	0.000	0.000 !ok
O- + H2O <=> H2O2 + E	3.613E+11	0.000	0.000 !ok
O2- + O <=> O- + O2	1.987E+14	0.000	0.000 !ok
!			
!!!!!!			
!BOTH!			
!!!!!!			
!			
!O2- + C2H3O+ <=> O2 + CH2CHO	2.090E+18	-0.500	0.000 !N
!O2- + C2H3O+ <=> O2 + HCCOH + H	1.000E+18	0.000	0.000 !N

```
!O- + C2H3O+ <=> O + CH2CHO                    2.090E+18   -0.500        0.000 !N
!
!!  DUPLICATE
!O- + C2H3O+ <=> O + HCCOH + H                 1.000E+18    0.000        0.000 !N
O- + C2H3O+ <=> O + CH2CHO                     1.000E+18    0.000        0.000 !ok
!  DUPLICATE
!
!!!!!!!!!!!!!!!!
!CH STAR NORRI!
!!!!!!!!!!!!!!!!
!
!C2+OH <=> CH*+ CO                             2.000E+14    0.000        0.000
!C2H + O <=> CH* + CO                          5.200E+11    0.000     2600.000
!C2H+O2 <=> CH* + CO2                          3.200E+11    0.000     1599.000
!H + O + M <=> OH* + M                         6.000E+14    0.000     6940.000
!CH + O2 <=> OH* + CO                          1.173E+14    0.400     4150.000
!CH* + H2O <=> CH + H2O                        2.000E+14    0.000        0.000
!CH* + CO2 <=> CH + CO2                        2.410E-01    4.3      -1694.000
!CH* + CO <=> CH + CO                          2.440E+12    0.5          0.000
!CH* + H2 <=> CH + H2                          1.470E+14    0.000     1361.000
!CH* + O2 <=> CH + O2                          2.480E+06    2.140    -1720.000
!CH* + N2 <=> CH + N2                          3.030E+02    3.400     -381.000
!CH* + CH4 => CH + CH4                         1.730E+13    0.000      167.000
!
!!!!!!
!WALSH!
!!!!!!!
!
!C2H + O <=> CH* + CO                          1.080E+13    0.000        0.000   !N
C2H + O2 <=> CH* + CO2                         2.170E+10    0.000        0.000   !
!CH* => CH                                     1.850E+06    0.000        0.000   !N
!CH* + N2 <=> CH + N2                          3.030E+02    3.400       -381.0   !N
!CH* + O2 <=> CH + O2                          2.480E+06    2.140      -1720.0   !N
!CH* + H2O <=> CH + H2O                        5.300E+13    0.000        0.000   !N
!CH* + H2 <=> CH + H2                          1.470E+14    0.000       1361.0   !N
CH* + CO2 <=> CH + CO2                         2.400E+01    4.300      -1694.0   !
CH* + CO <=> CH + CO                           2.440E+12    0.500        0.000   !
!CH* + CH4 <=> CH + CH4                        1.730E+13    0.000       167.00   !N
!!!!!                                                                           !
!OH*!                                                                           !
!!!!!                                                                           !
!CH + O2 <=> OH* + CO                          3.25E+13    0.000        0.000 !N
OH* => OH                                      1.45E+06    0.000        0.000 !
OH* + N2 <=> OH + N2                           1.08E+11    0.500      -1238.0!
OH* + O2 <=> OH + O2                           2.10E+12    0.500       -482.0 !
!OH* + H2O <=> OH + H2O                        5.92E+12    0.500       -861.0 !N
!OH* + H2 <=> OH + H2                          2.95E+12    0.500       -444.0 !N
```

```
!OH* + CO2 <=> OH + CO2                2.75E+12    0.500    -968.0 !N
!OH* + CO <=> OH + CO                  3.23E+12    0.500    -787.0 !N
!OH* + CH4 <=> OH + CH4                3.36E+12    0.500    -635.0 !N
END
```

Transport
AR	0	136.500	3.330	0.000	0.000	0.000		
C	0	71.400	3.298	0.000	0.000	0.000	!	*
C2	1	97.530	3.621	0.000	1.760	4.000		
C2O	1	232.400	3.828	0.000	0.000	1.000	!	*
CN2	1	232.400	3.828	0.000	0.000	1.000	!	OIS
C2H	1	209.000	4.100	0.000	0.000	2.500		
C2H2	1	209.000	4.100	0.000	0.000	2.500		
C2H2OH	2	224.700	4.162	0.000	0.000	1.000	!	*
C2H3	2	209.000	4.100	0.000	0.000	1.000	!	*
C2H4	2	280.800	3.971	0.000	0.000	1.500		
C2H5	2	252.300	4.302	0.000	0.000	1.500		
C2H6	2	252.300	4.302	0.000	0.000	1.500		
C2N	1	232.400	3.828	0.000	0.000	1.000	!	OIS
C2N2	1	349.000	4.361	0.000	0.000	1.000	!	OIS
C3H2	2	209.000	4.100	0.000	0.000	1.000	!	*
C3H4	1	252.000	4.760	0.000	0.000	1.000		
C3H6	2	266.800	4.982	0.000	0.000	1.000		
C3H7	2	266.800	4.982	0.000	0.000	1.000		
C4H6	2	357.000	5.180	0.000	0.000	1.000		
I*C3H7	2	266.800	4.982	0.000	0.000	1.000		
N*C3H7	2	266.800	4.982	0.000	0.000	1.000		
C3H8	2	266.800	4.982	0.000	0.000	1.000		
C4H	1	357.000	5.180	0.000	0.000	1.000		
C4H2	1	357.000	5.180	0.000	0.000	1.000		
C4H2OH	2	224.700	4.162	0.000	0.000	1.000	!	*
C4H8	2	357.000	5.176	0.000	0.000	1.000		
C4H9	2	357.000	5.176	0.000	0.000	1.000		
I*C4H9	2	357.000	5.176	0.000	0.000	1.000		
C5H2	1	357.000	5.180	0.000	0.000	1.000		
C5H3	1	357.000	5.180	0.000	0.000	1.000		
C6H2	1	357.000	5.180	0.000	0.000	1.000		
C6H5	2	412.300	5.349	0.000	0.000	1.000	!	JAM
C6H5O	2	450.000	5.500	0.000	0.000	1.000	!	JAM
C5H5OH	2	450.000	5.500	0.000	0.000	1.000	!	JAM
C6H6	2	412.300	5.349	0.000	0.000	1.000	!	SVE
C6H7	2	412.300	5.349	0.000	0.000	1.000	!	JAM
CH	1	80.000	2.750	0.000	0.000	0.000		
CH2	1	144.000	3.800	0.000	0.000	0.000		
CH2(S)	1	144.000	3.800	0.000	0.000	0.000		
CH2*	1	144.000	3.800	0.000	0.000	0.000		
CH2CHCCH	2	357.000	5.180	0.000	0.000	1.000	!	JAM
CH2CHCCH2	2	357.000	5.180	0.000	0.000	1.000	!	JAM
CH2CHCH2	2	260.000	4.850	0.000	0.000	1.000	!	JAM
CH2CHCHCH	2	357.000	5.180	0.000	0.000	1.000	!	JAM
CH2CHCHCH2	2	357.000	5.180	0.000	0.000	1.000	!	JAM
CH2CO	2	436.000	3.970	0.000	0.000	2.000		

CH2O	2	498.000	3.590	0.000	0.000	2.000
CH2OH	2	417.000	3.690	1.700	0.000	2.000
CH3	1	144.000	3.800	0.000	0.000	0.000
CH3CC	2	252.000	4.760	0.000	0.000	1.000 ! JAM
CH3CCCH2	2	357.000	5.180	0.000	0.000	1.000 ! JAM
CH3CCCH3	2	357.000	5.180	0.000	0.000	1.000 ! JAM
CH3CCH2	2	260.000	4.850	0.000	0.000	1.000 ! JAM
CH3CHCH	2	260.000	4.850	0.000	0.000	1.000 ! JAM
CH3CH2CCH	2	357.000	5.180	0.000	0.000	1.000 ! JAM
CH3CHO	2	436.000	3.970	0.000	0.000	2.000
CH2CHO	2	436.000	3.970	0.000	0.000	2.000
CH3CO	2	436.000	3.970	0.000	0.000	2.000
CH3O	2	417.000	3.690	1.700	0.000	2.000
CH3OH	2	481.800	3.626	0.000	0.000	1.000 ! SVE
CH4	2	141.400	3.746	0.000	2.600	13.000
CH4O	2	417.000	3.690	1.700	0.000	2.000
CN	1	75.000	3.856	0.000	0.000	1.000 ! OIS
CNC	1	232.400	3.828	0.000	0.000	1.000 ! OIS
CNN	1	232.400	3.828	0.000	0.000	1.000 ! OIS
CO	1	98.100	3.650	0.000	1.950	1.800
CO2	1	244.000	3.763	0.000	2.650	2.100
H	0	145.000	2.050	0.000	0.000	0.000
H2C4O	2	357.000	5.180	0.000	0.000	1.000 ! JAM
H2	1	38.000	2.920	0.000	0.790	280.000
H2CCCCH	2	357.000	5.180	0.000	0.000	1.000 ! JAM
H2CCCCH2	2	357.000	5.180	0.000	0.000	1.000 ! JAM
H2CCCH	2	252.000	4.760	0.000	0.000	1.000 ! JAM
H2CN	1	569.000	3.630	0.000	0.000	1.000 ! os/jm
H2NO	2	116.700	3.492	0.000	0.000	1.000 ! JAM
H2O	2	572.400	2.605	1.844	0.000	4.000
H2O2	2	107.400	3.458	0.000	0.000	3.800
HC2N2	1	349.000	4.361	0.000	0.000	1.000 ! OIS
HCCHCCH	2	357.000	5.180	0.000	0.000	1.000 ! JAM
HCCO	2	150.000	2.500	0.000	0.000	1.000 ! *
HCNN	2	150.000	2.500	0.000	0.000	1.000 ! *
HCCOH	2	436.000	3.970	0.000	0.000	2.000
HCN	1	569.000	3.630	0.000	0.000	1.000 ! OIS
HCO	2	498.000	3.590	0.000	0.000	0.000
HE	0	10.200	2.576	0.000	0.000	0.000 ! *
HCNO	2	232.400	3.828	0.000	0.000	1.000 ! JAM
HOCN	2	232.400	3.828	0.000	0.000	1.000 ! JAM
HNCO	2	232.400	3.828	0.000	0.000	1.000 ! OIS
HNNO	2	232.400	3.828	0.000	0.000	1.000 ! *
HNO	2	116.700	3.492	0.000	0.000	1.000 ! *
HNOH	2	116.700	3.492	0.000	0.000	1.000 ! JAM
HO2	2	107.400	3.458	0.000	0.000	1.000 ! *
N	0	71.400	3.298	0.000	0.000	0.000 ! *

N2	1	97.530	3.621	0.000	1.760	4.000
N2H2	2	71.400	3.798	0.000	0.000	1.000 ! *
N2H3	2	200.000	3.900	0.000	0.000	1.000 ! *
N2H4	2	205.000	4.230	0.000	4.260	1.500
N2O	1	232.400	3.828	0.000	0.000	1.000 ! *
NCN	1	232.400	3.828	0.000	0.000	1.000 ! OIS
NCO	1	232.400	3.828	0.000	0.000	1.000 ! OIS
NH	1	80.000	2.650	0.000	0.000	4.000
NH2	2	80.000	2.650	0.000	2.260	4.000
NH3	2	481.000	2.920	1.470	0.000	10.000
NNH	2	71.400	3.798	0.000	0.000	1.000 ! *
NO	1	97.530	3.621	0.000	1.760	4.000
NCNO	2	232.400	3.828	0.000	0.000	1.000 ! OIS
NO2	2	200.000	3.500	0.000	0.000	1.000 ! *
O	0	80.000	2.750	0.000	0.000	0.000
O2	1	107.400	3.458	0.000	1.600	3.800
OH	1	80.000	2.750	0.000	0.000	0.000
E	0	850.000	425.000	0.000	0.000	1.000 !Chemkin Transport file
HCO+	1	498.000	3.590	0.000	0.000	0.000 !Chemkin Transport file
H3O+	2	572.400	2.605	1.844	0.000	4.000 ! same as H2O (??)
C2H3O+	2	436.000	3.970	0.000	0.000	2.000 ! same as CH2CHO (??)
O2-	1	107.400	3.458	0.000	1.600	3.800 ! same as O2
OH-	1	80.000	2.750	0.000	0.000	0.000
CHO2-	2	232.400	3.828	0.000	0.000	1.000 ! JAM ! same as HNCO (??)
O-	0	80.000	2.750	0.000	0.000	0.000 ! same as O
C2	1	97.530	3.621	0.000	1.760	4.000 !Chemkin Transport file
OH*	1	80.000	2.750	0.000	0.000	0.000 !Chemkin Transport file OH
CH*	1	80.000	2.750	0.000	0.000	0.000 !Chemkin Transport file CH
CH2*	1	144.000	3.800	0.000	0.000	0.000 !Chemkin Transport file CH2
CH2*	1	144.000	3.800	0.000	0.000	0.000 ! Because

you have "CH2s" in the kinetic mechanism, and not "CH2(S)" (row 39).
C2H5OH 2 362.6 4.53 0.000 0.000 1.000

Thermo

```
THERMO
   300.000  1000.000  5000.000
! GRI-Mech Version 3.0 Thermodynamics released 7/30/99
! NASA Polynomial format for CHEMKIN-II
! see README file for disclaimer
O                 L 1/90O   1               G  200.000  3500.000  1000.000      1
 2.56942078E+00-8.59741137E-05 4.19484589E-08-1.00177799E-11 1.22833691E-15      2
 2.92175791E+04 4.78433864E+00 3.16826710E+00-3.27931884E-03 6.64306396E-06      3
-6.12806624E-09 2.11265971E-12 2.91222592E+04 2.05193346E+00                     4
O2                TPIS89O   2               G  200.000  3500.000  1000.000      1
 3.28253784E+00 1.48308754E-03-7.57966669E-07 2.09470555E-10-2.16717794E-14      2
-1.08845772E+03 5.45323129E+00 3.78245636E+00-2.99673416E-03 9.84730201E-06      3
-9.68129509E-09 3.24372837E-12-1.06394356E+03 3.65767573E+00                     4
H                 L 7/88H   1               G  200.000  3500.000  1000.000      1
 2.50000001E+00-2.30842973E-11 1.61561948E-14-4.73515235E-18 4.98197357E-22      2
 2.54736599E+04-4.46682914E-01 2.50000000E+00 7.05332819E-13-1.99591964E-15      3
 2.30081632E-18-9.27732332E-22 2.54736599E+04-4.46682853E-01                     4
H2                TPIS78H   2               G  200.000  3500.000  1000.000      1
 3.33727920E+00-4.94024731E-05 4.99456778E-07-1.79566394E-10 2.00255376E-14      2
-9.50158922E+02-3.20502331E+00 2.34433112E+00 7.98052075E-03-1.94781510E-05      3
 2.01572094E-08-7.37611761E-12-9.17935173E+02 6.83010238E-01                     4
OH                RUS 78O   1H   1          G  200.000  3500.000  1000.000      1
 3.09288767E+00 5.48429716E-04 1.26505228E-07-8.79461556E-11 1.17412376E-14      2
 3.85865700E+03 4.47669610E+00 3.99201543E+00-2.40131752E-03 4.61793841E-06      3
-3.88113333E-09 1.36411470E-12 3.61508056E+03-1.03925458E-01                     4
H2O               L 8/89H   2O   1          G  200.000  3500.000  1000.000      1
 3.03399249E+00 2.17691804E-03-1.64072518E-07-9.70419870E-11 1.68200992E-14      2
-3.00042971E+04 4.96677010E+00 4.19864056E+00-2.03643410E-03 6.52040211E-06      3
-5.48797062E-09 1.77197817E-12-3.02937267E+04-8.49032208E-01                     4
HO2               L 5/89H   1O   2          G  200.000  3500.000  1000.000      1
 4.01721090E+00 2.23982013E-03-6.33658150E-07 1.14246370E-10-1.07908535E-14      2
 1.11856713E+02 3.78510215E+00 4.30179801E+00-4.74912051E-03 2.11582891E-05      3
-2.42763894E-08 9.29225124E-12 2.94808040E+02 3.71666245E+00                     4
H2O2              L 7/88H   2O   2          G  200.000  3500.000  1000.000      1
 4.16500285E+00 4.90831694E-03-1.90139225E-06 3.71185986E-10-2.87908305E-14      2
-1.78617877E+04 2.91615662E+00 4.27611269E+00-5.42822417E-04 1.67335701E-05      3
-2.15770813E-08 8.62454363E-12-1.77025821E+04 3.43505074E+00                     4
C                 L11/88C   1               G  200.000  3500.000  1000.000      1
 2.49266888E+00 4.79889284E-05-7.24335020E-08 3.74291029E-11-4.87277893E-15      2
 8.54512953E+04 4.80150373E+00 2.55423955E+00-3.21537724E-04 7.33792245E-07      3
-7.32234889E-10 2.66521446E-13 8.54438832E+04 4.53130848E+00                     4
CH                TPIS79C   1H   1          G  200.000  3500.000  1000.000      1
 2.87846473E+00 9.70913681E-04 1.44445655E-07-1.30687849E-10 1.76079383E-14      2
 7.10124364E+04 5.48497999E+00 3.48981665E+00 3.23835541E-04-1.68899065E-06      3
 3.16217327E-09-1.40609067E-12 7.07972934E+04 2.08401108E+00                     4
CH2               L S/93C   1H   2          G  200.000  3500.000  1000.000      1
```

```
 2.87410113E+00 3.65639292E-03-1.40894597E-06 2.60179549E-10-1.87727567E-14    2
 4.62636040E+04 6.17119324E+00 3.76267867E+00 9.68872143E-04 2.79489841E-06    3
-3.85091153E-09 1.68741719E-12 4.60040401E+04 1.56253185E+00                   4
CH2(S)            L S/93C   1H   2          G   200.000  3500.000  1000.000     1
 2.29203842E+00 4.65588637E-03-2.01191947E-06 4.17906000E-10-3.39716365E-14    2
 5.09259997E+04 8.62650169E+00 4.19860411E+00-2.36661419E-03 8.23296220E-06    3
-6.68815981E-09 1.94314737E-12 5.04968163E+04-7.69118967E-01                   4
CH3               L11/89C   1H   3          G   200.000  3500.000  1000.000     1
 2.28571772E+00 7.23990037E-03-2.98714348E-06 5.95684644E-10-4.67154394E-14    2
 1.67755843E+04 8.48007179E+00 3.67359040E+00 2.01095175E-03 5.73021856E-06    3
-6.87117425E-09 2.54385734E-12 1.64449988E+04 1.60456433E+00                   4
CH4               L 8/88C   1H   4          G   200.000  3500.000  1000.000     1
 7.48514950E-02 1.33909467E-02-5.73285809E-06 1.22292535E-09-1.01815230E-13    2
-9.46834459E+03 1.84373180E+01 5.14987613E+00-1.36709788E-02 4.91800599E-05    3
-4.84743026E-08 1.66693956E-11-1.02466476E+04-4.64130376E+00                   4
CO                TPIS79C   10   1          G   200.000  3500.000  1000.000     1
 2.71518561E+00 2.06252743E-03-9.98825771E-07 2.30053008E-10-2.03647716E-14    2
-1.41518724E+04 7.81868772E+00 3.57953347E+00-6.10353680E-04 1.01681433E-06    3
 9.07005884E-10-9.04424499E-13-1.43440860E+04 3.50840928E+00                   4
CO2               L 7/88C   10   2          G   200.000  3500.000  1000.000     1
 3.85746029E+00 4.41437026E-03-2.21481404E-06 5.23490188E-10-4.72084164E-14    2
-4.87591660E+04 2.27163806E+00 2.35677352E+00 8.98459677E-03-7.12356269E-06    3
 2.45919022E-09-1.43699548E-13-4.83719697E+04 9.90105222E+00                   4
HCO               L12/89H   1C   10   1     G   200.000  3500.000  1000.000     1
 2.77217438E+00 4.95695526E-03-2.48445613E-06 5.89161778E-10-5.33508711E-14    2
 4.01191815E+03 9.79834492E+00 4.22118584E+00-3.24392532E-03 1.37799446E-05    3
-1.33144093E-08 4.33768865E-12 3.83956496E+03 3.39437243E+00                   4
CH2O              L 8/88H   2C   10   1     G   200.000  3500.000  1000.000     1
 1.76069008E+00 9.20000082E-03-4.42258813E-06 1.00641212E-09-8.83855640E-14    2
-1.39958323E+04 1.36563230E+01 4.79372315E+00-9.90833369E-03 3.73220008E-05    3
-3.79285261E-08 1.31772652E-11-1.43089567E+04 6.02812900E-01                   4
CH2OH             GUNL93C   1H   30   1     G   200.000  3500.000  1000.000     1
 3.69266569E+00 8.64576797E-03-3.75101120E-06 7.87234636E-10-6.48554201E-14    2
-3.24250627E+03 5.81043215E+00 3.86388918E+00 5.59672304E-03 5.93271791E-06    3
-1.04532012E-08 4.36967278E-12-3.19391367E+03 5.47302243E+00                   4
CH3O              121686C   1H   30   1     G   300.00    3000.00   1000.000    1
 0.03770799E+02 0.07871497E-01-0.02656384E-04 0.03944431E-08-0.02112616E-12    2
 0.12783252E+03 0.02929575E+02 0.02106204E+02 0.07216595E-01 0.05338472E-04    3
-0.07377636E-07 0.02075610E-10 0.09786011E+04 0.13152177E+02                   4
CH3OH             L 8/88C   1H   40   1     G   200.000  3500.000  1000.000     1
 1.78970791E+00 1.40938292E-02-6.36500835E-06 1.38171085E-09-1.17060220E-13    2
-2.53748747E+04 1.45023623E+01 5.71539582E+00-1.52309129E-02 6.52441155E-05    3
-7.10806889E-08 2.61352698E-11-2.56427656E+04-1.50409823E+00                   4
C2H               L 1/91C   2H   1          G   200.000  3500.000  1000.000     1
 3.16780652E+00 4.75221902E-03-1.83787077E-06 3.04190252E-10-1.77232770E-14    2
 6.71210650E+04 6.63589475E+00 2.88965733E+00 1.34099611E-02-2.84769501E-05    3
 2.94791045E-08-1.09331511E-11 6.68393932E+04 6.22296438E+00                   4
```

```
C2H2              L 1/91C   2H   2          G   200.000  3500.000  1000.000    1
 4.14756964E+00 5.96166664E-03-2.37294852E-06 4.67412171E-10-3.61235213E-14    2
 2.59359992E+04-1.23028121E+00 8.08681094E-01 2.33615629E-02-3.55171815E-05    3
 2.80152437E-08-8.50072974E-12 2.64289807E+04 1.39397051E+01                   4
C2H3              L 2/92C   2H   3          G   200.000  3500.000  1000.000    1
 3.01672400E+00 1.03302292E-02-4.68082349E-06 1.01763288E-09-8.62607041E-14    2
 3.46128739E+04 7.78732378E+00 3.21246645E+00 1.51479162E-03 2.59209412E-05    3
-3.57657847E-08 1.47150873E-11 3.48598468E+04 8.51054025E+00                   4
C2H4              L 1/91C   2H   4          G   200.000  3500.000  1000.000    1
 2.03611116E+00 1.46454151E-02-6.71077915E-06 1.47222923E-09-1.25706061E-13    2
 4.93988614E+03 1.03053693E+01 3.95920148E+00-7.57052247E-03 5.70990292E-05    3
-6.91588753E-08 2.69884373E-11 5.08977593E+03 4.09733096E+00                   4
C2H5              L12/92C   2H   5          G   200.000  3500.000  1000.000    1
 1.95465642E+00 1.73972722E-02-7.98206668E-06 1.75217689E-09-1.49641576E-13    2
 1.28575200E+04 1.34624343E+01 4.30646568E+00-4.18658892E-03 4.97142807E-05    3
-5.99126606E-08 2.30509004E-11 1.28416265E+04 4.70720924E+00                   4
C2H6              L 8/88C   2H   6          G   200.000  3500.000  1000.000    1
 1.07188150E+00 2.16852677E-02-1.00256067E-05 2.21412001E-09-1.90002890E-13    2
-1.14263932E+04 1.51156107E+01 4.29142492E+00-5.50154270E-03 5.99438288E-05    3
-7.08466285E-08 2.68685771E-11-1.15222055E+04 2.66682316E+00                   4
CH2CO             L 5/90C   2H   2O   1     G   200.000  3500.000  1000.000    1
 4.51129732E+00 9.00359745E-03-4.16939635E-06 9.23345882E-10-7.94838201E-14    2
-7.55105311E+03 6.32247205E-01 2.13583630E+00 1.81188721E-02-1.73947474E-05    3
 9.34397568E-09-2.01457615E-12-7.04291804E+03 1.22156480E+01                   4
HCCO              SRIC91H   1C   2O   1     G   300.00   4000.00   1000.000    1
 0.56282058E+01 0.40853401E-02-0.15934547E-05 0.28626052E-09-0.19407832E-13    2
 0.19327215E+05-0.39302595E+01 0.22517214E+01 0.17655021E-01-0.23729101E-04    3
 0.17275759E-07-0.50664811E-11 0.20059449E+05 0.12490417E+02                   4
HCCOH             SRI91C   2O   1H   2      G   300.000  5000.000  1000.000    1
 0.59238291E+01 0.67923600E-02-0.25658564E-05 0.44987841E-09-0.29940101E-13    2
 0.72646260E+04-0.76017742E+01 0.12423733E+01 0.31072201E-01-0.50866864E-04    3
 0.43137131E-07-0.14014594E-10 0.80316143E+04 0.13874319E+02                   4
H2CN              41687H   2C   1N   1      G   300.00   4000.000  1000.000    1
 0.52097030E+01 0.29692911E-02-0.28555891E-06-0.16355500E-09 0.30432589E-13    2
 0.27677109E+05-0.44444780E+01 0.28516610E+01 0.56952331E-02 0.10711400E-05    3
-0.16226120E-08-0.23511081E-12 0.28637820E+05 0.89927511E+01                   4
HCN               GRI/98H   1C   1N   1     G   200.000  6000.000  1000.000    1
 0.38022392E+01 0.31464228E-02-0.10632185E-05 0.16619757E-09-0.97997570E-14    2
 0.14407292E+05 0.15754601E+01 0.22589886E+01 0.10051170E-01-0.13351763E-04    3
 0.10092349E-07-0.30089028E-11 0.14712633E+05 0.89164419E+01                   4
HNO               And93 H   1N   1O   1     G   200.000  6000.000  1000.000    1
 0.29792509E+01 0.34944059E-02-0.78549778E-06 0.57479594E-10-0.19335916E-15    2
 0.11750582E+05 0.86063728E+01 0.45334916E+01-0.56696171E-02 0.18473207E-04    3
-0.17137094E-07 0.55454573E-11 0.11548297E+05 0.17498417E+01                   4
N                 L 6/88N   1               G   200.000  6000.000  1000.000    1
 0.24159429E+01 0.17489065E-03-0.11902369E-06 0.30226245E-10-0.20360982E-14    2
 0.56133773E+05 0.46496096E+01 0.25000000E+01 0.00000000E+00 0.00000000E+00    3
```

```
 0.00000000E+00 0.00000000E+00 0.56104637E+05 0.41939087E+01             4
NNH               T07/93N  2H  1          G  200.000  6000.000  1000.000  1
 0.37667544E+01 0.28915082E-02-0.10416620E-05 0.16842594E-09-0.10091896E-13  2
 0.28650697E+05 0.44705067E+01 0.43446927E+01-0.48497072E-02 0.20059459E-04  3
-0.21726464E-07 0.79469539E-11 0.28791973E+05 0.29779410E+01             4
N2O               L 7/88N  2O  1          G  200.000  6000.000  1000.000  1
 0.48230729E+01 0.26270251E-02-0.95850874E-06 0.16000712E-09-0.97752303E-14  2
 0.80734048E+04-0.22017207E+01 0.22571502E+01 0.11304728E-01-0.13671319E-04  3
 0.96819806E-08-0.29307182E-11 0.87417744E+04 0.10757992E+02             4
NH                And94 N  1H  1          G  200.000  6000.000  1000.000  1
 0.27836928E+01 0.13298430E-02-0.42478047E-06 0.78348501E-10-0.55044470E-14  2
 0.42120848E+05 0.57407799E+01 0.34929085E+01 0.31179198E-03-0.14890484E-05  3
 0.24816442E-08-0.10356967E-11 0.41880629E+05 0.18483278E+01             4
NH2               And89 N  1H  2          G  200.000  6000.000  1000.000  1
 0.28347421E+01 0.32073082E-02-0.93390804E-06 0.13702953E-09-0.79206144E-14  2
 0.22171957E+05 0.65204163E+01 0.42040029E+01-0.21061385E-02 0.71068348E-05  3
-0.56115197E-08 0.16440717E-11 0.21885910E+05-0.14184248E+00             4
NH3               J 6/77N  1H  3          G  200.000  6000.000  1000.000  1
 0.26344521E+01 0.56662560E-02-0.17278676E-05 0.23867161E-09-0.12578786E-13  2
-0.65446958E+04 0.65662928E+01 0.42860274E+01-0.46605230E-02 0.21718513E-04  3
-0.22808887E-07 0.82638046E-11-0.67417285E+04-0.62537277E+00             4
NO                RUS 78N  1O  1          G  200.000  6000.000  1000.000  1
 0.32606056E+01 0.11911043E-02-0.42917048E-06 0.69457669E-10-0.40336099E-14  2
 0.99209746E+04 0.63693027E+01 0.42184763E+01-0.46389760E-02 0.11041022E-04  3
-0.93361354E-08 0.28035770E-11 0.98446230E+04 0.22808464E+01             4
NO2               L 7/88N  1O  2          G  200.000  6000.000  1000.000  1
 0.48847542E+01 0.21723956E-02-0.82806906E-06 0.15747510E-09-0.10510895E-13  2
 0.23164983E+04-0.11741695E+00 0.39440312E+01-0.15854290E-02 0.16657812E-04  3
-0.20475426E-07 0.78350564E-11 0.28966179E+04 0.63119917E+01             4
HCNO              BDEA94H  1N  1C  1O  1G  300.000  5000.000  1382.000  1
 6.59860456E+00 3.02778626E-03-1.07704346E-06 1.71666528E-10-1.01439391E-14  2
 1.79661339E+04-1.03306599E+01 2.64727989E+00 1.27505342E-02-1.04794236E-05  3
 4.41432836E-09-7.57521466E-13 1.92990252E+04 1.07332972E+01             4
HOCN              BDEA94H  1N  1C  1O  1G  300.000  5000.000  1368.000  1
 5.89784885E+00 3.16789393E-03-1.11801064E-06 1.77243144E-10-1.04339177E-14  2
-3.70653331E+03-6.18167825E+00 3.78604952E+00 6.88667922E-03-3.21487864E-06  3
 5.17195767E-10 1.19360788E-14-2.82698400E+03 5.63292162E+00             4
HNCO              BDEA94H  1N  1C  1O  1G  300.000  5000.000  1478.000  1
 6.22395134E+00 3.17864004E-03-1.09378755E-06 1.70735163E-10-9.95021955E-15  2
-1.66599344E+04-8.38224741E+00 3.63096317E+00 7.30282357E-03-2.28050003E-06  3
-6.61271298E-10 3.62235752E-13-1.55873636E+04 6.19457727E+00             4
NCO               EA 93 N  1C  1O  1       G  200.000  6000.000  1000.000  1
 0.51521845E+01 0.23051761E-02-0.88033153E-06 0.14789098E-09-0.90977996E-14  2
 0.14004123E+05-0.25442660E+01 0.28269308E+01 0.88051688E-02-0.83866134E-05  3
 0.48016964E-08-0.13313595E-11 0.14682477E+05 0.95504646E+01             4
CN                HBH92 C  1N  1          G  200.000  6000.000  1000.000  1
 0.37459805E+01 0.43450775E-04 0.29705984E-06-0.68651806E-10 0.44134173E-14  2
```

```
   0.51536188E+05 0.27867601E+01 0.36129351E+01-0.95551327E-03 0.21442977E-05       3
  -0.31516323E-09-0.46430356E-12 0.51708340E+05 0.39804995E+01                       4
HCNN              SRI/94C   1N   2H   1      G   300.000  5000.000  1000.000          1
  0.58946362E+01 0.39895959E-02-0.15982380E-05 0.29249395E-09-0.20094686E-13         2
  0.53452941E+05-0.51030502E+01 0.25243194E+01 0.15960619E-01-0.18816354E-04         3
  0.12125540E-07-0.32357378E-11 0.54261984E+05 0.11675870E+02                        4
N2                121286N   2                G   300.000  5000.000  1000.000          1
  0.02926640E+02 0.14879768E-02-0.05684760E-05 0.10097038E-09-0.06753351E-13         2
 -0.09227977E+04 0.05980528E+02 0.03298677E+02 0.14082404E-02-0.03963222E-04         3
  0.05641515E-07-0.02444854E-10-0.10208999E+04 0.03950372E+02                        4
AR                120186AR   1                G   300.000  5000.000  1000.000          1
  0.02500000E+02 0.00000000E+00 0.00000000E+00 0.00000000E+00 0.00000000E+00         2
 -0.07453750E+04 0.04366000E+02 0.02500000E+02 0.00000000E+00 0.00000000E+00         3
  0.00000000E+00 0.00000000E+00-0.07453750E+04 0.04366000E+02                        4
C3H8              L 4/85C   3H   8           G   300.000  5000.000  1000.000          1
  0.75341368E+01 0.18872239E-01-0.62718491E-05 0.91475649E-09-0.47838069E-13         2
 -0.16467516E+05-0.17892349E+02 0.93355381E+00 0.26424579E-01 0.61059727E-05         3
 -0.21977499E-07 0.95149253E-11-0.13958520E+05 0.19201691E+02                        4
C3H7              L 9/84C   3H   7           G   300.000  5000.000  1000.000          1
  0.77026987E+01 0.16044203E-01-0.52833220E-05 0.76298590E-09-0.39392284E-13         2
  0.82984336E+04-0.15480180E+02 0.10515518E+01 0.25991980E-01 0.23800540E-05         3
 -0.19609569E-07 0.93732470E-11 0.10631863E+05 0.21122559E+02                        4
CH3CHO            L 8/88C   2H   4O   1       G   200.000  6000.000  1000.000          1
  0.54041108E+01 0.11723059E-01-0.42263137E-05 0.68372451E-09-0.40984863E-13         2
 -0.22593122E+05-0.34807917E+01 0.47294595E+01-0.31932858E-02 0.47534921E-04         3
 -0.57458611E-07 0.21931112E-10-0.21572878E+05 0.41030159E+01                        4
CH2CHO            SAND86O   1H   3C   2       G   300.000  5000.000  1000.000          1
  0.05975670E+02 0.08130591E-01-0.02743624E-04 0.04070304E-08-0.02176017E-12         2
  0.04903218E+04-0.05045251E+02 0.03409062E+02 0.10738574E-01 0.01891492E-04         3
 -0.07158583E-07 0.02867385E-10 0.15214766E+04 0.09558290E+02                        4
HCO+              121286H   1C   1O   1E  -1G  0300.00   5000.00   1000.00            1
  0.03692074E+02 0.03454732E-01-0.01316524E-04 0.02323551E-08-0.01554132E-12         2
  0.09890941E+06 0.02330722E+02 0.02496483E+02 0.08690658E-01-0.01060445E-03         3
  0.07882791E-07-0.02418385E-10 0.09915097E+06 0.08048178E+02                        4
!E                120186E   1                G  0300.00   5000.00   1000.00            1
! 0.02500000E+02 0.00000000E+00 0.00000000E+00 0.00000000E+00 0.00000000E+00         2
!-0.07453749E+04-0.01173403E+03 0.02500000E+02 0.00000000E+00 0.00000000E+00         3
! 0.00000000E+00 0.00000000E+00-0.07453750E+04-0.01173403E+03                        4
HCO+                      C   1H   1O   1E  -1G   290.15  20000.00   3654.180          1
  0.69157265E+01 0.16631107E-03-0.18476343E-07 0.90856429E-12-0.16454441E-16         2
  0.96129333E+05-0.18089510E+02 0.28762768E+01 0.49486020E-02-0.23085306E-05         3
  0.51121752E-09-0.43520631E-13 0.99130022E+05 0.65020266E+01                        4
H3O+                      H   3O   1E  -1     G   290.15  20000.00   5430.900          1
  0.89508803E+01 0.25281668E-03-0.24594397E-07 0.10878318E-11-0.18090837E-16         2
  0.64480749E+05-0.33873319E+02 0.26885232E+01 0.54453654E-02-0.17055566E-05         3
  0.24833293E-09-0.13769440E-13 0.70890268E+05 0.63608217E+01                        4
E  selle                  E 1 00 00   0 G     00.00  30100.00  27300.000              1
```

```
  0.25000000E+01 0.00000000E+00 0.00000000E+00 0.00000000E+00 0.00000000E+00    2
 -0.74537500E+03-0.11733975E+02 0.25000000E+01-0.81502608E-17 0.13029867E-20    3
 -0.72648333E-25 0.13066247E-29-0.74537500E+03-0.11733975E+02                   4
C2H3O+               C   2H   3O   1E  -1G   200.00   6000.000   1000.000       1
  0.53137165E+01 0.91737793E-02-0.33220386E-05 0.53947456E-09-0.32452368E-13    2
  0.76901865E+05-0.16757558E+01 0.40358705E+01 0.87729487E-03 0.30710010E-04    3
 -0.39247565E-07 0.15296869E-10 0.77864832E+05 0.78617682E+01                   4
O2-                            O   2E  +1G   290.15   6000.000   2008.710       1
  0.42592867E+01 0.22468072E-03-0.51397955E-07 0.73545978E-11-0.38558652E-15    2
 -0.72426252E+04 0.47599697E+00 0.31021718E+01 0.27980875E-02-0.22651126E-05    3
  0.86916517E-09-0.12721884E-12-0.68074793E+04 0.67609020E+01                   4
OH-                            H   1O   1E  +1G   290.15   6000.000   1000.000   1
  2.83405701E+00 1.07058023E-03-2.62459398E-07 3.08376435E-11-1.31383862E-15    2
 -1.80186974E+04 4.49464762E+00 3.43279956E+00 6.19656310E-04-1.89930992E-06    3
  2.37365946E-09-8.55103755E-13-1.82613086E+04 1.06053670E+00                   4
CHO2-                          H   1C   1O   2E  +1G   290.150 5000.000 1000.000 1
  5.97791811E+00 3.24247847E-03-1.46666291E-06 2.91808902E-10-2.10704956E-14    2
 -5.81813435E+04-7.12854015E+00-3.01936623E+01 2.54607495E-01-6.43484728E-04    3
  6.92943698E-07-2.65871657E-10-5.36791044E+04 1.47958586E+02                   4
O-   RUS 890                   O   1E  +1        G   290.150 6000.000 1000.000   1
  2.54474868E+00-4.66695419E-05 1.84912310E-08-3.18159131E-12 1.98962894E-16    2
  1.14822713E+04 4.52131018E+00 2.90805921E+00-1.69804907E-03 2.98069956E-06    3
 -2.43835127E-09 7.61229313E-13 1.14138341E+04 2.80339097E+00                   4
C2                             C   2            G   290.000 5000.000 1000.000   1
  0.04135978E+02 0.06531618E-03 0.01837099E-05-0.05295085E-09 0.04712137E-13    2
  0.09967272E+06 0.07472923E+01 0.06996045E+02-0.07400601E-01 0.03234703E-04    3
  0.04802535E-07-0.03295917E-10 0.09897487E+06-0.13862268E+02                   4
CH*                            C   1H   1        G   200.000 6000.000 1000.000   1
  2.78220752E+00 1.47246754E-03-4.63436227E-07 7.32736021E-11-4.19705404E-15    2
  1.04547060E+05 5.17421018E+00 3.47250101E+00 4.26443626E-04-1.95181794E-06    3
  3.51755043E-09-1.60436174E-12 1.04334869E+05 1.44799533E+00                   4
OH*                  RUS 78O   1H   1        G   200.000 6000.000 1000.000       1
  2.75582920E+00 1.39848756E-03-4.19428493E-07 6.33453282E-11-3.56042218E-15    2
  5.09751756E+04 5.62581429E+00 3.46084428E+00 5.01872172E-04-2.00254474E-06    3
  3.18901984E-09-1.35451838E-12 5.07349466E+04 1.73976415E+00                   4
C2H5OH               L 8/88C   2H   6O   1    0G   200.000 6000.000 1000.000     1
  0.65624365E+01 0.15204222E-01-0.53896795E-05 0.86225011E-09-0.51289787E-13    2
 -0.31525621E+05-0.94730202E+01 0.48586957E+01-0.37401726E-02 0.69555378E-04    3
 -0.88654796E-07 0.35168835E-10-0.29996132E+05 0.48018545E+01-0.28257829E+05    4
END
```

Appendix

G.   High Voltage Power Supply Paper

A supervised visiting researcher project.

8th U. S. National Combustion Meeting
Organized by the Western States Section of the Combustion Institute
and hosted by the University of Utah
May 19-22, 2013

The Influence of Electric Field Power Systems on Flame Behavior

Koji Yamashita[1]   Yu-Chien Chien[2]   Sunny Karnani[2]   Derek Dunn-Rankin[2]

[1]Department of Mechanical Engineering
Aoyama Gakuin University, Tokyo, Japan
[2] Department of Mechanical and Aerospace Engineering
University of California, Irvine, California 92697-3975

   This paper describes the effect of the electric field generated by two different high voltage power supplies on a coflowing jet flame. The paper is motivated by the increased availability of low-cost high-voltage power supplies and the question of whether their performance characteristics are suitable for flame-generated chemi-ion current measurements (nano/microamp) in sensitive environments. Economical designs, which may involve removing active current sinking components, can compromise a power supply's ability to respond on the millisecond time scales that have made the electric actuation of flames a unique approach to combustion sensing and control. The influence of several factors on the measured ion current, including rise time to a desired set point, precision and drift of the applied voltage, and voltage ripple, are important. Experiments are conducted using a small coflowing jet flame and two different power supplies; one supply is a high performance laboratory grade device and the other an inexpensive compact and lightweight unit. Methane is selected as the fuel source in order to reduce the potentially confounding influence of soot. Flame behavior is characterized optically and by the measured ion current. Optical measurements show the flame response and the response of the surrounding thermal field.

1. Introduction

   Utilizing electric fields is one of the interesting methods available to change flame behavior on short timescales. Electric fields have been shown to affect soot formation and transport, flame character, stabilization and extinguishment [1-3]. Under the conditions where the flame is strongly influenced by the electric field, it is likely that the involved electrical components, such as the power supply, need to have adequate capabilities with respect to the flame response.

   The flame has electrical character because of charge carriers created during chemical combustion reactions. For example, H_3O^+ is the most dominant charged specie that can survive the reaction zone when an external field is applied; it has much higher concentration than other ions such as $C_2H_3O^+$ and $C_3H_3^+$ in hydrocarbon flames [4]. Negative charge carriers in flames are mostly electrons but once leaving the flame may attach to other molecules and form negative ions. Electrons do not play a major role in the electrical actuation of flames because the high mobility limits the body force applied to the neutral gas. When placed in an electric field, charged species accelerate along a gradient towards the electrode of opposite polarity. The increased kinetic energy, which results from

electric field work over each mean free path, is transferred to neutral molecules through collisions, Charged particles therefore continuously lose and regain kinetic energy. The net direction of ion drift is from positive to negative polarity when positive ions are dominant in the flame. This ion behavior is sometimes called "Ion driven wind" [5].

The ion driven wind in small flames is on the order of meters/second and so it is confounded by natural convection under 1g conditions [6]. For this reason, micro- or zero-gravity experiments are desirable to investigate this subject. The Advanced Combustion via Microgravity Experiments (ACME) project of NASA encompasses a group of non-premixed flame experiments that require a microgravity environment. The E-FIELD experiment, within the ACME project, is focused on understanding and utilizing electrical effects of flames. In preparation for operation of E-FIELD aboard the International Space Station, this paper explores the similarities and differences between flame behavior when actuated by a typical laboratory high-voltage power supply and a lightweight compact power supply that is suitable for use in spaceflight experiments. In particular, there are some open questions regarding the relationship between temporal response of the power supply generating the potential gradient between the electrodes and that of the flame behavior. As mentioned earlier, micro- or zero-gravity experiments are needed for absolute certainty on this subject, but this paper begins to explore this relationship in the 1g laboratory environment. The paper compares the response of two power systems and the effects of that response on a small co-flow diffusion methane/air flame. The comparison includes measurements of voltage, ion current, and flame shape.

2. Methods

A co-flow burner is used for creating a small diffusion flame. It is produced with two stainless-steel double cylinders. The inner diameter is 2.13 mm and the outer diameter is 25 mm. The fuel flows through the inner tube. Air goes into the outer tube through a honeycomb mesh which is installed at the outlet in order to make the airflow more uniform. Further details on the burner can be found in [8]. A schematic of the experiment is shown in Figure 1.
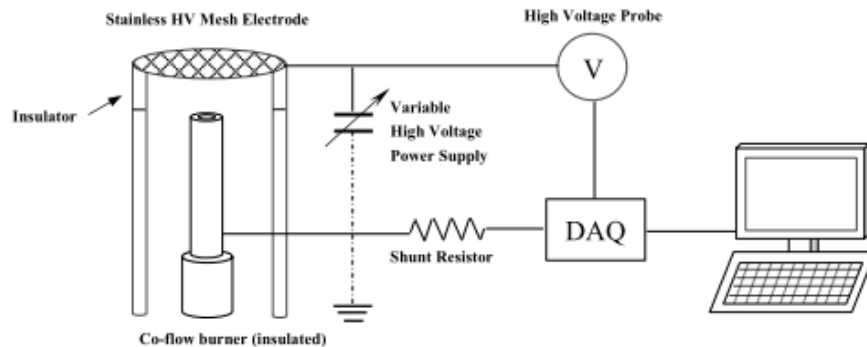
Figure. 1 Experimental schematic

Applying a large potential difference between the burner and a wire mesh 2.5 cm above the burner creates the electric field. The burner and mesh are insulated and isolated electrically. The field strength E is approximately determined as E=V/d [kV/cm] where d represents the distance between the mesh and the top of the burner. The potential drop across a shunt resistor, placed between the

234

burner and electric ground, is measured and related to ion current using Ohm's Law. Two high voltage power supplies are used in the comparison: A high performance laboratory grade device (TREK Model 609A-3) and an inexpensive compact and lightweight unit (UltraVolt HVPS Models 20A12-P4-F-M-C-AS and 20A12-N4-F-M-C-AS). Both supplies have a -10 kV to +10 kV voltage range. The UltraVolt power supplies are planned for the electric field combustion experiment in the ACME project. High-speed flame movies are taken with a Casio EX-F1 camera.

3. Results and Discussion

Power supplies capabilities

Figure 2 shows the power supply response time when large and small step inputs are requested: (a) asking for maximum output voltage from minimum output voltage (i.e. -10 kV - +10 kV), (b) asking for a 100 V step from 0 V. It should be noted that both responses have an approximately 4 ms delay between the request and reaction. This constant delay is the time that the control voltage needs to respond. In Fig. 2(a), the TREK shows that the output voltage rises almost vertically and immediately reaches the requested voltage with a small overshoot while the HVPS voltage rises slowly after the control voltage is applied. This curve asymptotically approaches the requested voltage. The HVPS requires time to respond between its own two supplies, one generating positive and the other generating negative voltage. Small fluctuations can be seen in the positive output region. In Fig. 2(b) with a small step request (100 V), the HVPS has quite a large ripple with an amplitude equivalent to the requested voltage.

The comparison of the rise time is a typical way to discuss the system response. In this paper, the rise time is defined as the time between 10% to 90% of the step height, which means -8 kV to +8 kV in those systems for the largest voltage step. The TREK response is on the order of milliseconds, while the HVPS takes approximately 100 ms.
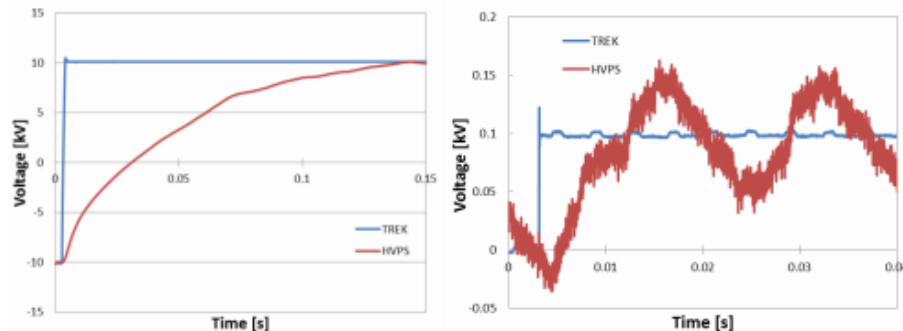
Figure. 2 Electric response to a step input for both supplies; (a) large step: -10kV to 10kV, (b) small step: 0V to 100V

Figure 3 shows the ramp response using a 1kV square wave signal with different cycle time, 200 ms, 100 ms and 50 ms respectively. The HVPS has an approximately 200 V overshoot before settling to the 1 kV request voltage. On the TREK side, the overshoot is much smaller and can be neglected (about 10 V). The HVPS maintains agreement with the requested voltage for 200 ms and 100 ms cycles, and the response starts delaying for 50 ms steps. The TREK is able to work with accurate response for nearly all conditions.

Figure 4 illustrates the voltage response when stepping up and down the request voltage in 500 V increments between 5kV and 0V (in a large triangle profile). This series mimics what will be a voltage-current characteristic curve sweep in the E-FIELD experiment. The steps are taken at higher frequency than the square wave according to the narrower stepping increment; Figure 4 (a_1), (b_1), and (c_1) show results with steps of 20 ms, 10 ms, and 7.5 ms each cycle; and (a_2), (b_2), and (c_2) show the same results but focused near the peak of the triangle profile. With the requested step getting smaller, the HVPS responds slower with higher cycle rates. The voltage overshoots and starts to fall before the value has converged to the request value; the step shape is no longer a square in (b), and (c). The TREK can reach the requested voltage, and its value converges immediately. Its voltage is a little higher than the requested voltage but the difference is not significant. The TREK can safely be used, therefore, as the ideal response case system for comparison.

As mentioned before, the HVPS shows good agreement on 100 ms timescales. However, this timescale is approximately the same as that associated with the buoyant flows, making it difficult in 1g to distinguish the effects of the power supply and that of the flame.
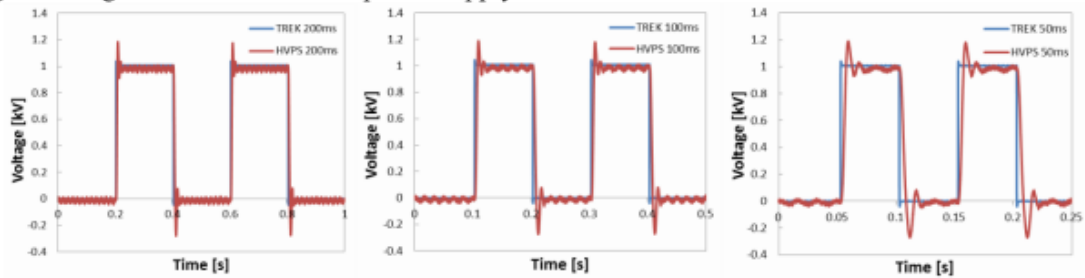
Figure. Three 1kV square wave with different cycles; (a) 200ms, (b) 100ms and (c) 50ms
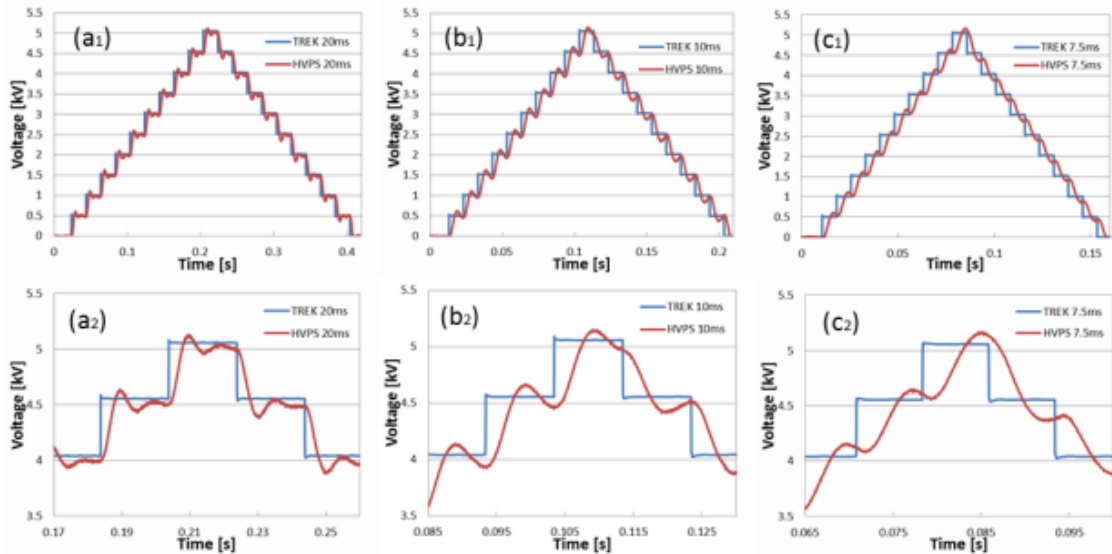
Figure. 4 500 V step response asked for 5kV and back to 0 V with different cycles; (a_1) 20 ms, (b_1) 10 ms, and (c_1) 7.5 ms and (a_2), (b_2), and (c_2) are detailed portion from above.

236

Ion current

Before discussing the ion current, the direction of the electric field needs to be defined. The high voltage power supply is wired to an insulated and isolated mesh above the burner. The output voltage is applied on the mesh, making the mesh the active potential surface. The burner is also isolated from the surroundings but it is kept at zero potential. For this reason, the definition of the polarity is based on the voltage applied to the upper mesh in this paper. Because of the presence of charged particles in the combustion field, a flame and its neutral gas surroundings can be regarded as a complex electrical resistor. The ion current is one of the significant characteristics describing the flame in an electric field since it reflects the resistance to current flow at a given voltage. The saturation ion current for the small diffusion flame in this set of experiments is on the order of a few microamps.

The measured steady ion current with five different flow conditions are shown as VCC (Voltage-Current Characteristic) curves in Figure 5, where (a) represents the entire data set, and (b) and (c) represent detailed positive and negative regions, respectively. The figure shows the typical distinct three regions of the ion current behavior in a flame. At first, the ion current rises (or falls) following a quadratic curve with increasing field strength. Then it reaches a plateau region and stops rising. With increasing field strength, the ion current rises again, following a parabolic curve until the flame blows off (upward directed ion driven wind – negative mesh) or is extinguished (downward directed ion driven wind – positive mesh). Those three regions are called the subsaturation region, the saturation region, and the supersaturation (or secondary ionization) region, respectively. The supersaturation region is often complicated by corona discharge effects from the burner and mesh so it often better to avoid the extreme voltages when trying to understand the electrical aspects of the flame alone.

The results in Figure 5 demonstrate that both supplies correspond to each other in the saturation region. However, there are considerable differences in the other regions. The ion current measured using the HVPS rises (or falls) with smaller field strength in the subsaturation and supersaturation regions. Therefore transition points in between the regions appear at lower field strength with the HVPS. That trend is more significant under the higher flow condition. The power supplies are in good agreement with each other under the lower flow speed condition. This is a promising finding for the zero-gravity studies planned because electrical effects and their competition with buoyancy are much more pronounced when there is lower forced convective momentum.

The flame response in terms of ion current is shown in Figure 6 following a step input from 0 V to 5 kV. The initial spike observed in the TREK case corresponds to the capacitance of the burner/mesh electrode system. The current then decays to a steady value representative of the flame/electrode gap space. This phenomenon was characterized fairly extensively in [9]. The rising ion current after the initial spike is likely due to the flame finding a new accommodation with the ion driven wind. The flame then settles to a steady condition after 30-40 ms. The HVPS results show a much less prominent spike because the slower response time does not engage the small system capacitance. It is very interesting to note, however, that the settling time of the ion current, and its ultimate value matches very well the results obtained when using the TREK. The insensitivity results because the requested voltage of this measurement is in the saturation region where the ion current does not rise with electric field strength. Therefore, the electric response is largely unaffected by the power supply response time. This a fortuitous condition that provides an important opportunity to maximize the

understanding of flame behavior even when using a slow responding power supply. That is, operating with step changes between saturated regions can create more rapid response changes in the ion current than is strictly available in the voltage.
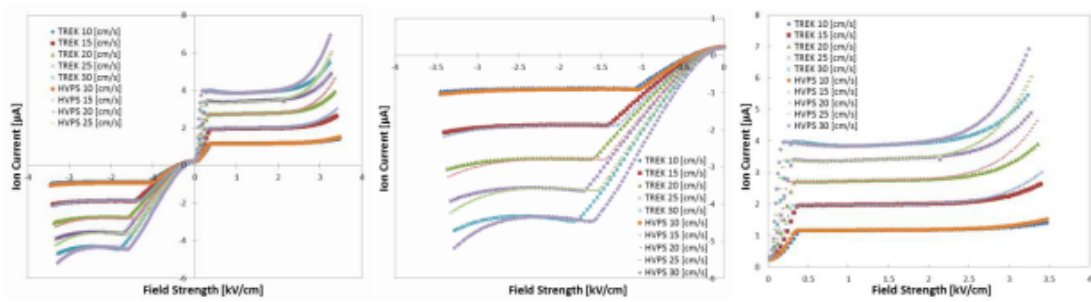
Figure. 5 VCC curve under the different flow speed conditions; (a) overall, (b) detailed negative polarity, (c) detailed positive polarity
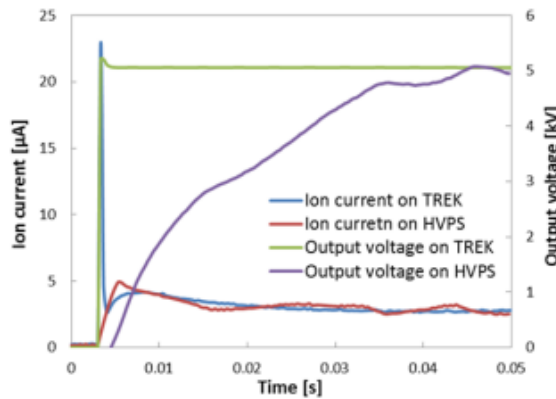
Figure. 6 Ion current response comparison asking for 5 kV step input on two supplies

Visualized flame response

While there is experimental verification that the ion current response between the two power supplies is quite similar in time, the connection between this ion current and the flame behavior is still needed. Visualized flame response following steps of voltage using the TREK and the HVPS are illustrated in Figure 7. The images are extracted from flame videos captured with a camera filming at a rate of 300 fps. Starting with an initially negative potential applied at the mesh, a positive step voltage is then applied, which produces an increasing voltage range from -9 kV to +9 kV. A LED light is placed right next to the flame to indicate when the control voltage is applied from the power supplies in order to set the zero time on the images.

The results show that the TREK takes about 20.3 ms while the HVPS takes 130 ms to reach +9 kV (Figure 7). Generally, the flame is stabilized while the high voltage is applied. When the mesh is negative, the flame is extended vertically upward, and it becomes thinner. Conversely, while the mesh is positive, a downward wind is imposed, opposing natural convection. While only qualitative, it appears from Figure 7 that with a simple time stretching the flame character matches between the two power supplies. This is slightly different from the ion current finding, which would have

indicated that the flame response time should be unaffected. The difference is that in the -9 kV to 9 kV test the step is not into a saturated ion current condition but between two conditions in the supersaturated regions. In this circumstance, there will be sensitivity in the ion current. In any case, the still images are slightly misleading, and the high speed movies show more dynamic processes. In the TREK case, for example, the video shows that the flame is stabilized just 10 ms after the polarity is reversed. The flame transitions smoothly with little fluctuation from the narrow stretched shape with the upward wind to the flattened shape with the downward wind. On the other hand, when using the HVPS, the flame takes more than 100 ms to stabilize, and it continues to exhibit oscillations. With this slower responding power supply, the flame development seems separated into two stages where the flame reacts quickly at first and then slowly widens. This behavior corresponds to the electric response of the HVPS shown in Figure 2. The high voltage ripple in the output is likely responsible for the oscillations. The ripple does not affect the steady state ion current results because they are average values. Further study is needed but the dynamic differences noted above are consistent with considering the flame an active element of the system with a response time on the order of 30 ms [10,11]. In the TREK case, the flame finds itself instantaneously facing an electric field condition that it then accommodates with a self-consistent change in shape and ion current generation. In the case of the HVPS the environment conditions (i.e., the electric field imposed) is continually changing as the flame tries to accommodate the variation. This leads naturally to a more unstable behavior, particularly when the field is coupled with the ion current response.
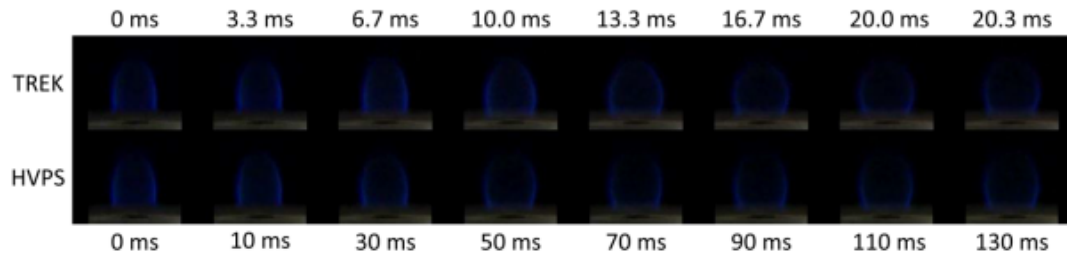
Figure.7 Flame response from -9kV to +9kV on two supplies

4. Conclusions

  This work contributes to clarifying the interaction between electric forcing and flame behavior. The data helps provide information that can be used to create a transfer function between flame and electric supply system. Ultimately, the goal of this research is to describe the relationship between flames and an imposed electric field with sufficient clarity to allow active control. More immediately, the results show that there are conditions where a slower responding power supply can provide reliable performance in an electrically actuated flame system. In particular, these conditions include steady averaged VCC sweeps and step changes between saturated ion current conditions. These findings will certainly contribute to more effective use of the data to be obtained during the International Space Station ACME experiments.

Disclaimer
Product names and models are provided only for clarification and are in no way an endorsement on the part of NASA or the federal government.

References
1. J. Kuhl, G. Jovicic, L. Zigan, and A. Leipertz. Study of laminar premixed flame in transient electric fields using PLIF and PIV techniques. 16th International Symposium on Applications of Laser Techniques to Fluid Mechanics, July 09-12 2012.

2. Y. Wang, G. Nathan, Z. Alwahabi, K. King, K. Ho, and Q. Yao. Effect of a uniform electric field on soot in laminar premixed ethylene/air flames. Combustion and Flame, 157(7):1308–1315, 2010.

3. S. Won, S. Ryu, M. Kim, M. Cha, S. Chung, "Effect of electric fields on the propagation speed of tribrachial flames in coflow jets" Combustion and Flame, 152, 496-506, 2008.

4. T. Pedersen and R.C. Brown, (1993) "Simulation of electric field effects in premixed methane flames" *Combust. Flame*, 94, 433–448.

5. J. Lawton and F. J. Weinberg, (1969) "Electrical Aspects of Combustion" Clarendon Press. Oxford.

6. S. Karnani, D. Dunn-Rankin, F. Takahashi, Z.-G. Yuan, and D. Stocker. Simulating gravity in microgravity combustion using electric fields. Combustion Science and Technology Special Issue: The 23rd International Colloquium on the Dynamics of Explosions and Reactive Systems, 184(10-11), 2012.

8. S. Karnani, and D. Dunn-Rankin, "Electric field effects on a small co-flow diffusion flame" In Proceedings of the 6th U.S. National Combustion Meeting, Ann Arbor, MI, May 17-20, 2009.

9. F. Borgatelli, and D. Dunn-Rankin, (2006) "Feedback Control of Ion Current from a Small Diffusion Flame," Paper 06S-44, Western States Section/The Combustion Institute Spring Meeting, University of Idaho, Boise, March 27--28.

10. M.J. Papac, and D. Dunn-Rankin, "Modeling Electric Field Driven Convection in Small Combustion Plasmas and Surrounding Gases," Combustion Theory and Modeling, 2007.

11. F. Borgatelli, D. Dunn-Rankin, "Behavior of a small diffusion flame as an electrically active component in a high-voltage circuit" Combustion and Flame, 159, 210-220

12. Y.C. Chien, D. Dunn-Rankin, "Electric Field Effects on Carbon Monoxide Release from Impinging Flames", 8th US National Combustion Meeting, 2013